Localised structures in reaction-diffusion equations

By

FAHAD SAIF HAMOOD AL SAADI

Department of Engineering Mathematics
UNIVERSITY OF BRISTOL

A dissertation submitted to the University of Bristol in accordance with the requirements of the degree of DOCTOR OF PHILOSOPHY in the Faculty of Engineering.

July 11, 2022

Abstract

This thesis is concerned with reaction-diffusion systems in one-dimensional infinite domains. Using the theory of spatial dynamics, in which time is represented by the spatial coordinates of a state, it can be analysed whether or not localised patterned states exist and are stable. In essence, this dissertation addresses two major objectives.

Our first objective is to illustrate the relation between the theory of homoclinic snaking and other theories of the from-equilibrium formation of localised patterns; so called semi-strong interaction asymptotic analysis. We demonstrate how these different paradigms fit together within a class of activator inhibitor-systems that include the commonly studied examples such as the Brusselator and Schnakenberg models. An essential contribution is a demonstration that in the limit of an infinite domain, using a semi-strong asymptotic analysis allows the calculation to provide a large amplitude exponentially localised pattern arising from the bifurcation at a fold. As part of this work, we also demonstrate a universal two-parameter bifurcation diagram that emerges for a wide class of models of the activator-inhibitor type. We also investigate the stability of these localised patterned states and the instability mechanisms. Moreover, we illustrate that bifurcation diagrams that appear in Schnakenberg-like models can also appear in other models with more complex nonlinear terms, including Gray-Scott, Gierer-Meinhardt and predator-prey models.

The second objective of this study is to investigate what can be learned about cell polarisation from various experimental models of activator-inhibitor type that have been proposed in the literature. These models typically have two activator and two inhibitor fields. Our study investigates the polarisation models of cells within two distinct regimes, in which the amount of protein is either conserved or not conserved. In the non-conservative regime, two types of patterns are obtained; interleaved and overlaid. The temporal stability analysis shows that the localised patterns created in the interleaved case are stable. Compared to the overlaid pattern, the localised patterns are unstable and evolve into interleaved case. Passing to the mass conservation limit also suggests a novel mechanism for creation heteroclinic states.

The conservative regime exhibits several distinct equilibrium solutions that can be characterised using catastrophe theory. We specify the conditions under which these steady states are destroyed and the forms of heteroclinic connection created and destroyed during this process. As a final step, we provide numerical simulations for the entire PDE system which indicate how distinct polarised states arise as a result of different total initial concentration.

Dedication and acknowledgements

I thank Allah for providing me with tolerance, strength, and the ability to complete this thesis.

My sincere gratitude goes out to Alan Champneys, my incredible supervisor, for supporting, encouraging, and nurturing me into an independent researcher.

I would also like to extend my deep gratitude to my wife and my four children, Ahmed, Maryam, Mahmood, and Mohammed, for doing so much to make my academic career as successful as it was. Their love, support, and encouragement always helped me in this journey. I wish to take this opportunity to express my appreciation for the support, love, and prayers that have been extended to me by my father, mother, siblings and all my family in Oman.

I would like to express my gratitude to my collaborators Mark Nelson, Mike Jeffery, Nicolas Verschueren van Rees, Pedro Parra-Rivas, Theodore Kolokolnikov, Chunyi Gai, Haifaa Alrihieli, and Ahmed Msmali. Also, I would like to convey my special gratitude to Annette Worthy for her support and encouragement. It was her who had introduced me to nonlinear dynamics.

I would like to thank everyone at the University of Bristol who has made it an enjoyable place to work. During my time in Bristol, I have had the opportunity to meet many interesting people, Hilal, saud, Noah, Aron, Zohar, Ben, Robert, Tom, Stanislaw, Debraj, Simon and Sophie. Special thanks go to Seeralan Sarvaharman for all those stimulating discussions. I would also like to thank everyone at Military Technological College who has supported me during my study in Bristol.

Last but not least, I would like to express my sincere thanks to the University of Bristol for providing such a comfortable, educational environment for a postgraduate student. I would also like to thank the Ministry of Higher Education, Research and Innovation, Oman, and the Military Technological College for their financial support.

AUTHOR'S DECLARATION

I declare that the work in this dissertation was carried out in accordance with the requirements of the University's Regulations and Code of Practice for Research Degree Programmes and that it has not been submitted for any other academic award. Except where indicated by specific reference in the text, the work is the candidate's own work. Work done in collaboration with, or with the assistance of, others, is indicated as such. Any views expressed in the dissertation are those of the author.

SIGNED: ..... DATE: .....

Table of Contents

LIST OF TABLES

TABLE **Page**

List of Figures

Figure **Page**

CHAPTER 1

INTRODUCTION

1.1 Introduction

Patterns of regular spatial variation of concentration or density within a seemingly homogenous medium is a phenomenon that is widely observed in nature. These patterns arise from entirely homogenous random backgrounds. The undisturbed background of such patterns does not provide any information to the observer about the final emergent pattern. Over decades, a substantial number of studies have tried to understand the formation of such patterns stemming from the last published work of Alan Turing in 1952 (see also [47] for information on Turing's further results that were unpublished at the time of his death). The instability that bears his name, also known as a diffusion-driven instability, occurs when an activator chemical species or component of the medium diffuses more slowly than a separate inhibitor component. Starting from a stable homogeneous equilibrium state under equal diffusion rates, Turing instability occurs upon varying the ratio of diffusion constants, when the growth rate associated with a critical wavenumber of a perturbation becomes positive. Typically, at least in one spatial dimension, this corresponds to a supercritical pitchfork bifurcation of steady-state solutions, leading to the onset of spatially periodic patterns, see e.g. [112, 119]. In two or more spatial dimensions, depending on the shape of the domain and boundary conditions, many different forms of pattern can be obtained, see e.g. [172] and references therein.

Many reaction-diffusion models of activator-inhibitor type have been proposed in different fields such as physics, biological science, chemistry and ecology [98, 105, 120, 150]. Widely studied examples of such models include the Schnakenberg [143], Gierer and Meinhardt [69], Gray-Scott [71] and Brusselator [62] systems. All these models have been used to study pattern formation and the localisation of stripes, spots, etc, as well as their instability leading to complex spatio-temporal behaviour.

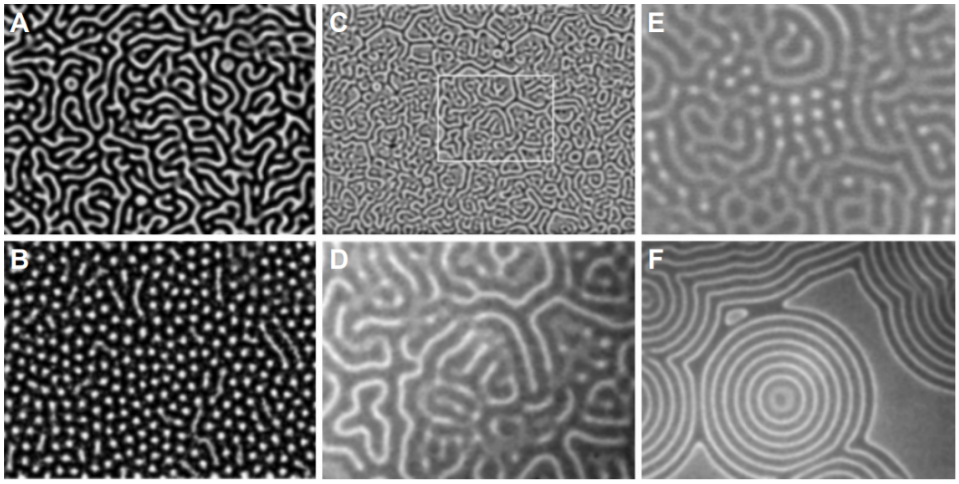

Figure 1.1: Examples of patterns in the BZ-AOT chemical reaction system; adapted from [163].

Figure 1.2: Examples of biological patterns observed in nature; adapted from [107].

An example of pattern formation in a chemical laboratory system is the BZ-AOT (Belousov Zhabotinsky reaction in a water-in-oil microemulsion), see e.g. [34] for experimental details and for how the system can be modelled mathematically. This experiment demonstrates various patterns, such as Turing patterns [160], oscillons [162] and spirals [161] see Figure 1.1.

In biology, the term pattern formation is too broad. We can observe it in both internal and external contexts. The external context studies the exterior structures like spots and stripes in animal skins, see e.g. [92]. The internal context considers the variation that within organs, tissues or individual cells results from the mechanical-chemical interaction, see e.g. [119]. Examples of Turing patterns which emerge in biology are shown in Figure 1.2.

1.2 Localised patterns

In recent years attention has been given to localised patterns, which means that the pattern is confined to a portion of the domain with exponential decay into the perifery. In one spatial

dimension these patterns can occur due to what is known as the homoclinic snaking mechanism [20, 171]. Bistability and different diffusion rates between activator and inhibitor are the two main elements for such a theory of localised structure formation [46]. Here, bistability is between stable states of spatially uniform and spatially periodic patterns. In the context of bifurcation theory, a subcritical Turing bifurcation leads to the existence of a small-amplitude unstable pattern and a large-amplitude stable pattern that coexist with a stable homogeneous state [46]. In [171] the homoclinic snaking mechanism is shown to arise as a heteroclinic connection between the homogeneous state and the spatial pattern which causes the expansion of a Maxwell point into a so-called pinning region. A Maxwell point is the point in parameter space where the free energy of the two bistable states are equal. One explanation of the broadening of the Maxwell point is that a finite energy difference is required in order to displace the front connecting the coexisting states by one wavelength of the periodic pattern [134]. This interaction is also known as the pining of spatially periodic fronts. Upon bringing two fronts back to back, a stationary solution is established that consists of a finite domain of a spatial periodic state connected to a background of the flat state. This is known as a spatially localised structure, see e.g [**?**] for an explanation. Moreover, in [32] the authors argue that a broad class of reaction-diffusion systems can generate localised patterns via this mechanism close to a certain codimension-two point where they occur at small amplitude. Furthermore, they argue that subcritical instability leading to localised structure is more robust compared to the normal Turing instability patterns that form from the supercritical bifurcation. This is because the former patterns which are spatially extended are born from zero amplitude, and in a large domain, these patterns are subject to further instability due to mode interaction. On the other hand, in the subcritical case there is a jump with well defined amplitude to a pattern that is localised in the spatial domain. In addition these localised patterns are more robust and hard to destroy under small perturbation in parameters space. This is because of the hysteretic nature of the fold bifurcation underlying the snaking bifurcation.

Another key ingredient of the theory of homoclinic snaking, as typified in scalar partial differential equations (PDEs) such as the Swift-Hohenberg model

$$u_t = f(u) + (q_c^2 + \nabla^2)^2 u,$$

is that there should be competing nonlinear terms, see e.g. the review [89]. For example, the paper [82] was one of the first to contrast the localised patterns seen in fourth-order PDEs with cubic-quintic or quadratic-cubic forms like $f(u) = \alpha u^3 - u^5$ or $f(u) = \alpha u^2 - u^3$, with α a tunable positive parameter. As we shall see in chapter 3, the simplest activator-inhibitor systems such as those due to Schnakenberg [143] or Gray & Scott [71], as well as the so called Brusselator [136],

$$\begin{pmatrix} u \\ v \end{pmatrix}_t = \boldsymbol{c} + A \begin{pmatrix} u \\ v \end{pmatrix} + \begin{pmatrix} 1 \\ -1 \end{pmatrix} u^2 v + \begin{pmatrix} \delta^2 \nabla^2 u \\ \nabla^2 v \end{pmatrix},$$

tend to have a single autocatalytic nonlinear term $\pm u^2 v$ with the sign '+' in the equation for the rate of change of the activator u and the sign '−' in the equation for the inhibitor v. Thus, it might seem that such models are not likely to feature competing nonlinear terms. However, adding constant terms to the linear-cubic kinetics, leads to non-trivial equilibria in the system. Taylor expansion about such an equilibrium leads to quadratic as well as cubic terms, providing the necessary competing nonlinearity for homoclinic snaking.

There are numerous examples of these localised patterns in nature, which in two spatial dimension may occur as such as spotty, hexagonal and target-like patterns. These localised patterns have been reported in a wide range of experiments such as: binary fluid convection [122], plain Couette flow [68], solidification [84], gas discharge [12], optical systems [18, 114], magnetic material [2], ocean circulation [46], optical cavities [63] and desertification [46].

The recent special issue [36] gives an overview in state-of art theory and application of the localised patterns formation due to homoclinic snaking. Here we will report a few examples. In nonlinear optics, the authors of [128] used Lugiato-Lefever equation

$$A_t = -(1 + i\omega)A + iv\partial_x^2 A + i|A|^2 A + S$$

to demonstrate the occurrence of the localised patterns. They consider two regimes: anomalous and normal dispersion. In the first regime, their study shows that the localised patterns formed on the homoclinic snaking which is ultimately destroyed resulting in a foliated snaking. The second regime reveals that the localised patterns undergo a collapsed snaking.

In fluid convection, Alrihieli et al [8] have used the normal form analysis around Takens-Bogdanov bifurcation to show that localised patterns tail can take two different shapes: a trivial and a modulated wave.

Bramburger et al. [29] investigate symmetric and asymmetric localised patterns in a spatially discrete setting. They obtain the localised pattern from the homoclinic snaking and the isolas structures as the continuum case. Also, they show a discrete localised patterns solution posed on a hexagonal lattice, which agrees with the result presented [104] in the continuum case. Another example of the homoclinic snaking in the discrete can be found in [96]

The existence of the homoclinic snaking in a non-reversible system is addressed in [90]. The authors have provided conditions that guarantee the existence of the homoclinic snaking bifurcation.

The study in [109] reports a significant relationship between the localised patterns in networks and the localised pattern formation seen throughout science. Also in [37], the authors presented an extensive review of the how the theory of homoclinic snaking and localised patterns applies in a number of reaction-diffusion systems arising in development biology and in ecology. Part of the contribution of this thesis is to attempt to understand certain universal properties of the organisation and stability of localised patterns in activator-inhibiter systems; keeping our eye on biological motivation.

1.3 Cell polarity

An ultimate motivation for this thesis is to understand models of patterns formation that apply to the morphology of individual cells. Cell polarity is a fundamental and essential aspect of many cell processes; its structure drives all functions that require asymmetry within a cell [126]. Plant cells exhibit various types of polarities leading to complex geometric structure, asymmetric cell growth, division or simply molecules and organelles asymmetric distribution within the cell. Therefore, polarised cells contribute to the patterning via differentiation of tissues and organs [158]. Consequently, polarised cells are involved in the overall shape of the organism. During embryogenesis, animals often establish their adult plan and adapt their behaviour to environmental change. In contrast, plants need to modify their body plan continuously throughout their life cycle to accommodate environmental changes [40]. This is because of the lack of nervous systems in plants [52]. Furthermore, the essential difference between plant cells and animal cells is that the former cannot travel in the tissue during the patterning processes because they are held by a rigid extra-cellular matrix, the cell wall. These differences push the plants to generate alternative mechanisms to control plant development which depend on rearrangement or establishment of cell polarities through processes such as embryogenesis, organogenesis, vascular tissue formation, and regeneration [88, 138]. All these processes organise the connection between polarity of individual cells in the tissue and within the wider tissue.

1.3.1 The biology of cell polarisation

The key plant hormone, auxin, helps regulate the cross-relationship and acts as a polarising signal. Hence, cell polarisation is the primary cellular mechanism for plant growth [52, 100]. In general, cell polarisation is required initiated via an internal or external signal which can cause a break in cell symmetry and start the polarisation event [43, 126]. The auxin pattern distribution can provide just such a signal for establishing cell polarity. In particular, polar auxin transport, which is largely mediated by the PIN-FORME (PIN) auxin efflux carriers, has a significant role in the generation of various polarity formation processes such as polar positioning of root hairs in trophoblast cells [24, 142, 159]. The precise gradient of auxin has been found to activate polar for cell growth in a single cell model such as root hair [30]. These auxin-mediated cell polarisation mechanisms tend to begin via the formation of patches of activated signalling module (PIK-ROP GTPase) known collective as G-proteins or Rhos (in animals) and ROPs (Rhos of plants) in plants; [51, 176]. In this thesis we shall mostly consider plant cells.

Work by Abley et al. [1] in theoretical biology suggests that ROPs hold all essential properties to enable a cell that is initially in homogeneous state to generate a polarity within the cell spontaneously. The guanine of exchange factor (GEFs) and GTPase-activating proteins (GAPs) allow switching to occur between inactive and active form of ROPs, while guanine disassociation inhibitors (GDIs) drive the inactive form to the cytosol [23, 121]. Thus active ROPs are thought

to diffuse more slowly as they are bound to the cell membrane.

In various modelling studies, it has been demonstrated that a system can generate stable polarisation within a cell under two conditions: i) at least a single chemical species must appear in both active and inactive forms, which directly or indirectly enable self-activation; ii) the active form diffusion constant needs to be slower in comparison with inactive form [108, 115]. One particular mechanism that occurs in such system is so-called wave pinning, in which a particular region or multiple cell regions are brought into an active state.This spatial transition between the active and inactive state can be modelled heteroclinic connection between bistable states composed of high and low concentrations of the activated state, see [80, 86, 116] for full explanation. It has been shown how this mechanism can enable a single cell to establish and maintain active localised ROP along with the membrane at different levels even without any localised signal or external perturbation. This process has been shown to be robust to a certain extent [72].

Tissues of plants represent distinct coordination of cell polarities over long domains. Two essential types of coordination, namely, lateral and longitudinal, are defined to guide the understanding of tissue cell polarities [1]. Both the longitudinal and the lateral coordinates can be described as a single file of cells, yet the polarities of the former are aligned from head to tail; whereas, the polarities of the latter are aligned from the lateral to the polarity direction. Both types of coordination can occur in a sheet of cells because each cell's polarity may be regulated with both. The key question here is how lateral and longitudinal coordination patterns are established in an extended domain. Several models attempt to provide an explanation for the establishment of both types of coordination. For instance, the model presented by Simon [147] assumes that the neighbouring cells compare the concentration of a specific molecule and set their polarities accordingly. Another model in plant cells proposes that the polarity of cells depends on the concentration of auxin in the neighbouring cells see e.g. Jönsson [87]. In [67], a model is presented to describe the establishment of polarities through differential molecular interaction at cell interface.

Our concern here though will be another hypothesis as typified by the model of Abley et al. [1], who propose a framework of intracellular partitioning, which suggests that the cells can polarise in the absence of an asymmetric signal or their neighbours polarity. In this model, there is intracellular partitioning via coupling between surrounding cells and operations of tissue polarity organisers. There are three attributes of the intercellular portioning model. First, it can be used to describe the polarity in both animals and plants. Second, it helps create a new polarity coordination model in plants that does not require measuring fluxes, comparing concentrations between cells, responding to physical stresses or measuring of gradients across the cell walls thickness. Third, the model permits the placement of various cell polarity systems in an evolutionary context.

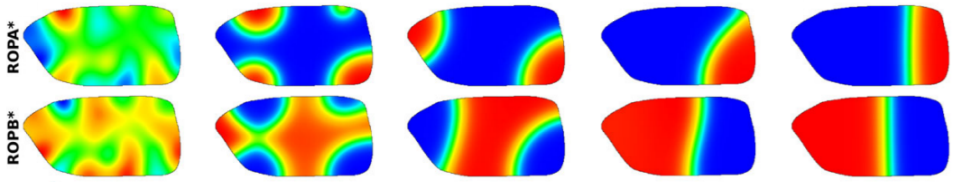

Figure 1.3: Examples for cell polarisation dynamics in 2D through two generic ROPs (A^*, B^*) adapted from [72].

1.3.2 Cell polarity models:

Let us describe the overall model as described in [1] and [72]. To explain how intracellular partitioning may occur, consider a simple system containing two types of molecular components (A, B). Each component may include many molecular entities (types of ROP), but each component is treated as a single entity. These components can be of two types; one is active in the membrane denoted by (A^*, B^*), and the other one is inactive in the cytosol denoted by (A, B). The inactive components in cytosol will diffuse faster than the active components in the membrane. The active components are autocatalytic, which means that A^* promotes A's activation to produce more A^*. There is also cross inhibitory; specifically, A^* reinforces deactivation of B^* and vice versa. Beginning from a homogeneous concentration of polarity components in a cell, then introducing some perturbation into the concentration of the active form (A^*, B^*) may lead to polarity with a high concentration of A^* at one end and high concentration of B^* at the other end. With the initially homogeneous fluctuation of active (A^*, B^*), a disturbance within the cell can lead to orientation from one cell to the next, leading to intracellular partitioning, which causes the polarities, see [1, 72] for more details. Figure 1.3 shows the dynamics of cell polarisation through two generic ROPs (A^*, B^*).

In this thesis, for simplicity, we ar not considering an elongated cell such as trophoblast modulated by a 1D domain which represent the homogenate through the cell's thickness including both membrane and cytosol. The dynamics of this intracellular partitioning includes auto-activation and cross-inhibition is mathematically expressed by the following system of diffusion equations.

$$\frac{\partial A^*}{\partial t} = D_{A^*}\frac{\partial^2 A^*}{\partial x^2} + F(A^*, A, B^*, B), \quad x \in (-l, l), \tag{1.1a}$$

$$\frac{\partial A}{\partial t} = D_A\frac{\partial^2 A}{\partial x^2} - F(A^*, A, B^*, B), \quad x \in (-l, l), \tag{1.1b}$$

$$\frac{\partial B^*}{\partial t} = D_{B^*}\frac{\partial^2 B^*}{\partial x^2} + G(A^*, A, B^*, B), \quad x \in (-l, l), \tag{1.1c}$$

$$\frac{\partial B}{\partial t} = D_B\frac{\partial^2 B}{\partial x^2} - G(A^*, A, B^*, B), \quad x \in (-l, l). \tag{1.1d}$$

Here functions F and G describe the autocatalytic activation step. We suppose $D_{A^*}, D_{B^*} \ll D_A, D_B$ specifically that $D_{A^*} = D_{B^*} = \delta$ and $D_A = D_B = 1$. Since the active and inactive components can

not leave or enter the cell, we enforce the Neumann boundary condition with a 1-dimension slice along which we suppose represent portion of the cells' boundary.

Note the inter-conversion between the ROP components causes a switch between active and inactive forms, yet no components are created or destroyed. Therefore, the total amount of the ROP components within the cell must satisfy conservation statements. Hence,

$$\int_{-l}^{l}(A+A^*)dx = A_T. \tag{1.2}$$

and similar for B component. Based on different choices for F and G, one can obtain different GTPase models that illustrate the intracellular partitioning dynamics. Several of such models have been described in the literature which can be:

- Model I: intracellular partitioning model for tissue cell polarity in plants and animals presented by Abley et al [1]

$$F = \left(\eta A^* + \rho\right)A - \left(\alpha B^* + \mu\right)A^* \tag{1.3a}$$

$$G = \left(\eta B^* + \rho\right)B - \left(\alpha A^* + \mu\right)B^*. \tag{1.3b}$$

  Here α is the cross-inhibition rate between the bound membrane polarity component, η is the auto-activation rate, μ is the membrane unbinding rate, ρ describes the membrane binding rate of polarity component.

- Model II: a modification of the model in [1]:

$$F = \left(\eta A^{*2} + \rho\right)A - \left(\alpha B^* + \mu\right)A^* \tag{1.4a}$$

$$G = \left(\eta B^{*2} + \rho\right)B - \left(\alpha A^* + \mu\right)B^*, \tag{1.4b}$$

  where the parameters α, η, μ and ρ have the same definition as in (1.3).

- Model III: intracellular partitioning model for juicy fruit by Grieneisen et al [72]:

$$F = \left(\beta + \eta\alpha\mu^2 A^{*2}\left(\mu^2 + A^{*2} + B^{*2} + \frac{\alpha}{c_a}\right)^{-1}\right)A - \rho A^*, \tag{1.5a}$$

$$G = \left(\beta + \eta\alpha\mu^2 B^{*2}\left(\mu^2 + A^{*2} + B^{*2} + \frac{\alpha}{c_a}\right)^{-1}\right)B - \rho B^*. \tag{1.5b}$$

  Here α denotes the homogeneous auxin level, β is capturing the auxin-independent basal activation rate, η gives the auto-activation strength, μ is the saturation constant in ROP auto-activation and cross-inhibition, c_a define the saturation constant in activation by auxin and ρ defines the deactivation rate .

- Model IV: mutual inhibition introduced by Holmes et al [80]

$$F = \left(b + \frac{\alpha}{1+B^{*n}}\right)A - dA^*, \tag{1.6a}$$

$$G = \left(b + \frac{\alpha}{1+A^{*n}}\right)B - dB^*. \tag{1.6b}$$

  Here the parameters α and b represent the strength of feedback and basal components, respectively, and d is the rate of GTPase inactivation.

Later in chapter 6 we shall consider the model (1.1) with the inclusion of the source and loss terms for the A and B species similar idea where apply for single species can be found in [165].

1.4 Research goals

The overall focus of this study is on reaction-diffusion systems posed on infinite one-dimensional domains. One can analyse the existence and stability of localised patterned states using the theory of spatial dynamics, in which the spatial coordinate plays the role of time. In this case, a Turing bifurcation can be shown (see e.g. [32]) to be completely analogous to a Hamiltonian Hopf or pattern-formation instability, which gives rise to localised patterns in the form of modulated periodic states. Such homoclinic orbits are the building blocks of the onset of localised patterns through the homoclinic snaking mechanism as described in [171]. The main distinction, though, is that the pattern-formation instability leading to the homoclinic snaking is a *sub-critical* instability, whereas the classical Turing mechanism typically involves a supercritical bifurcation. This thesis has two broad aims.

The first aim is to show connections between the theory of homoclinic snaking [20, 33, 171] and other theories of far-from-equilibrium formation of localised so called semi-strong interacting spikes, these structures have been shown to occur in activator-inhibitor reaction-diffusion system either using matched asymptotics (as in the work of Ward and co-workers [168]) or geometric perturbation theory (as in the work of Doelman and co-workers [56, 58]). We demonstrate through this study how these two theoretical paradigms fit together, using the most common activator-inhibitor systems found in the literature namely the Schnakenberg, Brusselator and related models. In particular, we show how the semi-strong asymptotic analysis applied in the limit of an infinite domain can show the onset of large amplitude exponentially localised patterns through a fold bifurcation. Here semi-strong implies a scaling where the activator field is much more highly localised than the inhibitor. We also show how there are ubiquitous two-parameter bifurcation diagram that emerges for wide class of models of activator-inhibitor type. We also shall seek to explain the stability of these localised patterned states, and to probe instability mechanism.

The second aim of this study is to investigate cell polarisation in various models of activator inhibitor type that have been proposed in the literature. Here, we seek to show how the theory of localised patterns can help explain how ROP dynamics can create a range of spatial patterns that explain the shapes of cells observed in the literature. In this thesis, we utilise two modelling approaches to show whether the dynamics of ROPs may explain cells shapes and migration. The first approach is breaking the mass conservation law by adding generic source and loss terms in model (1.1). The second approach is studying the heteroclinic connections that the ROPs generate in mass-conserved limit and explore how these can underline different forms of polarity.

1.5 Thesis outline

This thesis contains eight chapters, including this one.

In chapter 2, we introduce all the technical methods required throughout this study. These methods include linear stability analysis, weakly nonlinear stability analysis, and various numerical methods for finding, tracing and examing the stability of the localised patterns. All these methods are developed for general n-dimensional system or reaction-diffusion equation in one spatial dimension.

In chapter 3, we study systems of activator-inhibitor reaction-diffusion equations posed on an infinite line using a variety of analytical and numerical methods. A canonical form is considered that contains all known models with simple cubic autocatalytic nonlinearity and arbitrary constant and linear kinetics. Restricting attention to models that have a unique homogeneous equilibrium, this class includes the classical Schnakenberg and Brusselator models, as well as other systems proposed in the literature to model morphogenesis. Such models are known to feature Turing instability, when activator diffuses more slowly than inhibitor, leading to stable spatially periodic patterns. Conversely in the limit of small feed rates, semi-strong interaction asymptotic analysis shows existence of isolated spike-like patterns. Chapter 3 then describes the broad bifurcation structures that connects these two regimes. A certain universal two-parameter state diagram is revealed in which the Turing bifurcation becomes sub-critical, leading to the onset of homoclinic snaking. This regime then morphs into the spike regime, with the outer-fold being predicted by the semi-strong asymptotics. A rescaling of parameters and field concentrations shows how this state diagram can be studied independently of the diffusion rates. Temporal dynamics is found to strongly depend on the diffusion ratio though. A Hopf bifurcation occurs along the branch of stable spikes, which is subcritical for small diffusion ratio, leading to collapse to the homogeneous state. As the diffusion ratio increases, this bifurcation typically becomes supercritical, interacts with the homoclinic snaking and also with a supercritical homogeneous Hopf bifurcation, leading to complex spatio-temporal dynamics. The details are worked out for a number of different models that fit the theory using a mixture of weakly nonlinear analysis, semi-strong asymptotics and different numerical continuation algorithms.

In chapter 4, we extend the results obtained in chapter 3 to include models with bistability of homogeneous equilibria such as the Gray-Scott system. A homotopy is studied that takes a Schnakenberg-like glycolysis model to the Gray-Scott model. Numerical continuation is used to understand the complete sequence of transitions to two-parameter bifurcation diagrams within the localised pattern parameter regime as the homotopy parameter varies. Several distinct codimension-two bifurcations are discovered, including cusp and quadruple zero points for homogeneous steady states, a degenerate heteroclinic connection and a change in the connectedness of the homoclinic snaking structure. The analysis is repeated for the Gierer-Meinhardt system, which lies outside the canonical framework shown in chapter 3. Similar transitions are found under homotopy between bifurcation diagrams for the case where there is a constant feed in the active field, to it being in the inactive field.

In chapter 5, we undertake investigations into simple predator-prey models with rational interaction terms in one and two spatial dimensions. Focusing on a case with linear interaction and saturation, an analysis for long domains in 1D is undertaken using ideas from spatial dynamics. Parameter regions for localised patterns and isolated spots are delineated and shown to only the qualitatively the same structure as in chapter 3. Detailed spectral computations and numerical simulations reveal various of homogenous and localised patterns Hopf bifurcations give rise to both temporally periodic and chaotic localised attractors. Simulation results in 2D confirm the onset of complex spatiotemporal patterns within the corresponding parameter regions. We briefly discussed the implications for ecology.

In chapter 6, we study intracellular ROPs dynamic models when the generic source and loss terms are introduced. Here the canonical systems have two activator and two inhibitor field, and two distinct branches of Turing bifurcation are formed. Implementing the weakly nonlinear analysis shows that both Turing bifurcations become subcritical, which leads to the creation of two forms of localised patterns; so-called interleaved and overlaid cases. The temporal stability analysis reveals that the localised patterns created within the overlead case are stable. In contrast, the localised patterns found in the overlaid are unstable. The generality of the results is established by qualitatively presenting the same bifurcations diagrams for different models with different nonlinearities. We also consider the limit that the loss terms vanish, which motivates the analysis in the following chapter.

Chapter 7 considers intracellular partitioning models without the generic source and loss terms. We show that the heteroclinic solutions found in these models can be characterised by looking into the steady states that connect them. We demonstrate that there are up to nine steady states that can be distributed in two ways: symmetric and non-symmetric. Then using catastrophe theory, we provide conditions under which these steady states are destroyed and which forms of heteroclinic connection are created and destroyed in the process. Finally, we provide conformation of the results with numerical simulations for the full PDEs systems. The simulations reveal that different total amount of the two active-inactive pairs of ROPs leads to

different form of polarisation.

Chapter 8 contains overall conclusions and outlines possibility for future work.

CHAPTER 2

METHODOLOGY

2.1 Reaction-diffusion systems

In this study, we look at systems of nonlinear reaction-diffusion equations that have many physical, chemical and biological applications (see e.g. [1, 14, 63, 86, 127, 132, 165]). Such systems of equations are of the form:

$$\partial \boldsymbol{U}_t = D\nabla^2 \boldsymbol{U} + F(\boldsymbol{U}, \boldsymbol{p}). \tag{2.1}$$

Here, $\boldsymbol{U}(x,t) \in \mathbb{R}^n$ is an unknown vector of state variables that represent a group of biological or physical species and $D \in \mathbb{R}^{n\times n}$, its a positive definite diffusion matrix which for the purpose of this thesis we assume to be diagonal. ∇ is the Laplacian operator, $F(\boldsymbol{U}, \boldsymbol{p})$ denotes a nonlinear function of the concentrations which characterises the chemical or biological reaction and its control parameters $p \in \mathbb{R}^p$. Without loss of generality, we shall consider one spatial dimension in the rest of the analysis unless otherwise stated. However, the extension to a higher order is possible in principle. For $\boldsymbol{U} \in \mathbb{R}^n$ and $x \in (-\infty, \infty)$, we use asymptotically flat boundary conditions

$$\boldsymbol{U}(x,t) \to \boldsymbol{U}_0 \quad \text{as} \quad x \to \pm\infty, \tag{2.2}$$

where $\boldsymbol{U}_0$ is homogeneous steady state. For practical computation purposes we shall sometimes pose the system (2.1) on a long finite interval $x \in [-l, l]$ with $l \gg 1$ and replace (2.2) with Neumann boundary conditions

$$\boldsymbol{U}_x(\pm l, t) = 0. \tag{2.3}$$

2.2 Linear stability analysis

This section considers linear stability analysis about an isolated homogeneous steady state $\boldsymbol{U}(x) = \boldsymbol{U}_0$. Implementing the linear stability analysis in (2.1) around the homogeneous steady state $\boldsymbol{U}_0$ provides the conditions where this equilibrium loses its stability. Accordingly, we adapt the method in [44, 119]. Specifically, we investigate the conditions under which the homogeneous equilibrium undergoes the simplest kinds of temporal instability: a spatially homogeneous Hopf bifurcation; or a so-called Turing bifurcation, a pitchfork bifurcation corresponding to a non-trivial spatial wavelength. To analyse such bifurcations, we start by introducing a new variable as follows

$$\boldsymbol{U} = \boldsymbol{U}_0 + \boldsymbol{u}. \tag{2.4}$$

Hence, we write (2.1) in the following form

$$\boldsymbol{u}_t = (J_F(\boldsymbol{U}_0) + D\partial_{xx}\,)\boldsymbol{u} + NL(\boldsymbol{U}_0, \boldsymbol{u}) \tag{2.5}$$

where $J_F(\boldsymbol{U_0}) = J$ is the Jacobian matrix of F at the homogeneous equilibrium and NL contains nonlinear terms which are given as follow

$$NL = NL^1 + NL^2 + NL^3 + ..., \tag{2.6a}$$

$$NL^{(j)} = \sum_{\mathbf{n}=(n_1,...n_d):|\mathbf{n}|=j} \left(\frac{(u_1)^{n_1}...(u_d)^{nd}}{n_1!..n_d!}\right)\left(\frac{\partial^{n_1+...+n_d}F}{\partial u_1^{n_1}...\partial u_d^{n_d}}\right)(\boldsymbol{U}_{01},...,\boldsymbol{U}_{0d}). \tag{2.6b}$$

Considering the linear order of (2.5) and assuming the following ansatz

$$\boldsymbol{u} = \boldsymbol{v}e^{ikx+\lambda t} + c.c., \quad \|\boldsymbol{v}\| \ll 1, \tag{2.7}$$

where k and λ are the spatial wave number and the growth factor (temporal eigenvalue), respectively, we have the following eigenvalue problem:

$$\left[J - k^2 D - \lambda(k) I\right]\boldsymbol{v} = \boldsymbol{0}. \tag{2.8}$$

Here $I \in (n \times n)$ represents the identity matrix and 0 is the zero vector. Since we are concerned with non-trivial solutions, the dispersion relation $\lambda(k)$ is

$$\det\left(J - k^2 D - \lambda(k) I\right) = \boldsymbol{0}. \tag{2.9}$$

Now, we can study the stability of $\boldsymbol{U}_0$ such as $\boldsymbol{U}_0$ will be stable (unstable), if $\Re(\lambda(k)) < 0$ (> 0).

A Hopf bifurcation arises when

$$\Im(\lambda) \neq 0, \quad \Re(\lambda) = 0, \quad k = 0, \tag{2.10}$$

with angular frequency $\omega_H = \Im(\lambda)$ and the corresponding period $\dfrac{2\pi}{\omega_H}$. Alternatively, a Turing bifurcation occurs when $\lambda(k)$ has an extremum crossing 0, which leads to the following conditions:

$$\Re(\lambda(k_c)) = 0 \quad \text{and} \quad \Re(\partial_k \lambda(k_c)) = 0, \quad k_c \neq 0. \tag{2.11}$$

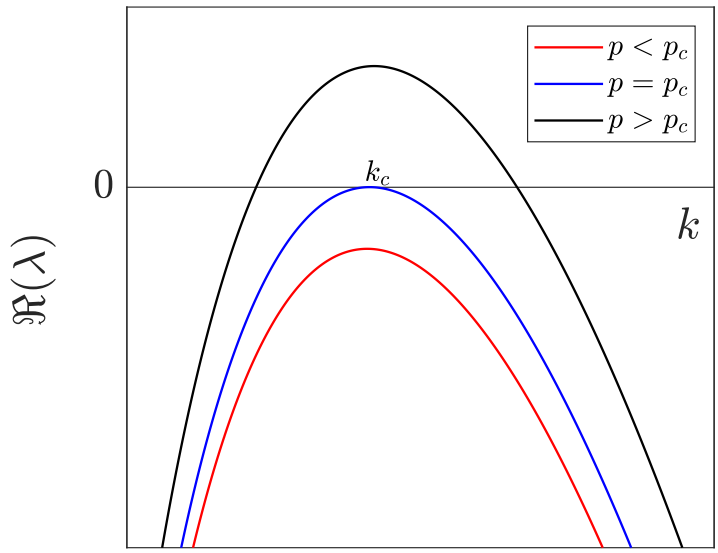

Figure 2.1: Dispersion relation curves for $\Re(\lambda)$ in (2.8) versus k. For $p > p_c$ (black curve) indicates the case of spatial instability of solution, while using $p = p_c$ (blue curve) represents the case of the double zero root and using $p < p_c$ (red curve) represents the case of a stable solution.

Here k_c is the critical value of the wave number. These conditions are specifically the conditions for $\lambda(k)$ to represent a double zero at k_c. The wavelength of these patterns is given by

$$\Omega = \frac{2\pi}{k_c}. \tag{2.12}$$

As argued for example in [32], the above conditions for a temporal Turing bifurcation can be interpreted as a so-called Hamiltonian-Hopf bifurcation in terms of spatial dynamics (that is when the time-independent problem is posed on the infinite domain and the spatial variable x is considered to be time-like, see e.g. [76] and section 2.5 below). In Figure 2.1, we show the three possible cases for the dispersion relation. If the real part of the dispersion relation is less than zero for all values of k then the homogeneous steady state $\boldsymbol{U}_0$ is stable. $\Re(\lambda(k))$ may touch 0 for some values of the parameter $p = p_c$ and become positive for a certain values of k when $p > p_c$. This value of k is called the critical value of the wave number donated as k_c. The system (2.1) undergoes spatial instability if the maximum of $\lambda(k)$ becomes positive for some value of the parameters $p > p_c$. Then the spatial homogeneity is broken, and stationary patterns in time and oscillatory in space will emerge.

If we consider the pattern solution to be time independent, the eigenvalue problem (2.8) takes the following form

$$\left[J - k_c^2 D\right] \boldsymbol{\psi} = 0. \tag{2.13}$$

Here $\left[J - k_c^2 D\right]$ is the linear operator which is singular and the vector $\boldsymbol{\psi}$ is in its kernel. Therefore, the general solution for the linear problem of (2.5) is given as

$$\boldsymbol{u} = \boldsymbol{\psi}(A e^{ik_c x} + c.c), \tag{2.14}$$

where $c.c$ stands for the complex conjugate and A is the amplitude of the pattern.

2.3 Weakly nonlinear analysis for Turing bifurcation

After achieving the conditions for Turing instability and linear solution for (2.5), we apply weakly nonlinear analysis to obtain the equation that controls the dynamics of the envelope. We achieve such an equation by adopting the method of normal forms, see [61, 76, 165] for more detail. This method initially was proposed by Poincaré [60] to find a coordinate transformation for a nonlinear system to simplify the dynamics to that of few pre-analysed cases. This transformation takes place in the equilibrium's neighbourhood and such that Taylor's expansion of the transformed nonlinear vector field has a minimal number of terms at each order. The analysis here is inspired by [165], which is based on the treatment in [76]. Here though we generalise the analysis to a general system of the form (2.1).

Specifically, the normal form in the vicinity of the Turing bifurcation can be written in the form of a complex Ginzburg-Landau equation with real coefficients, see e.g. [112]. Note that the region of validity of such approximations have been rigorously established through the work of Schneider [144]. Particularly, we seek an amplitude equation for a scalar complex variable $A(x,t)$ that has the form

$$\partial_t A = \epsilon L_1 A + L_3 A|A|^2 + L_5 A|A|^4 + O(A|A|^6), \tag{2.15}$$

where the coefficients L_i, $i = 1,3,5$ are real functions of the system parameters at the bifurcation point, and ϵ is an unfolding parameter that represents the perturbation of a bifurcation parameter from its critical value. Without loss of generality, we can assume $L_1 > 0$ such that the homogeneous state passes from stable to unstable as ϵ increases through 0. Then, the criticality of the bifurcation is determined by the sign of L_3. We are interested in establishing the presence of a codimension-two bifurcation where $L_3 = 0$ [76]. We seek a change of variable of the form

$$\partial_t A = f^{(1)}(A) + f^{(2)}(A) + f^{(3)}(A) + ..., \tag{2.16a}$$

$$\boldsymbol{u} = \boldsymbol{W}^{(1)}(A,x) + \boldsymbol{W}^{(2)}(A,x) + \boldsymbol{W}^{(3)}(A,x) + ... \tag{2.16b}$$

Here we shall use the superscript as the counter for the order in the normal form analysis. Now, we are ready to proceed with the normal form analysis order by order.

Order 1

At order (1) the equation (2.5) corresponds to the linear stability analysis. Consequently, the equation and the change of variable are

$$f^{(1)} = 0, \quad \boldsymbol{W}^{(1)} = \boldsymbol{\psi}(Ae^{ik_c x} + \text{c.c}). \tag{2.17}$$

Order 2

At this order, we have the following for the transformation and its temporal derivative

$$\boldsymbol{u}_2 = \boldsymbol{W}^{(1)} + \boldsymbol{W}^{(2)}, \quad \partial_t \boldsymbol{u}_2 = \partial_A \boldsymbol{W}^{(1)} f^{(2)} + \text{h.o.t}, \tag{2.18}$$

where h.o.t refers to higher-order terms. Hence, at this order (2.5) becomes

$$\partial_A \boldsymbol{W}^{(1)} f^{(2)} + \text{c.c} = [J + D\partial_{xx}]_c \boldsymbol{W}^{(2)} + NL^{(2)}(\boldsymbol{W}^{(1)}), \tag{2.19}$$

where the sub-index c indicates that the linear operator is at the critical point. The nonlinear term reads

$$NL^{(2)}\left(\boldsymbol{W}^{(1)} \boldsymbol{m}_{20}\left(\boldsymbol{\psi}^2, \boldsymbol{\psi}, \boldsymbol{U}_0\right)|A|^2 + \boldsymbol{m}_{22}\left(\boldsymbol{\psi}^2, \boldsymbol{\psi}, \boldsymbol{U}_0\right)\left(A^2 e^{2ik_c x} + \text{c.c}\right)\right). \tag{2.20}$$

Here $\boldsymbol{m}_{20}$ and $\boldsymbol{m}_{22}$ are vectors of the coefficients of the nonlinear terms where the two indices stand for the order and the multiple of k_c in the exponent respectively. We will apply the same convention in the rest of the analysis. It is clear that the right-hand side of (2.19) appears not to have any term that is proportional to the kernel of the linear operator $\boldsymbol{W}^{(1)}$. Thus, there are no secular terms. Naturally, this will be the situation for every even order. Since the secular terms are not exiting in the second-order; we can assume $f^{(2)} = 0$. Accordingly, we can obtain the solution in this order straightforward by substituting the following ansatz into (2.19);

$$\boldsymbol{W}^{(2)} = \boldsymbol{Q}_{20}(|A|^2 + c.c) + \boldsymbol{Q}_{22}(A^2 e^{2ik_c x} + \text{c.c}), \tag{2.21}$$

where $\boldsymbol{Q}_{ij}$ is unknown vector coefficient. The result at this order is given by the uncoupled linear system

$$J\boldsymbol{Q}_{20} = -\boldsymbol{m}_{20}\left(\boldsymbol{\psi}^2, \boldsymbol{\psi}, \boldsymbol{U}_0\right), \tag{2.22a}$$

$$(J - 4k_c^2 D)\boldsymbol{Q}_{22} = -\boldsymbol{m}_{22}\left(\boldsymbol{\psi}^2, \boldsymbol{\psi}, \boldsymbol{U}_0\right). \tag{2.22b}$$

By solving the above two uncoupled equations, we have the solution for $\boldsymbol{Q}_{20}$ and $\boldsymbol{Q}_{22}$ then the solution for $W^{(2)}$.

Order 3

Following a similar approach that applies at the previous two orders, at the third order we have the following for the change of variable and its temporal derivative

$$\boldsymbol{u}_3 = \boldsymbol{W}^{(1)} + \boldsymbol{W}^{(2)} + \boldsymbol{W}^{(3)}, \quad \partial_t \boldsymbol{u}_3 = \partial_A \boldsymbol{W}^{(1)} f^{(3)} + \text{h.o.t}. \tag{2.23}$$

Thus, equation (2.5) is written as

$$\partial_A \boldsymbol{W}^{(1)} f^{(3)} + \text{c.c} = [J + D\partial_{xx}]_c \boldsymbol{W}^{(3)} + NL^{(3)}\left(\boldsymbol{W}^{(1)} + W^{(2)}\right), \tag{2.24}$$

where the nonlinear term and the temporal derivative at this order are

$$NL^{(3)}(\boldsymbol{W}^{(1)} + \boldsymbol{W}^{(2)}) = \boldsymbol{m}_{31}(\boldsymbol{Q}_{21}, \boldsymbol{Q}_{22})\left(A|A|^2 e^{ik_c x} + \text{c.c}\right) + \boldsymbol{m}_{33}(\boldsymbol{Q}_{21}, \boldsymbol{Q}_{22})\left(A^3 e^{3ik_c x} + \text{c.c}\right), \tag{2.25a}$$

$$\partial_A \boldsymbol{W}^{(1)} f^{(3)} + \text{c.c} = f^{(3)} \boldsymbol{W}^{(1)} + \text{c.c}. \tag{2.25b}$$

Then, we can rewrite (2.24) as follows

$$[J + D\partial_{xx}]_c \boldsymbol{W}^{(3)} = f^{(3)}\boldsymbol{W}^{(1)} + \text{c.c} - \boldsymbol{m}_{31}\left(A|A|^2 e^{ik_c x} + \text{c.c}\right) - \boldsymbol{m}_{33}\left(A^3 e^{3ik_c x} + \text{c.c}\right) \tag{2.26}$$

According to the theory of multiple scales, the presence of the secular term at this order (namely the second term on the right-hand side of (2.26)) will break the asymptotic expansion; because e^{ikx} is in the kernel at the linear operator on the LHS, so this will lead to resonance. To ensure the solubility of (2.26), we apply the Fredholm alternative condition (see e.g. [76] for more detail about the theory). Specifically, if B is a Fredholm operator on a vector space of finite or infinite dimensions and $\boldsymbol{b}$ is a vector in that space, we have

$$B\boldsymbol{x} = \boldsymbol{b} \quad \text{is solvable} \quad \Leftrightarrow \quad \langle \boldsymbol{b}, \boldsymbol{v} \rangle = 0 \quad \forall \quad \boldsymbol{v} \in \text{Ker}(B^\dagger). \tag{2.27}$$

where $B^\dagger$ is an adjoint of B. The natural vector space to take is the Banach space of L_2 functions of period T_c then we use the inner product such that

$$\langle f(x), g(x) \rangle = \frac{1}{\Omega}\int_0^\Omega f^*(x) g(x) dx, \tag{2.28}$$

where $*$ refer to the complex conjugate and Ω was defined in (2.12). Applying integration by parts, it is clear that the adjoint matrix of the linear operator is given as

$$(J + D\partial_{xx})^\dagger = \left(J^T + D\partial_{xx}\right), \tag{2.29}$$

and the kernel of the adjoint reads

$$\boldsymbol{\psi}^\dagger \in \text{Ker}\left(J^T - Dk_c^2\right). \tag{2.30}$$

For the solvability condition, it suffices to demonstrate that the right-hand side of (2.26) is orthogonal to the kernel of the adjoint operator (2.30). Hence, from the inner product (2.28), the following orthonormality relation is met:

$$\frac{1}{\Omega}\int_0^\Omega e^{-isk_c x} e^{ink_c x} dx = \begin{cases} 0 & \text{if} \quad s \neq n \\ 1 & \text{if} \quad s = n \end{cases}, \tag{2.31}$$

Accordingly, the solvability condition becomes

$$f^{(3)}\langle \boldsymbol{\psi}, \boldsymbol{\psi}^\dagger \rangle + \langle -\boldsymbol{m}_{31}, \boldsymbol{\psi}^\dagger \rangle |A|^2 A = 0. \tag{2.32}$$

Solving for $f^{(3)}$, we have

$$f^{(3)} = \frac{\langle \boldsymbol{m}_{31}, \boldsymbol{\psi}^\dagger \rangle}{\langle \boldsymbol{\psi}, \boldsymbol{\psi}^\dagger \rangle} |A|^2 A = L_3 |A|^2 A. \tag{2.33}$$

By imposing the condition (2.33) and substituting the following ansatz into (2.26)

$$\boldsymbol{W}^{(3)} = \boldsymbol{Q}_{31}(|A|^2 A e^{ik_c x} + \text{c.c.}) + \boldsymbol{Q}_{33}(A^3 e^{3ik_c x} + \text{c.c.}), \tag{2.34}$$

we obtain the uncoupled solvable linear system given by

$$[J - k_c^2 D]\boldsymbol{Q}_{31} = \boldsymbol{\psi} L_3 - \boldsymbol{m}_{31}(\boldsymbol{Q}_{21}, \boldsymbol{Q}_{22}), \tag{2.35a}$$

$$[J - 9k_c^2 D]\boldsymbol{Q}_{33} = -\boldsymbol{m}_{33}(\boldsymbol{Q}_{21}, \boldsymbol{Q}_{22}). \tag{2.35b}$$

By solving (2.35) we can gain a solution for $W^{(3)}$. Note that the existence of the secular term will repeat each odd order.

Order 4

At the fourth order, the change of variable equation and the temporal derivative are

$$\boldsymbol{u}_4 = \boldsymbol{W}^{(1)} + \boldsymbol{W}^{(2)} + \boldsymbol{W}^{(3)} + \boldsymbol{W}^{(4)}, \quad \partial_t \boldsymbol{u}_4 = \partial_A \boldsymbol{W}^{(1)} f^{(4)} + \partial_A \boldsymbol{W}^{(2)} f^{(3)} + \text{h.o.t.} \tag{2.36}$$

Accordingly, we can write (2.5) as follows

$$\partial_A \boldsymbol{W}^{(1)} f^4 + \partial_A \boldsymbol{W}^{(2)} f^3 = [J + D\partial_{xx}]_c \boldsymbol{W}^{(4)} + NL^{(4)}(\boldsymbol{W}^{(1)} + \boldsymbol{W}^{(2)} + \boldsymbol{W}^{(3)}), \tag{2.37}$$

here $NL^{(4)}$ and $\partial_A \boldsymbol{W}^{(2)} f^3$ are given by

$$NL^{(4)} = \boldsymbol{m}_{40}(\boldsymbol{Q}_{31}, \boldsymbol{Q}_{33})\left(|A|^4 + cc\right) + \boldsymbol{m}_{42}(\boldsymbol{Q}_{31}, \boldsymbol{Q}_{33})\left(A^2|A|^2 e^{2ik_c x} + c.c\right) + \boldsymbol{m}_{44}(\boldsymbol{Q}_{31}, \boldsymbol{Q}_{33})\left(A^4 e^{4ik_c x} + \text{c.c}\right),$$

$$\partial_A \boldsymbol{W}^{(2)} f^3 = L_3 \boldsymbol{Q}_{20}(|A|^4 + \text{c.c}) + 2L_3 \boldsymbol{Q}_{22}\left(A^2|A|^2 e^{2ik_c x}\right).$$

Therefore, the equation (2.37) reads

$$[J + D\partial_{xx}]_c \boldsymbol{W}^{(4)} = (L_3 \boldsymbol{Q}_{20} - \boldsymbol{m}_{40})\left(|A|^4 + \text{c.c}\right) + (2L_3 \boldsymbol{Q}_{22} - \boldsymbol{m}_{42})\left(A^2|A|^2 e^{2ik_c x} + \text{c.c}\right) - \boldsymbol{m}_{44}$$

$$\left(A^4 e^{4ik_c x} + \text{c.c}\right) + \partial_A \boldsymbol{W}^{(1)} f^{(4)}. \tag{2.39}$$

Since we do not have any resonant terms at this order, then we can choose $f^{(4)} = 0$ and introduce the following ansatz

$$\boldsymbol{W}^{(4)} = \boldsymbol{Q}_{40}\left(|A|^4 + \text{c.c}\right) + \boldsymbol{Q}_{22}\left(A^2|A|^2 e^{2ik_c x} + \text{c.c}\right) + \boldsymbol{Q}_{44}\left(A^4 e^{4ik_c x} + \text{c.c}\right). \tag{2.40}$$

This gives the uncoupled solvable system

$$J\boldsymbol{Q}_{40} = L_3 \boldsymbol{Q}_{20} - \boldsymbol{m}_{40}, \tag{2.41a}$$

$$\left(J - 4k_c^2 D\right)\boldsymbol{Q}_{42} = 2L_3 \boldsymbol{Q}_{22} - \boldsymbol{m}_{42}, \tag{2.41b}$$

$$\left(J - 16k_c^2 D\right)\boldsymbol{Q}_{44} = -\boldsymbol{m}_{44}. \tag{2.41c}$$

By solving this system, we achieve an expression for $\boldsymbol{W}^{(4)}$

Order 5

The main equation (2.5), at this order is given by

$$\begin{aligned}\partial_A \boldsymbol{W}^{(1)} f^{(5)} + \partial_A \boldsymbol{W}^{(3)} f^{(3)} = [J + D\partial_{xx}]_c \boldsymbol{W}^{(5)} + \boldsymbol{m}_{51}(\boldsymbol{Q}_{40}, \boldsymbol{Q}_{42}, \boldsymbol{Q}_{44})\Big(A|A|^4 e^{ik_c x} + c.c\Big) \\ + \boldsymbol{m}_{53}(\boldsymbol{Q}_{40}, \boldsymbol{Q}_{42}, \boldsymbol{Q}_{44})\Big(A^3|A|^2 e^{3ik_c x} + \text{c.c}\Big) + \boldsymbol{m}_{55}(\boldsymbol{Q}_{40}, \boldsymbol{Q}_{42} \\ , \boldsymbol{Q}_{44})\Big(A^5 e^{5ik_c x} + \text{c.c}\Big). \end{aligned} \tag{2.42}$$

We simplify (2.42) by substituting for $\boldsymbol{W}^{(1)}$, $\boldsymbol{W}^{(3)}$ and $f^{(3)}$ to obtain

$$\begin{aligned}[J + D\partial_{xx}]\boldsymbol{W}^{(5)} = &\psi\Big(f^{(5)} e^{ik_c x} + \text{c.c}\Big) + (2\boldsymbol{Q}_{31} L_3 - \boldsymbol{m}_{51})\Big(A|A|^4 e^{ik_c x} + \text{c.c}\Big) \\ &(3\boldsymbol{Q}_{33} L_3 - \boldsymbol{m}_{53})\Big(A^3|A|^2 e^{3ik_c x} + c.c\Big) - \boldsymbol{m}_{55}\Big(A^5 e^{5ik_c x} + \text{c.c}\Big). \end{aligned} \tag{2.43}$$

It is clear; we have a secular term at this order, namely any e^{ikx} terms in $f^{(5)}$. Consequently, we use the solvability condition which gives

$$f^{(5)} = \frac{\langle \boldsymbol{m}_{51}, \boldsymbol{\psi}^\dagger \rangle - \langle 2L_3 \boldsymbol{Q}_{31}, \boldsymbol{\psi}^\dagger \rangle}{\langle \boldsymbol{\psi}, \boldsymbol{\psi}^\dagger \rangle} A|A|^5 = L_5 A|A|^5. \tag{2.44}$$

By imposing the above condition and using the following ansatz

$$W^{(5)} = \boldsymbol{Q}_{51}\Big(A|A|^4 e^{ik_c x} + c.c\Big) + \boldsymbol{Q}_{53}\Big(A^3|A|^2 e^{3ik_c x} + \text{c.c}\Big) + \boldsymbol{Q}_{55}\Big(A^5 e^{5ik_c x} + \text{c.c}\Big), \tag{2.45}$$

We obtain an uncoupled linear system which is

$$\big(J - k_c^2 D\big)\boldsymbol{Q}_{51} = \boldsymbol{\psi} L_5 + 2L_3 \boldsymbol{Q}_{31} - \boldsymbol{m}_{51}, \tag{2.46a}$$

$$\big(J - 9k_c^2 D\big)\boldsymbol{Q}_{53} = 3L_3 \boldsymbol{Q}_{33} - \boldsymbol{m}_{53}, \tag{2.46b}$$

$$\big(J - 25k_c^2 D\big)\boldsymbol{Q}_{51} = -\boldsymbol{m}_{55}. \tag{2.46c}$$

The solution of the system gives the solution of the fifth-order change of variables $\boldsymbol{W}^{(5)}$

Unfolding

To complete the analysis, we need to understand how the normal form parameter ϵ depends on the perturbation of the control parameters p in (2.1) from their critical value. To that end, we introduce a new multi-index notation $i \to (i, j)$, where the first index gives the power of A and the second index indicates the power of ϵ. Accordingly, we re-write the change of variables and the equation in the form

$$\boldsymbol{u} = \Big[\boldsymbol{W}^{(1,0)} + \boldsymbol{W}^{(2,0)} + \boldsymbol{W}^{(3,0)} + \ldots\Big] + \Big[\boldsymbol{W}^{(1,1)} + \boldsymbol{W}^{(2,1)} + \ldots\Big] + \ldots, \tag{2.47}$$

$$\partial_t A = \Big[f^{(1,0)} + f^{(2,0)} + \ldots\Big] + \Big[f^{(1,1)} + f^{(2,1)} + \ldots\Big] + \ldots. \tag{2.48}$$

Notice that so far we have computed (2.47) and (2.48) at $\epsilon = 0$, which corresponds to the terms in the first square bracket. To determine L_1 in (2.15), it is sufficient to compute the dependence in ϵ and A at first order. More precisely, at order (1,1), equation (2.5) reads

$$\partial_t \boldsymbol{u}^{(1,0)} = \partial_A \boldsymbol{W}^{(1,0)} f^{(1,1)} + \text{c.c}, \tag{2.49a}$$

where

$$\partial_A \boldsymbol{W}^{(1,0)} f^{(1,1)} + c.c = (J + D\partial_{xx})\boldsymbol{W}^{(1,1)} + \epsilon \mathscr{L}_P W^{(1,0)}, \tag{2.50}$$

and $\mathscr{L}_P$ is the derivative of J_F with respect to the relevant system parameter p where p is component of the vector parameters $\boldsymbol{p}$, evaluated at the critical point. The last term on the right-hand side of equation (2.50) is secular. Following the same procedure as described in order 3, the solvability condition becomes

$$f^{(1,1)} = \epsilon \frac{\langle \mathscr{L}_p \boldsymbol{\psi}, \boldsymbol{\psi}^\dagger \rangle}{\langle \boldsymbol{\psi}, \boldsymbol{\psi}^\dagger \rangle} A = \epsilon L_1 A. \tag{2.51}$$

Upon substituting (2.51) into (2.50), we have

$$(J + d\partial_{xx})\boldsymbol{W}^{(1,1)} = \epsilon \left(-\mathscr{L}\boldsymbol{\psi} + L_1 \boldsymbol{\psi} \right) \left(A e^{ik_c x} + \text{c.c} \right). \tag{2.52}$$

Using the following ansatz

$$\boldsymbol{W}^{(1,1)} = \boldsymbol{\phi} \left(A e^{ik_c x} + \text{c.c} \right), \tag{2.53}$$

we can solve (2.52) at this order.

In summary, we have gained the amplitude equation up to fifth order, which is given as

$$\partial_t A = \epsilon L_1 A + L_3 A|A|^2 + L_5 A|A|^4, \tag{2.54}$$

and we have found the change of variable between the original variable $\boldsymbol{U}$ and A as follows:

$$\begin{aligned} \boldsymbol{U} = \boldsymbol{U}_0 &+ (\boldsymbol{\psi} + \boldsymbol{\phi}) \left(A e^{ik_c x} + \text{c.c} \right) + \boldsymbol{Q}_{20} \left(|A|^2 + \text{c.c} \right) + \boldsymbol{Q}_{22} \left(A|A|^2 A e^{2ik_c x} + c.c \right) + \boldsymbol{Q}_{31} (|A|^2 A e^{ik_c x} + \text{c.c}) \\ &+ \boldsymbol{Q}_{33} (A^3 e^{3ik_c, x} + \text{c.c}) + \boldsymbol{Q}_{40} \left(|A|^4 + \text{c.c} \right) + \boldsymbol{Q}_{22} \left(A^2 |A|^2 e^{2ik_c x} + cc \right) + \boldsymbol{Q}_{44} \left(A^4 e^{4ik_c x} + \text{c.c} \right) \\ &+ \boldsymbol{Q}_{51} \left(A|A|^4 e^{ik_c x} + \text{c.c} \right) + \boldsymbol{Q}_{53} \left(A^3 |A|^2 e^{3ik_c x} + \text{c.c} \right) + \boldsymbol{Q}_{55} \left(A^5 e^{5ik_c x} + \text{c.c} \right). \end{aligned} \tag{2.55}$$

Since we have obtained an analytical expression for the coefficients of the normal form (2.15), we can identify the changing of the sign of L_3 from positive to negative at the point where the Turing bifurcation passes from subcritical to supercritical; see Figure 2.2. This transition point presents a codimension-two bifurcation point. An unfolding of the presence of a codimension-two point guarantees the existence of the bi-stability region between the homogeneous state and the pattern state only in the case that $L_1 < L_5 < 0$ [171]. As we shall show in section 2.5 such

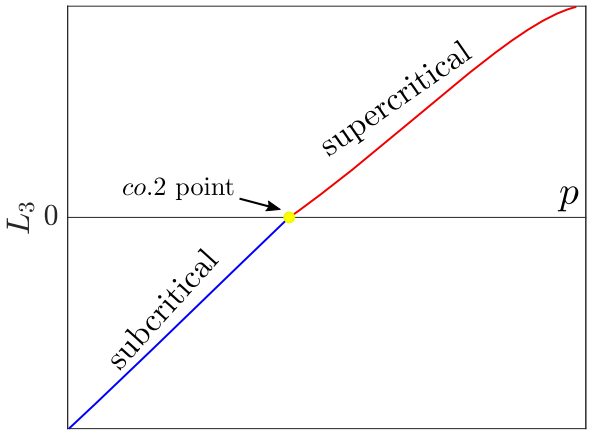

Figure 2.2: A plot of an example for $L_3 = L_3(p)$ here the yellow coloured circle indicates the zero of L_3 where a Turing bifurcation changes from being subcritical (blue curve) to supercritical (red curve); see Figure 2.4 for specific numerical example.

bistability naturally leads to localised structures. In addition to the analytically determined points of bifurcation up to the fifth order of the normal form, we developed a general Maple code that can calculate the point of bifurcation automatically. As a result, the remainder of the thesis will not discuss the finding the codimension-two point in more detail except for section 2.4.2 where we give an example of the method to be used.

2.4 Example: a two-component model

In the calculations that follow in this chapter, whenever complete generality for the general system (2.1) is not possible, we shall use a single example model by default, with free parameters d and b. This system was first proposed by Tyson & Kauffman [154] as an adaptation of the Brusselator to model the chemical oscillator thought to control cellular mitosis. The model is often used as a simple model for glycolysis, one of the most basic metabolic processes that turn sugars into energy (see e.g. [70]). We shall use this model as a motivation example throughout this chapter and by default we shall call it the glycolysis model.

Writing the equations in the form

$$\frac{\partial u}{\partial t} = F(u,v) + \delta^2 \frac{\partial^2 u}{\partial x^2} = dv - u + u^2 v + \delta^2 \frac{\partial^2 u}{\partial x^2}, \quad x \in [-l,l], \quad t > 0 \tag{2.56a}$$

$$\frac{\partial v}{\partial t} = G(u,v) + \frac{\partial^2 v}{\partial x^2} = b - dv - u^2 v + \frac{\partial^2 v}{\partial x^2}, \quad x \in [-l,l], \quad t > 0, \tag{2.56b}$$

with boundary conditions

$$\frac{\partial u}{\partial x}(\pm l) = \frac{\partial v}{\partial x}(\pm l) = 0, \quad \text{or in the case} \quad l \to \pm\infty, \quad \text{that} \quad u, v \to u_s, v_s, \tag{2.57}$$

where u_s and v_s are the homogeneous steady state for u and v respectively given by $u_s = b$ and $v_s = \dfrac{b}{d+b^2}$. Here u, v, represent the activator and the inhibitor cell concentration, respectively.

The term u^2v in (2.56a) and (2.56b) refers to autocatalytic production of u from v and the consumption of v. The parameter δ is the ratio between the activator and inhibitor rate of diffusivity, $d > 0$ is the dimensionless input flux and $b > 0$ is a dimensionless rate constant for the inhibitor.

2.4.1 Linear stability analysis

In this section, we study the linear stability analysis and find a sufficient condition on parameters to allow pattern formation for the system in (2.56) subject to (2.57). Since $d > 0$ and $b > 0$, then both u_s and v_s are positive also. The stability analysis is achieved by setting $U = u_s + u$ and $V = v_s + v$ and then substituting into (2.56). Hence we obtain the following system

$$\begin{pmatrix} U \\ V \end{pmatrix}_t = (J + D\partial_{xx}) \begin{pmatrix} U \\ V \end{pmatrix} + \begin{pmatrix} 1 \\ -1 \end{pmatrix} NL(U, V, u_s, v_s), \tag{2.58}$$

where J is the Jacobian matrix which is given by

$$J|_{(u_s,v_s)} = \begin{pmatrix} \dfrac{b^2-d}{b^2+d} & b^2+d \\ -\dfrac{2b}{d+b^2} & -(b^2+d) \end{pmatrix}, \tag{2.59}$$

D is a diagonal diffusion matrix which reads

$$D = \begin{pmatrix} \delta^2 & 0 \\ 0 & 1 \end{pmatrix}, \tag{2.60}$$

and NL corresponds to nonlinear terms. By considering the linear order of (2.58), we can rewrite the linear system in terms $\boldsymbol{w} = (U, V)^T$ as

$$\boldsymbol{w}_t = (J + D\partial_{xx})\boldsymbol{w}, \tag{2.61}$$

By substituting the ansatz (2.7) into (2.61), we obtain an eigenvalue problem for $\lambda(k)$ which has the following dispersion relation

$$\lambda(k)_{\pm} = \frac{1}{2}\left(T_k \pm \sqrt{T_k^2 - 4\det(J)_k}\right), \tag{2.62a}$$

where

$$T_k = -(\delta^2 + 1)k^2 + \frac{b^2-d}{b^2+d} - b^2 - d, \tag{2.62b}$$

$$\det(J)_k = \delta^2 k^4 - \left(\left(\frac{b^2-d}{b^2+d}\right) - \delta^2(b^2+d)\right)k^2 + (b^2+d). \tag{2.62c}$$

Implementing the conditions (2.10) on (2.62) for the particular case of the glycolysis model (2.56) gives the Hopf bifurcation curve in the (b, d)-plane which can be written explicitly as

$$d_H = -b^2 - \frac{1}{2} + \frac{1}{2}\sqrt{8b^2 + 1}. \tag{2.63}$$

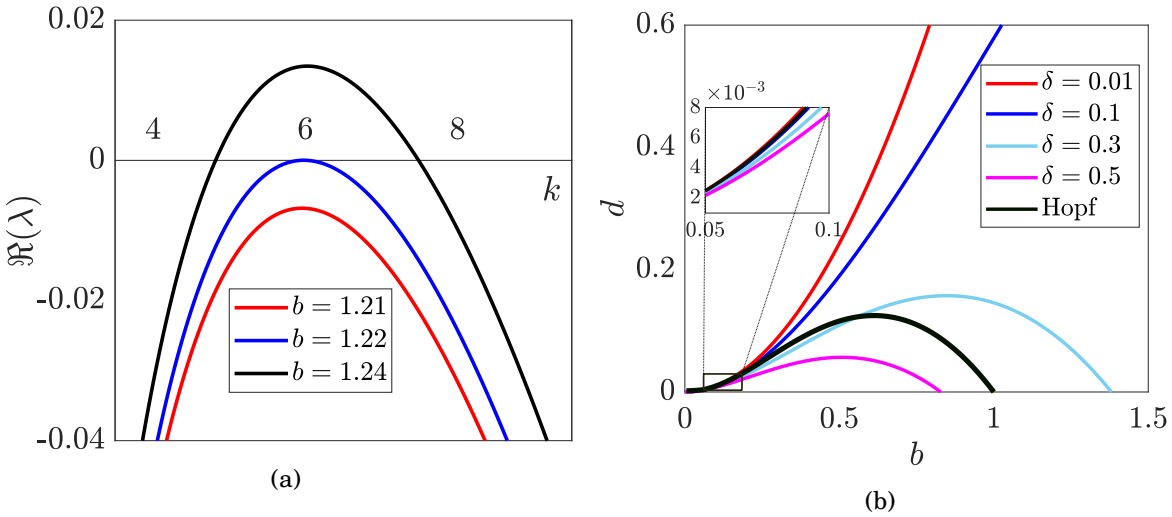

Figure 2.3: (a) Dispersion relation $\lambda(k)$ of (2.56) for $\delta = 0.045$, $d = 1.1$ and three different values of b. The black curve corresponds to the case where is an interval of k-values corresponding to instability, the blue curve corresponds to where a Turing bifurcation occurs with the wave number $k = k_c \approx 6$ and the red curve corresponds to stability for all k. (b) Loci of Turing bifurcation points of (2.56) in (b,d)-plane for four different values of δ, and the δ-independent locus of spatially homogeneous Hopf bifurcations.

Note that this condition is necessarily independent of the diffusion ratio δ.

Applying the conditions (2.11) to (2.62), we gain conditions for Turing instability and the critical value of wavenumber, which are given by

$$(b^2+d)\,\delta\sqrt{-\delta^2\left(b^2+d\right)^2+6b^2+2d}=b^2-d,\quad k_c^2=\frac{-\left(b^2+d\right)^2\delta^2+b^2-d}{2\left(b^2+d\right)\delta^2}. \tag{2.64}$$

Note that the conditions for this instability are δ-dependent. Whether the instability is super- or sub-critical requires weakly nonlinear analysis, which we consider in Sec. 2.4.2 below. Figure 2.3a depicts the dispersion relation (2.62) for three different values of b. Figure 2.3b shows the Hopf bifurcation curve of the homogeneous equilibrium, obtained from (2.63) and the Turing instability curve (2.64) in the (b,d)-plane for different values of $\delta < 1$. In the diagram, instability occurs for either the Hopf or Turing bifurcation as we pass from the upper left to the lower right. It is clear that, for sufficiently small δ, the Turing instability always occurs before the Hopf bifurcation upon increasing b from zero, with no Hopf bifurcation at all for d sufficiently large. For larger δ, the Hopf and Turing loci intersect; for example at the depicted value $\delta = 0.3$ the intersection occurs at at $(b,d) \approx (0.558444, 0.122870)$. For $\delta = \delta_c = \sqrt{2}-1 \approx 0.414213$, both Turing and Hopf bifurcation curves intersect the b-axis at $b = 1$. Thus, for all $\delta > \delta_c$ (see e.g. the depicted case $\delta = 0.5$) the Turing bifurcation curve lies exclusively inside (i.e. for lower d-values) the Hopf bifurcation curve. In that case the Hopf bifurcation is the exclusive instability by which the homogeneous equilibrium loses stability upon either decreasing d or increasing b.

Considering that the pattern solution is time independent, we can rewrite the eigenvalue problem using (2.13) for which we can choose eigenvector $\boldsymbol{\psi}$ to be

$$\boldsymbol{\psi} = \left(-\frac{\left(b^2+d\right)\left(b^2+k_c^2+d\right)}{2b^2}, 1 \right)^T. \tag{2.65}$$

Consequently, the general solution of the linear problem in (2.58) is given by (2.14).

2.4.2 Weakly nonlinear analysis

A necessary ingredient for the onset of localised patterns due to homoclinic snaking is that the Turing bifurcation should be subcritical [32]. Therefore the technique that we have developed in section 2.3 is utilized to examine criticality of Turing bifurcation in (2.56)

Now, we start the normal forms calculations.

Order 1

It is clear that at this order the equation (2.58) is equivalent to the linear problem. Accordingly, we have

$$f^{(1)} = 0, \quad \boldsymbol{W}^{(1)} = \left(\psi_1, \psi_2\right)^T \left(A e^{ik_c x} + c.c\right), \tag{2.66}$$

here ψ_1 and ψ_2 are referring to the first and the second component of vector (2.65), respectively.

Order 2

At this order equation (2.58) becomes

$$f^{(2)} \partial_A \boldsymbol{W}^{(1)} + c.c. = (J + D\partial_{xx})_c \boldsymbol{W}^{(2)} + \frac{1}{2} \begin{pmatrix} \frac{\partial^2 F}{\partial u^2} & \frac{\partial^2 F}{\partial v^2} \\ \frac{\partial^2 G}{\partial v^2} & \frac{\partial^2 G}{\partial v^2} \end{pmatrix} \begin{pmatrix} U_1^2 \\ V_1^2 \end{pmatrix} + \begin{pmatrix} \frac{\partial^2 F}{\partial u \partial v} \\ \frac{\partial^2 G}{\partial u \partial v} \end{pmatrix} U_1 V_1. \tag{2.67}$$

where the subscript c in the linear operator refers to the critical value of the parameters, which satisfy (2.64). We will drop the subindex in what follows, because we will assume all functions are evaluated at the critical value of the parameters unless otherwise stated. Since there are no secular terms, the solution at second-order can be computed in a straightforward manner by choosing $f^{(2)} = 0$ and substituting the ansatz (2.21) into (2.67). Then we obtain an uncoupled linear system given by (2.22) where

$$\begin{aligned} m_{20}^1 &= \frac{b}{(d+b^2)} \psi_1^2 + 2b\psi_1\psi_2, \\ m_{20}^2 &= -m_{20}^1, \\ m_{22}^1 &= m_{20}^1, \\ m_{22}^2 &= -m_{20}^1, \end{aligned}$$

Note the superscript 1 or 2 on m_{ij} corresponds to the first or the second component of this vector.

Solving the system of equations (2.22), we gain the second order solution.

Order 3

At the third order (2.58) is given by

$$f^{(3)}\partial_A \boldsymbol{W}^{(1)} + c.c. = \quad (J + D\partial_{xx})\boldsymbol{W}^{(3)} + \frac{1}{2}\begin{pmatrix} \frac{\partial^2 F}{\partial u^2} & \frac{\partial^2 F}{\partial v^2} \\ \frac{\partial^2 G}{\partial u^2} & \frac{\partial^2 G}{\partial v^2} \end{pmatrix}\begin{pmatrix} 2U_1U_2 \\ 2V_1V_2 \end{pmatrix} + \begin{pmatrix} \frac{\partial^2 F}{\partial u \partial v} \\ \frac{\partial^2 G}{\partial u \partial v} \end{pmatrix}\Big(U_2V_1 + U_1V_2\Big)$$

$$+\frac{1}{3!}\begin{pmatrix} \frac{\partial^3 F}{\partial u^3} & \frac{\partial^3 F}{\partial v^3} \\ \frac{\partial^3 G}{\partial u^3} & \frac{\partial^3 G}{\partial v^3} \end{pmatrix}\begin{pmatrix} U_1^3 \\ V_1^3 \end{pmatrix} + \frac{3}{3!}\begin{pmatrix} \frac{\partial^3 F}{\partial u^2 \partial v} \\ \frac{\partial^3 G}{\partial u^2 \partial v} \end{pmatrix}\Big(U_1^2V_1\Big) + \frac{3}{3!}\begin{pmatrix} \frac{\partial^3 F}{\partial u \partial v^2} \\ \frac{\partial^3 G}{\partial u \partial v^2} \end{pmatrix}\Big(U_1V_1^2\Big). \tag{2.69}$$

By writing the terms explicitly, the above expression becomes

$$(J + D\partial_{xx})\boldsymbol{W}^{(3)} = (f^{(3)}\boldsymbol{W}^{(1)} + c.c.) - \boldsymbol{m}_{31}(|A|^2 A e^{ik_c x} + c.c.) - \boldsymbol{m}_{33}(A^3 e^{3ik_c x} + c.c.), \tag{2.70}$$

here

$$\begin{aligned} m_{31}^1 =& \frac{4b}{d+b^2}\psi_1 Q_{20}^1 + \frac{2b}{d+b^2}\psi_1 Q_{22}^1 + 4b\psi_2 Q_{20}^1 + 2b\psi_2 Q_{22}^1 \\ &+4b\psi_1 Q_{20}^2 + 2b\psi_1 Q_{22}^2 + 3\psi_1^2\psi_2, \\ m_{31}^2 =& -m_{31}^1, \\ m_{33}^1 =& \frac{2b}{(d+b^2)}\psi_1 Q_{22}^1 + 2b\psi_2 Q_{22}^1 + 2b\psi_1 Q_{22}^2 + \psi_1^2\psi_2, \\ m_{33}^2 =& -m_{33}^1. \end{aligned}$$

The kernel of the adjoint can be computed to be

$$\boldsymbol{W}^\dagger = \left(\psi_1^\dagger, \psi_2^\dagger\right)^T \left(e^{ik_c x} + c.c\right) = \left(\frac{-2b^2}{k_c^2\left(b^2+d\right)\delta^2 - b^2 + d}, 1\right)^T (e^{ik_c x} + c.c.). \tag{2.72}$$

For solvability, it is sufficient to show the orthogonality between the right-hand side of (2.70) and the kernel of the adjoint. Therefore, the solvability condition is

$$f^{(3)}\left\langle \left(\psi_1, \psi_2\right)^T, \left(\psi_1^\dagger, \psi_2^\dagger\right)^T \right\rangle + \left\langle -\boldsymbol{m}_{31}, \left(\psi_1^\dagger, \psi_2^\dagger\right)^T \right\rangle |A|^2 A = 0. \tag{2.73}$$

Solving for $f^{(3)}$, we obtain

$$f^{(3)} = \frac{\left\langle \boldsymbol{m}_{31}, \left(\psi_1^\dagger, \psi_2^\dagger\right)^T \right\rangle}{\left\langle \left(\psi_1, \psi_2\right)^T, \left(\psi_1^\dagger, \psi_2^\dagger\right)^T \right\rangle} |A|^2 A = L_3 |A|^2 A. \tag{2.74}$$

By applying the above condition and imposing the ansatz (2.34) on (2.70), we obtain the uncoupled solvable linear system given by (2.35). By solving the system (2.35) we can find an expression for $\boldsymbol{W}^{(3)}$ and obtain an analytic expression for the third order coefficient which is given by

$$L_3 = \frac{\left\langle \boldsymbol{m}_{31}, \left(\psi_1^\dagger, \psi_2^\dagger\right)^T \right\rangle}{\left\langle \left(\psi_1, \psi_2\right)^T, \left(\psi_1^\dagger, \psi_2^\dagger\right)^T \right\rangle}. \tag{2.75}$$

Order 4

At this order, the main equation (2.58) is written as follows

$$\begin{aligned}
\partial_A \boldsymbol{W}^{(1)} f^{(4)} + \partial_A \boldsymbol{W}^{(2)} f^{(3)} =& (J + D\partial_{xx})\boldsymbol{W}^{(4)} + \frac{1}{2}\begin{pmatrix} \frac{\partial^2 F}{\partial u^2} & \frac{\partial^2 F}{\partial v^2} \\ \frac{\partial^2 G}{\partial u^2} & \frac{\partial^2 G}{\partial v^2} \end{pmatrix}\begin{pmatrix} 2U_1U_3 + U_2^2 \\ 2V_1V_3 + V_2^2 \end{pmatrix} + \begin{pmatrix} \frac{\partial^2 F}{\partial u \partial v} \\ \frac{\partial^2 G}{\partial u \partial v} \end{pmatrix} \\
&\times \Big(U_1V_3 + U_2V_2 + U_3V_1\Big) + \frac{1}{3!}\begin{pmatrix} \frac{\partial^3 F}{\partial u^3} & \frac{\partial^3 F}{\partial v^3} \\ \frac{\partial^3 G}{\partial u^3} & \frac{\partial^3 G}{\partial v^3} \end{pmatrix}\begin{pmatrix} 3U_1^2U_2 \\ 3V_1^2V_2 \end{pmatrix} \\
&+ \frac{3}{3!}\begin{pmatrix} \frac{\partial^3 F}{\partial u^2 \partial v} \\ \frac{\partial^3 G}{\partial u^2 \partial v} \end{pmatrix}\Big(U_1^2V_2 + 2U_1U_2V_1\Big) + \frac{3}{3!}\begin{pmatrix} \frac{\partial^3 F}{\partial u \partial v^2} \\ \frac{\partial^3 G}{\partial u \partial v^2} \end{pmatrix} \\
&\times \Big(U_2V_1^2 + 2U_1V_1V_2\Big) + \frac{1}{4!}\begin{pmatrix} \frac{\partial^4 F}{\partial u^4} & \frac{\partial^4 F}{\partial v^4} \\ \frac{\partial^4 G}{\partial u^4} & \frac{\partial^4 G}{\partial v^4} \end{pmatrix}\begin{pmatrix} U_1^4 \\ V_1^4 \end{pmatrix} + \frac{1}{6}\begin{pmatrix} \frac{\partial^4 F}{\partial u^3 \partial v} \\ \frac{\partial^4 G}{\partial u^3 \partial v} \end{pmatrix} \\
&\times U^3V_1 + \frac{1}{4}\begin{pmatrix} \frac{\partial^4 F}{\partial u^2 \partial v^2} \\ \frac{\partial^4 G}{\partial u^2 \partial v^2} \end{pmatrix}U_1^2V_1^2 + \frac{1}{6}\begin{pmatrix} \frac{\partial^4 F}{\partial u \partial v^3} \\ \frac{\partial^4 G}{\partial u \partial v^3} \end{pmatrix}U_1V_1^3.
\end{aligned} \tag{2.76}$$

By substituting the exact value for the above expression, we obtain

$$\begin{aligned}
[J + D\partial_{xx}]_c \boldsymbol{W}^{(4)} =& (L_3\boldsymbol{Q}_{20} - \boldsymbol{m}_{40})\left(|A|^4 + c.c\right) + (2L_3\boldsymbol{Q}_{22} - \boldsymbol{m}_{42})\left(A^2|A|^2 e^{2ik_c x} + cc\right) \\
&- \boldsymbol{m}_{44}\left(A^4 e^{4ik_c x} + c.c\right) + \partial_A \boldsymbol{W}^{(1)} f^{(4)},
\end{aligned} \tag{2.77}$$

where

$$m^1_{40} = \frac{b}{(d+b^2)}\left(2\psi_1 Q^1_{31} + 2(Q^2_{20})^2 + 2(Q^2_{22})^2\right) + 2(d+b)\left(\psi_1 Q^2_{31} + 2Q^1_{20}Q^2_{20} + Q^1_{22}Q^2_{22} + \psi_2 Q^1_{31}\right)$$
$$+ \left(2\psi_1^2 Q^2_{20} + \psi_1^2 Q^2_{22} + 2\psi_1\psi_2 Q^1_{20} + 2\psi_1\psi_2 Q^1_{22}\right),$$

$$m^1_{40} = -\,m^2_{40},$$

$$m^1_{42} = \frac{b}{(d+b^2)}\left(2\psi_1 Q^1_{31} + 2\psi_1 Q^1_{33} + 4Q^1_{20}Q^1_{22}\right) + 2(d+b)(\psi_1 Q^2_{31} + \psi_1 Q^2_{33} + 2Q^1_{20}Q^2_{22}$$
$$+ Q^1_{22}Q^2_{20} + \psi_2 Q^1_{31} + \psi_2 Q^1_{33}) + \left(2\psi_1^2 Q^2_{20} + 2\psi_1^2 Q^2_{22} + 4\psi_1\psi_2 Q^1_{20} + 4\psi_1\psi_2 Q^1_{22}\right)$$

$$m^1_{42} = -\,s^2_{42},$$

$$m^1_{44} = \frac{b}{(d+b^2)}\left((Q^1_{22})^2 + 2\psi_1 Q^1_{33}\right) + 2(d+b)\left(\psi_1 Q^2_{33} + Q^1_{22}Q^2_{22} + \psi_2 Q^1_{33}\right) + (\psi_1^2 Q^2_{22}$$
$$+ 2\psi_1\psi_2 Q^1_{22}),$$

$$m^1_{44} = -\,m^2_{44}.$$

The equation (2.77) does not contain any secular terms. Hence, we can take $f^{(4)} = 0$ and use the ansatz (2.40). This leads to the uncoupled system which was given in (2.41). By solving the system we achieve the solution for $\boldsymbol{W}^{(4)}$.

Order 5

At this order (2.58) becomes

$$\begin{aligned}
\partial_A \boldsymbol{W}^{(1)} f^{(5)} + \partial_A \boldsymbol{W}^{(3)} f^{(3)} =& (J + D\partial_{xx})\boldsymbol{W}^{(4)} + \frac{1}{2}\begin{pmatrix} \frac{\partial^2 F}{\partial u^2} & \frac{\partial^2 F}{\partial v^2} \\ \frac{\partial^2 G}{\partial u^2} & \frac{\partial^2 G}{\partial v^2} \end{pmatrix}\begin{pmatrix} 2U_1U_4 + 2U_2U_3 \\ 2V_1V_4 + 2V_2V_3 \end{pmatrix} + \begin{pmatrix} \frac{\partial^2 F}{\partial u \partial v} \\ \frac{\partial^2 G}{\partial u \partial v} \end{pmatrix} \\
&\times \left(U_1V_4 + U_2V_3 + U_3V_2 + U_4V_1\right) + \frac{1}{3!}\begin{pmatrix} \frac{\partial^3 F}{\partial u^3} & \frac{\partial^3 F}{\partial v^3} \\ \frac{\partial^3 G}{\partial u^3} & \frac{\partial^3 G}{\partial v^3} \end{pmatrix}\begin{pmatrix} 3U_1^2U_3 + 3U_1U_2^2 \\ 3V_1^2V_3 + 3V_1V_2^2 \end{pmatrix} \\
&+ \frac{3}{3!}\begin{pmatrix} \frac{\partial^3 F}{\partial u^2 \partial v} \\ \frac{\partial^3 G}{\partial u^2 \partial v} \end{pmatrix}\left(U_1^2V_3 + 2U_1U_2V_2 + 2U_1U_3V_1 + U_2^2V_1\right) + \frac{3}{3!}\begin{pmatrix} \frac{\partial^3 F}{\partial u \partial v^2} \\ \frac{\partial^3 G}{\partial u \partial v^2} \end{pmatrix} \\
&\times \left(U_1V_2^2 + V_1^2U_3 + 2U_1V_1V_3 + 2U_2V_1V_2\right) + \frac{1}{4!}\begin{pmatrix} \frac{\partial^4 F}{\partial u^4} & \frac{\partial^4 F}{\partial v^4} \\ \frac{\partial^4 G}{\partial u^4} & \frac{\partial^4 G}{\partial v^4} \end{pmatrix}\begin{pmatrix} 4U_1^3U_2 \\ 4V_1^3V_2 \end{pmatrix} \\
&+ \frac{1}{6}\begin{pmatrix} \frac{\partial^4 F}{\partial u^3 \partial v} \\ \frac{\partial^4 G}{\partial u^3 \partial v} \end{pmatrix}\left(U^3V_2 + 3U_1^2U_2V_1\right) + \frac{1}{4}\begin{pmatrix} \frac{\partial^4 F}{\partial u^2 \partial v^2} \\ \frac{\partial^4 G}{\partial u^2 \partial v^2} \end{pmatrix}\left(2U_1^2V_1V_2 + 2U_1U_2V_1^2\right) \\
&+ \frac{1}{6}\begin{pmatrix} \frac{\partial^4 F}{\partial u \partial v^3} \\ \frac{\partial^4 G}{\partial u \partial v^3} \end{pmatrix}\left(3U_1V_1^2V_2 + U_2V_1^3\right) + \frac{1}{5!}\begin{pmatrix} \frac{\partial^5 F}{\partial u^5} & \frac{\partial^5 F}{\partial v^5} \\ \frac{\partial^5 G}{\partial u^5} & \frac{\partial^5 G}{\partial v^5} \end{pmatrix}\begin{pmatrix} U_1^5 \\ V_1^5 \end{pmatrix} + \frac{1}{24}\begin{pmatrix} \frac{\partial^5 F}{\partial u^4 \partial v} \\ \frac{\partial^5 G}{\partial u^4 \partial v} \end{pmatrix} \\
&\times U_1^4V_1 + \frac{1}{12}\begin{pmatrix} \frac{\partial^5 F}{\partial u^3 \partial v^2} \\ \frac{\partial^5 G}{\partial u^3 \partial v^2} \end{pmatrix}U_1^3V_1^2 + \frac{1}{12}\begin{pmatrix} \frac{\partial^5 F}{\partial u^2 \partial v^3} \\ \frac{\partial^5 G}{\partial u^2 \partial v^3} \end{pmatrix}U_1^2V_1^3 + \frac{1}{24}\begin{pmatrix} \frac{\partial^5 F}{\partial u \partial v^4} \\ \frac{\partial^5 G}{\partial u \partial v^4} \end{pmatrix}V_1^4U_1.
\end{aligned} \tag{2.79}$$

By evaluating the expression we obtain

$$[J+D\partial_{xx}]\boldsymbol{W}^{(5)} = \boldsymbol{\psi}\left(f^{(5)}e^{ik_c x}+c.c\right)+(2\boldsymbol{Q}_{31}L_3-\boldsymbol{m}_{51})\left(A|A|^4e^{ik_c x}+c.c\right)$$

$$\times(3\boldsymbol{Q}_{33}L_3-\boldsymbol{m}_{53})\left(A^3|A|^2e^{3ik_c x}+c.c\right)-\boldsymbol{m}_{55}\left(A^5e^{5ik_c x}+c.c\right), \tag{2.80}$$

here

$$\begin{aligned}
m^1_{51} =& \frac{2b}{(d+b^2)}\left(2\psi_1Q^1_{40}+\psi_1Q^1_{42}+2Q^1_{20}Q^1_{31}+Q^1_{22}Q^1_{31}+Q^1_{22}Q^1_{33}\right)+2(d+b)(2\psi_1Q^2_{40}\\
&+\psi_1Q^2_{42}+2Q^1_{20}Q^2_{31}+Q^1_{22}Q^2_{31}+Q^1_{22}Q^2_{33}+2Q^1_{20}Q^1_{31}+Q^2_{22}Q^1_{31}+Q^2_{22}Q^1_{33}+2\psi_2Q^1_{40}\\
&+\psi_2Q^1_{42})+(\psi^2_1Q^2_{31}+\psi^2_1Q^2_{33}+2\psi^2_2Q^2_{31}+2(4\psi_1Q^1_{20}Q^2_{20}+2\psi_1Q^1_{22}Q^2_{20}+2\psi_1Q^1_{20}Q^2_{22}\\
&+2\psi_1Q^1_{22}Q^2_{22}+\psi_1\psi_2Q^1_{31}+3\psi_1\psi_2Q^1_{33})+\psi_2(Q^2_{20})^2+4\psi_2Q^2_{20}Q^2_{22}+2\psi_2(Q^2_{22})^2),
\end{aligned}$$

$$m^1_{51} = -m^2_{51},$$

$$\begin{aligned}
m^1_{53} =& \frac{2b}{(d+b^2)}(\psi_1Q^1_{44}+\psi_1Q^1_{42}+2Q^1_{20}Q^1_{33}+Q^1_{22}Q^1_{31})+2(d+b)(\psi_1Q^2_{44}+\psi_1Q^2_{42}+2Q^1_{20}Q^2_{33}\\
&+Q^1_{22}Q^2_{31}+2Q^2_{20}Q^1_{33}+Q^2_{22}Q^1_{31}+\psi_2Q^1_{44}+\psi_2Q^1_{42})+(\psi^2_1Q^2_{31}+2\psi^2_1Q^2_{33}+2(2\psi_1Q^1_{22}Q^2_{20}\\
&+2\psi_1Q^1_{20}Q^2_{22}+\psi_1Q^1_{22}Q^2_{22}+\psi_1\psi_2Q^1_{31}+2\psi_1\psi_2Q^1_{33})+4\psi_2Q^2_{20}Q^2_{22}+\psi_2(Q^2_{22})^2),
\end{aligned}$$

$$m^1_{53} = -m^2_{53},$$

$$\begin{aligned}
m^1_{55} =& \frac{2b}{(d+b^2)}(\psi_1Q^1_{44}+Q^1_{22}Q^1_{33})+2(a+b)(\psi_1Q^2_{44}+Q^1_{22}Q^2_{33}+Q^2_{22}Q^1_{33}+\psi_2Q^1_{44})+(\psi^2_1Q^2_{33}\\
&+2\psi_1Q^1_{22}Q^2_{22}+2\psi_1\psi_2Q^1_{33}+\psi_2(Q^2_{22})^2),
\end{aligned}$$

$$m^1_{55} = -m^2_{55}.$$

Since the equation (2.80) has a resonant term, we apply the solvability condition

$$f^{(5)} = \frac{\left\langle \boldsymbol{m}_{51},\boldsymbol{\psi}^\dagger\right\rangle-\left\langle 2L_3Q_{31},\boldsymbol{\psi}^\dagger\right\rangle}{\left\langle \boldsymbol{\psi},\boldsymbol{\psi}^\dagger\right\rangle}A|A|^5 = L_5A|A|^5, \tag{2.82}$$

and we substitute the ansatz (2.44). In consequence, the solution for the fifth order ($W^{(5)}$) can be obtained by solving the uncoupled system which was given in (2.46).

Unfolding

The main equation at this order from section 2.3 is expressed as

$$\partial_A\boldsymbol{W}^{(1,0)}f^{(1,1)}+c.c = (J+D\partial_{xx})\boldsymbol{W}^{(1,1)}+\epsilon\mathscr{L}_P\boldsymbol{W}^{(1,0)}, \tag{2.83}$$

where $\mathscr{L}_P$ is the linear operator for variation of the parameters around the critical point and ϵ stands for small change in the parameters. Thus, we have two possible choices for $\mathscr{L}_P$ depend on the choice of the control parameter which are

$$\mathscr{L}_d = \begin{pmatrix} -\dfrac{2b^2}{\left(d+b^2\right)^2} & 1 \\ \dfrac{2b^2}{\left(d+b^2\right)^2} & -1 \end{pmatrix}, \quad \mathscr{L}_b = \begin{pmatrix} \dfrac{4bd}{\left(d+b^2\right)^2} & 2b \\ -\dfrac{4bd}{\left(d+b^2\right)^2} & -2b \end{pmatrix}. \tag{2.84}$$

Since we have a secular term in equation (2.83), the solivability condition is

$$f^{(1,1)} = \epsilon \frac{\left\langle \mathscr{L}_p \left(\psi_1, \psi_2\right)^T, \left(\psi_1^\dagger, \psi_2^\dagger\right)^T \right\rangle}{\left\langle \left(\psi_1, \psi_2\right)^T, \left(\psi_1^\dagger, \psi_2^\dagger\right)^T \right\rangle} A = \epsilon L_1 A. \tag{2.85}$$

Introducing the condition (2.85) and substituting the ansatz (2.53) into (2.83), we obatin the solution of $W^{(1,1)}$ at this order.

Now, we can write the amplitude equation as follow

$$\partial_t A = \epsilon L_1 A + L_3 A|A|^2 + L_5 A|A|^4, \tag{2.86}$$

and the change of variable equation

$$\begin{aligned}\begin{pmatrix} U \\ V \end{pmatrix} = &\begin{pmatrix} b \\ \dfrac{b}{d+b^2} \end{pmatrix} + \left(\begin{pmatrix} \psi_1 \\ \psi_2 \end{pmatrix} + \phi\right)\left(Ae^{ik_c x} + c.c\right) + \boldsymbol{Q}_{20}\left(|A|^2 + c.c\right) + \boldsymbol{Q}_{22}\left(A|A|^2 Ae^{2ik_c x} + c.c\right) \\ &+ \boldsymbol{Q}_{31}(|A|^2 Ae^{ik_c x} + c.c.) + \boldsymbol{Q}_{33}(A^3 e^{3ik_c, x} + c.c.) + \boldsymbol{Q}_{40}\left(|A|^4 + c.c\right) + \boldsymbol{Q}_{22}\left(A^2|A|^2 e^{2ik_c x} + cc\right) \\ &+ \boldsymbol{Q}_{44}\left(A^4 e^{4ik_c x} + c.c\right) + \boldsymbol{Q}_{51}\left(A|A|^4 e^{ik_c x} + c.c\right) + \boldsymbol{Q}_{53}\left(A^3|A|^2 e^{3ik_c x} + c.c\right) \\ &+ \boldsymbol{Q}_{55}\left(A^5 e^{5ik_c x} + c.c\right).\end{aligned} \tag{2.87}$$

After obtaining the amplitude equation, we can determine that the bifurcation switches from being subcritical to supercritical whenever L_3 changes sign from positive to negative at the transition point. Figure 2.4 shows the result of computation of the locus of Turing bifurcation for the glycolysis model. We have used Maple to numerically evaluate the expression (2.75) for L_3 along this curve. We find a point for which $L_3 = 0$. Figure 2.4b shows the existence of a codimension-two bifurcation in the parameter space. The black circle expresses the point where the spatial pattern changes from being subcritical (red) to supercritical (blue). Finally, we use Maple to calculate the value of L_5 from the expression (2.82) which is found to be -0.09380157.

2.5 Inhomogeneous steady state patterns via spatial dynamics

Reaction-diffusion equations of the form (2.1) can describes the spatial structures that are stable in time. In this case, the dynamics of (2.1) is expected to tend to the steady state solution after long time. Therefore, these type of system permits two kinds of steady state: an homogeneous steady state $\boldsymbol{U} = \boldsymbol{U}_0$ independent of x which solves $F(\boldsymbol{U}_0, p) = 0$ and an inhomogeneous steady state $\boldsymbol{U}(x)$ which solves

$$D\frac{\mathrm{d}^2 \boldsymbol{U}}{\mathrm{d}x^2} + F(\boldsymbol{U}, p) = 0. \tag{2.88}$$

Thus an inhomogeneous steady state associated with (2.1) can be expressed as a system of first order ordinary differential equations for the spatial evolution which is a particular type of the

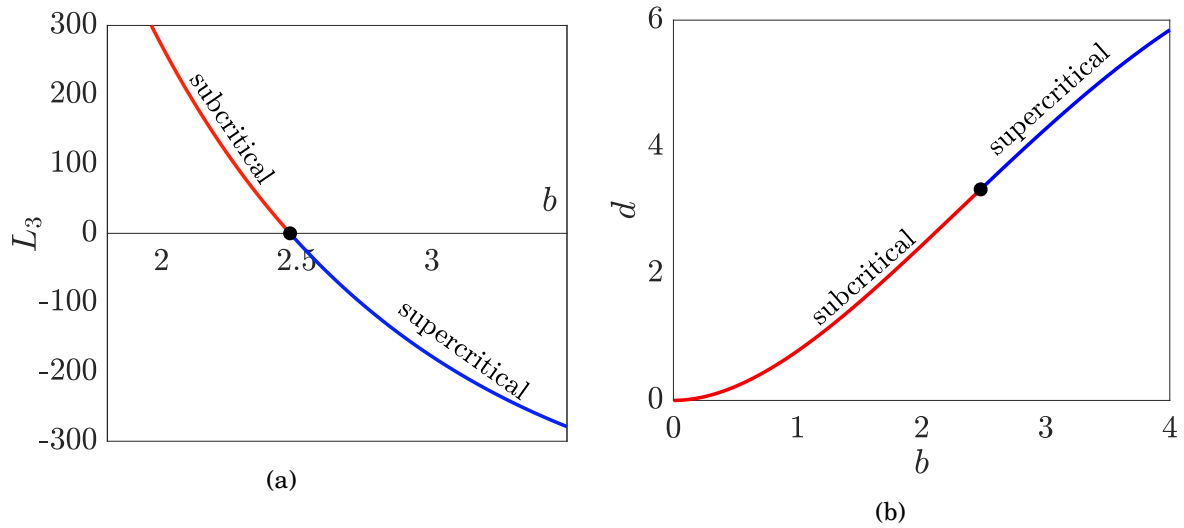

Figure 2.4: Plot of L_3 for (2.56) at the Turing bifurcation point. (a) Projection onto the (L_3, b)-plane. (b) Projection onto the (b,d)-plane. The other parameter value $\delta = 0.045$.

dynamical system in which space takes the role of the time, and we treat $x \in (-\infty, \infty)$. This paradigm has been referred to as so-called spatial dynamics [76, 171]. Specifically, if we write

$$\frac{\mathrm{d}\boldsymbol{V}_1}{\mathrm{d}x} = \boldsymbol{V}_2, \tag{2.89a}$$

$$\frac{\mathrm{d}\boldsymbol{V}_2}{\mathrm{d}x} = -D^{-1}F(\boldsymbol{V}_1, p) \tag{2.89b}$$

then we can set $\boldsymbol{W} = (\boldsymbol{V}_1, \boldsymbol{V}_2) = (\boldsymbol{U}, \boldsymbol{U}_x) \in \mathbb{R}^{2n}$ from which we can obtain

$$\frac{\mathrm{d}\boldsymbol{W}}{\mathrm{d}x} = \mathscr{F}(\boldsymbol{W}, p). \tag{2.90}$$

Systems of the form (2.89) or (2.90) present many interesting properties. Firstly, the system is conservative [20]. Secondly, it is reversible [20, 35, 171] such that there is a linear involution transformation R that fixes half phase-plane, that is

$$R\mathscr{F}(\boldsymbol{W}, p) = -\mathscr{F}(R\boldsymbol{W}, p), \quad R^2 = I, \quad S = \mathrm{fix}(R) \sim \mathbb{R}^n. \tag{2.91}$$

Specifically for (2.90) we have

$$S = \{\boldsymbol{W}; \boldsymbol{V}_2 = 0\}, \quad \text{and} \quad R : (\boldsymbol{V}_1, \boldsymbol{V}_2)^T \to (\boldsymbol{V}_1, -\boldsymbol{V}_2)^T.$$

The linear subspace S is called the symmetric section of reversibility.

2.5.1 Linearisation

In this framework, the homogeneous state of (2.1) which is $\boldsymbol{U} = \boldsymbol{U}_0$ is equivalent to an equilibrium $\boldsymbol{W}_0 = (\boldsymbol{U}_0, 0)$ in the spatial dynamics system (2.89). Now, we linearise (2.89) around the spatial

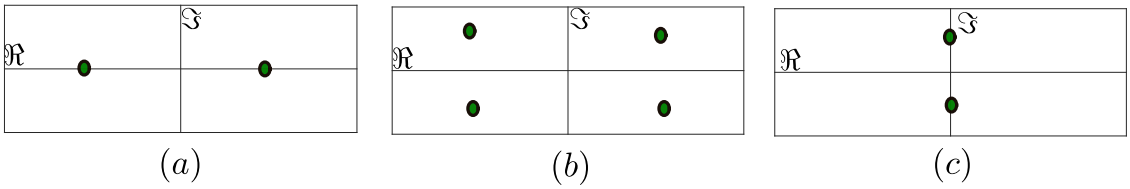

Figure 2.5: Possible spatial eigenvalues of an homogeneous steady state configuration.

equilibrium to give

$$\boldsymbol{W}_x = J_s(F(\boldsymbol{W}_0))\boldsymbol{W}(x) + NL_s(\boldsymbol{W}(x)). \tag{2.92}$$

Here J_s is the Jacobian matrix and NL_s contains the nonlinear terms evaluated at the steady state $\boldsymbol{W}_0$. Investigating the linear term of (2.92) can provide us with much information about dynamics around the equilibrium points, the natures of those equilibria and the behaviours of the manifolds that approach and leave $\boldsymbol{W}_0$. The linear stability analysis is performed for (2.92) by considering a spatial perturbation of the form $\boldsymbol{W}(x) = \boldsymbol{W}_0 + \boldsymbol{A}e^{\sigma x}$. Here σ is complex in general and $\boldsymbol{A}$ is an eigenvector. Therefore, we can understand the possible existence of homoclinic orbit to $\boldsymbol{W}_0$ and predict the shape of the localised pattern's tail.

In general, there are $2n$ spatial eigenvalues, but the eigenvalues with the largest real part (in absolute value) demonstrate the qualitative behaviour of the system as they determine the asymptotic approach to the steady state [125]. Accordingly, we have three cases for spatial eigenvalues see Figure 2.5:

(a) The leading eigenvalues are purely real $\sigma = \pm q_0$.

(b) The leading eigenvalues are complex conjugates $\sigma = \pm q_0 \pm ik_0$.

(c) The leading eigenvalues are purely imaginary $\sigma = \pm ik_0$.

There are two main transformations for the spatial eigenvalues which cause a transition from case (a) to case (b) and from (c) to case (b). The first transition from (a) to (b) is a result of a collision of two real eigenvalues which leads to complex eigenvalues. In this context of the localised pattern formation transition is known as a Belyakov-Devaney (BD) transition [35, 53, 125, 166], which does not represent a local bifurcation of $\boldsymbol{W}_0$ in the classical sense, because it does not involve any eigenvalues crossing the imaginary axis. The second transition is the transition from (c) to (b), which corresponds to the collision of imaginary spatial eigenvalues on the imaginary axis to became complex conjugate eigenvalues. This transition is called a Hamiltonian Hopf bifurcation, and is also known as a reversible $1:1$ resonance [76].

2.5.2 Localised patterns and homoclinic snaking

Now let us consider the dynamics of the reversible spatial system and the localised structures associated with an orbit $\boldsymbol{W}(x)$ which is a homoclinic connection to a homogeneous steady state

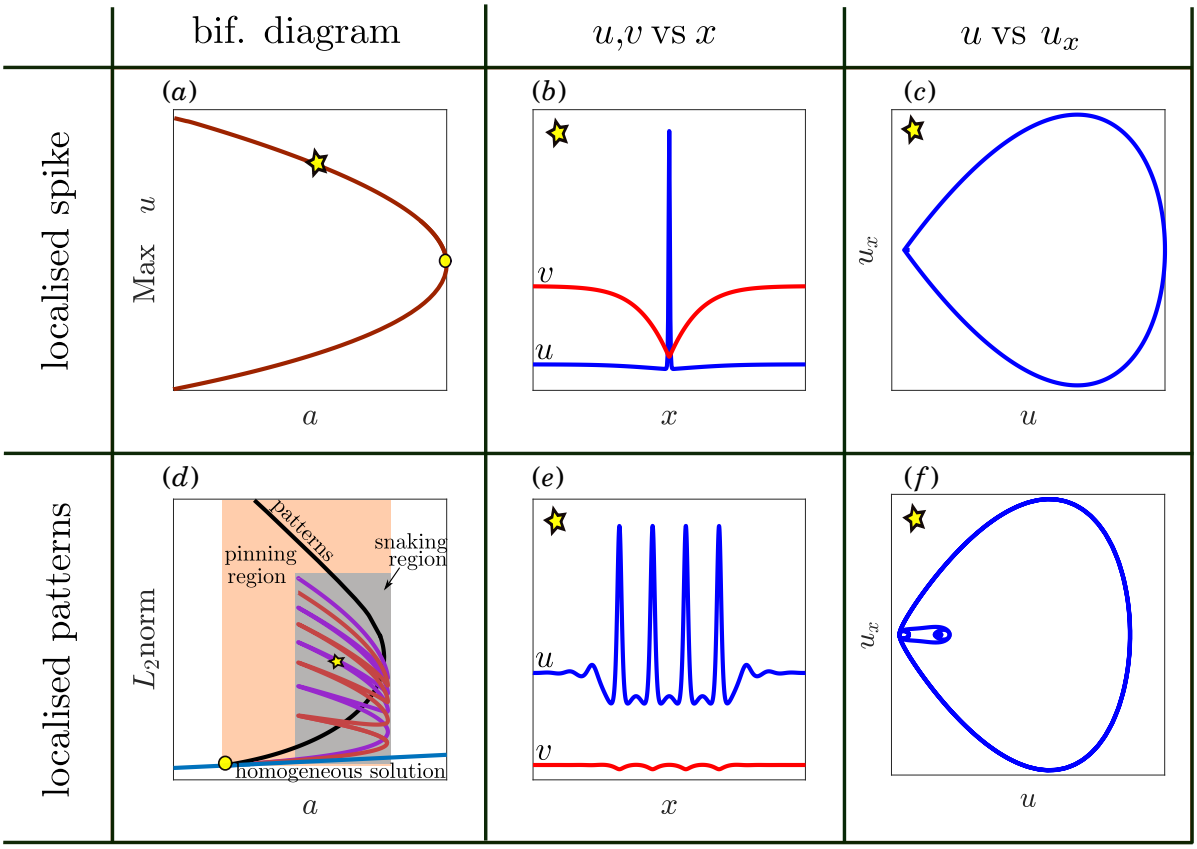

Figure 2.6: Qualitative differences between localised spikes (top half) and localised patterns (bottom half). In the *leftmost* column, a sketch of the bifurcation diagram of each solution is represented, in which the vector L_2-norm is plotted against a scalar parameter γ. The *middle* column depicts one representative component of a particular solution (distinguished with a star on the left), as a graph against x. The *rightmost* column shows a planar projection of the solution in phase space.

$\boldsymbol{W}_0$. Hence we can make use of the homoclinic theory to study the existence of the localised structures under parameter variation. We can observe a variety of behaviour depending on spatial eigenvalues—the real eigenvalues corresponding to a single spike solution, whereas the complex eigenvalues associate with the localised patterns (see Figure 2.6).

The localised patterns represent steady-state solutions to (2.1). These solutions have some features which are an internal spatial wavelength and an oscillatory decaying of the tail as the solution approaches the homogeneous steady state in the far-field. They typically form a group of a countable infinite family of solutions which can be described by their number of peaks outside the tail region (see Figure 2.6 (e) as an example). We can illustrate localised patterns in several ways.

One approach to characterising localised patterns is to think of them as the interaction between two fronts where at least one of the steady-states that the fronts connect to posseses a spatial wavelength. In this situation, it is possible to apply weakly nonlinear analysis to obtain

the bifurcation diagram of the localised structures with the assumption that the fronts are apart from each other [134]. An alternative way to describe the localised patterns is based on a heteroclinic connection between the homogeneous solution and the periodic patterns. Because of the reversibility, infinity many homoclinic orbits are created from the unfolding of the heteroclinic connection [171]. These homoclinic orbits are corresponding to the localised patterns. Hence, the internal wavelength is provided by the period of the periodic patterns. The bifurcation diagram in this case have referred to as homoclinic snaking [171]. There are a significant number of studies that focus on the homoclinic snaking scenario [33, 38, 46, 49, 93, 94]. For instance, the work by Burke and Knoloch [33] investigates the Swift-Hohenberg equation to explain the appearance of the homoclinic snaking close to a transition of the Hamiltonian-Hopf bifurcation from a subcritical to a supercritical. Here, the term 'snaking' bifurcation diagram refers to a particular scenario when the an appropriate norm of the localised structure is plotted as a function of the bifurcation parameter (see Figure 2.6 (d)). The peculiarity of this structure is that there is a pair of curves that wind back and forth as they extend vertically. If the domain was infinitely long, there would be an infinite number of localised patterns whose width tends to infinity. In contrast, on a finite domain, there are only a finite number of localised patterns (as in Figure 2.6 (d)). The authors of [20] provided rigorous explanation of what will happen generically for localised patterns. Furthermore, in [104] the possibility of obtaining localised pattern in a higher spatial dimensions is analysed where the localised patterns can be observed in different shapes such as rolls, hexagonal lattices and target patterns.

Another type of localised pattern solution is an isolated spikes which correspond to homoclinic orbits to a homogeneous steady state with real leading spatial eigenvalues. In contrast to the localised patterns, the isolated spike solution decays monotonically in the far the field (see Figure 2.6 (b)). Consequently, it does not occur as part of an infinite family that would result from having an oscillatory tail. The single spike solution can be found in a variety of applications of a reaction-diffusion system which can be explored by either geometric singular perturbation theory [56] or semi-strong interaction [168] which we will considered in chapter 3. In [166] an analyses is undertaking of what happen to the ∞-many additional patterns solutions as we cross the BD transition from the snaking to the spike region essentially the pules of the multi-pules orbits become infinity for separated.

2.5.3 Two-component example continued

As a specific example, we shall reconsider the glycolysis model (2.56). Hence the time-independent solution $(u(x), v(x))$ in one spatial dimension satisfies the coupled differential equations in x,

$$d v - u + u^2 v + \delta^2 \frac{\partial^2 u}{\partial x^2} = 0, \tag{2.93a}$$

$$b - d v - u^2 v + \frac{\partial^2 v}{\partial x^2} = 0. \tag{2.93b}$$

Precisely, we let $w(x) = [u, u_x, v, v_x]$, hence, we have the following

$$\frac{\mathrm{d}w_1}{\mathrm{d}x} = w_2, \tag{2.94a}$$

$$\frac{\mathrm{d}w_2}{\mathrm{d}x} = \frac{(w_1 - dw_3 - w_1^2 w_3)}{\delta^2}, \tag{2.94b}$$

$$\frac{\mathrm{d}w_3}{\mathrm{d}x} = w_4, \tag{2.94c}$$

$$\frac{\mathrm{d}w_4}{\mathrm{d}x} = dw_3 + w_1^2 w_3 - b. \tag{2.94d}$$

This system is invariant under spatial reflection

$$(x, w_1, w_2, w_3, w_4) \to (-x, w_1, -w_2, w_3, -w_4), \tag{2.95}$$

which means that the system (2.94) is reversible in space. As all localized structures are connected to the homogeneous solution as $x \longrightarrow \pm\infty$, therefore, we require that the homogeneous solution has both stable and unstable spatial eigenvalues. To check this requirement, we perform linear stability analysis around the homogeneous state. This analysis provides sufficient information about the eigenvalues and the corresponding trajectory. Moreover, it gives information about the tail of the solution profile. The linearisation of (2.94) around the steady state point which is $(w_1, w_2, w_3, w_4) = (b, 0, b/(b^2 + d), 0)$ yields

$$\frac{\mathrm{d}}{\mathrm{d}x}\boldsymbol{W}(x) = J\boldsymbol{W}(x) \tag{2.96}$$

where $\boldsymbol{W}(x) = (w_1, w_2, w_3, w_4)^T$ and J is the Jacobian matrix of the spatial system given by

$$J = \begin{pmatrix} 0 & 1 & 0 & 0 \\ \dfrac{d - b^2}{\delta^2(d + b^2)} & 0 & \dfrac{-(d + b^2)}{\delta^2} & 0 \\ 0 & 0 & 0 & 1 \\ \dfrac{2b}{d + b^2} & 0 & d + b^2 & 0 \end{pmatrix}. \tag{2.97}$$

The general solution for the linear problem for (2.96) takes the form $\boldsymbol{W}(x) = Ae^{i\lambda x}$, here A stands for the pattern amplitude and λ is the eigenvalue of the spatial system. To drive the conditions for the spatial instability one must obtain the eigenvalues of J which satisfy the following characteristic polynomial

$$\lambda^4 - B\lambda^2 + C = 0, \tag{2.98}$$

where $B = \dfrac{\delta^2\left(b^2 + d\right)^2 - b^2 + d}{\left(b^2 + d\right)\delta^2}$ and $C = \dfrac{b^2 + d}{\delta^2}$. Therefore, the solutions of (2.98) are defined by

$$\lambda_{1,2,3,4} = \pm\sqrt{\frac{1}{2}(B \pm \sqrt{B^2 - 4C})}. \tag{2.99}$$

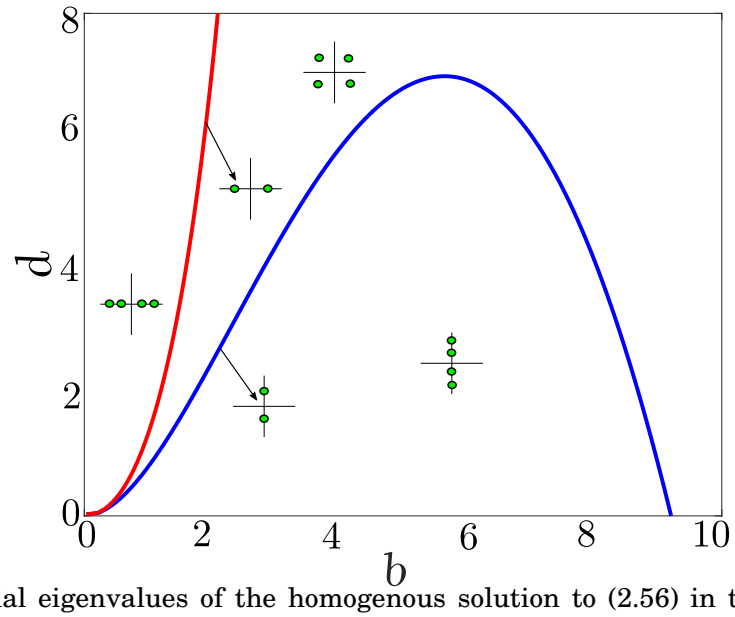

Figure 2.7: Spatial eigenvalues of the homogenous solution to (2.56) in the (b,d)-plane for $\delta = 0.045$ where the blue curve indicates the Hamiltonian-Hopf bifurcation and the red curve expresses Belyakov-Devaney transition. The sketches in the figure show the organization of the spatial eigenvalues which satisfy equation (2.98).

Considering (2.98) we can identify how the possible configuration of the spatial eigenvalues depend on the values of the control parameters d and b (see Figure 2.98).

The first case we have is a set of four purely real repeated eigenvalue ($\lambda_{1,2} = \pm q_1, \lambda_{3,4} = \pm q_2$). These undergo a transition to a double real eigenvalue pair at the Belyakov-Devaney (BD) line (see the red curve in Figure 2.7) which reads

$$\delta\left(b^2+d\right)\sqrt{-\left(b^2+d\right)^2\delta^2+2(3\,b^2+d)} = d-b^2. \tag{2.100}$$

Note that this is obtained from the same condition for a Turing instability in linear stability analysis but when the critical wavenumber is less then zero, $k_c < 0$. The second case we can have is pure imaginary eigenvalues ($\lambda_{1,2} = \pm ik_1, \lambda_{3,4} = \pm ik_2$). These eigenvalues become double imaginary eigenvalues at a Hamiltonian Hopf line (which is equivalent to a Turing bifurcation in the time domain) see the blue curve in Figure 2.7. The last interesting case when the eigenvalues are quartet complex ($\lambda_{1,2} = \pm q_1 \pm ik_1, \lambda_{3,4} = \pm q_2 \pm k_2$).

So far we have described the spatial eigenvalues and their transition in (b,d)-plane. However, we are interested in finding the localized structures and study the complex behaviour which exist. By applying the normal form method (see Section 2.3 for the detail of the method), we gain the codimension two point which implies the existence of small-amplitude localised structures from the Hamiltonian Hopf bifurcation [171]. Figure 2.8a shows the (b,d)-plane with the codimension two point, which we obtained by linear analysis coupled to the weakly nonlinear analysis described in Section 2.2 and 2.3, and the localized structures region found by the numerical continuation

AUTO [54]. Here, we use numerical continuation to track and understand the behaviour of the localized solutions far from the codimension two point.

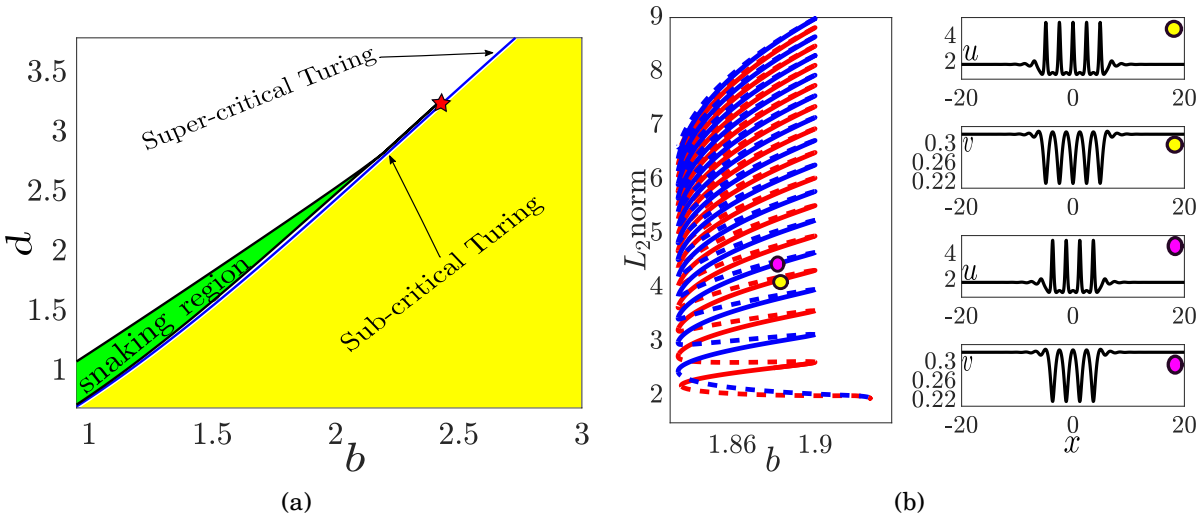

Figure 2.8: The figure depict the snaking region of the glycolysis model (2.56) for $\delta = 0.045$. The red star indicates the condition $L_3 = 0$ in (2.75) where the Turing instability changes from subcritical to supercritical. (b) Homoclinic snaking for $d = 2.11885$ as b varies. The continuous (dashed) line presents stable (unstable) solutions. Here the red (blue) line relates to even (odd) number of peaks. In the right profile example of even (odd) numbers of peak solution that mark by magenta (yellow) circle in snaking digram is presented.

Figure 2.8b shows the pair of the homoclinic orbits undergoing homoclinic snaking. It is clear from the figure the wiggle of the two branches of the localized structures. The solution measure used in the diagram is the vector L_2 norm which is given by

$$L_2\,\text{norm} = \sqrt{\frac{1}{L}\int_0^L \sum_{j=0}^{4} w_j^2(y)dy}\,. \tag{2.101}$$

where $[0,L]$ is the truncated interval used by AUTO to approximate the infinity dimension using Neumann boundary conditions. Also indicated on the branches are the stability of the localised states by use of a solid (stable) or dashed (unstable) line. Here stability was computed using the methods outlined in Section 2.6 below. The colour used in each branch corresponds to different numbers of peaks; the blue curve represent an even number of peaks while the red curve accords with an odd number of peaks (see Figure 2.8b). Furthermore, these branches emerge subcritically from the Hamiltonian-Hopf bifurcation. Moreover, the localised pattern solutions are symmetric under the reversibility because of the spatial reflection $x \longrightarrow -x$. At each subsequent pair of the saddle node bifurcations the homoclinic orbit gains an extra pairs of peaks close to the periodic solution [171].

The spike solution corresponds to a homoclinic connection of system (2.93) whose tails are decaying monotonically in the far field. This solution arises from a single branch of the homoclinic

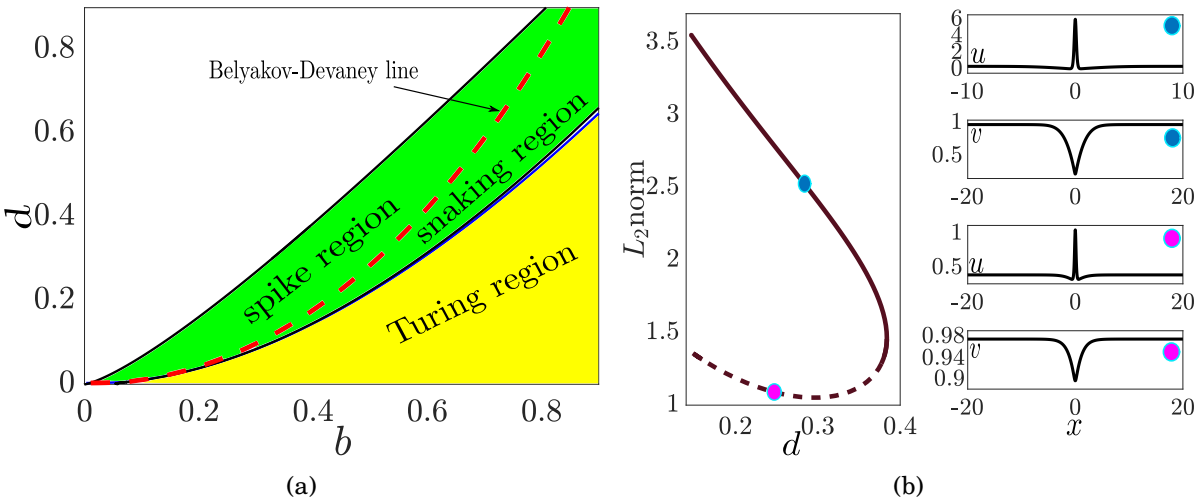

(a) (b)

Figure 2.9: (a) Similar to Figure 2.8a but for lower part of (a,b)-plane where the spike solution is existing. (b) The fold of the spike type solution is presented in vector L_2 – norm against the parameter d for fixed $b = 0.5$. The continuous (dashed) line indicates the stable (unstable) branch of the fold . The panels to the right correspond to the solution of the fold branches.

solution that bifurcates from the homogeneous equilibrium forming an unstable spike with small amplitude which grows to become stable after crossing a fold. Figure 2.9 depicts the spike region in (b,d)-plane, and examples of stable and unstable single spike type solutions. In chapter 3 we show how to construct approimate solutions for the spike using semi-strong interaction asymptotic analysis.

2.6 Numerical methods

In this section, we describe the numerical techniques which we apply to investigate the existence and the stability of the solutions in this thesis.

2.6.1 Direct numerical integration

This section outlines the numerical technique of solving reaction-diffusion system of the form (2.1), which we will be utilized in this thesis. The procedure uses finite difference approximations with zero flux boundary conditions [25, 50]. The essential advantage of the finite difference method is its applicability to many problems without requiring much mathematical detail of the individual problem [25]. Furthermore, the approach is straightforward to implement as it can handle any boundary conditions. In principle, the finite difference method employs Taylor expansion for the discretisation of the spatial derivative.

The initial step of the technique is to discretise the domain by a set of equal space mech points—such that

$$x_i = i\Delta x, \quad i = 0,...,N_x,$$

and

$$t_j = j\Delta t, \quad j = 0,...,N_t,$$

where N_x and N_t are the number of mesh points in x and t, respectively. Therefore we can write $U(x_i,t_j)$ as a mesh function U_i^j for $i = 0,..,N_x$ and $j = 0,..,N_t$. In consequence, the system (2.1) at a mesh point (x_i,t_j) is expressed by

$$\partial \boldsymbol{U}_t(x_i,t_j) = D\nabla \boldsymbol{U}(x_i,t_j) + F(\boldsymbol{U}(x_i,t_j),\boldsymbol{p}), \quad x \in [-l,l], \quad t > 0, \tag{2.102}$$

The next step is replacing the derivative with finite difference approximation using forward difference in time and central in space. Hence, system (2.102) become

$$\frac{\boldsymbol{U}_i^{j+1} - \boldsymbol{U}_i^j}{\Delta t} = D\frac{\boldsymbol{U}_{i+1}^j - 2\boldsymbol{U}_i^j + \boldsymbol{U}_{i-1}^j}{\Delta x^2} + F(\boldsymbol{U}_i^j, p). \tag{2.103}$$

let us suppose U_i^j is given, so U_i^{j+1} is the only unknown. Solving (2.103) for U_i^{j+1}, we obtain

$$\boldsymbol{U}_i^{j+1} = \boldsymbol{U}_i^j + \frac{D\Delta t}{\Delta x^2}\left(\boldsymbol{U}_{i+1}^j - 2\boldsymbol{U}_i^j + \boldsymbol{U}_{i-1}^j\right) + \Delta t F(\boldsymbol{U}_i^j, \boldsymbol{p}),$$

with homogeneous Neumann boundary conditions

$$\boldsymbol{U}_i^{j+1} = \boldsymbol{U}_{i+1}^{j+1}, \quad \text{and} \quad \boldsymbol{U}_{N_x}^{j+1} = \boldsymbol{U}_{N_x-1}^{j+1}.$$

The term $\Omega = \dfrac{D\Delta t}{\Delta x^2}$ is known as the Courant number [42]. This term plays an essential role in the method's stability. In order to obtain a numerically stable solution, we require $\Omega \leqslant 0.5$ [99]. All computation were carried out in Matlab.

As an example, let us recall the two-components example glycolysis model (2.56). Accordingly, the discrete system is

$$u_i^{j+1} = u_i^j + \frac{\delta^2\Delta t}{\Delta x^2}\left(u_{i+1}^j - 2u_i^j + u_{i-1}^j\right) + \Delta t\left(dv_i^j - u_i^j + (u_i^j)^2 v_i^j\right), \tag{2.105a}$$

$$v_i^{j+1} = v_i^j + \frac{\Delta t}{\Delta x^2}\left(v_{i+1}^j - 2v_i^j + v_{i-1}^j\right) + \Delta t\left(b - dv_i^j - (u_i^j)^2 v_i^j\right), \tag{2.105b}$$

with Neumann boundary conditions

$$\begin{aligned} &u_{N_x}^{j+1} = u_{N_x-1}^{j+1}, \quad u_{N_x}^{j+1} = u_{N_x-1}^{j+1}, \\ &v_{N_x}^{j+1} = v_{N_x-1}^{j+1} \quad \text{and} \quad v_{N_x}^{j+1} = v_{N_x-1}^{j+1}. \end{aligned} \tag{2.105c}$$

2.6.2 Numerical continuation using Auto

Here we briefly introduce the AUTO continuation package. AUTO is a continuation code that intends to find and continue a solution of a system of ordinary differential equations of the form

$$\frac{\mathrm{d}\boldsymbol{U}}{\mathrm{d}x} = f(\boldsymbol{U}, \boldsymbol{p}), \quad x \in [0, l] \tag{2.106}$$

which is subject to boundary conditions. Implementing AUTO requires two Fortran files. These files are given named as ***.f90 and c.*** where *** is the abbreviated name of the example in question. The first file contains the information of the right-hand side of (2.106). The second file defines the individual constants set by the user to specify what problem AUTO should solve and how.

The purpose of the continuation is to explore and compute families of the steady state solutions to spatially periodic orbits and localised solutions of (2.106) as the parameters vary. This allows us to acquire substantial information about the system dynamics for a diverse range of the parameter values. Using the theory of reversible system, note that both homoclinic and periodic orbit can be captured using Neumann boundary conditions which is equivalent to saying $x(\pm l) \in S$; see for example [35] and references therein. Through the continuation, we can identify the first bifurcation point from the branch of the steady state solution which will typically be spatially periodic. The localised solution will typically be found as secondary bifurcations when computing on finite domain. We also employed the reading of data from Matlab simulation as starting solution for continuation.

We found a variety of AUTO demos to be useful. The demo *ab* was useful to find the steady state solutions and the location of Hopf bifurcation of these steady states. The second demo we utilised is the boundary-value problem (*exp* demo). We have adapted this demo to obtain solutions to the boundary-value problem and continue these solutions in the parameter space. By implementing such approach, we achieved the homoclinic snaking diagram. By continuing folds of such diagram in two parameters we were able to find the boundary of the region of the localised structures. The final demo we use is the HomCont demo (*she* demo). The demo has been applied to find the heteroclinic connection between two homogenous steady states; (see chapters 4 and 7).

2.6.3 Spectral computation

Once we have found the steady solution using AUTO, we investigate its stability using a combination of direct numerical simulation as in section 2.6.1 and computation of the spectrum linearised about the steady state [25]. To illustrate the implementation of spectral computation, let us consider (2.1) in one dimension domain. We assume the system has a non-constant equilibrium solution

$$\boldsymbol{U}(x,t) = \hat{\boldsymbol{U}}(x). \tag{2.107}$$

Firstly, we linearise the system (2.1) at the above equilibrium by introducing new variable $\boldsymbol{U}(x,t) = \hat{\boldsymbol{U}}(x) + \boldsymbol{u}(x,t)$ and neglecting nonlinear terms, we obtain the following linear problem

$$\boldsymbol{u}_t = \mathscr{L}\boldsymbol{u}. \tag{2.108}$$

Here $\mathscr{L} = (J_F(\hat{\boldsymbol{U}}(x)) + D\partial_{xx}\ )$, where $J_F(\hat{\boldsymbol{U}}(x))$ is the Jacobian matrix of F at the equilibrium solution. Considering the linear order of (2.108) and assuming the following anasatz

$$\boldsymbol{u} = \boldsymbol{w}(x)e^{\lambda t}, \tag{2.109}$$

where λ is the growth factor or temporal eigenvalue, we have the following eigenvalue problem:

$$[\mathscr{L} - \lambda I]\boldsymbol{w} = 0. \tag{2.110}$$

The main steps to calculate the eigenvalues of a solution using a finite differences are

1. Discretising the spatial domain such that $\Delta x = \dfrac{l}{N_x}$.

2. Replacing the linear operator by the discretised operator.

3. Using a numerical eigenvalue solver to compute the eigenvalues that correspond to the discretised linear problem.

Therefore, for any given Δx or N_x, some eigenvalues and their corresponding eigenvectors are computed. Hence, to increase the number of eigenvalues, we require to increase N_x. Moreover, we have a more accurate approximation for the linear elements. However, this causes increase in the computational time for the solver. Nevertheless, studied theorems on spectral approximation show that the spectrum of the discretised problem converges to that of the continuum problem in the limit that $N_x \to \infty$ [151].

Now the spectrum for (2.1) can be determined. To do so, the finite difference method is applied to discretise the linear operator such that

$$\partial_{xx}\boldsymbol{w}(x) \approx \frac{\boldsymbol{w}(x+\Delta x) - 2\boldsymbol{w}w(x) + \boldsymbol{w}(x-\Delta x)}{(\Delta x)^2} \tag{2.111}$$

Therefore, the matrix of discretised linear operator $\mathscr{L}_{\Delta x}$ is tridiagonal with zeros away from the main diagonal and the diagonals either side of it. In this study Neumann boundary conditions are used. Accordantly, the discretised matrix is

$$\mathscr{L}_{\Delta x} = \begin{pmatrix} A_0 & 2B & 0 & \dots & \dots & \dots & 0 \\ B & A_1 & B & 0 & \dots & \dots & 0 \\ 0 & B & A_2 & B & 0 & \dots & 0 \\ \vdots & \ddots & \ddots & \ddots & \ddots & \ddots & \vdots \\ \vdots & \ddots & \ddots & \ddots & \ddots & \ddots & \vdots \\ \vdots & \ddots & \ddots & \ddots & & & \\ 0 & 0 & \dots & 0 & B & A_{N-1} & B \\ 0 & 0 & \dots & 0 & 0 & 2B & A_N \end{pmatrix} \tag{2.112}$$

where

$$A_i = \begin{pmatrix} \dfrac{\partial F_1}{\partial U_1} - \dfrac{2D_1}{(\Delta x)^2} & \dfrac{\partial F_1}{\partial U_2} & \dots & \dots & \dfrac{\partial F_1}{\partial U_n} \\ \dfrac{\partial F_2}{\partial U_1} & \dfrac{\partial F_2}{\partial U_2} - \dfrac{2D_2}{(\Delta x)^2} & \dots & \dots & \dfrac{\partial F_2}{\partial U_n} \\ \vdots & \dots & \dots & \ddots & \vdots \\ \dfrac{\partial F_n}{\partial U_1} & \dfrac{\partial F_n}{\partial U_2} & \dots & \dots & \dfrac{\partial F_n}{\partial U_n} - \dfrac{2D_n}{(\Delta x)^2} \end{pmatrix}_{|(U(x_i))} , \tag{2.113a}$$

$$B = \begin{pmatrix} \dfrac{D_1}{(\Delta x)^2} & 0 & \dots & \dots & 0 \\ 0 & \dfrac{D_2}{(\Delta x)^2} & 0 & \dots & 0 \\ \vdots & \dots & \dots & \ddots & \vdots \\ 0 & \dots & \dots & 0 & \dfrac{D_n}{(\Delta x)^2} \end{pmatrix}. \tag{2.113b}$$

The index in the matrix A stands for number of the grid point in x and the dimension of matrix $\mathscr{L}_{\Delta x}$ is $n(N_x+1) \times n(N_x+1)$. Then we can use a numerical eigenvalue solver to compute the eigenvalues that corresponding to the discretised linear problem.

Now, let us recall the example model equation (2.56), accordingly the matrices A_i and B are written as follows

$$A_i = \begin{pmatrix} \dfrac{\partial F}{\partial u} - \dfrac{2\delta^2}{(\Delta x)^2} & \dfrac{\partial F}{\partial v} \\ \dfrac{\partial G}{\partial u} & \dfrac{\partial G}{\partial v} - \dfrac{2}{(\Delta x)^2} \end{pmatrix}_{|(u(x_i),v(x_i))} , \tag{2.114a}$$

$$B = \begin{pmatrix} \dfrac{\delta^2}{(\Delta x)^2} & 0 \\ 0 & \dfrac{1}{(\Delta x)^2} \end{pmatrix}. \tag{2.114b}$$

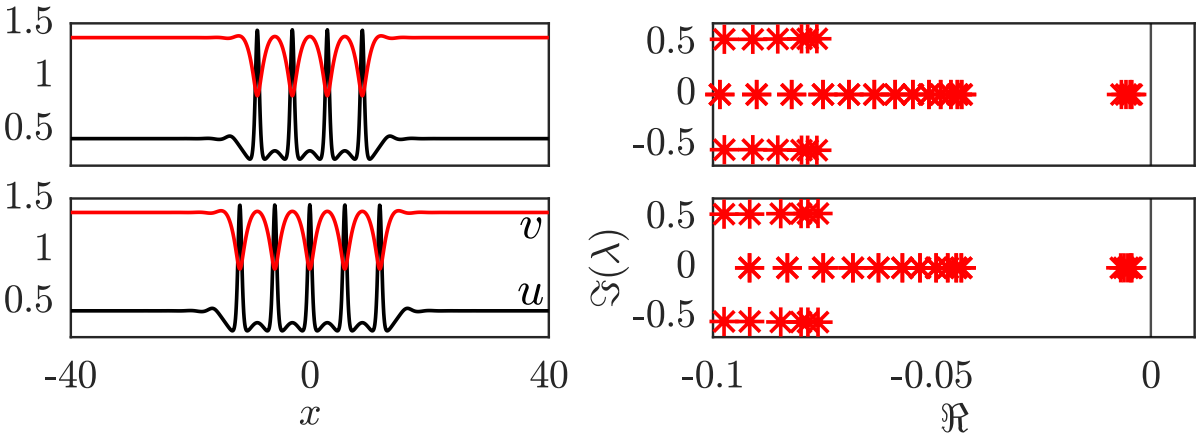

Figure 2.10: [Left:]Examples of stable solution for (2.56) with [Right:] profile of the corresponding largest eigenvalues. Parameters are $b = 0.45$, $d = 0.31$ and $\delta = 0.17$.

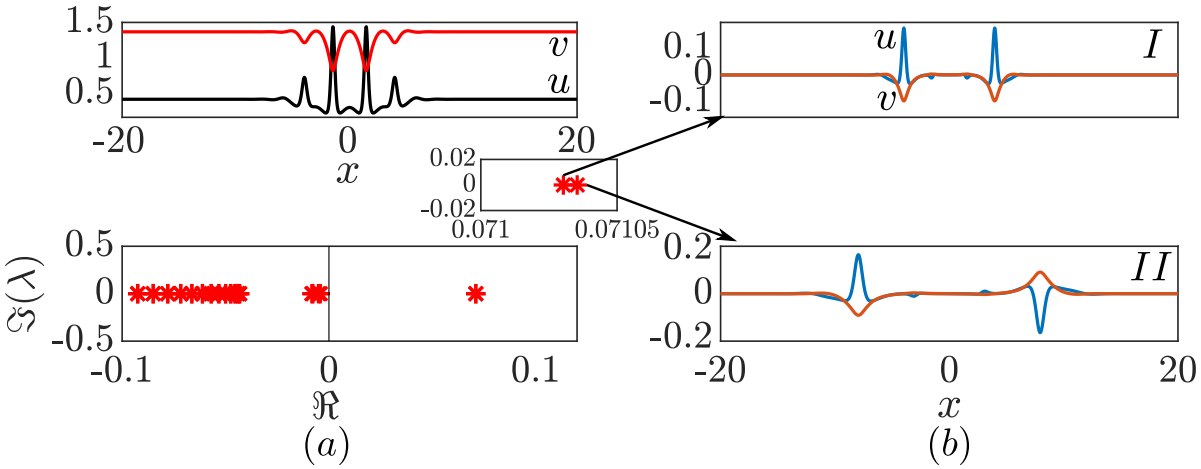

Figure 2.11: (a) From top to bottom, unstable localised solution, their eigenvalues for (2.56). (b) The corresponding eigenfunction: I the symmetric mode and II the anti-symmetric mode. Parameters are $b = 0.45$, $d = 0.13$ and $\delta = 0.17$.

As a baseline test, we use Matlab and the spectrum of the linearised operator to obtain the stability of some solutions for (2.56). In the following, we are going to distinguish between different types of spectrum that can be found in (2.56) using Δx within the ranges $\Delta x \in (0.1, 0.001)$. We start with the Figure 2.10 which shows a sample of stable solutions and the corresponding largest real-part eigenvalues of the linear operators.

In Figure 2.11(a), we depict an unstable solution with the largest real-part associate eigenvalues. The corresponding eigenfunctions of the positive real-part eigenvalues are shown in Figure 2.11(b). There are two eigen-modes which are symmetric and anti-symmetric (see Figure2.11(b) I and II respectively) [33]. We show another example of an unstable solution in Figure 2.12. Here the eigenvalues are complex with positive real part.

Finally, we illustrate the Goldstone mode, which is the mode of the eigenvalue at the origin

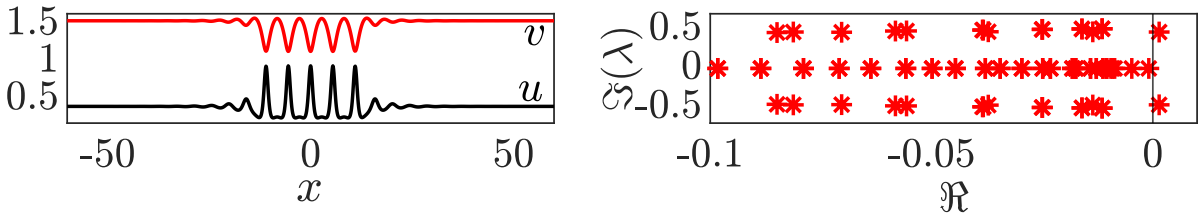

Figure 2.12: [Left:] Example of unstable solutions with [Right:] profile of the corresponding largest eigenvalues for (2.56). Parameters are $b = 0.31$, $d = 0.0987$ and $\delta = 0.17$.

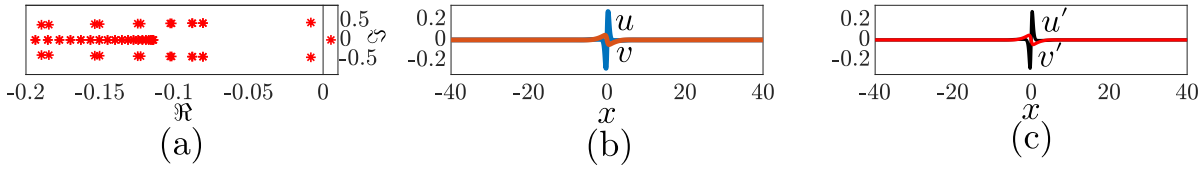

Figure 2.13: (a) Example of Goldstone eigenvalue, (b) profile of the corresponding eigenfunction, and (c) profile of the derivative of the variables of the localised solution. Parameters are $b = 0.45$, $d = 0.13$ and $\epsilon = 0.17$.

in the complex plane [9, 33] (see Figure 2.13(a)). This mode is not related to the instability, but it is a sign that the discretisation is too coarse or the interval is too long. The corresponding eigenfunction is displayed in Figure 2.13(b). Note, the profile of the eigenfunction of the Goldstone mode is indistinguishable to the derivative of the variables of the solution whose stability we are investigated (see Figure 2.13(c)). In the coming chapters we will discuss all cases in more detail.

2.7 Conclusion

This chapter outlines the methods that will be required throughout the thesis. In the chapter, we have introduced the type of reaction-diffusion equation that will be studied in this thesis. Further, we provide in detail the techniques used to find and study localised patterns. These techniques can be listed as follows:

1. Linear stability analysis is used to obtain the conditions for Hopf bifurcation of the homogenous steady-state, Turing instability (Hamiltonian-Hopf) and BD transition.

2. Weakly nonlinear analysis is employed to find the codimension-two point where Turing bifurcation change from being subcritical to supercritical (or vice versa).

3. The spatial dynamics method and numerical continuation are used to find and trace the localised patterns in the parameters space.

4. Numerical methods for stability are utilised to provide information about the stability of localised patterns. Direct numerical is used to determine what happens beyond the instability

CHAPTER 3

BIFURCATION OF LOCALIZED STRUCTURES IN BIOLOGICALLY INSPIRED REACTION-DIFFUSION EQUATIONS

This chapter is based on publications [4, 5] and partly on [37]

3.1 Introduction

This chapter aims to show theoretical paradigms in how the pattern formation and dynamics of spatially localised patterns fit together by studying models of the generalised Schnakenberg type in one spatial dimension. In particular, we aim to show how the semi-strong asymptotic analysis applied in the limit of an infinite domain, can show the onset of large-amplitude exponentially localised patterns through a fold bifurcation. Here semi-strong implies a scaling where the activator field is much more highly localised than the inhibitor. When this fold is followed numerically into a different pattern regime, we find that it forms the extremity of the homoclinic snaking region. Moreover, the semi-strong limit allows for analysis of the stability of the localised patterns. Theory can then be extended to argue the existence of a temporal Hopf bifurcation as one passes from the snaking regime to the semi-strong limit.

We will consider the general model for a bounded nonlinear reaction diffusion system of equations. We will use biological interaction between two species to give a physical interpretation of the model and the results. In this chapter, we will investigate models with two components which can be written as:

$$\begin{pmatrix} u \\ v \end{pmatrix}_t = \boldsymbol{c} + A \begin{pmatrix} u \\ v \end{pmatrix} + \begin{pmatrix} 1 \\ -1 \end{pmatrix} u^2 v + \begin{pmatrix} \delta^2 \nabla^2 u \\ \nabla^2 v \end{pmatrix}, \tag{3.1}$$

for $u(x,t), v(x,t) \in \mathbb{R}$ and $x \in (-\infty, \infty)$ with asymptotically flat boundary conditions

$$(u_x(x,t), v_x(x,t)) \to (0,0) \quad \text{as} \quad x \to \pm\infty. \tag{3.2}$$

Name	fixed parameters	free parameters
Schnakenberg [143]	$c=1$, $d=h=j=0$,	a, b.
Brusselator[136]	$h=c-1>0$, $b=d=j=0$,	a, c.
Glycolysis [154]	$c=1$, $d=j$, $a=h=0$,	d, b.
Sel'kov-Schnakenberg [145]	$c=1$, $d=j$, $h=0$,	a, b, d.
Root-hair [131]	$a=0$, $d=j$, $h>c>0$,	b, c, d, h.

Table 3.1: Reaction-diffusion models of the form (3.1), and the corresponding coefficients (3.3) of the constant and linear terms.

Here $\mathbf{c}$ is a 2-vector with non-negative entries that models a constant influx or feed of the two different reactants, an activator u and inhibitor v. A is a constant 2×2 matrix where the coefficients are chosen so that diagonal terms are non-positive and the off-diagonal terms non-negative (to model decay and mass transfer respectively) and $\delta^2 \ll 1$ measures the ratio of the diffusion rates of activator u and inhibitor v. Specifically, we assume

$$\mathbf{c}=\begin{pmatrix} a \\ b \end{pmatrix}, \quad A=\begin{pmatrix} -c & d \\ h & -j, \end{pmatrix}, \quad \text{where } a,b,c,d,h,j\geq 0. \tag{3.3}$$

For practical computation purposes we shall sometimes pose the system (3.1) on a long finite interval $x\in[-l,l]$ with $l\gg 1$ and replace (3.2) with Neumann boundary conditions as in chapter 2.

$$(u_x(-l,t),v_x(l,t))=(0,0). \tag{3.4}$$

Our interest is in patterns that are truly localised, that is, are not influenced by effects coming from boundary conditions.

This chapter shall specifically concern the case where there is a unique strictly positive homogeneous steady state $(u,v)=(u_s,v_s)$, which places some constraints on the coefficients of $\mathbf{c}$ and A (see Sec. 3.2). In this case the asymptotic boundary condition (3.2) is equivalent to $(u,v)\to(u_s,v_s)$ as $x\to\pm\infty$. Despite these restrictions, there are still many problems that arise in the literature that fall into this general category of model; See Table 3.1. Note that another important model, the so-called Gray-Scott system, [71] has three homogeneous steady states in the typical parameter regime in which localised patterns are known to occur [66, 179]. Hence this system falls outside the scope of the present chapter and will be considered in chapter 4.

The overall message of this chapter will be the emergence of a universal two-parameter bifurcation diagram for the existence of localised patterns of activator-inhibitor reaction-diffusion systems, and a certain universality in the manner that such patterns become unstable as the diffusion ratio becomes less extreme. In fact, similar bifurcation diagrams have already been found in other models with more complex nonlinear terms than the simple form (3.1), such as models for

cell polarisation [165], crime waves [103], virus-host interaction [7] and desertification [180]; see also [166]. In chapter 5 shall also consider examples with more general nonlinear terms arising as models of predator-prey interaction. In this chapter we shall study each of these models in Table 3.1.

The rest of the chapter is outlined as follows. Section 3.2 makes some preliminary calculations for the general model (3.1) and establishes conditions under which homogeneous Turing and Hopf bifurcations take place. It also considers several rescalings for large and for small values of the constant and linear parameters. Section 3.3 to 3.7 then introduce the Schnakenberg model and applied different method to study existence and stability of the localised patterns. These methods are then applied to the other form models in the subsequent chapters. Sections 3.8 to 3.10 present a brief presentation of analogous results for the other models in Table 3.1. Finally, section 3.11 draws conclusions and points to many avenues for future work.

3.2 General model

Our starting point is to obtain conditions under which a unique homogeneous equilibrium exists for (3.1). Accordingly, upon setting all time and space derivatives to zero we find that steady solutions $(u(x,t),v(x,t)) = (u_s, v_s)$ must satisfy

$$v_s = \frac{cu_s - a}{u_s^2 + d}, \tag{3.5a}$$

where u_s solves

$$(h-c)u_s^3 + (a+b)u_s^2 + (dh - cj)u_s + aj + bd = 0. \tag{3.5b}$$

By Descartes' rule of signs, necessary conditions for the equation (3.5b) to have a unique positive root are

$$a + b > 0, \quad h < c, \quad d = j. \tag{3.6}$$

Henceforth we shall assume that (3.6) applies and shall drop any reference to the parameter j in favour of d. In this case, equation (3.5b) can be solved explicitly and we obtain a closed form expression for the homogeneous equilibrium:

$$(u_s, v_s) = \left(\frac{a+b}{c-h}, \frac{cu_s - a}{u_s^2 + d} \right). \tag{3.7}$$

Note that the Gray-Scott model does not satisfy (3.6) because, when written in the form (3.1), $0 = d \neq j > 0$.

3.2.1 Turing and Hopf bifurcation

We next investigate the conditions under which the homogeneous equilibrium undergoes the simplest kinds of temporal instability; specifically a spatially homogeneous Hopf bifurcation or Turing bifurcation.

Following the linear stability analysis established in section 2.2, conditions for the Turing and the Hopf bifurcation are achieved. Applying conditions (2.10) to (3.7), gives an expression for Hopf bifurcation to arise which reads

$$u_s^2 - 2u_s v_s + c + d = 0. \tag{3.8}$$

This expression defines a codimension-one surface in parameter space at which Hopf bifurcation occurs. Note that this is necessarily independent of the diffusion ratio δ.

By applying conditions (2.11) to the steady state (3.7) for (3.1) we find a codimension-one surface in parameter space on which a Turing bifurcation occurs is defined implicitly via

$$\delta^2 {u_s}^2 + d\delta^2 - 2\,u_s\,v_s + c = -2\delta\sqrt{\left({u_s}^2 + d\right)(c-h)}. \tag{3.9}$$

3.2.2 Large parameter limit

There are two natural kinds of scales that can be applied to (3.1) leading to simpler models, one in a certain limit of large values of the production-rate parameters a and b, the other for small values of these parameters.

For large values of a and b we can obtain a distinguished limit by setting

$$a = \delta^{-1}\alpha, \quad b = \delta^{-1}\beta, \quad d = j = \delta^{-2}\rho, \tag{3.10}$$

and introducing a scale for space and dependent variables as follows:

$$u = \frac{U}{\delta}, \quad , v = \delta V, \quad x = \delta y. \tag{3.11}$$

Substitution of (3.10) and (3.11) into (3.1) leads to the following system

$$\alpha - cU + \rho V + U^2 V + \frac{\partial^2 U}{\partial y^2} = \frac{\partial U}{\partial t}, \quad y \in \mathbb{R}, \tag{3.12a}$$

$$\beta + hU - \rho V - U^2 V + \frac{\partial^2 V}{\partial y^2} = \delta^2 \frac{\partial V}{\partial t}, \quad y \in \mathbb{R}. \tag{3.12b}$$

(3.12c)

Now, if we consider the steady-state problem, by setting the right-hand-sides of the above equations to zero, we see that we have the identical form of equations to the steady problem for (3.1), with a, b and d replaced by α, β and ρ, respectively, but with $\delta = 1$. Hence the study of existence of steady patterns can be conducted independently of the diffusion ratio. Nevertheless,

owing to the factor δ^2 on the right-hand side of the second equation in (3.1), the dynamics of these localised patterns will strongly depend on the diffusion ratio.

Note in particular, that the location of the Turing bifurcation (3.9) is independent of δ in the new parameter regime, whereas the values of ρ, β and α for the Hopf bifurcation to occur, increase uniformly in δ. Thus, any localised pattern that is stable for small δ is likely to be destabilised by the homogeneous Hopf bifurcation for δ sufficiently large.

3.2.3 Small parameter limit

Alternatively, for small values of a and b we can obtain a scaling that naturally fits into the so-called semi-strong interaction asymptotic regime [55, 59, 168]. Such a regime is naturally suited to the method of multiple scales for the finding of pulse-like steady patterns. In an inner regime, the v-field is approximately constant and the u-field is given by a sech or sech^2 profile, whereas in the outer regime u is approximately equal to u_s and v solves a simple linear differential equation. On the infinite domain this leads to exponential relaxation to v_0 [4], whereas on the finite domain v is typically piecewise quadratic [168].

Looking for general parameter choices that can be applied in the inner and the outer regime we seek a scaling of the form

$$a = \delta\alpha, \quad b = \delta^n\beta, \quad c = \delta^p\eta \quad d = j = \delta^n\rho, \quad n \geq 1, \quad p \geq 0. \tag{3.13}$$

For the inner solution, we can then scale space as

$$x = \delta y, \tag{3.14}$$

and in the outer domain the following scale is used

$$u = \delta\hat{u}, \quad x = \delta^m z, \quad m < 0. \tag{3.15}$$

As we shall see in the following, the natural scaling in the general case of (3.1) is

$$m = \frac{-1}{2}, \quad n = 1 \quad \text{and } p = 0. \tag{3.16}$$

However, as we shall see later in the chapter, for special cases of constraints on the parameters a, b, c, d, h such as for some of the models in Table 3.1, a distinguished limit is obtained for other choices of m, n and p.

The rest of this section presents a brief calculation for the semi-strong interaction method for the general model (3.1)-(3.3), and we will provide the details in Section 3.4 specifically applied to the Schnakenberg case. We begin by introducing the scalings (3.13)-(3.16). In the new parameters, steady state system of (3.1) satisfy

$$\delta\alpha + \delta\rho v - cu + u^2 v + \delta^2 \frac{\partial^2 u}{\partial x^2} = 0, \tag{3.17a}$$

$$\delta\beta - \delta\rho v + hu - u^2 v + \frac{\partial^2 v}{\partial x^2} = 0. \tag{3.17b}$$

3.2.4 Inner solution

Introducing the inner spatial scale (3.14) into (3.17) and collecting the leading order terms of δ, we obtain

$$\bar{u}_{0yy} - c\bar{u}_0 + \bar{u}_0^2\bar{v}_0 = 0, \tag{3.18a}$$

$$\bar{v}_{0yy} = 0. \tag{3.18b}$$

Solving system (3.18), we find that v_0 is a constant to be determined

$$\bar{v}_0 \equiv \kappa. \tag{3.19}$$

Then, from the u-equation we need to find a solution

$$\bar{u}_0 = (1/\kappa)w(y), \tag{3.20}$$

where $w(y)$ satisfies

$$w'' - cw + w^2 = 0, \quad -\infty < y < \infty, \tag{3.21a}$$

$$w \to 0 \quad as \quad y \to \pm\infty; \quad w'(0) = 0, \quad w(0) > 0. \tag{3.21b}$$

The unique solution to (3.21) is

$$w = \frac{3c}{2\kappa}\mathrm{sech}^2\left(\frac{\sqrt{c}\,y}{2}\right). \tag{3.22}$$

Hence the inner solutions are

$$\bar{v} = \bar{v}(0) = \text{constant} := \kappa, \tag{3.23a}$$

$$\bar{u} = \frac{3c}{2\kappa}\mathrm{sech}^2\left(\frac{\sqrt{c}\,y}{2}\right), \tag{3.23b}$$

where κ is an unknown real parameter.

3.2.5 Outer solution

The next step is to obtain the outer solution. Taking into account the rescaled variables in (3.15) and (3.16) an outer solution can be written as

$$\hat{u} = \frac{\alpha + \rho\hat{v}}{c}, \tag{3.24a}$$

where

$$\hat{v} = \left(\kappa - \frac{\alpha h + \beta c}{\rho\,(c-h)}\right)e^{-\frac{\sqrt{\rho}\sqrt{c-h}\,|\,z\,|}{\sqrt{c}}} + \frac{\alpha h + \beta c}{\rho\,(c-h)}. \tag{3.24b}$$

Recalling the condition (3.6) we can guarantee that (3.24) provides a real solution. Note this solution has a derivative jump at $z = 0$.

3.2.6 Matching

In order to match inner and outer solutions, we have freedom to choose a value of the free variable κ. A typical approach would be to match derivatives of the inner and outer solutions at $x = 0$. But the outer solution is not differentiable there. So, following Ward et al. [168] we look to match the solutions in a weak sense. The novelty here though is to use a matching method that does not rely on l being finite. Adding the inner and outer solutions and substituting into a weak form of form of the v equation, we obtain

$$\int_{\mathscr{D}} [\delta\beta + hu - \delta\rho v - u^2 v + v_{xx}]dx = 0, \tag{3.25}$$

where $u = \delta\hat{u} + u_0$ and $v = \delta\hat{v} + v_0$. Here, the domain $\mathscr{D}$ of integration corresponds to an extended interval around the inner asymptotic region that includes a matching zone: $\int_{\mathscr{D}} = \int_{-\epsilon}^{\epsilon}$ where ϵ is an arbitrary number, assumed to have the asymptotic order $\delta \ll \epsilon \ll 1$. It would seem that condition (3.25) for the matching of the inner and outer solutions (which contrasts with that in [168] where integration is taken over the entire outer domain) can be seen as somewhat akin to the vanishing of a Melnikov integral, as used in geometric singular perturbation theory, e.g. [59]. A detailed comparison between the different asymptotic theories is beyond the scope of this thesis.

The integral condition (3.25) evaluated by substituting the expression for u_0, v_0, $\hat{u}$ and $\hat{v}$. This evaluator leads to known expression for integrals of powers of $sech(x)$ from $-\infty$ to ∞ and for the jump in the derivative of $\hat{v}_{xx}$. We give the detail in section 3.4. Setting the integral to zero, we obtain the following

$$\frac{-2\sqrt{d\,(c-h)}}{\sqrt{c}}\kappa^2 + \frac{2\sqrt{d\,(c-h)}\,(a\,h + b\,c)}{d\,\sqrt{c}\,(c-h)}\kappa - 6\sqrt{c}\,\delta\,(c-h) = 0, \tag{3.26}$$

which is valid up to $O(\delta^2)$. Hence, the constant κ can determined by solving the above quadratic equation. It turns out that in order to find the fold bifurcation of these localised solutions it is necessary to go beyond the leading order in δ.

To start with, we assume the solutions of κ have the expansion of form:

$$\kappa = \sum_{i=0}^{\infty} \delta^i \gamma_i. \tag{3.27}$$

Up to first-order in γ we obtain

$$\frac{-2\sqrt{d\,(c-h)}}{\sqrt{c}}\gamma_0^2 + \frac{2\sqrt{d\,(c-h)}\,(a\,h + b\,c)}{d,\sqrt{c}\,(c-h)}\gamma_0 = 0, \tag{3.28a}$$

$$\frac{-2\sqrt{d\,(c-h)}}{\sqrt{c}}\gamma_0\gamma_1 + \frac{2\sqrt{d\,(c-h)}\,(a\,h + b\,c)}{d\,\sqrt{c}\,(c-h)}\gamma_1 - 6\sqrt{c}\,(c-h) = 0. \tag{3.28b}$$

These simultaneous equations can be solved for γ_0 and γ_1 separately and recombined to form two roots of κ, written as

$$\kappa_1 \approx \frac{3\delta\, cd\,(c-h)^2}{\sqrt{d\,(c-h)}\,(a\,h+b\,c)} + O(\delta^2), \tag{3.29a}$$

$$\kappa_2 \approx \frac{a\,h+b\,c}{d\,(c-h)} - \frac{3\delta\, cd\,(c-h)}{\sqrt{d\,(c-h)^2}\,(a\,h+b\,c)} + O(\delta^2). \tag{3.29b}$$

Here, κ_1 is the value of κ on an 'upper' (large $U(0)$) branch κ_2 is matching the value of κ on a 'lower' (small $U(0)$) branch. Moreover, a fold bifurcation can be obtained by setting the discriminant of (3.26) to be zero. The details will be worked out for each model in the subsequent sections.

3.3 The Schnakenberg model and its underlying dynamics

We start the investigation by considering the Schnakenberg model. The model in question was first proposed in [143] and has many applications in biology; see e.g. [21, 146] and references therein. The equations describe an autocatalytic reaction between two chemical products U, V and two sources A and B as follows:

$$\mathrm{U} \rightleftharpoons \mathrm{A}, \quad \mathrm{B} \longrightarrow \mathrm{V}, \quad 2\mathrm{U} + \mathrm{V} \longrightarrow 3\mathrm{U}.$$

The reaction is assumed to take place in a closed domain, such that the activator U and inhibitor V are free to diffuse in one spatial dimension, across a domain of size $2l$, and that the sources A and B are abundant everywhere and do not diffuse. Applying the law of mass action, after non-dimensionalisation, one can obtain the following system of reaction-diffusion equations:

$$\frac{\partial u}{\partial t} = a - u + u^2 v + \delta^2 \frac{\partial^2 u}{\partial x^2}, \tag{3.30a}$$

$$\frac{\partial v}{\partial t} = b - u^2 v + \frac{\partial^2 v}{\partial x^2}, \tag{3.30b}$$

Here u and v represent the activator and the inhibitor concentration, respectively, and the parameters $a, b > 0$ are the respective constant concentrations of A and B. The dimensionless parameter $\delta > 0$ measures the ratio of the diffusion rate of the activator to that of the inhibitor. In what follows we shall be interested in the case that $\delta \ll 1$ and in the limit of an infinitely long domain $l \to \infty$.

Upon setting the diffusion terms in (3.30) to zero, a straightforward calculation shows there is a unique homogeneous equilibrium:

$$(u_s, v_s) = \left(a+b, \frac{b}{(a+b)^2}\right). \tag{3.31}$$

Following the standard linear stability analysis that is found in Section 2.2, we obtain the condition for Turing instability and the critical wave number as:

$$b-(a+b)^3\delta^2-a=2(a+b)^2\delta, \tag{3.32}$$

$$k_c^2=\frac{-(a+b)^3\delta^2-a+b}{2\delta^2(a+b)}.$$

Another linear transition we shall be interested in is when the far field of the purely spatial problem posed around the homogeneous equilibrium switches from having monotone to oscillatory decay. Such a BD transition occurs whenever there is a pair of double real eigenvalues of the spatial dynamics problem linearised about the homogeneous equilibrium. This gives the condition

$$b-(a+b)^3\delta^2-a=-2(a+b)^2\delta. \tag{3.33}$$

The curve (3.32) is plotted in Figure 3.1a in the (a,b)-plane for fixed δ (solid red line). Using weakly nonlinear analysis (for details see Section 2.3) we find that for sufficiently large a, stable periodic patterns bifurcate supercritically from the Turing bifurcation as b increases (into the yellow shaded region in the figure). For smaller a, the bifurcation is subcritical and a fold in the periodic structures occurs for lower b-values, creating a Pomeau pinning region (shaded green in the figure) in which localised structures are observed. The large a-limit of the localised structures region is formed by the codimension-two point where the Turing bifurcation changes from being sub- to supercritical (indicated by the pink circle in the figure). Here the codimension two point was computed using the method in section 2.3.

Figure 3.1 also contains numerical results obtained using AUTO [54] on the bifurcation structure of localised solutions within the green shaded region.

The BD curve defined by (3.33) is also depicted in Figure 3.1a; note how it divides the localised-structure region into two parts. The region to the right of the BD line is where spatial eigenvalues are complex and localised solutions have oscillatory tails, whereas to the left line the spatial eigenvalues are purely real and solutions have monotonic tails. Recently [166], in a class of reaction diffusion equations which includes (3.30) it is argued that a single-spike localised pattern crossing a BD from right to left in the sense of Figure 3.1a should result in the destruction of all but a finite number of localised pattern solutions. Figures 3.1b and 3.1c show one-parameter bifurcation diagrams of localised structures obtained numerically, which appear to confirm this prediction. The figures also indicate which among the various solutions are found numerically to be stable.

In particular, note that the localised solutions for small a and b shown in the inset to Figure 3.1c consist of a highly localised spike in u, but are more spread out in the inhibitor field v. This observation is suggestive that there may be a semi-strong asymptotic analysis that can predict the bifurcation diagram observed for these two spike solutions. Note that the v-field appears exponentially localised, which would suggest a different approach to the finite-domain assumption

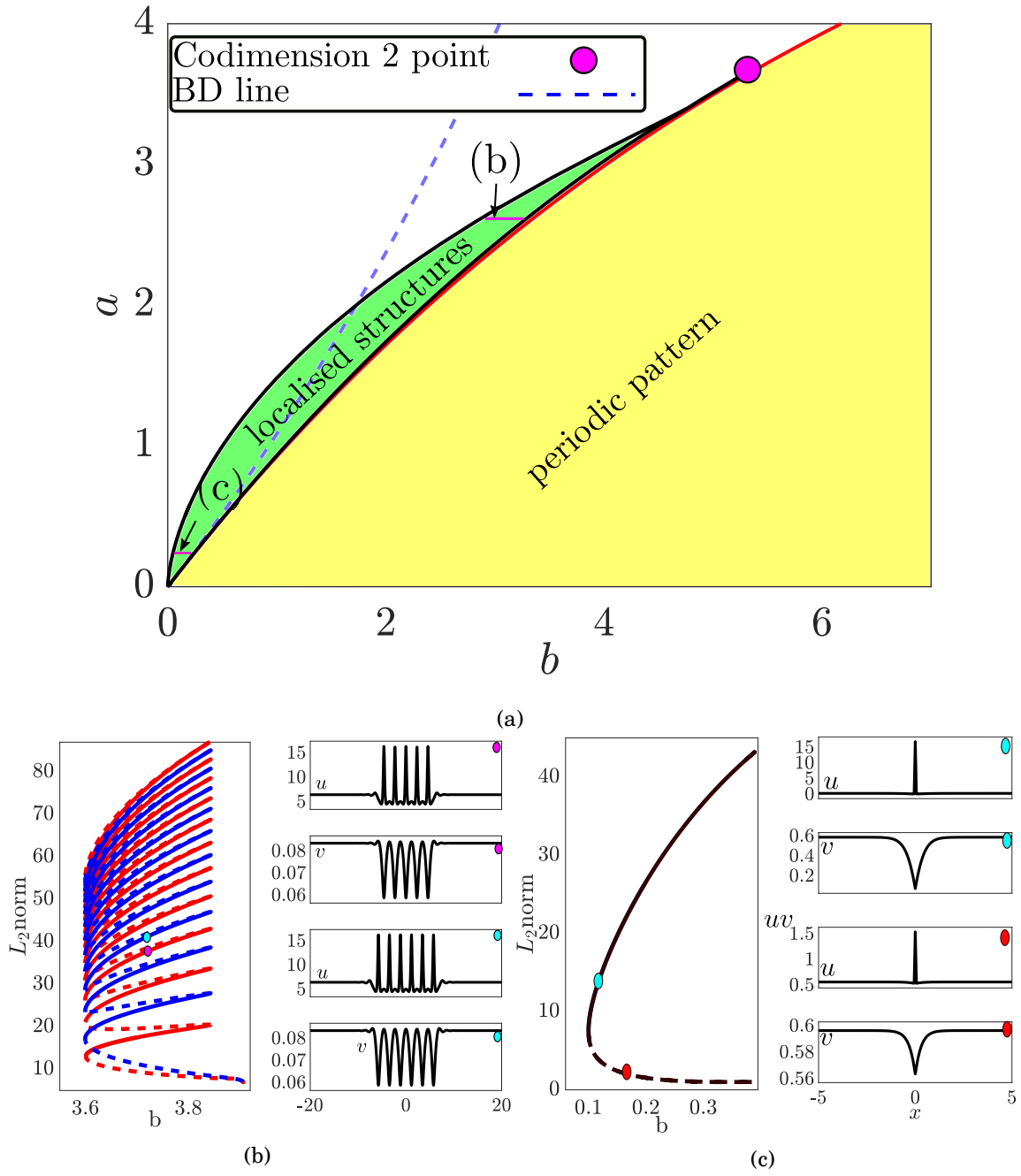

Figure 3.1: (a) The (b,a) bifurcation diagram for fixed $\delta = 0.01$ and $l = 100$. The red curve represents a Turing bifurcation and black lines represent the (outer) folds of a bifurcation diagram of localised solutions. (b) One-parameter numerical bifurcation diagram showing snaking of multi-pulsed solutions for $a = 2.7$ as b varies. A continuous (or dashed) line indicates where spectral computation indicates that the solution is stable (unstable). A pink (blue) colour indicates that the number of peaks in the solution is odd (even). Insets show u and v solution profiles at the two indicated points in the bifurcation diagram. (c) One-parameter numerical bifurcation diagram as b varies for $a = 0.3785$ where a fold bifurcation connects spike solutions that are computed to be stable (unstable) as indicated by a continuous (dashed) line. Insets show the u and v solution profiles at the indicated points.

typically used in previous works, e.g. [91, 168] in which the v-field is approximately two reflected quandratic functions. Moreover, the stability results here with two branches connected by a fold cannot be predicted using the usual finite-domain method.

3.4 Semi-strong asymptotic construction of spike solutions

Consider the steady-state version of (3.30):

$$a - u + u^2 v + \delta^2 \frac{\partial^2 u}{\partial x^2} = 0, \tag{3.34a}$$

$$b - u^2 v + \frac{\partial^2 v}{\partial x^2} = 0, \tag{3.34b}$$

subject to Neumman boundary conditions. We are interested a homoclinic orbit in space to the homogeneous equilibrium

$$u \to a + b, \qquad v \to \frac{b}{(a+b)^2}, \quad \text{as } x \to \pm\infty.$$

We show how semi-strong interaction method introduced in section 3.2.3, applies in this case when both parameters a and b are small. In particular, we find a natural distinguished limit by considering $n = 2$ in (3.13). Therefore, we can introduce α and β as $O(1)$ parameters to obtain

$$0 = \delta^2 \frac{\partial^2 u}{\partial x^2} + u^2 v - u + \delta\alpha, \tag{3.35a}$$

$$0 = \frac{\partial^2 v}{\partial x^2} + \delta^2 \beta - u^2 v. \tag{3.35b}$$

We then seek solutions expanded in powers of δ

$$u(x) = u_0 + \delta u_1 + O(\delta^2), \qquad v(x) = v_0 + \delta v_1 + O(\delta^2),$$

in the inner and outer asymptotic regimes, separately.

Introducing the new spatial scale (3.14) for the inner into (3.35) and collecting the leading order terms of δ, we gain the leading-order solutions for (3.35) on an infinite domain with asymptotically flat boundary conditions to be (3.23) with $c = 1$

We introduce a new scaling within an outer region, given by (3.16) with $m = -1$ into (3.35). Collecting terms in (3.35) that have the same order of δ, to leading order we find

$$\hat{u}_0(z) = \alpha, \qquad \text{and} \qquad \hat{v}_{0zz} - \hat{u}_0^2 \hat{v}_0 + \beta = 0.$$

However, it is useful to include the $O(\delta)$-correction to the u solution, so that we can explain the Neumman boundary conditions solution on a finite domain transforms into the case of asymptotic boundary conditions in the limit $l \to \infty$. Thus, we set

$$\hat{u}(z) = \alpha + \delta\beta, \tag{3.36}$$

in which case, we find that the leading-order solution for v needs to satisfy

$$\hat{v}_0(z) \to \frac{\beta}{(\alpha+\delta\beta)^2} \text{ as } z \to \pm\infty.$$

Note that, in either the case of finite or infinite l, the boundary conditions on $\hat{v}_0$ mean that (3.36) cannot be satisfied by a single smooth function. Instead we must solve separately on the intervals $z \in [-\delta l, 0]$ and $z \in [0, \delta l]$. Solving separately on these domains, we get

$$\hat{u}(z) = \alpha + \delta\beta,$$

and

$$\hat{v}(z) = \frac{\left(\kappa(\alpha+\delta\beta)^2 - \beta\right)}{(\alpha+\delta\beta)^2 \cosh(\delta l(\alpha+\delta\beta))} \cosh\left(\left(\alpha+\delta\beta\right)(|z|-\delta l)\right) + \frac{\beta}{(\alpha+\delta\beta)^2}. \tag{3.37}$$

In the limit $l \to \infty$ this function can be written as

$$\hat{v}(z) = \left(\kappa - \frac{\beta}{\left(\delta\beta+\alpha\right)^2}\right) \exp\left[-(\delta\beta+\alpha)|z|\right] + \frac{\beta}{\left(\delta\beta+\alpha\right)^2}. \tag{3.38}$$

Next we need to match the inner and outer solutions, by finding feasible values for κ. Hence we follow the technique outline in section 3.2.6.

Adding the inner and outer solutions from the previous sections we obtain we obtain

$$u(x) = \frac{3}{2\kappa}\text{sech}^2\left(\frac{y}{2}\right) + \delta\hat{u}\left(\frac{z}{\delta}\right), \quad v(x) = \hat{v}\left(\frac{z}{\delta}\right),$$

which we then substitute into a weak form of the v equation:

$$\int_{\mathscr{D}} [\,\delta^2\beta - u^2 v + v_{xx}\,]dx = 0 \tag{3.39}$$

Consider the three terms in the integrand of (3.39) separately. The first term integrates to zero because $\delta^2\beta$ is vanishingly small in the limit $\delta \to 0$. The second term can be approximated as

$$\int_{-\infty}^{\infty} \delta\kappa u_0^2(y)dy = \int_{-\infty}^{\infty} \frac{\delta}{\kappa}\text{sech}^4\left(\frac{y}{2}\right)dy = \frac{6\delta}{\kappa}. \tag{3.40}$$

Finally, the third term can be approximated as

$$\int_{0^-}^{0^+} \hat{v}_{zz}dz = [\hat{v}_z]_{0^+} - [\hat{v}_z]_{0^-} = -2\left(\kappa - \frac{\beta}{\left(\alpha+\delta\beta\right)^2}\right)\delta\left(\alpha+\delta\beta\right)\tanh(\delta\alpha l). \tag{3.41}$$

Substitution of (3.40) and (3.41) into (3.39) yields the following quadratic equation for κ

$$\left(-2\left(\alpha+\delta\beta\right)\kappa^2 + \frac{2\beta\kappa}{\left(\alpha+\delta\beta\right)}\right)\delta\tanh(\delta\alpha l) - 6\delta = 0. \tag{3.42}$$

Note that when $l \to \infty$, $\tanh(\delta\alpha l) \sim 1$, which yields

$$-2\left(\alpha+\delta\beta\right)\kappa^2 + \frac{2\beta\kappa}{\left(\alpha+\delta\beta\right)} - 6 = 0. \tag{3.43}$$

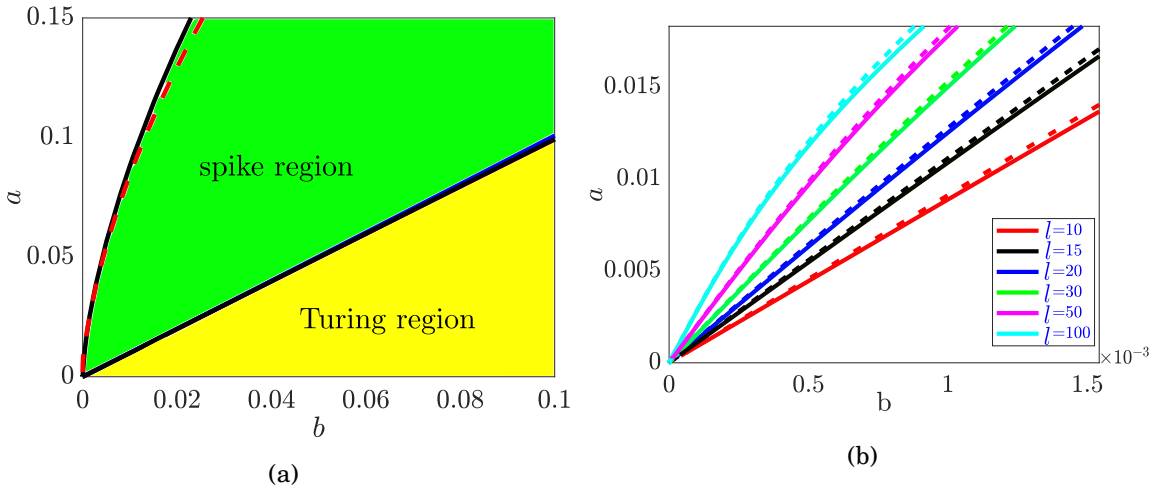

Figure 3.2: A zoom of the spike region of Figure 3.1a. (a) The dashed red line indicates the analytical upper expression (3.45) in the limit $l = 100$, which can be compared to the the solid black fold line computed numerically. (b) The corresponding fold curves for different finite values of l; with dashed (solid) lines representing analytic (numerical) approximations.

On the other hand, the domain l must be much larger than the width of the spike in order for the asymptotics to be consistent. This means that we must assume $l \gg O(\delta)$.

Solving (3.43), we obtain two values for κ, which correspond to a small and a large value. Specifically,

$$\kappa_1 = \frac{\beta - \sqrt{-12\left(\delta\beta+\alpha\right)^3+\beta^2}}{2\left(\delta\beta+\alpha\right)^2}, \tag{3.44a}$$

$$\kappa_2 = \frac{\beta + \sqrt{-12\left(\delta\beta+\alpha\right)^3+\beta^2}}{2\left(\delta\beta+\alpha\right)^2}. \tag{3.44b}$$

We shall refer to κ_1 as corresponding to an 'upper branch' of the spike solution, and κ_2 to a 'lower branch'. Finally, we can find a fold bifurcation of spikes by setting the discriminant of (3.42) to zero, which gives a curve in the (a,b)-plane given by

$$\beta^2\tanh(\delta\alpha l) - 12\left(\alpha+\delta\beta\right)^3 = b^2\tanh(\alpha l) - 12\delta\left(\alpha+b\right)^3 = 0. \tag{3.45}$$

The two spike solutions exist for a-values less that this curve, and b-values above it. Note we find in the limit $l \to \infty$ both tanh $\to 1$ leading to a much sampler expression.

3.4.1 Comparison with numerics

Figure 3.2a plots a zoom of the left-hand corner of Figure 3.1a, comparing the computed left-hand fold with the formula (3.45) in the limit $l \to \infty$ as a red dashed line. It is clear that the two lines are in good agreement in the limit of small a and b where the asymptotic analysis applies.

Figure 3.2b shows (3.45) for different values of l (dashed lines) which is again shown to have good agreement with the corresponding numerical results from AUTO on a finite domain.

Figures 3.3 and 3.4 show a comparison between the approximate solutions obtained via asymptotic analysis and the corresponding numerical solution obtained using AUTO. It is clear from the figures that there is good agreement for both the upper/stable and lower/unstable branch of solutions, both on a finite domain and an infinite domain. Note how the agreement gets better as $l \to \infty$. Also note how the v component transforms from being exponentially localised to being more quadratic-shaped as l is decreased from $+\infty$. In the rest of this chapter, we shall apply the same method of the analysis to the other models in Table 3.1. In all subsequent cases though we shall only consider the infinite-domain problem although we expect the same results for finite domain as $l \to \infty$.

3.5 Stability analysis of spike solutions

In the paper with our collaborators [4], the stability of the spike solution was obtained by so-called non-local eigenvalue problem. Here we are able to obtain so-called breathing pulses. In general, these breathing pulses can be considered to be the result of Hopf bifurcation of the spike solutions in which the statinary spike becomes oscillatory in time [75].

The results of the analysis can be summarised in the following proposition.

Proposition 1. *The one-spike solution $u(x), v(x)$ given in (3.23b), (3.37) with $v(0) = \kappa_1$ is stable only when $0 < \alpha < \alpha_h$. As α increases past α_h, a breathing Hopf bifurcation in the amplitude of the spikes is triggered. The numerical computation of an eigenvalue problem shows that α_h is defined implicitly by*

$$\kappa = 15.7^{\frac{1}{4}}\delta \tag{3.46}$$

In particular if we consider the regime $\beta \gg 1$ and $\alpha \sim O(1)$, then to leading order we have from (3.44a) that

$$\kappa_1 \approx \frac{3\left(\alpha+\delta\beta\right)}{\beta} + \frac{9\left(\alpha+\delta\beta\right)^4}{\beta^3} + O\left(\frac{1}{\beta^5}\right) \approx \frac{3\alpha}{\beta} + 3\delta + O(\frac{1}{\beta^2}, \delta^2). \tag{3.47}$$

Therefore combining (3.46) *and* (3.47)*, we get*

$$\alpha_h \approx \frac{15.7^{\frac{1}{4}}\delta^{\frac{1}{2}}\beta}{3} \approx 0.6636\delta^{\frac{1}{2}}\beta, \tag{3.48}$$

to the leading order in δ and $\frac{1}{\beta}$.

To verify the proposition, we can compare with numerical computation of the spectrum using a finite difference approach. The result is shown in Figure 3.5, which shows good agreement when we take various different approximations to κ_1 that are accurate to $O(\delta)$

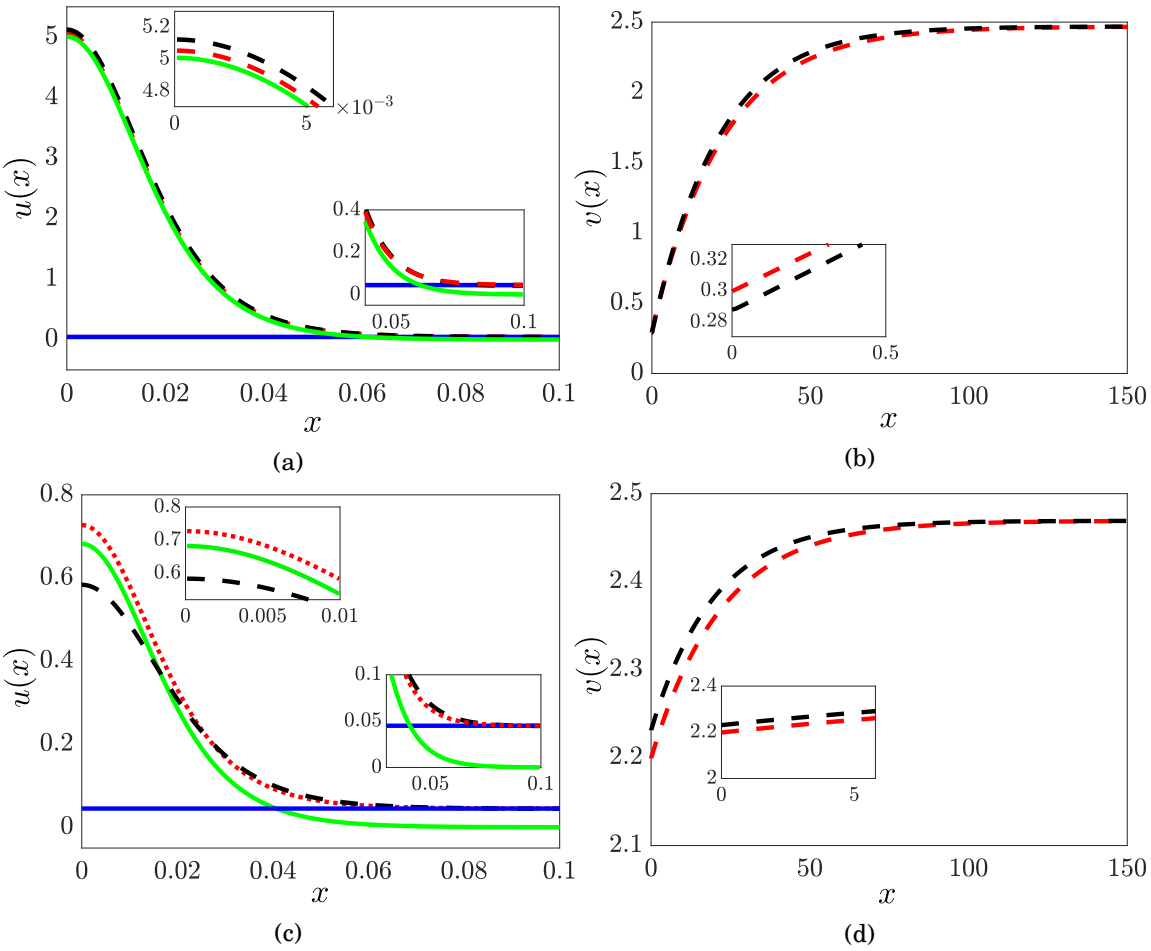

Figure 3.3: Comparison between the semi-strong asymptotic solution and the numerical solution for $a = 0.04$, $b = 0.005$ and $\delta = 0.01$ in the limit $l \to \infty$ (computations performed with $l = 1000$). (a) Solution profile $u(x)$ for $x > 0$ on the upper branch; green and blue continuous lines indicate the inner and the outer solution, respectively. The red dashed lines represent the sum of the inner and outer solutions, and the black dashed line is the numerical solution. (b) Solution profile for $v(x)$ for $x > 0$ on the upper branch with red and black dashed lines indicating the analytical and numerical solutions, respectively. (c)-(d) Solutions for the lower branch plot identically to panels (a)-(b), respectively.

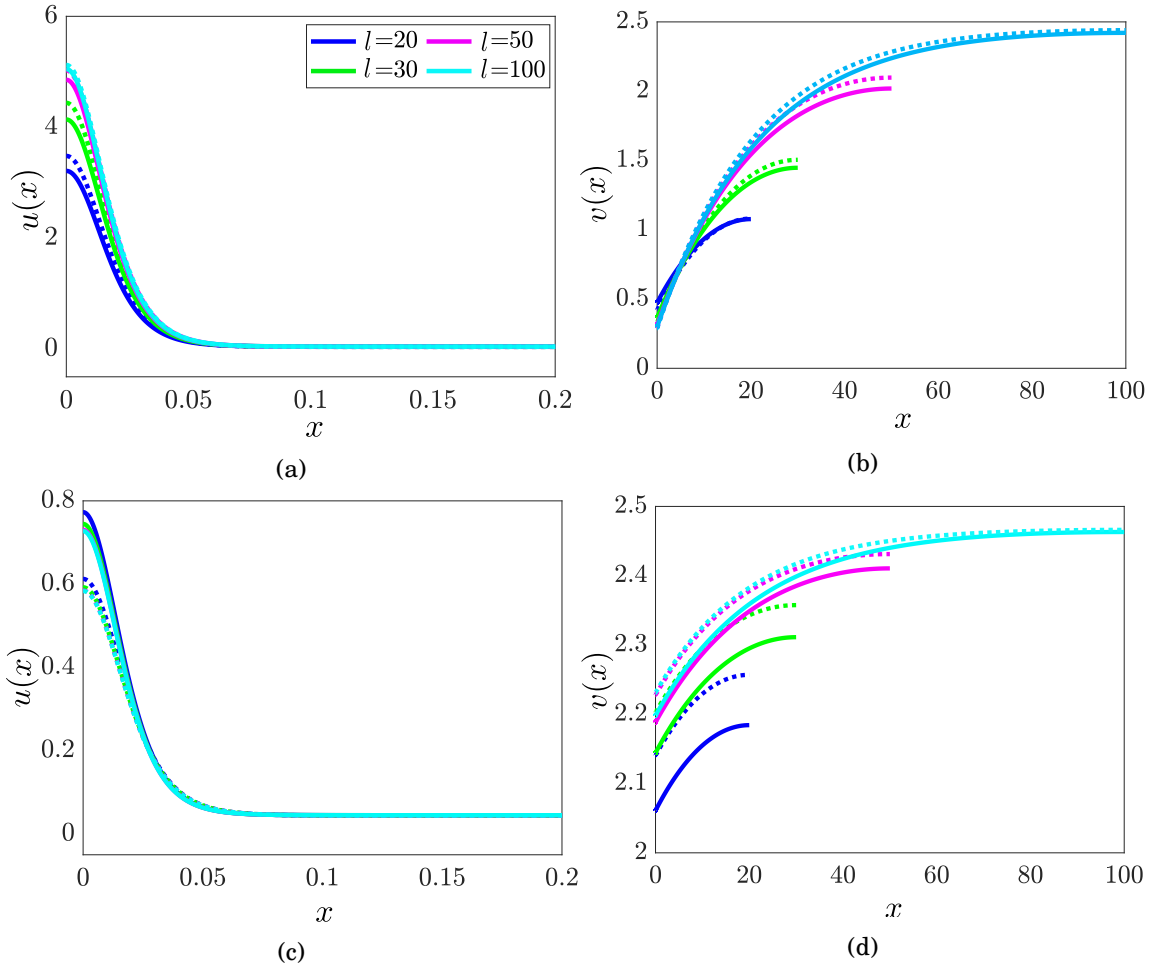

Figure 3.4: Similar to Figure. 3.3 but on a finite domain. (a) and (b) Analytical approximations to solution profiles for $u(x)$ and $v(x)$ respectively, for the upper branch (solid lines) and their numerically obtained counterparts (dashed lines). (c) and (d). Solutions for the lower branch plot identically to panels (a)-(b), respectively.

Note the apparent contrast between this asymptotic result and the depicted numerical stability result of the spike solutions in Fig. 3.1c for which no Hopf bifurcation on the upper branch was found. To resolve the apparent descrepancy, note however that the numerical results in that figure were for $a = 0.3785$, which for $\delta = 0.01$ is outside of the present asymptotic regime. Figure 3.6a shows a similar computation for $a \approx 0.1$ and $\delta = 0.05$ which is consistent with the asymptotic limit. Here we see that as for small a there is indeed a breathing Hopf bifurcation on the upper branch, before it connects to the lower branch in the fold. As a increases, the Hopf point gets closer to the fold and disappears in a codimension-two point for $a \approx 0.2$. For larger a-values the upper branch is stable all the way up to the fold point. Here the location of the Hopf instability was found by computing the spectrum of the spike solution and using a simple bisection method developed in section 2.6.3 to find where a pair of imaginary eigenvalues cross

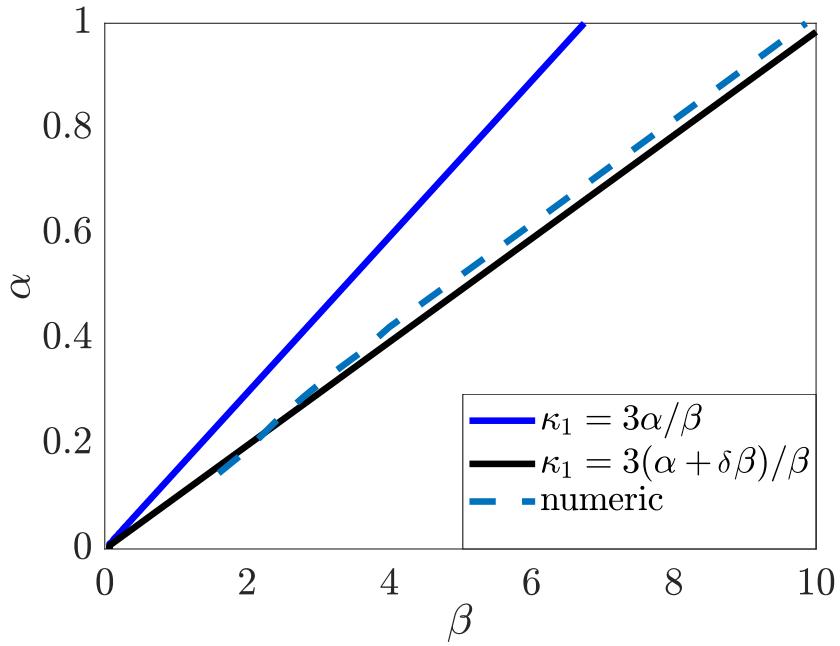

Figure 3.5: Hopf bifurcation threshold given by (3.48) . The parameters are $\delta = 0.05, l = 100$. Here dashed line are obtained through numerical spectral discretisation of system (3.30); different coloured solid lines are obtained by computing α_h such that κ_1 solved in (3.47) using two different level of approximation.

the imaginary axis (see Fig. 3.6b.

To establish whether the Hopf bifurcation is super or sub-critical, we use direct numerical simulation of (3.30). Based on the computation in figure 3.23b, it is possible to select two points; one just before the Hopf bifurcation and the other just after. Figure 3.7(a),(b) illustrates the results of the direct simulation of (3.30) as the maximum of the u-component as a function of time for $b = 0.09$ and $\delta = 0.05$, given small spatially uniform perturbations to the spike solutions. That is the initial condition is $(u(x,0), v(x,0)) = u_0(x) + \epsilon, v_0(x) + \epsilon)$ where u_0 and v_0 represents steady spike solutions computed by AUTO. For these values of the parameters, the Hopf bifurcation occurs at $a_h = 0.1658$. Figure 3.7a shows that the spike solution before the Hopf point $a = 0.1657$, seems to be stable under small perturbations ($\epsilon \leq 0.085$), yet for a perturbation that is slightly bigger, the solution leaves the basin of attraction of the spike solution and completely collapses to the homogeneous steady state. As we move beyond the Hopf point, any size of perturbation is found to oscillate with increasing amplitude until it collapses completely back to the homogeneous steady state; see figure 3.7b. Hence, it can be concluded from the numerical simulation that the Hopf bifurcation is subcritical.

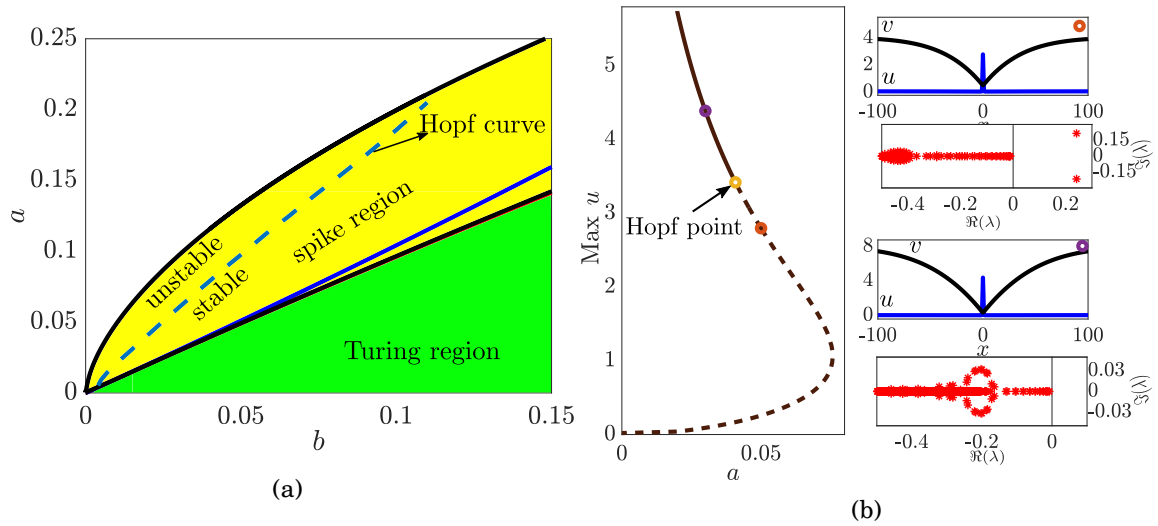

(a) (b)

Figure 3.6: A zoom of the numerical two-parameter bifurcation diagram for small a and b with region $\delta = 0.05$ in the limit of large l. (a) The dashed (blue) curve indicates the location of the Hopf bifurcation. (b) Bifurcation diagram of max u versus a for fixed $b = 0.01$ and $\delta = 0.05$ showing the stable and unstable branches joining at the Hopf point $a_h = 0.0408$. The insets represent solutions and corresponding linear spectrum either side of the Hopf bifurcation.

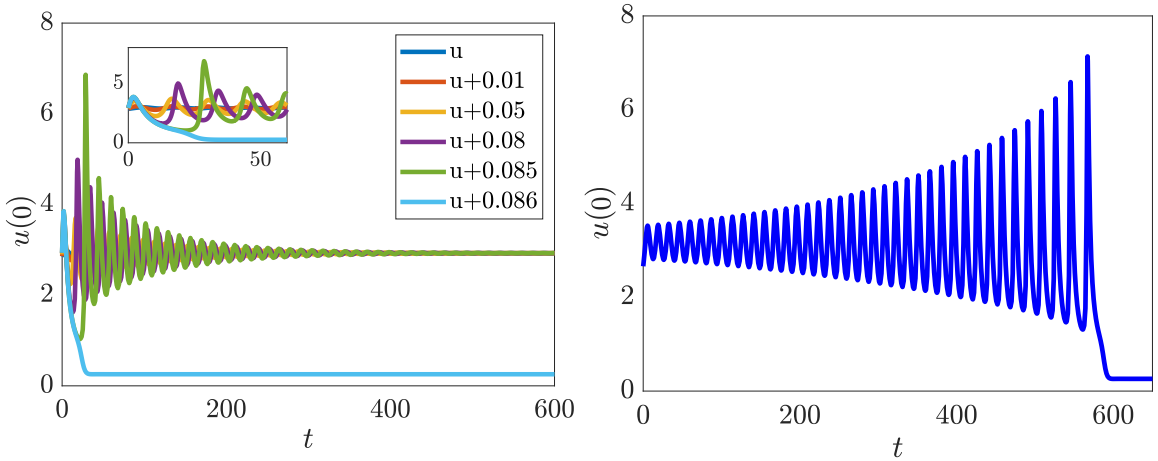

(a) (b)

Figure 3.7: The direct simulation results of the full system (3.30) express by the plot of u component of the spike at $x = 0$ as function of time for fixed $b = 0.09$, $\delta = 0.05$ and two different values of a (a) $a = 0.1657$ before the Hopf point and (b) $a = 0.171$ after the Hopf point.

3.6 Glycolysis Model

The second example we consider is the model of Glycolysis first proposed by Tyson & Kauffman [154] in their study on cellular mitosis which we introduce as a canonical example in chapter 2.

Recall that the model equations can be written

$$\frac{\partial u}{\partial t} = dv - u + u^2 v + \delta^2 \frac{\partial^2 u}{\partial x^2}, \tag{3.49a}$$

$$\frac{\partial v}{\partial t} = b - dv - u^2 v + \frac{\partial^2 v}{\partial x^2}. \tag{3.49b}$$

The system (3.49) has a unique homogeneous steady state which is given by

$$u_s = b, \quad v_s = \frac{b}{d + b^2} \tag{3.50}$$

Here u and v, represent the activator and the inhibitor concentration, respectively. The term $u^2 v$ in (3.49a) and (3.49b) refers to the production of u in the presence of v and the consumption of v in the presence of u, respectively. The parameter δ is activator and inhibitor rate of diffusivity ratio, $d > 0$ is the dimensionless input flux and $b > 0$ is dimensionless rate constant for the low activity state. The steady state bifurcation analysis for the model found in (3.49) subject to the Neuman boundary conditions has been investigated in [170] and the model dynamics were considered in [11]. For the case $d = 0$, Ward et at. [168] investigated the existence of symmetric spatial patterns. Iron et at. [83] studied the stability of spatial pattern while Zhou [182] extended this analysis to show the existence of more generalised patterns and their stability analysis.

Figure 3.8a shows the overall bifurcation diagram, which was already presented in section 2.4.1, represented in the (b,d)-plane for a fixed value of δ. Additionally, we have included the condition for the Turing bifurcation change from the super- to sub- critical using the normal form method from; see section 2.4.2. This point is depicted by a pink circle along the Turing curve in Figure 3.8a. Using AUTO, the region of localised patterns region (snaking, spikes) is obtained which is represented by the green shaded region in Figure 3.8a. Note, the localised patterns region is divided into two subregion (spike and snaking) by BD curve

$$\left(b^2 + d\right)\delta \sqrt{-\delta^2 \left(b^2 + d\right)^2 + 6b^2 + 2d} = d - b^2. \tag{3.51}$$

In Figures 3.8b and 3.8c the results of one-parameter continuation from within the snaking and the spike regions respectively are shown. The solid (dashed) lines presents stable (unstable) patterns. In the homoclinic snaking region (the upper portion of Figure 3.8a), there are infinity many of localised patterns which have decaying oscillation in the far field and have an arbitrary wide spatial extent. In addition, the homoclinic snaking exists on two intertwined snakes where branches of a solutions with an odd and an even number of spikes alternate. Examples of stable solutions from each branch are produced in Figure 3.8b. Moving from the snaking region to the spike by crossing the BD curve, the solutions in this region have a single spike with a monotonic tail (see Figure 3.8c).

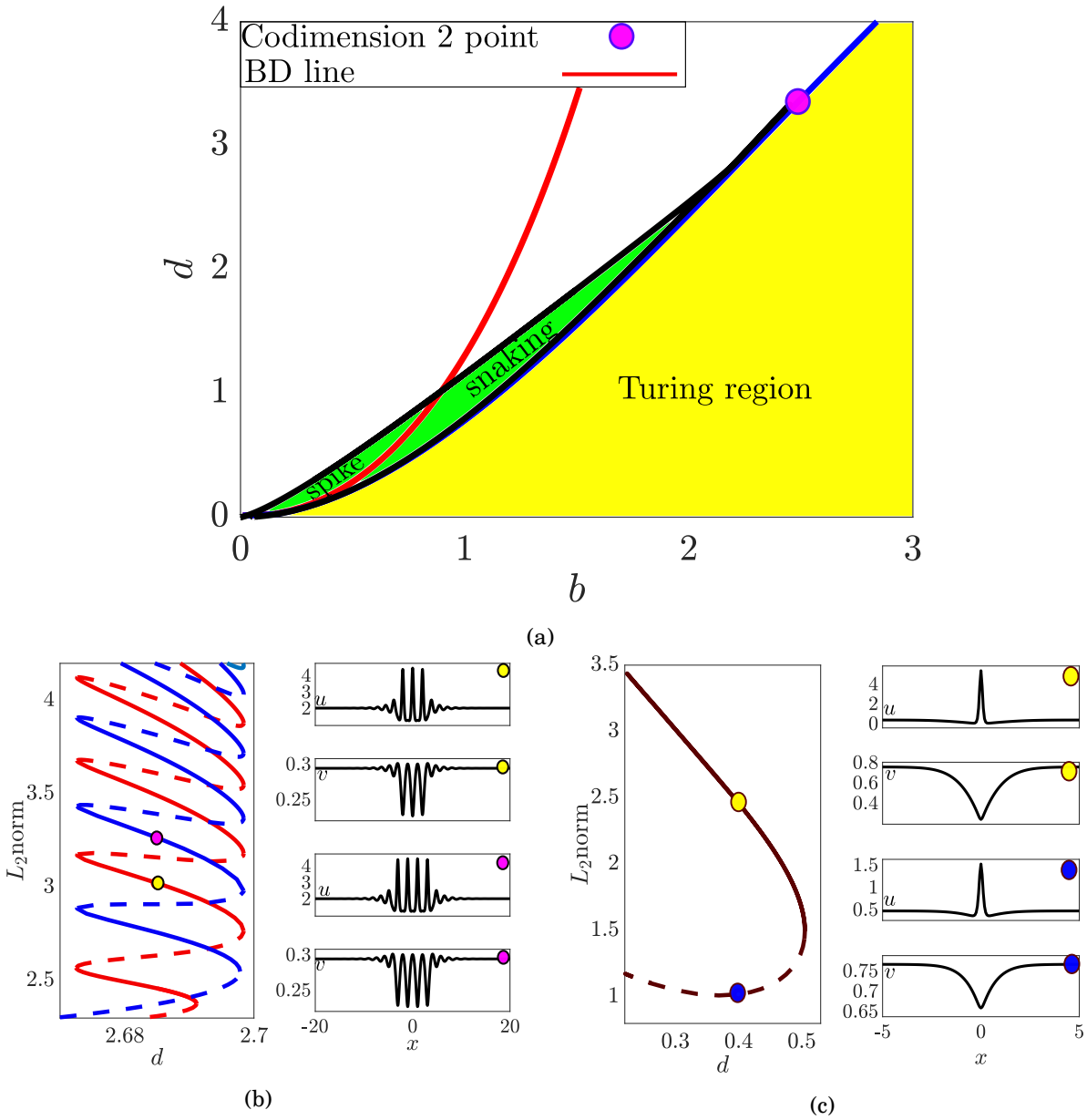

Figure 3.8: (a) Similar to Figure 3.1 but for model (3.49) with parameters b and d varying and $\delta = 0.045$. (b)-(c) Results of one parameter continuation from the snaking and the spike regions for $b = 1.8$ and $b = 0.49$ respectively when d is varied.

3.6.1 Semi-strong interaction asymptotic analysis

As shown in section 3.4 by applying the semi-strong interaction asymptotic analysis a good approximation solution for the spike can be achieved. In this section the same method is applied to obtain an approximate solution for the spike solution; see figure 3.8c.

To implement the semi-strong interaction asymptotic analysis, starting from the spike region in Figure 3.8 and doing continuation along the parameter d, we find a fold that joins two types

of solutions; a spike with large (small) peak; see figure 3.8c. For the purpose of gaining an appropriate scaling for the spike solution, we consider $n = 1$ in (3.13) so that the parameters d and b are small. We consider the steady-state problem of (3.49) and seek solutions expanded in the power of δ in inner and outer asymptotic regimes separately.

Hence, the solutions for the inner problem to leading order of δ are given by (3.23) with $c = 1$

Now, on the outer scale we choose $m = -\frac{1}{2}$ in (3.15). Consequently, the outer solutions are given by (3.24) where $c = 1$ and $h = 0$. As in the general case, it is more convenience to write the outer solutions with included the next order of δ to match asymptotic boundary conditions. Consequently, the outer solutions are

$$\hat{v}(z) = (\kappa - \frac{\beta}{\rho + \delta\beta^2})e^{-\sqrt{\rho}|z|} + \frac{\beta}{\rho + \delta\beta^2}, \tag{3.52a}$$

$$\hat{u}(z) = ((\rho + \delta\beta^2)\kappa - \beta)e^{-\sqrt{\rho}|z|} + \beta. \tag{3.52b}$$

In order to match the inner with outer solutions, we follow the same technique used in the previous section 3.2.6. Accordingly, the values of κ are

$$\kappa_1 \approx \frac{6\delta\left(d + b^2\right)}{2\sqrt{d}\,b} + O(\delta^2), \tag{3.53a}$$

$$\kappa_2 \approx \frac{b}{d + b^2} - \frac{6\delta\left(d + b^2\right)}{2\sqrt{d}\,b} + O(\delta^2). \tag{3.53b}$$

As before, we refer to κ_1 as corresponding to the value of κ in the 'upper branch', and κ_2 is correlating the value of κ in the 'lower branch'.

Based on the above analysis, the fold bifurcation for the spike region in (b, d)-plane of the spike region is given by

$$-24d^{3/2}b^2\delta - 12\sqrt{d}\,b^4\delta - 12d^{5/2}\delta + ab^2 = 0. \tag{3.54}$$

Figure 3.9 depicts the spike region where the pink curve indicates the equation (3.54) while the black curve presents the numerical upper extant which was obtained by AUTO. It clear that the two lines agree in the lower limit where the values of the parameter are small as assumed.

Figures 3.10a and 3.10b show a comparison between the approximate solution obtained using the semi-strong method and the numerical solution for the upper branch. Figures 3.10c and 3.10d present a comparison between the semi-strong solution and the numerical solution for the lower branch. It is clear from the figures that there is a good agreement.

3.7 Stability of localised patterns

As already discussed in section 3.2.2, under the rescaling (3.10), (3.11), steady states of the general system (3.1) can be studied independently of the diffusion ration δ. Temporal stability, however, is δ-dependent. In particular, for δ sufficiently *large* all localised patterns are unstable

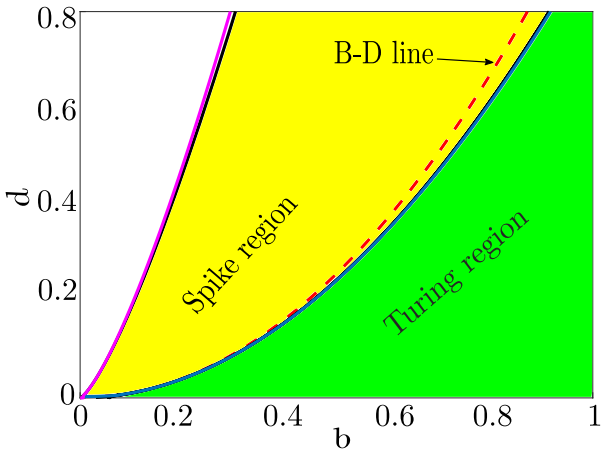

Figure 3.9: Zoom of the spike region of the glycolysis model (3.49) with $\delta = 0.01$. See the text for details.

to a homogeneous Hopf bifurcation of their background state. Also, for the Schnakenberg example, it was proved in Section 3.5 that for *small* δ the spike solution is subject to a subcritical localised (that is breathing) Hopf bifurcation for small values of the parameters a and b.

Our aim now is to investigate the relation between these two contrasting instability results, and more generally how stability of patterns changes as δ varies. Here, we shall exclusively consider the the glycolysis model (3.49). Results for the other models will be considered in the remaining sections of the chapter.

3.7.1 $\delta = 0.045$; subcritical breathing Hopf bifurcation

Figure 3.11a shows a computation of a curve of Hopf bifurcations of the localised spikes for small (b,d)-values for $\delta = 0.045$. This result is typical of what we observe for small δ-values, with the region of instability emanating from $(b,d) = 0$ and ending on the curve of the fold of the spike solution. This instability region becomes a vanishing small proportion of the spike region as $\delta \to 0$.

Figure 3.11b shows a one-parameter continuation of the spike solution undergoing both Hopf and fold bifurcation for fixed $b = 0.1$. Insets also depict the leading eigenvalues and eigenfunctions close to the Hopf bifurcation point. Note that the complex conjugate critical eigenfunctions are spatially localised, indicating that the corresponding instability represents a 'breathing mode of the spike.

For the $b = 0.16$ the Hopf bifurcation occurs at $d \approx 0.1118$. Figure 3.12 shows simulations for d-values just below and just above this d-value. The results strongly indicate that the bifurcation is subcritical. In particular, Figure 3.12a indicates that before the bifurcation, there is a threshold on the initial perturbation such that small perturbations decay back to the spike solution, whereas larger perturbations lead to a massive departure. In fact, when viewing the entire spatio-temporal trajectory (result not shown), the dynamics is found to relax back to the stable homogeneous

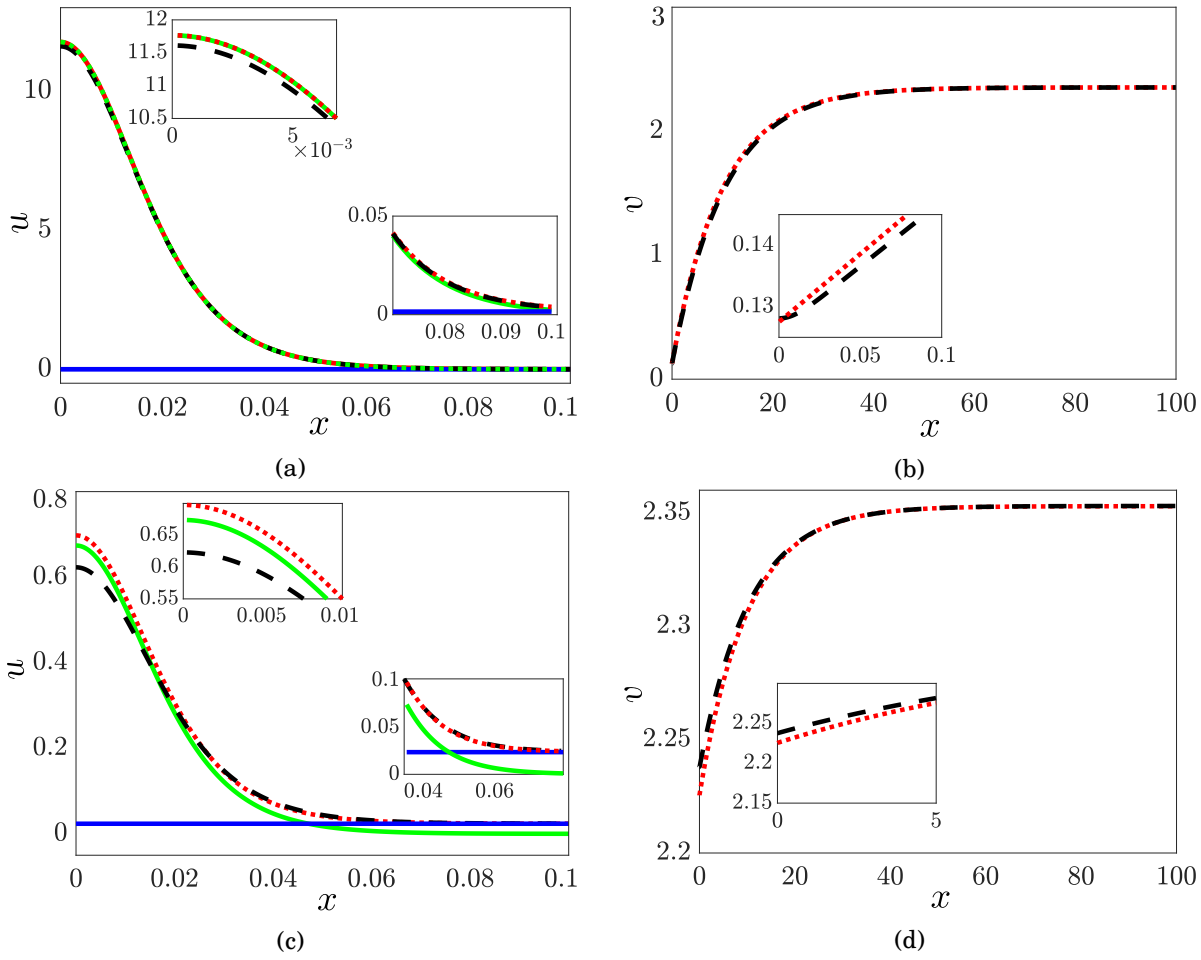

Figure 3.10: Similar to Figure 3.3 but for (3.49) with $d = 0.01$, $b = 0.025$, $\delta = 0.01$, and $l = 1000$. (a)-(b) Analytical approximations to solution profiles for $u(x)$ and $v(x)$ respectively, for the upper branch (solid lines) and their numerically obtained counterparts (dashed lines) where $\kappa = 0.1275$. (c)-(d) Solutions for the lower branch plot identically to panels (a)-(b), respectively where $\kappa = 2.22544$.

steady state. For a d-value just beyond the bifurcation, all initial conditions are found to lead to a large departure from the neighbourhood of the spike, albeit after a long transient breathing oscillation (see Figure 3.12b). Once again, the trajectory eventually collapses to the homogeneous steady state.

3.7.2 $\delta = 0.17$; supercritical breathing and global Hopf bifurcations

Figure 3.13a shows analogous results to Figure 3.8 and 3.11 for $\delta = 0.17$. Note that the portion of the localised pattern region that is unstable to the breathing Hopf bifurcation is much larger. The instability now crosses the BD line and encroches significantly into the homoclinic snaking region. Figure 3.13b depicts the equivalent of Fig. 3.8b for this δ-value. Note how the entire right-hand portion of the snaking diagram is Hopf unstable. That is, the Hopf bifurcation of

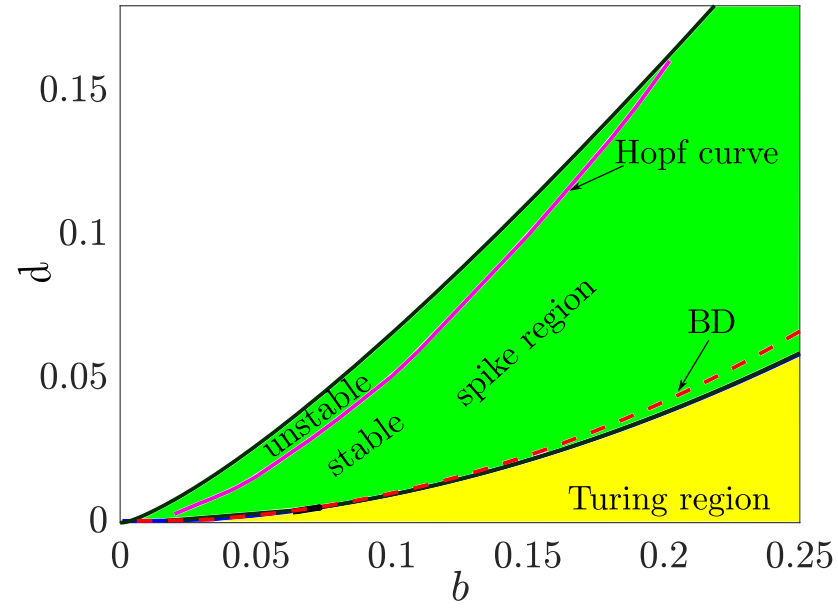

(a)

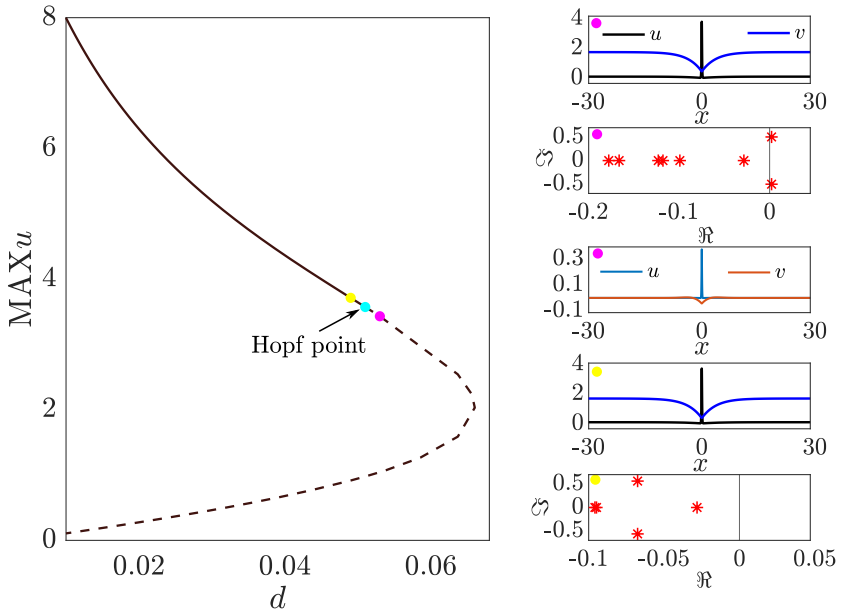

(b)

Figure 3.11: Bifurcation diagrams for (3.49) for $\delta = 0.045$. (a) The lower part of the (b,d)-plane, A (magenta) curve show the location of the breathing Hopf bifurcation. (b) One-parameter bifurcation diagram of spikes, depicting the maximum of $u(x)$ against d for $b = 0.1$; continuous (dashed) lines indicates stable (unstable) solutions where $d = 0.049(0.053)$. Panels to the right show the spectrum and corresponding absolute value of the eigenfunction of the complex-conjugate pair of eigenvalues with largest real part at the two indicated points. Here, the Hopf point is at $d_H \approx 0.051$.

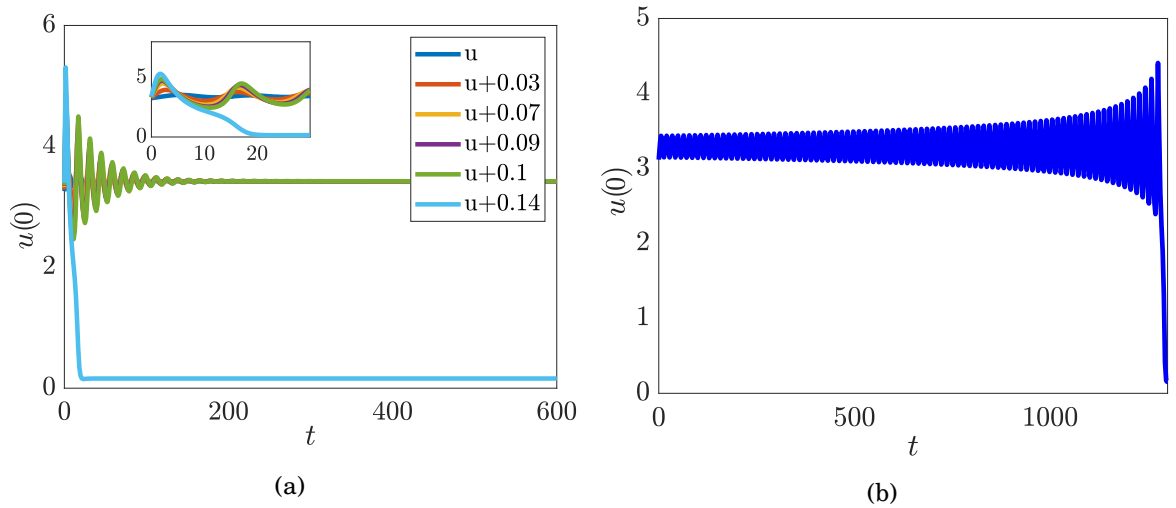

Figure 3.12: Similar to Figure 3.7 but for (3.49) for fixed $b = 0.16$, $\delta = 0.045$ and two different values of d (a) $d = 0.1115$ before the Hopf point and (b) $d = 0.1139$ after the Hopf point.

the primary (single pulse) branch that can be continued from the spike region, is reflected in Hopf bifurcation of the multi-pulse patterns too, at more or less the same d-value. The nature of the instability is indicated by the spectral computations in Figure 3.13b for a three-pulse pattern, presented in separate panels either side of the Hopf bifurcation. Note how the instability corresponds to a complex conjugate pair of eigenvalues crosses the imaginary axis. The corresponding eigenfunctions are localised, indicating that breathing-mode instability. Numerical simulations indicate that this Hopf bifurcation is supercritical (see Figure 3.14).

A zoom of the lower portion of Figure 3.13a shows that for $\delta = 0.17$ the Hopf bifurcation of the homogeneous steady state (given analytically by (2.63)) crosses the Turing bifurcation line (given analytically by (2.64)). Hence there is a small portion of the spike region that is subject to this Hopf instability. Given that localised solutions have tails that become asymptotic to the homogeneous steady state, it is clear that this instability of the background must be inherited by any localised states. In contrast to the *breathing* Hopf bifurcation of a spike, we refer to this as a *global* Hopf bifurcation.

Figure 3.13c shows one-parameter continuation in d from within the spike region, showing the location of the two separate Hopf bifurcations. The sub-plots to the right show the solution profile, spectrum and critical eigenfunction at each of the two bifurcations. Note that the larger-d bifurcation corresponds to a breathing Hopf, as can be seen by the localised eigenfunction. In contrast, the smaller-d bifurcation is a global Hopf, corresponding to a delocalised eigenfunction. Numerical evidence suggests that both bifurcations are supercritical. In particular, simulation results are depicted in Figure 3.15 for small perturbation to the spike, at parameter values that are just 'beyond' each of the two bifurcations. For the breathing Hopf, which occurs for $d \approx 0.0270$, a simulation is presented in Figure 3.15a for $d = 0.02889$. The global Hopf occurs for $d \approx 0.0230$ and Figure 3.15b presents a simulation for $d = 0.228$. Note how the time series plot of the centre

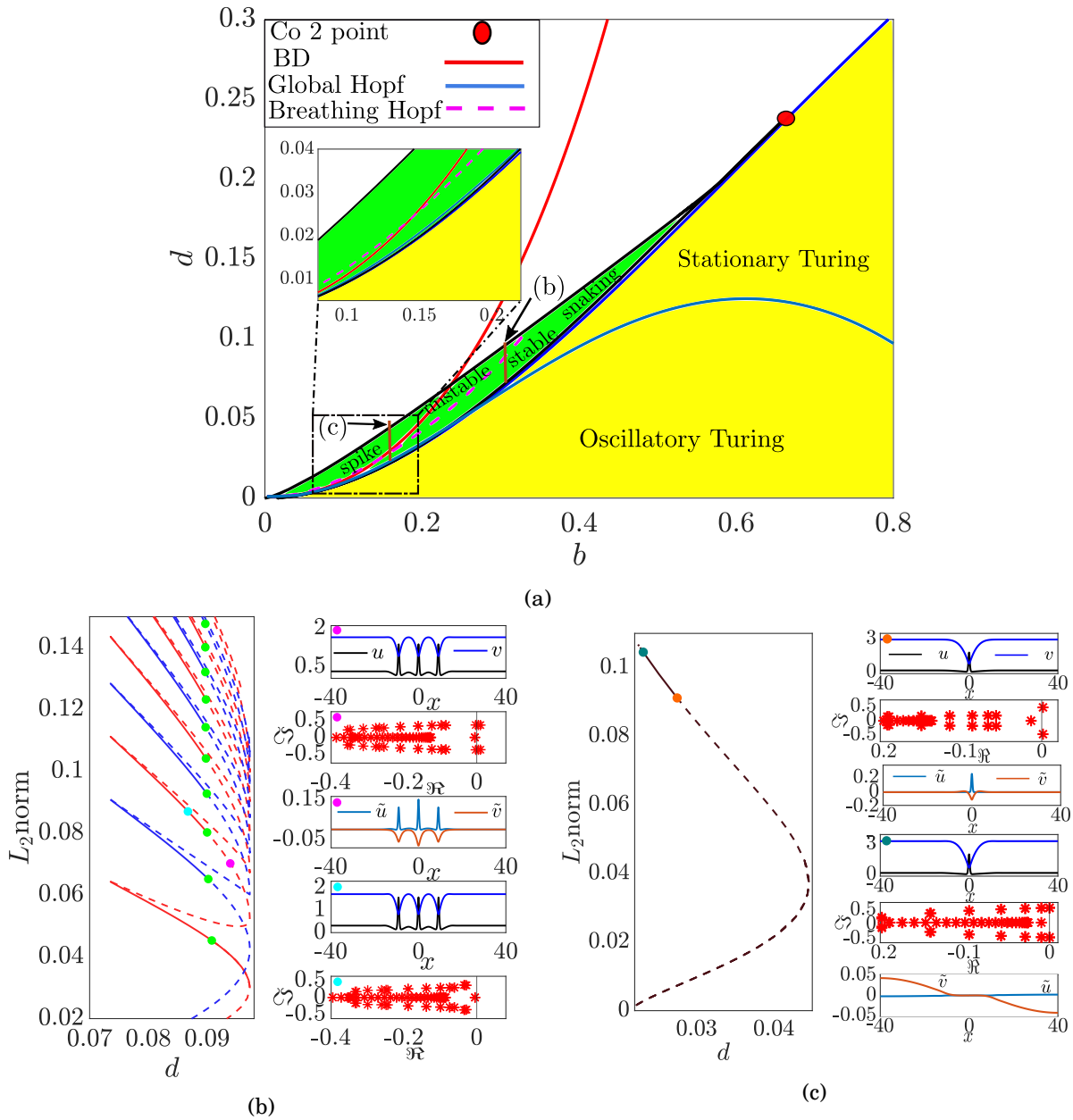

Figure 3.13: (a) Similar to Figure 3.1 for model (3.49) for $\delta = 0.17$, with location of Hopf bifurcations superimposed. (b)-(c) Results of one parameter continuation in d within the snaking and the spike regions for $b = 0.31$ and $b = 0.16$, respectively. See text for details.

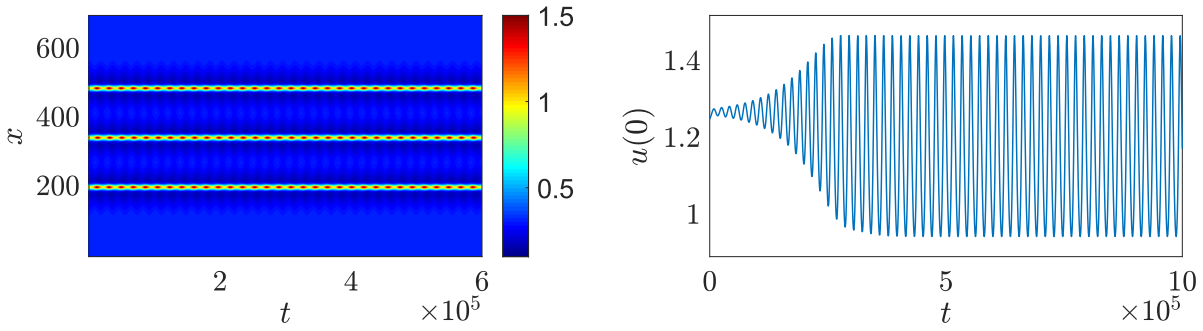

Figure 3.14: Direct simulation results of the full system (3.49) depicting the u component of the spike as function of time for fixed $b = 0.31$, $\delta = 0.17$ and $d = 0.092$, after the Hopf point for the breathing Hopf.

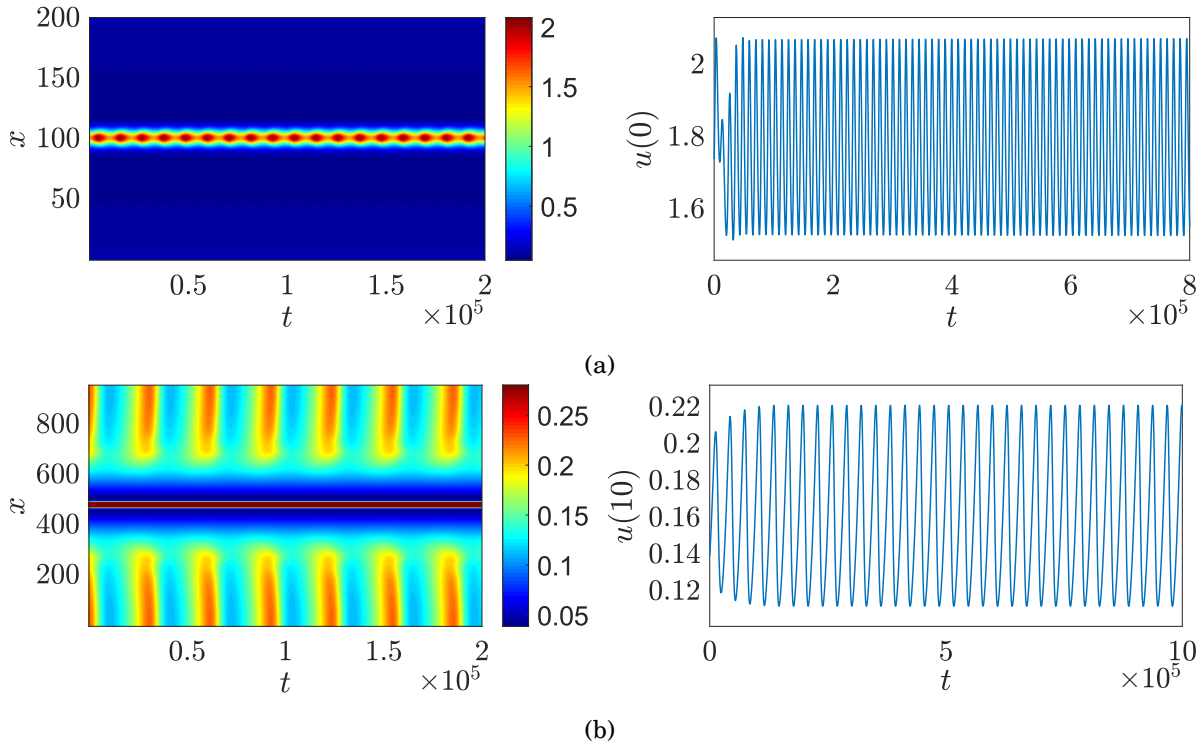

Figure 3.15: Similar to Figure 3.14 but for fixed $b = 0.16$, $\delta = 0.17$ and two different values of d (a) $d = 0.02889$ after the Hopf point for the breathing Hopf and (b) $d = 0.0228$ after the Hopf point for the global Hopf.

point of the spatio-temporal patterns indicate a stable limit cycle in each case. However, the colourmap plots indicate the that the mode of oscillation is very different between the breathing and global cases.

3.7.3 $\delta = 0.23$; breathing Hopf bifurcation of multi-pulse patterns

Figure 3.16 displays stability results for a slightly larger value of the diffusion ratio, $\delta = 0.23$. Comparing this with Figure 3.13, we observe that the breathing Hopf bifurcation has now moved significantly further up and to the right in the (b,d)-plane, and now all of the spike region and almost all of the snaking region is unstable to this instability. The inset to Figure 3.16a suggests only a tiny portion of the (green) snaking region, beyond the (magenta) breathing Hopf bifurcation is stable.

Figure 3.16b presents a detailed computation of the snaking bifurcation diagram within this tiny region, specifically for $d = 0.4$. Here, we note that, although the primary pattern is stable, we can find a sequence of breathing Hopf bifurcations (green dots) that is causing instability in the branches of the snake that correspond to higher-pulse patterns. In particular, the Hopf bifurcation first appears on the four-pulse branch (as illustrated in the spectral computations to the right). Moreover, the d-value of the instability of each successive branch is observed to increase so that a greater proportion of the region of existence of each successive n-pulse is unstable as $n \to \infty$. We remark that this type of successive Hopf instability within a homoclinic snaking region has been reported recently [129] in a model representing an optical parametric resonator.

For $\delta > 0.24$ we find that the entire localised pattern region is unstable to a breathing-mode Hopf bifurcation. This is in addition to the global Hopf instability also engulfing the whole localised pattern region for δ sufficiently large, as indicated in Figure 2.3b.

3.8 Brusselator model

We present the standard Brusselator model as a next example. This model is a well-known nonlinear model for an autocatalytic reaction. Turing and Hopf instability were shown to occur for the Brusselator in many studies, see e.g. [97, 132, 177] and the references therein. In [48, 111] the spatiotemporal dynamics near the codimension-two point where Hopf and Turing combine was considered. In this model the existence of homoclinic snaking [155] and the localized structures [93] have been reported. More recent, Tzou et al. [156] studied the stability of the localized spike. The activator-inhibitor Brusselator model is given by

$$\frac{\partial u}{\partial t} = a - (c+1)u + u^2 v + \delta^2 \frac{\partial^2 u}{\partial x^2}, \tag{3.55a}$$

$$\frac{\partial v}{\partial t} = cu - u^2 v + \frac{\partial^2 v}{\partial x^2}, \tag{3.55b}$$

where u and v are the concentration of two chemical species that interact with each other as activator and inhibitor respectively and $\delta \ll 1$ is the diffusion ratio between them. The positive parameter a is feeding parameter for activator and c represent the linear rate of conversion rate of activator into inhibitor whereas the rate at destruction of activator has been set to unity. The

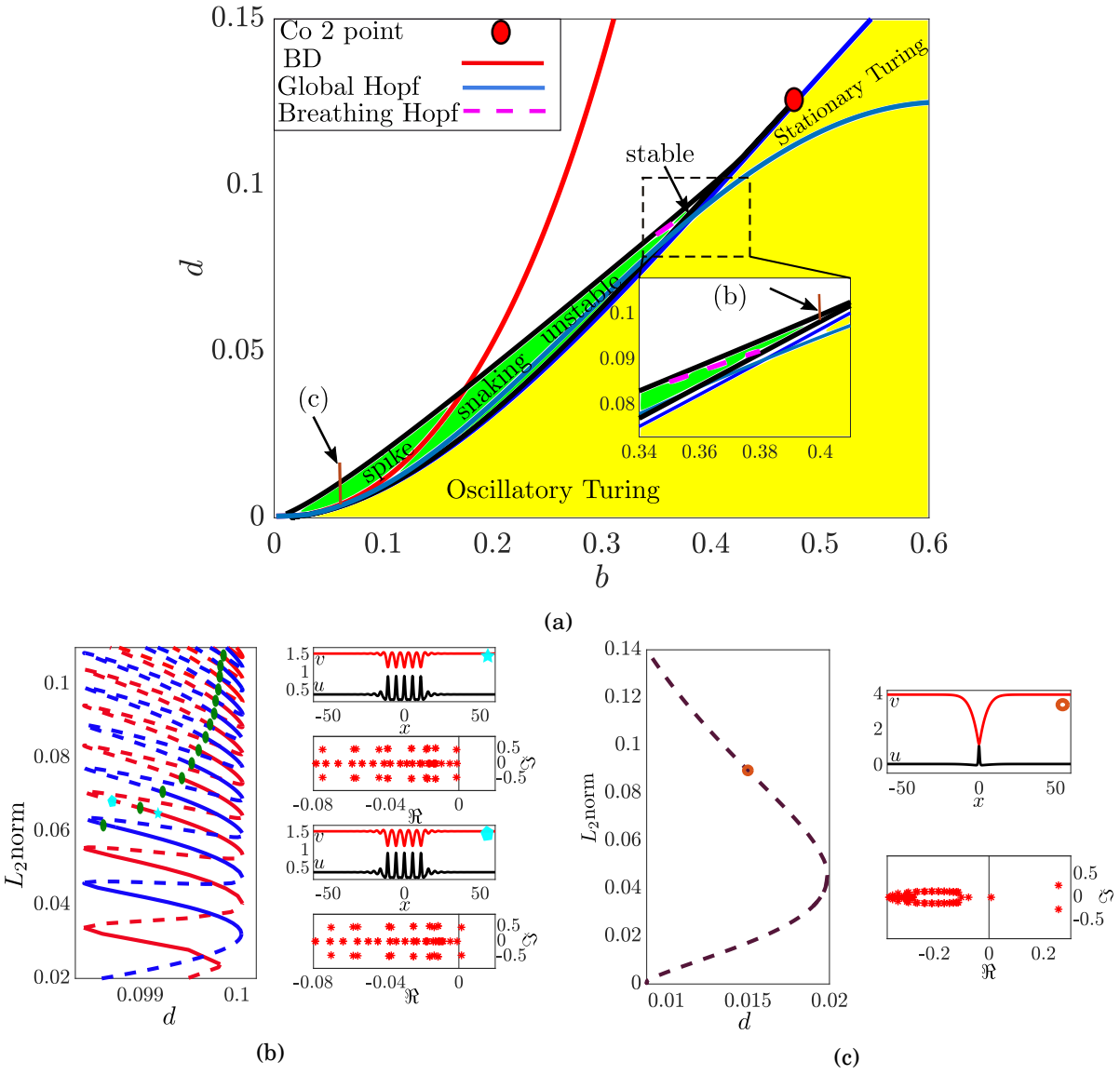

Figure 3.16: (a) Similar to Figure 3.1 for (3.49) with parameters b and d varying and $\delta = 0.17$. (b)-(c) Results of one parameter continuation from the snaking and the spike regions for $b = 0.4$ and $b = 0.1$ as d varies respectively.

system (3.55) admits one spatially homogeneous steady state solution given by

$$u_0 = a, \quad v_0 = \frac{c}{a}. \tag{3.56}$$

Using the methodology of section (2.2) we find the condition for Turing instability and obtain the critical value for the wave number k_c as follow

$$-a^2\delta^2 - 2\delta a + c - 1 = 0, \quad k_c = -\frac{a^2\delta^2 - c + 1}{2\delta^2}, \tag{3.57}$$

and a double real root eigenvalue curve (BD transition) can be found at

$$-a^2\delta^2 + 2\delta a + c - 1 = 0. \tag{3.58}$$

The codimension-two point where the Turing bifurcation changes to be subcritical is obtained by weakly nonlinear analysis, see section 2.3 for the details. In order to display all the results, we show the boundaries of different behaviour in (c,a)-plane; see Figure 3.17. Note how the behaviour is qualitatively the same as the previous two examples except that as $a \to 0$ istead of the localised region collapsing to a point in parameter space, here it occupies the whole interval from $c = 0$ to $c = 1$.

Here once again, we apply the semi-strong interaction asymptotic analysis to achieve an approximate solution for the spike in the Brusselator model. As the method is applied in the limit of small value of parameters, we take $p = 1$ in (3.13) and substitute into the (3.55). Taking into consideration the steady-state problem, we can seek an isolated spike solution. Based in the assumptions that the spike centre at $x = 0$ and introducing the coordinate (3.14) the inner solution for the leading order in δ is given by (3.23) where $c = 1$. For the outer solution, we consider $m = -1$ in (3.15) then substituting (3.15) into the steady-state problem and collecting the leading order terms in δ, one finds that

$$\hat{u_0}(z) = a, \quad \hat{v_0}(z) = \left(\kappa - \frac{\eta}{a}\right) e^{-\alpha|z|} + \frac{\eta}{a}. \tag{3.59}$$

Finally, we need to match the inner and outer solutions to find the unknown value of κ. To do this, we consider a weak form of v-equation over an interval that contains the inner region see Section 3.2.6 for details. Sample calculation give a quadratic equation for κ

$$-2a\kappa^2 + 2c\kappa - 6\delta = 0 \tag{3.60}$$

Hence, the first root which is provided the value of κ in higher-u is found to be

$$\kappa_1 = \frac{c - \sqrt{-12\delta a + c^2}}{2a} \approx \delta\left(\frac{3}{c} + \frac{9a}{c^3}\delta + O(\delta^2)\right).$$

Whereas the second root that correspond to the value of κ in the lower-u is given as

$$\kappa_2 = \frac{c + \sqrt{-12\delta a + c^2}}{2a} \approx \frac{c}{a} - \frac{3}{c}\delta + O(\delta^2).$$

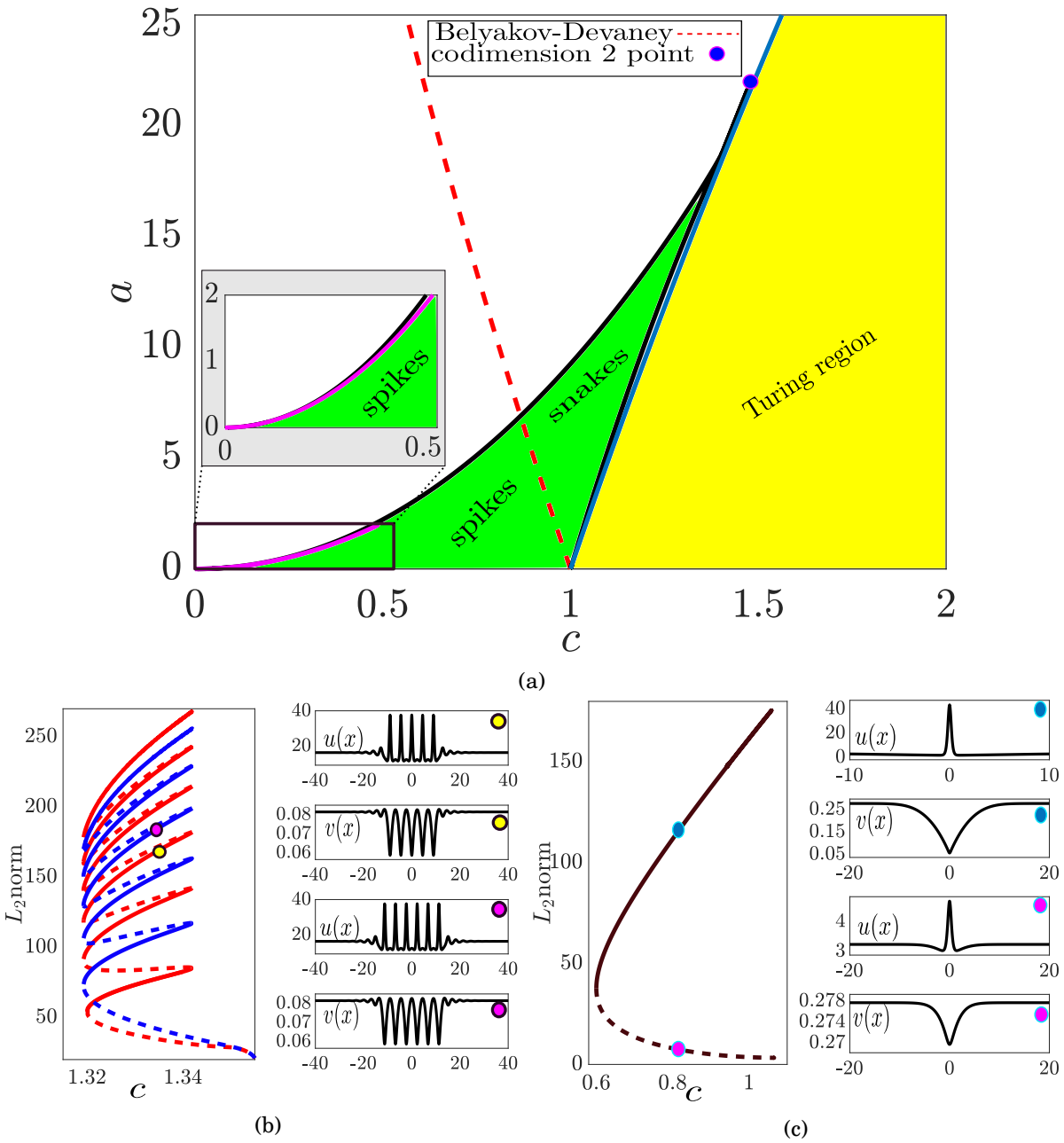

Figure 3.17: (a) Similar to Figure 3.1 for (3.55) with parameters c and a varying and $\delta = 0.01$. (b)-(c) Results of one parameter continuation from the snaking and the spike regions for $a = 16.4211$ and $a = 2.6$ as c varies respectively.

In order to gain the fold in the spike region one requires the discriminant of (3.60) to be zero. This is given by the condition

$$-12\delta a + c^2 = 0. \tag{3.61}$$

Therefore, equation (3.61) is corresponds to the boundary curve of localized structures in the

spike region. In the panel in Figure 3.17a we compare between the curve obtained by (3.61) (pink line) and that obtained from AUTO (black line).

Figure 3.18 depicts a comparison between the approximation solution obtained by the semi-strong method and the numerical solution for the upper and the lower branch.

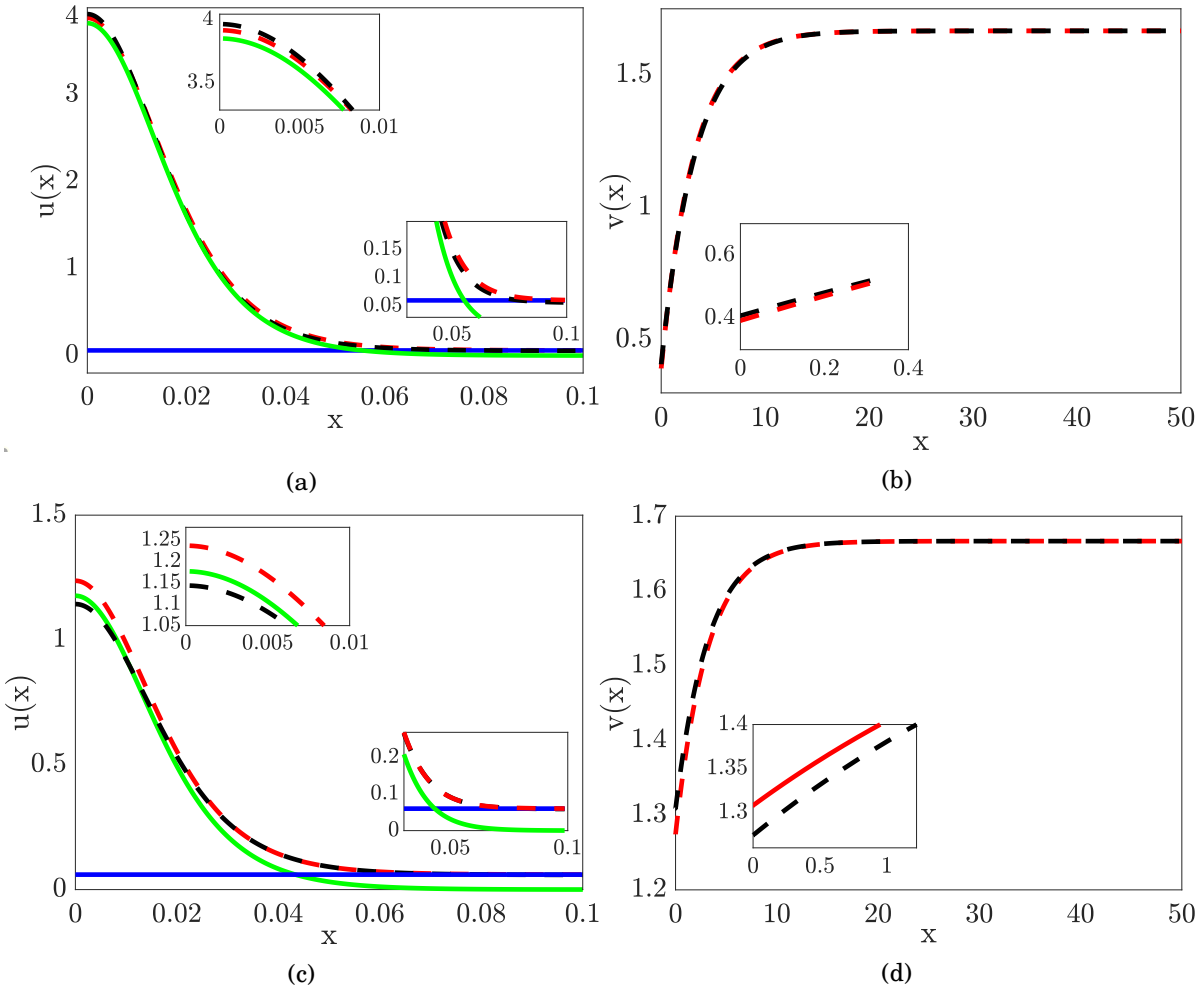

Figure 3.18: Similar to Figure 3.3 but for (3.55) with $a = 0.06$, $c = 0.1$, $\delta = 0.01$ and $L = 1000$. (a)-(b) Analytical approximations to solution profiles for $u(x)$ and $v(x)$ respectively, for the upper branch (solid lines) and their numerically obtained counterparts (dashed lines) where $\kappa = 0.39237478$. (c)-(d) Solutions for the lower branch plot identically to panels (a)-(b), respectively where $\kappa = 1.2742918$.

A natural question arises whether there is a Hopf bifurcation of the localised state in the Brusselator model , which was the case in the Schnakenberg and the glycolysis models. To find out, numerical computation of the spectrum using the method in section 2.6.3 is applied. The results are shown in Figure 3.19a, which shows the existence of a Hopf bifurcation. Figure 3.19b depicts a one-parameter bifurcation diagram where the Hopf bifurcation occurs on the upper branch before it connects to the lower branch at the fold. To the right, a sample of a stable

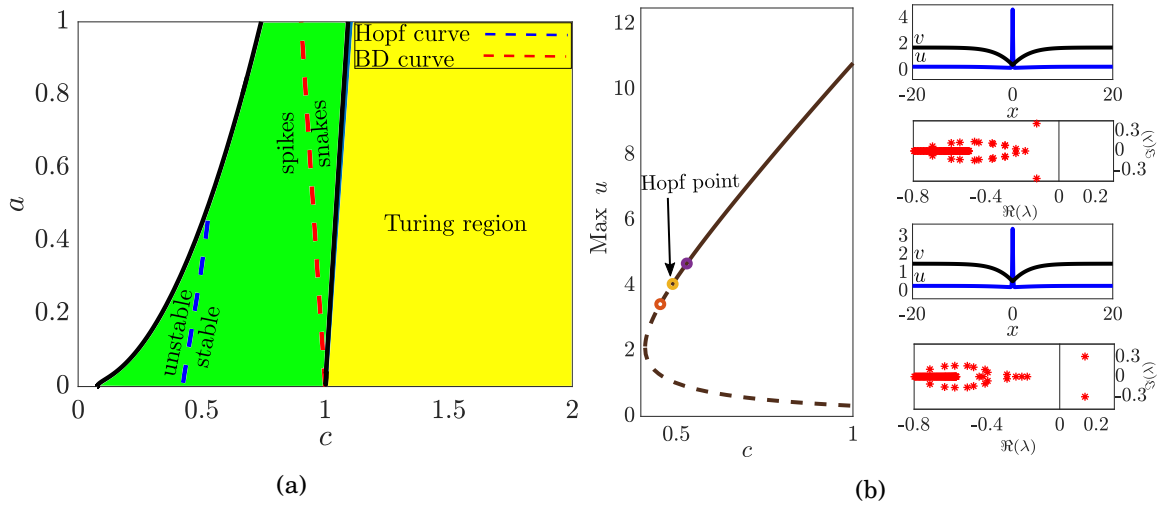

(a) (b)

Figure 3.19: A zoom of the numerical two-parameter bifurcation diagram of the Brusselator model (3.55) for small a and c with region $\delta = 0.05$ in the limit of large l. (a) The dashed (blue) curve indicates the location of the Hopf bifurcation. (b) Bifurcation diagram of max u versus c for fixed $a = 0.3$ and $\delta = 0.05$ showing the stable and unstable branches joining at the Hopf point $a_h = 0.494$. The insets represent solutions and their corresponding linear spectrum either side of the Hopf bifurcation.

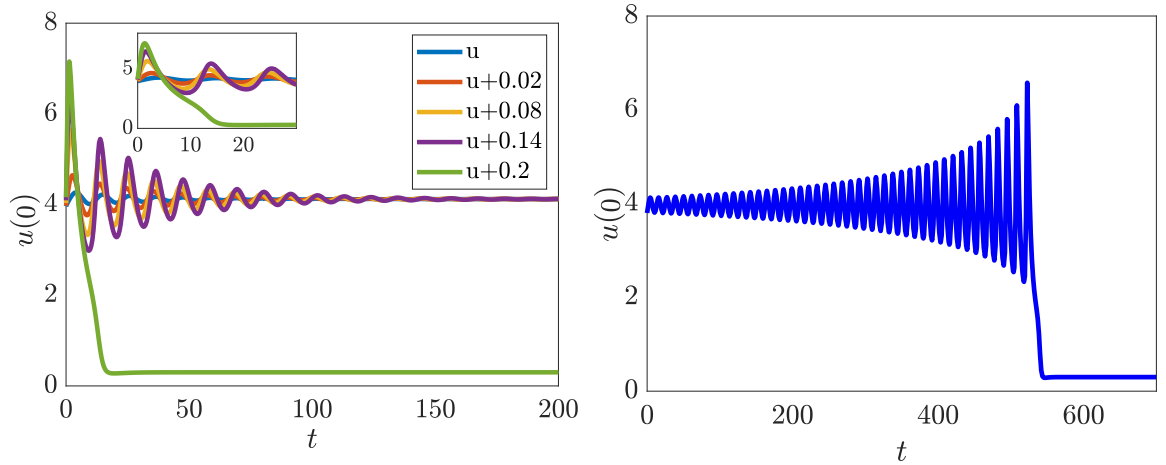

(a) (b)

Figure 3.20: Similar to Figure 3.7 for (3.55) with fixed $a = 0.3$, $\delta = 0.05$ and two different values of c (a) $c = 0.484$ before the Hopf point and (b) $c = 0.475$ after the Hopf point.

and an unstable solution with their spectrum is shown. Figure 3.20 illustrates the results of the examination of the criticality of the bifurcation by direct numerical simulation. The results demonstrate that the Hopf bifurcation is subcritical.

3.9 Sel'kov-Schnakenberg model

We study a generalised Sel'kov-Schnakenbarge as our next example. The model has been analysed in many research problems. The interested reader can refer to [101, 157] and references within. The model describes an autocatalytic chemical reaction between two chemical products X, Y and two chemical sources A, C as follows:

$$\mathrm{X} \rightleftharpoons \mathrm{C}, \quad \mathrm{A} \longrightarrow \mathrm{Y}, \quad 2\mathrm{X} + \mathrm{Y} \longrightarrow 3\mathrm{X}.$$

Applying the law of mass action and after non-dimensienalisation we can obtain a system of reaction diffusion equation as follows [143]

$$\frac{\partial u}{\partial t} = a - u + dv + u^2 v + \delta^2 \frac{\partial^2 u}{\partial x^2}, \tag{3.62a}$$

$$\frac{\partial v}{\partial t} = b - dv - u^2 v + \frac{\partial^2 v}{\partial x^2}, \tag{3.62b}$$

(3.62c)

Here u and v, represent the activator and the inhibitor concentration respectively. $\delta \ll 1$ is the diffusion ratio, and a, b and d are positive constants that discribe feed rate and linear activation rates, respectively. It easy to show that the (3.62) has a unique positive homogeneous equilibrium point given by

$$u_0 = a + b, \quad v_0 = \frac{b}{(a+b)^2 + d}. \tag{3.63}$$

Therefore, the Turing bifurcation of (3.62) can be straightforwardly obtained by the linear stability analysis (see Section (2.2) for details) around the steady state (3.63). Hence, we have the conditions for Turing instability which are given by

$$\left((a+b)^2 + d\right)^2 \delta^2 + a^2 - b^2 + d = -2\delta \left((a+b)^2 + d\right)^{3/2}, \tag{3.64a}$$

and the critical value for the wavenumber is define as

$$k_c = \frac{-\left((a+b)^2 + d\right)^2 \delta^2 - a^2 + b^2 - d}{2\left((a+b)^2 + d\right)\delta^2}. \tag{3.64b}$$

Moreover, the BD curve is given by

$$\left((a+b)^2 + d\right)^2 \delta^2 + a^2 - b^2 + d = 2\delta \left((a+b)^2 + d\right)^{3/2}. \tag{3.64c}$$

Figure 3.21a depicts these curves and other bifurcation lines in the (b, a)-plane for fixed $d = 0.001$ and $\delta = 0.01$. The solid blue circle represents the result of weakly nonlinear analysis to find the condition for the Turing bifurcation to change from super- to sub-critical (see section 2.3). The green shaded region shows the localised region, which was computed by AUTO. This region is

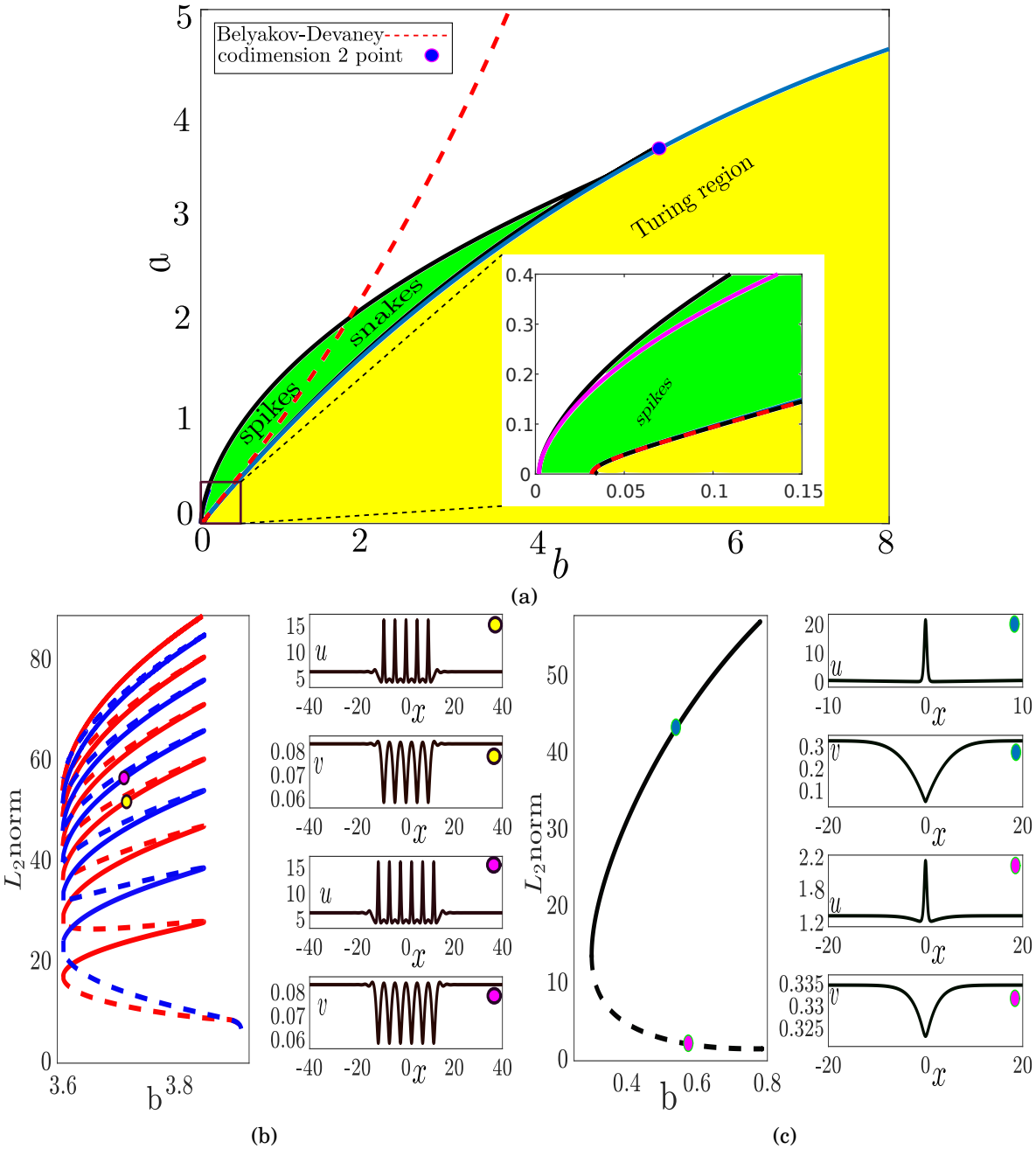

Figure 3.21: (a) Similar to Figure 3.1 but for Sel'kov- Schnakenberg model (3.62) with parameters b and a varying and fixed $d = 0.001$ and $\delta = 0.01$. (b)-(c) Results of one parameter continuation from the snaking and the spike regions as b varies for $a = 2.9$ and $a = 0.58$ respectively.

divided into two regions by the BD curve given by (3.64c). Note the limit $a \to 0$ leads, like for the Brusselator to an interval of value of the second parameter for the (green) spike region.

These two regions define the pining (snaking) region where the spatial eigenvalues are complex conjugates, and the solution has an oscillatory tail. Where the other region is called the spike region, here, the spatial eigenvalues ar pure real and the localised solutions have monotonic tails. Figure 3.21b shows the behaviour of homoclinic snaking of (3.62) where branches of a solution with odd and even number of peaks snake back and forth through saddle node bifurcation. Each fold of the snake connects two types of a solution; stable and unstable. We compute the stability of the snaking branches numerically using Matlab. In Figure 3.21b we present the homoclinic snaking and two examples of stable solution. Figure 3.21c shows the saddle-node bifurcation from the spike region with two example solutions.

We next compute the analytical approximation for the spike using semi-strong asymptotic analysis. Choosing $n = 2$ in (3.13), we Follow the technique apply of section 3.2. As we know from previous cases the spike for the inner solution is centred at $x = 0$, and the space coordinate in the inner solution is (3.14) . Consequently, the solutions for the leading order in δ is given by (3.23) where $c = 1$. For the outer solution, we start by rescaling (3.15) with $m = -1$. Under these rescaling the asymptotic approximation for the localised solutions in the outer region to the leading order in δ reads

$$\hat{u}_0(z) = \alpha + \delta\beta, \tag{3.65a}$$

$$\hat{v}_0(z) = \left(\kappa - \frac{\beta}{\rho + (\alpha+\delta\beta)^2}\right) e^{-\sqrt{\rho+(\alpha+\delta\beta)^2}\,|\,z\,|} + \frac{\beta}{\rho+(\alpha+\delta\beta)^2}. \tag{3.65b}$$

To match the solutions we follow the technique developed in section 3.2.6. The relevant quadratic equation is

$$-2\sqrt{(a+b)^2+d}\,\kappa^2 + \frac{2b\sqrt{(a+b)^2+d}}{(a+b)^2+d}\kappa - 6\delta = 0. \tag{3.66}$$

Figure 3.21a shows a zoom in the spike region. The pink curve corresponds to the zero discriminant of (3.66) which is given by

$$b^2 - 12\left(a^2 + 2ab + b^2 + d\right)^{3/2}\delta = 0, \tag{3.67}$$

whereas the black curve indicates the outer fold of the localised structures region that was obtained from AUTO.

To test the accuracy of the approximate solutions, we display in figures 3.22a and 3.22b the asymptotic approximation with the numerical solution for $u(x)$ and $v(x)$ respectively on the upper branch. It is clear from the figures that the numerical and the asymptotic solution are essentially indistinguishable. In Figures 3.22c and 3.22d we show solutions for the lower branch, where we again find a great agreement between the numerical and the asymptotic solution.

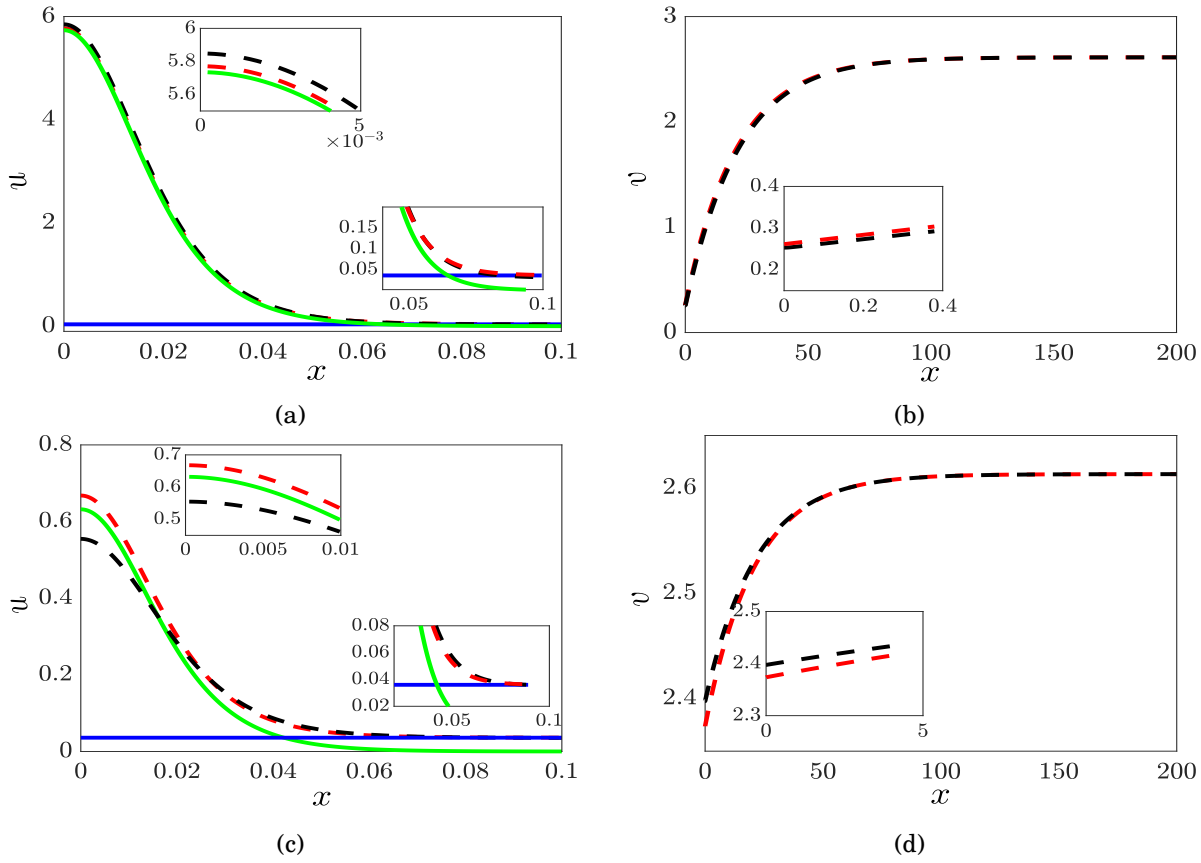

Figure 3.22: Similar to Figure 3.3 but for for Sel'kov- Schnakenberg model (3.62) with $a = 0.03$, $b = 0.006$, $d = 0.001$, $\delta = 0.01$ and $L = 1000$. (a)-(b) Analytical approximations to solution profiles for $u(x)$ and $v(x)$ respectively, for the upper branch (solid lines) and their numerically obtained counterparts (dashed lines) where $\kappa = 0.2615480377$. (c)-(d) Solutions for the lower branch plot identically to panels (a)-(b), respectively where $\kappa = 2.37365744$.

Finally, we investigate the stability of the spike solution by numerical computation of the spectrum using a finite difference approach. In Figure 3.23a we show the existence of a Hopf bifurcation, which was found by the direct simulation of the full system (3.62) to be subcritical; see Figure 3.24. Whereas in Figure 3.23b the one parameter continuation diagram is shown which indicates that the Hopf bifurcation occurs before the upper branch connects to the lower branch.

3.10 The Root hair model

Payne and Grierson [131] proposed a Schnakenberg-like model of the form (3.1) with constant and linear terms as described in Table 3.1 to describe the process of activation of small G-proteins known as ROPs which are thought to be the precursor to cell polarity formation and morphogenesis in plant cells. In applying this to the canonical problem of the formation of hair-

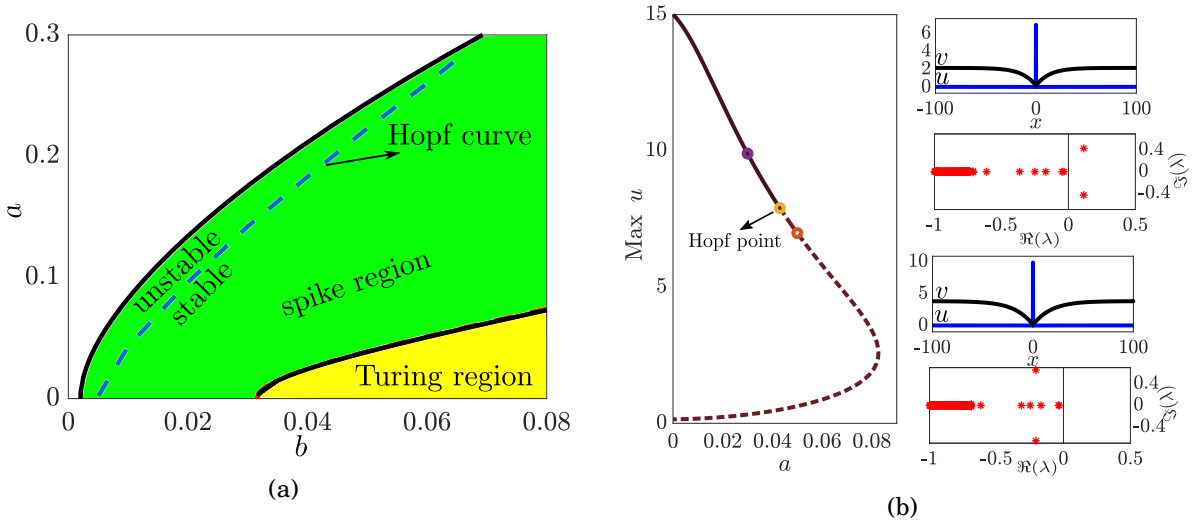

(a) (b)

Figure 3.23: A zoom of the spike region with $\delta = 0.01$ and $d = 0.001$ in the limit $l \to \infty$ for (3.62). (a) The blue curve indicates the Hopf. (b) Bifurcation diagram of vector max u versus a for fixed $b = 0.01$, showing the stable and unstable branches joining at the Hopf point. The insert plots represent solutions and the corresponding linear spectrum stability.

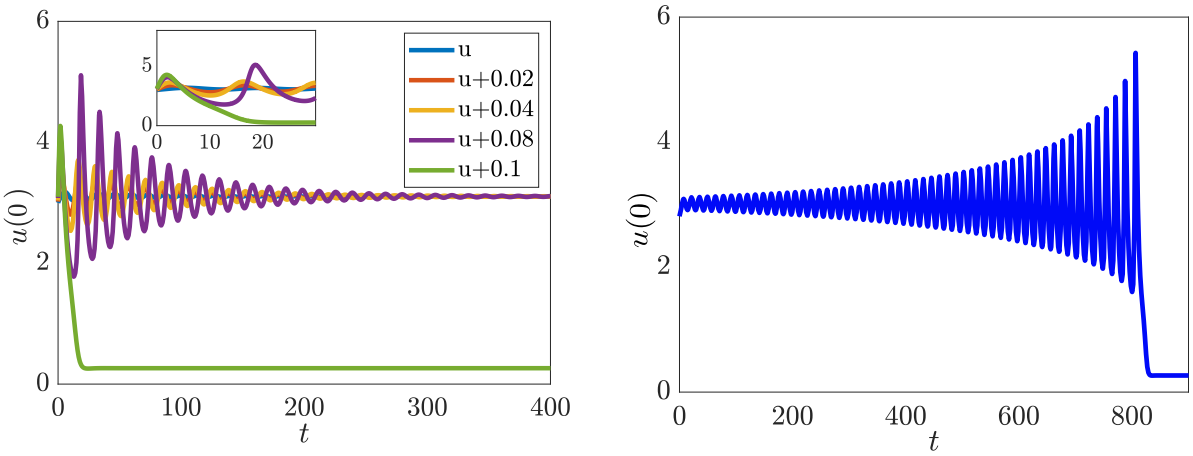

(a) (b)

Figure 3.24: Similar to Figure 3.7 for for Sel'kov-Schnakenberg model (3.62) with fixed $b = 0.09$, $\delta = 0.045$ and two different values of a (a) $a = 0.173$ before the Hopf point and (b) $a = 0.1755$ after the Hopf point.

like protuberances in *Arabidopsis* root surfaces, they imagined that there is a spatial gradient of a parameter that multiplies the parameter we call d and the active u^2v term in the u-equation of (3.1), in order to model the flux of the plant hormone auxin. That model was further studied by Breña-Medina et al [13, 30, 31] and shown to have good agreement with behaviour observed in experiments on both wild type and mutant pants. Moreover, in [32] the spatially homogeneous model is studied, which fits into the framework of the present chapter, see also [102]. Hence, the equations for a root hair cell is given by

$$\frac{\partial u}{\partial t} = dv - cu + vu^2 + \delta^2 \frac{\partial^2 u}{\partial x^2}, \tag{3.68a}$$

$$\frac{\partial v}{\partial t} = b - dv + hu - vu^2 + \frac{\partial^2 v}{\partial x^2}. \tag{3.68b}$$

Clearly, the model (3.68) has a unique homogeneous equilibrium which is given by

$$(u_s, v_s) = \left(\frac{b}{c-h}, \frac{(c-h)cb}{b^2 + d(c-h)^2} \right). \tag{3.69}$$

Applying the linear stability analysis around (3.69) (see section 2.2 for details), we obtain that Turing instability occurs when

$$\left(b^2 + d(c-h)^2\right)^2 \delta^2 + c(c-h)^2 \left(d(c-h)^2 - b^2\right) = -2\delta \left((c-h)\left(b^2 + d(c-h)^2\right)\right)^{3/2}, \tag{3.70}$$

where the critical wave number is

$$k_c = \frac{\left(b^2 + d(c-h)^2\right)^2 \delta^2 + c(c-h)^2 \left(d(c-h)^2 - b^2\right)}{\left(2b^2 + 2d(c-h)^2\right)(c-h)^2 \delta^2}. \tag{3.71}$$

Moreover, the BD transition curve is found to be

$$\left(b^2 + d(c-h)^2\right)^2 \delta^2 + c(c-h)^2 \left(d(c-h)^2 - b^2\right) = 2\delta \left((c-h)\left(b^2 + d(c-h)^2\right)\right)^{3/2}. \tag{3.72}$$

Recalling weakly nonlinear analysis from section 2.3, we find a codimension-two point where the Turing curve changes from sub- to super-critical. Figure 3.25a displays the results of the linear and weakly nonlinear analysis. Also, it represents the localised structures region (snaking and spike) obtained from AUTO. Figures 3.25b and 3.25c show typical behaviours of one-parameter continuation from within the snaking and the spike regions, respectively (recall section 2.5 for details).

Next, we summarise the semi-strong interaction asymptotic analysis for (3.68). By introducing the scale (3.13) with $n = 1$ and $p = 0$ into (3.68), we have the following steady-state problem

$$\delta\rho v - cu + vu^2 + \delta^2 \frac{\partial^2 u}{\partial x^2} = 0, \tag{3.73a}$$

$$\delta\beta - \delta\rho v + hu - vu^2 + \frac{\partial^2 v}{\partial x^2} = 0. \tag{3.73b}$$

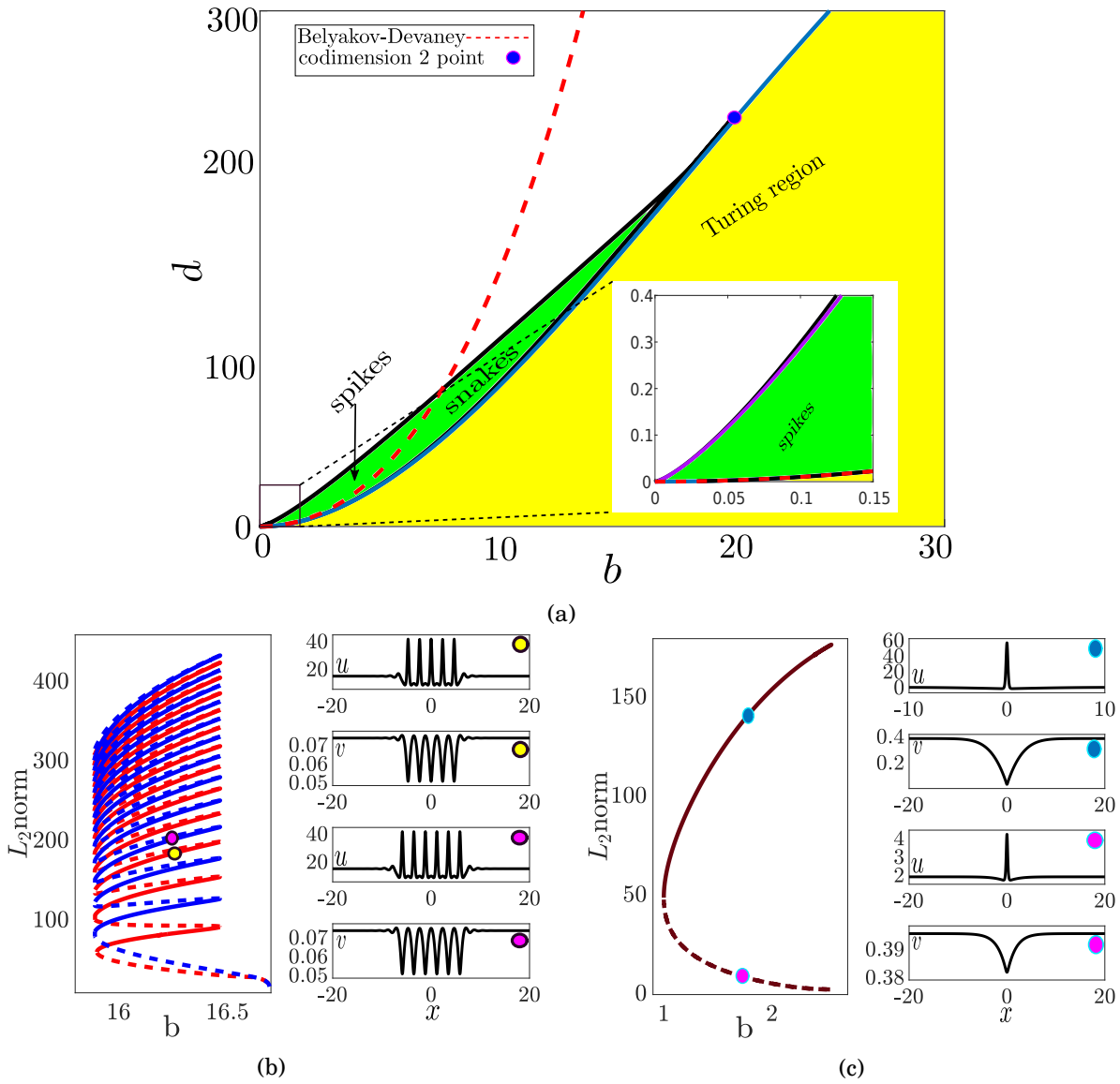

Figure 3.25: (a) Similar to Figure 3.1 for (3.68) with parameters b and d varying and fixed $\delta = 0.01$, $c = 2$ and $h = 1$. (b)-(c) Results of one parameter continuation from the snaking and the spike regions for $d = 149.899$ and $d = 6.099$ as b varies respectively.

In consideration of the scaling established in section 3.1 which is $x = \delta y$ and collecting the leading order terms of δ, the inner solution is given by (3.23).

Next we investigate the outer solutions. Applying the change of variables found in (3.15) to (3.73) with $m = -\frac{1}{2}$ and taking the leading-order term of δ. To obtain a better approximation in the far field, we again rewrite (3.24) with inclusion of additional terms to match the boundary

conditions. Consequently, the solutions for the outer region are given by

$$\hat{u}_0 = \frac{d^2 + d\,(c-h)^2}{c\left(c-h^2\right)}\hat{v}_0, \tag{3.74a}$$

$$\hat{v}_0 = \left(\kappa - \frac{(c-h)\,b\,c}{b^2 + d\,(c-h)^2}\right) e^{-\frac{\sqrt{d(c-h)}\,|z|}{\sqrt{c}}} + \frac{(c-h)\,\beta\,c}{b^2 + d\,(c-h)^2}. \tag{3.74b}$$

Intending to match the inner solutions with the outer solutions, we adopt the procedure in section 3.2.6 . The result is a quadratic equation in κ to solve which reads

$$-2\,\frac{\sqrt{(c-h)\,d}\,\kappa^2}{\sqrt{c}} + 2\,\frac{(c-h)\,b\sqrt{c}\,\sqrt{(c-h)\,d}\,\kappa}{b^2 + d\,(c-h)^2} - 6\,\delta\,\sqrt{c} = 0. \tag{3.75}$$

Consequently, the curve of folds of the localized spikes can be achieved by setting the discriminant of (3.75) to zero:

$$4\,(c-h)^3\,b^2\,c\,d - 48\,\sqrt{(c-h)\,d}\,\delta\left(b^2 + d\,(c-h)^2\right)^2 = 0. \tag{3.76}$$

Figure 3.25a shows the curve given by of (3.76) (pink) compared to the curve obtained from AUTO (black).

To examining the accuracy of the semi-strong method solution we demonstrate in Figure 3.26 a comparison with the numerical result obtained from AUTO for the upper and the lower branches.

In addition, we inspect the stability of solutions. The conclusions of the analysis reveal the appearance of Hopf bifurcation in the left-hand edge of the spike region; see Figure 3.27a. This result is consistent with the results obtained from other generalised Schnakenberg models considered in this chapter. Figure 3.27b shows continuation in d. It is clear that the the fold that connects between the stable single spike solution and unstable single spike happens after the Hopf point. To analyse the criticality of Hopf bifurcation, we apply direct simulation of the full system (3.68). Figure 3.28 illustrates the results of the simulation for two points which are before and after the Hopf point; see Figure 3.27b. For $d = 0.16$, which is before the Hopf point which occurs for $b \approx 0.161$, the spike is stable for small perturbation and collapses for large perturbation as shown in Figure 3.28a. As d is increased to after the Hopf point, we observe that a slight perturbation causes the spike to oscillate with increasing amplitude until it collapses completely back to the homogenous steady state; see Figure 3.28b. Consequently, we conclude that the Hopf bifurcation is subcritical.

3.11 Conclusion

This chapter has demonstrated a certain universality at least in the existence and stability of localised patterns on a long 1D domain, for a range of different activator-inhibitor models that have been proposed in the literature as models for widely different physical processes. For each

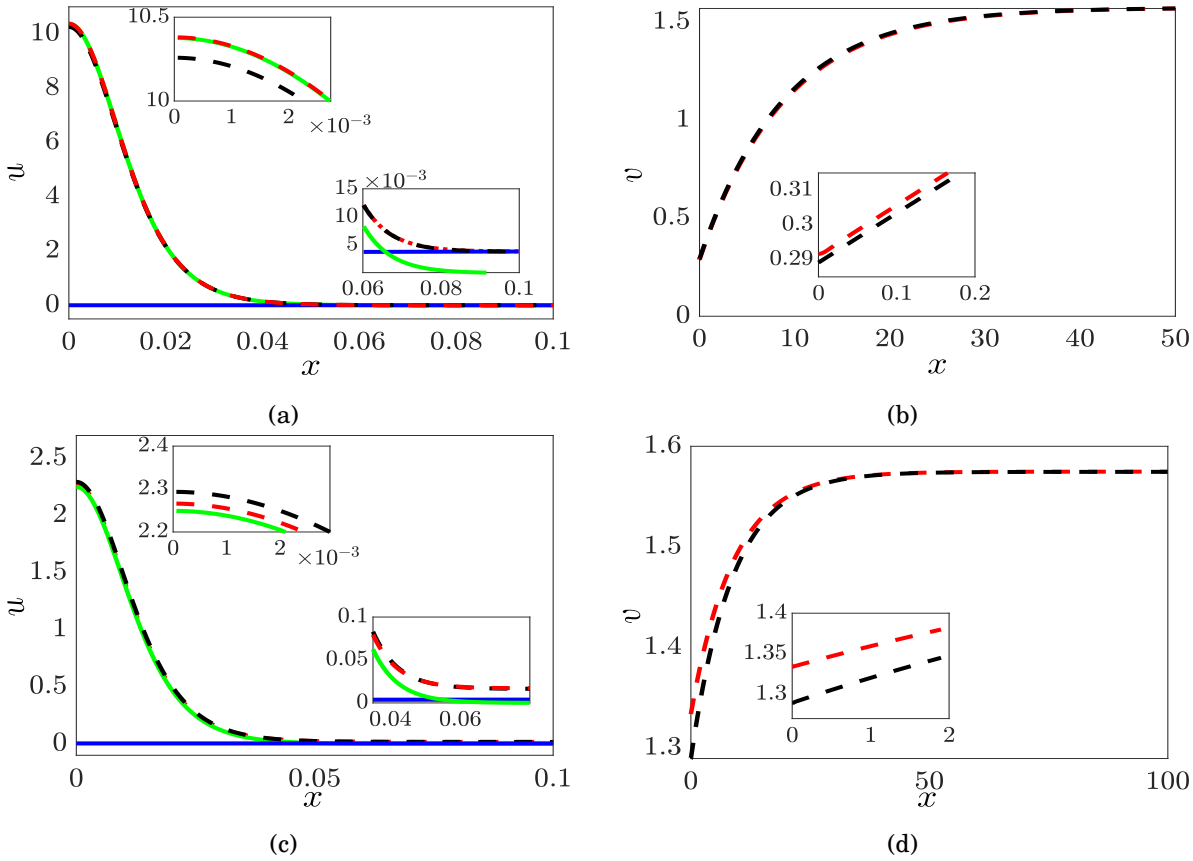

Figure 3.26: Similar to Figure 3.3 but for (3.68) with $a = 0.025$, $b = 0.02$, $c = 2$, $h = 1$, $\delta = 0.01$ and $L = 1000$. (a)-(b) Analytical approximations to solution profiles for $u(x)$ and $v(x)$ respectively, for the upper branch (solid lines) and their numerically obtained counterparts (dashed lines) where $\kappa = 0.28911$. (c)-(d) Solutions for the lower branch plot identically to panels (a)-(b), respectively where $\kappa = 1.33383$.

of these models we find a limit for the constant and linear reaction parameters in which the fundamental pattern-formation or Turing instability becomes subcritical. This creates a bubble in parameter space inside which there are localised patterns that are described by the homoclinic snaking scenario. Upon crossing the BD transition, this region morphs into one in which there are isolated spike solutions that can be captured by weakly nonlinear asymptotic analysis.

A Turing bifurcation is often referred to as a 'diffusion-driven instability' which occurs due to the activator diffusing much more slowly that the inhibitor. Interestingly, the parameter scaling presented in Sec. 3.2.2 shows that neither the presence of the Turing bifurcation nor its transition to sub-criticality and the onset of homoclinic snaking requires the diffusion ratio δ^2 to be small. However, when one considers the temporal stability of these patterns, everything is unstable to a global Hopf bifurcation unless δ is sufficiently small. We have also shown the presence of a breathing Hopf bifurcation and interactions between these two instabilities within the localised pattern regime for intermediate values of δ.

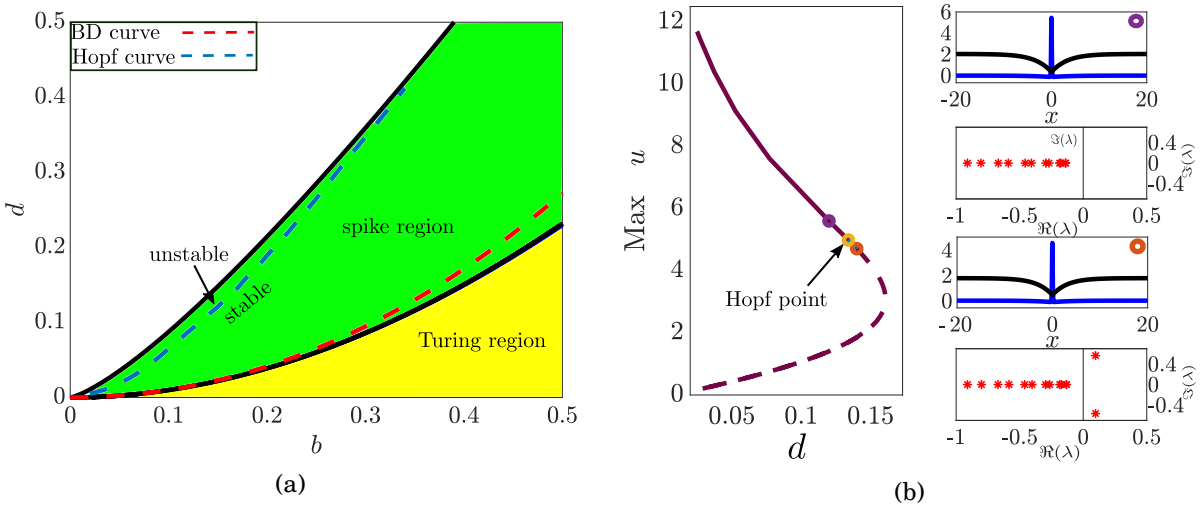

(a) (b)

Figure 3.27: A zoom of the spike region for the root-hair model (3.68) with $\delta = 0.06$, $c = 2$ and $h = 1$ in the limit $l = 100$. (a) The blue curve indicates the Hopf bifurcation. (b) Bifurcation diagram of vector maximum u versus d for fixed $b = 0.16$, showing the stable and unstable branches joining at the Hopf point $d = 0.134$. The insert plots represent solutions and the corresponding linear spectrum stability.

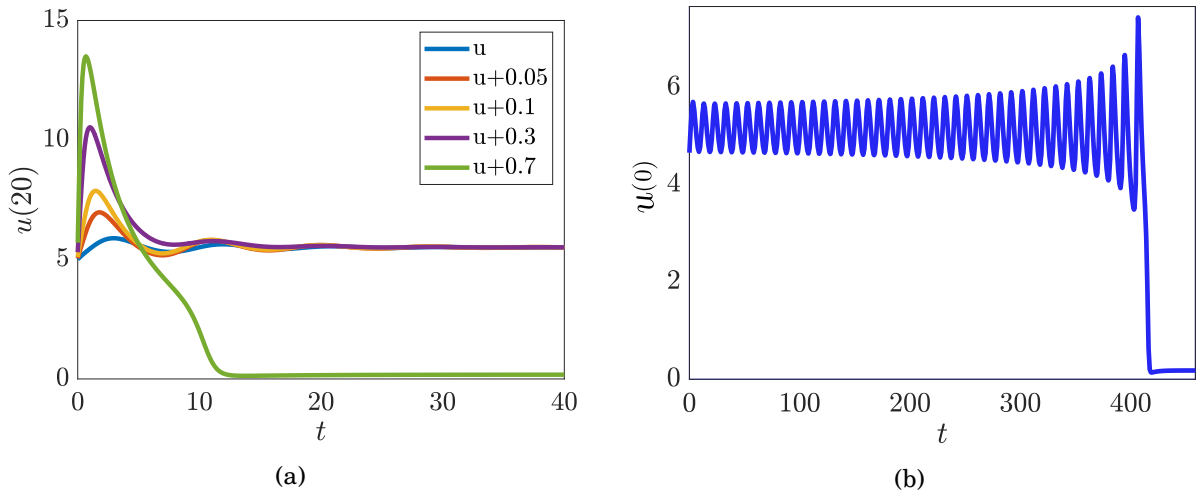

(a) (b)

Figure 3.28: Similar to Figure 3.7 but for the root-hair model (3.68) with fixed $b = 0.18$, $\delta = 0.06$ and two different values of d (a) $d = 0.16$ before the Hopf point and (b) $d = 0.165$ after the Hopf point.

There remains much left to be fully explained. Open questions remain about the seeming transition from sub- to super-criticality of the breathing Hopf bifurcation as δ increases in each of the models. More generally, more is be explained relating to the global dynamics beyond the fold and Hopf instabilities of the different kinds of localised patterns. For example, in [4] there is evidence that both spike replication [56] and spike insertion may occur in the form of the Schnakenberg model investigated there. There may also be subtle differences between the qualitative results for each of the models that we have yet to uncover. Then there is the question of rigorous justification of the results, for example by exploring various limits in which geometric singular perturbation theory approaches may yield fruitful results (see e.g. [58] and references therein). Finally, a big unknown is whether and to what extent the results presented here extend to systems posed in two or three spatial dimensions.

As already mentioned in section 3.1 , bifurcation diagrams that appear qualitatively similar have already been found in other models with more complex nonlinear terms than the simple form (3.1); models for cell polarisation, crime waves, desertification and predator-prey systems [7, 103, 165, 166, 180]. The similarity of the results presented here to the Gierer-Meinhardt system [69] and other model with rational nonlinearity as well as the extension beyond two-component models will be presented in coming chapters. These observations suggest that there may be a more general criterion than the simple $\pm u^2 v$-type activator-inhibitor two-component model that leads to the the kinds of bifurcation structures seen here.

We also mentioned in section 3.1 how the results here do not explain the form of localised structures that have been observed in the Gray-Scott system [66]. Those results are more akin to that seen in the Lugiato-Lefever system and related models that arise in nonlinear optics (see the review by Parra-Rivas *et al* [128]). The key to the bifurcation structures in those systems is the presence of a pair of fold bifurcations of the homogenous steady states, connected by a cusp point in an appropriate parameter plane. The next chapter will consider an explanation of such structures by looking at a homotopy from models of the form considered here to Gray-Scott-like models.

CHAPTER 4

THE GRAY-SCOTT AND GIERER-MEINHARDT CASES

This chapter is based on the publication [3]

4.1 Introduction

In chapter 3, we studied the morphology of localised patterns for a canonical class of activator-inhibitor reaction-diffusion models on infinite one-dimensional domains. Specifically we considered systems of partial differential equations (3.1). There we restricted attention to Schnakenberg-like models that have a unique homogeneous equilibrium, which was guaranteed by setting

$$a + b > 0, \quad h < c, \quad d = j. \tag{4.1}$$

One notable exclusion from the list of models studied in chapter 3 is the much studied system due to Gray and Scott [71]. In its most usual form, this model is equivalent to (3.49) with $a = 0$, $c = 1$, $d = 0$, $h = 0$ and $j > 0$. The system was originally proposed as a minimal model of a cubic autocatalytic process, inspired by the famous Belyousov-Zhabotinsky chemical reaction. The system is known to display complex spatio-temporal dynamics, see e.g. [56, 123]. Recent results by Gandhi *et al* [66] have provided a detailed study of the existence and stability of periodic and localised patterns when this model is posed on a long interval. The bifurcation diagrams found there are much more reminiscent of those for the Lugiato-Lefever equation, see e.g. [127–129]. In particular, there is a bistability region between homogeneous steady states, and both peak-like and hole-like localised patterns can occur. This bifurcation diagram is very different from that of that Schnakenberg-like models considered in chapter 3 .

The natural question, which we address here then is: given the subtle differences in the functional form of the Gray-Scott model to Schnakenberg-like models, how does one bifurcation diagram morph into the other? The main novelty of the present chapter is to tackle this question

head on by studying the sequence of codimension-two bifurcations that occur under such a homotopy. To point to the possible genericity of such bifurcations, we also consider an analgous sequence of bifurcations for two different cases of the widely studied Gierer-Meinhardt model, one with and one without bi-stability between homogeneous steady states.

The rest of the chapter is outlined as follows. Section 4.2 concerns results for a generalisation of the Gray-Scott system which contains a homotopy parameter r that transforms the Gray-Scott model (when $r = 1$) into the simple glycolysis model (when $r = 0$). Starting from $r = 0$ we use numerical continuation and spectral computations to produce a detailed set of one- and two-parameter bifurcation diagrams for homogeneous and localised patterns to describe how the universal bifurcation diagram morphs into the more complex one for the Gray-Scott model. Section 4.3 describes the same process for the more complex Gierer Meinhardt model, which has a rational nonlinearity. Here the case where the feed term is in the active field leads to a single homogeneous equilibrium and the 2-parameter bifurcation diagram of localised structures is found to be qualitatively the same as the glycolysis model. In contrast, when the feed term is in the inhibitor field, there is bistability between homogeneous equilibria and the bifurcation structure of localised solutions is Gray-Scott like. We again show the process of how these two extremes morph into each other via a case with feed terms in both activator and inhibitor fields. The results show many similarities, and some differences with those in section 4.2. Finally section 4.4 draws conclusions, discusses possible biological implications of the results and suggests avenues for future work.

4.2 A generalised Gray-Scott system

We study localised patterns arising in the following model written in the form :

$$u_t = d(1-r)v - u + u^2 v + \delta^2 u_{xx}, \tag{4.2a}$$

$$v_t = b - dv - u^2 v + v_{xx}, \tag{4.2b}$$

where all parameters b, d, r and δ are assumed positive. Note this system (4.2) satisfies (4.1) only when $r = 0$, in which case we recover the glycolysis model. When $r = 1$ we recover the usual form of the Gray-Scott model, see e.g. [66]. Therefore, we treat r as a homotopy parameter that interpolates between the two models.

4.2.1 Preliminaries

We begin by studying homogeneous steady state (HSS) solutions. These are found by setting both spatial and time derivatives to be zero in (4.2). Consequently, we have

$$v_s = \frac{b}{u_s^2 + d},$$

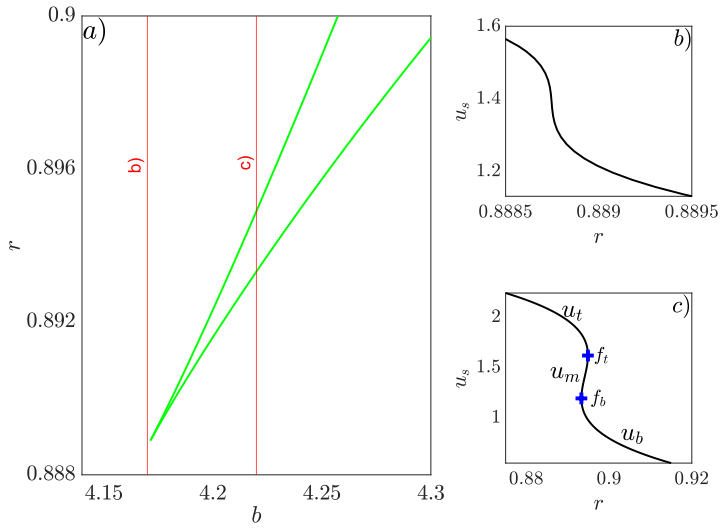

Figure 4.1: (a) Bifurcation diagram in the (b,r)-plane with $d = 5.6$ for homogeneous steady states of (4.3), showing the location of a pair of fold bifurcations connected via a cusp. (b,c) One-parameter slices along the red lines indicated in (a), for (b) $b = 4.17$ and (c) $b = 4.22$. In (c), $u_t > u_m > u_b$ refer to the u-values of the top, middle and bottom steady states and f_t and f_b to the fold points.

where u_s satisfies the following cubic equation

$$Z(u_s,b,d,r) =: u_s^3 - bu_s^2 + du_s + bd(r-1) = 0. \tag{4.3}$$

If Z is monotonic in u_s, then there is a unique solution. In contrast, if there there is pair of turning points, then there are three distinct HSSs. By looking at the discriminant of (4.3) we can determine the location of a cusp point at $r = \frac{8}{9}$, $b = \sqrt{d}$. Moreover for $r < \frac{8}{9}$ there is a unique equilibrium and for $r > \frac{8}{9}$ there are two folds, with u-values at

$$u_{t,b} = \frac{b \pm \sqrt{b^2 - 3d}}{3}, \tag{4.4}$$

see Figure. 4.1.

In addition, each steady state can in principle undergo a steady-state pattern-formation bifurcation, with wavenumber k, which can by found by substituting the ansatz (2.7) into (4.2) and neglecting nonlinear terms. Consequently, we obtain the dispersion relation (2.9) from which we seek critical wavenumbers k_c under the conditions (2.11). Such conditions are said to lead to a Turing *instability* upon variation of a parameter if the underlying HSS against homogeneous perturbations. Applying the conditions (2.11) to (2.9) gives analytical expressions for Turing instability and the critical wavenumber, respectively:

$$\delta^2\left(u_s^2+d\right)^2 + u_s(u_s-2b) + d = -2\delta\sqrt{\left(u_s^2+d\right)\left(\left(u_s^2+d\right)^2 - 2u_s dbr\right)}, \tag{4.5a}$$

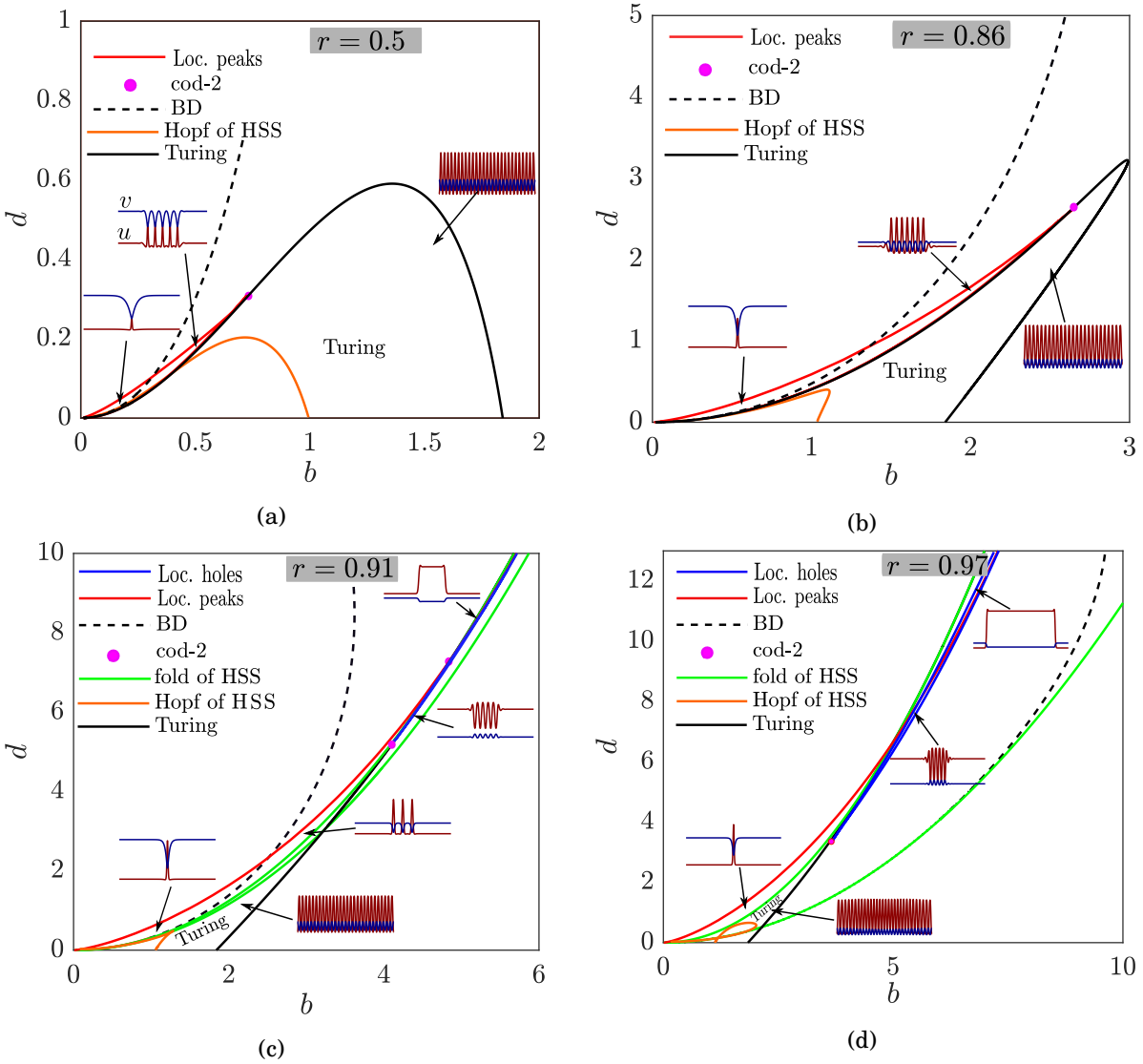

Figure 4.2: Bifurcation diagram in the (b,d)-plane for (4.2) showing numerically determined regions of pattern solutions for $\delta = 0.225$ and (a) $r = 0.5$, (b) $r = 0.86$, (c) $r = 0.91$ and (d) $r = 0.97$. See text for further explanation.

and

$$k_c^2 = -\frac{\delta^2\left(u_s^2+d\right)^2 + u_s(u_s-2b)+d}{2\delta^2\left(u_s^2+d\right)}. \tag{4.5b}$$

Crucial to the development of localised patterns is also the identification of codimension-two points where Turing instabilities change from being super- to sub-critical. These points can be identified using weakly nonlinear analysis [61, 76] using the procedure outlined in 2.3, which we have implemented using the computer algebra software Maple.

For the rest of this section we shall take a fixed value of $\delta = 0.225$ and consider b and d to be the main bifurcation parameters, with r a homotopy parameter.

4.2.2 (b,d)-bifurcation diagrams

Figure 4.2 shows a summary of the (b,d)-bifurcation diagram for HSS, periodic and localised structures, for four different values of r. The location of Turing bifurcations and super-to-sub codimension-two points are indicated; in all cases the sub-critical Turing bifurcation occurs for smaller b and d values.

Another important transition, depicted by a black dashed line in Figure. 4.2, is a so-called Belyakov-Devaney transition (BD) which occurs under the same algebraic condition as a Turing bifurcation but with a pure imaginary critical wavenumber. This corresponds to a double real eigenvalue in the spatial dynamics. That is, for b-values to the left of the BD line any localised structure will have monotonically decaying tails in the far field, whereas to the right of the line the tails will decay in an oscillatory manner. The significance of this line is that it marks the boundary between a region where there is a multiplicity of localised patterns (with oscillatory tails) and where we should expect to see isolated spikes (with monotonic tails); see [166] for details on unfolding this transition.

Note that for the chosen value of δ, any temporal Hopf bifurcations are found to occur only for small values of b and d, and so they do not affect the majority of the dynamics we present here. A curve of global (i.e. with spatial wavenumber 0) Hopf bifurcations is represented by an orange curve in Figure4.2. The bifurcation is found to be supercritical with stable periodic motion existing below this curve.

Let us briefly describe the qualitative transitions to the bifurcation structures with r that are illustrated in Figure 4.2. Figure 4.2a shows the (b,d)-bifurcation diagram for $r = 0.5$, which is typical of all $r < \frac{8}{9}$. For these parameter values there is a unique HSS and the two-parameter diagram is like each of the models studied in chapter 3 (see also [166] for other models that display the same broad bifurcation diagram). In particular we note the wedged shaped region inside which localised structures occur, which emanates from the codimension-two Turing bifurcation, as described by the theory of homoclinic snaking; see [89] for a review. This region is bounded by fold bifurcations of the localised states, which are indicated in the figure by red curves. The

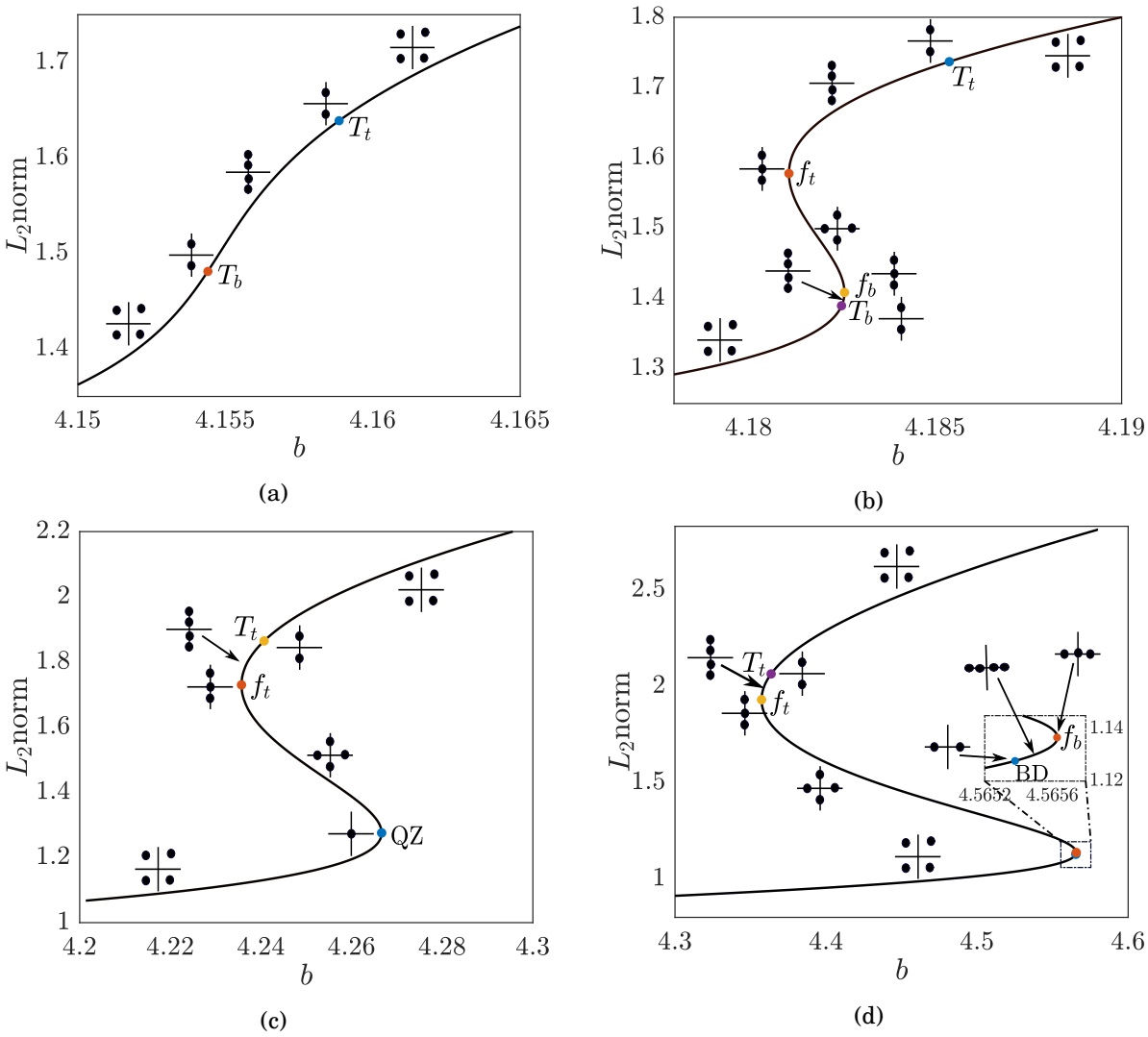

Figure 4.3: Bifurcation diagram of homogeneous steady states and their spatial eigenvalue configuration for fixed $d = 5.8$, $\delta = 0.225$ and four different values of r as b varies. The ordinate in this an subsequent one-parameter bifurcation diagrams is the usual vector L_2-norm= $\sqrt{\frac{1}{l}\int_0^l \left(u^2(x)+u_x^2(x)+v^2(x)+v_x^2(x)\right)dx}$ which is used by AUTO. (a) $r = 0.8871$, (b) $r = 0.89$, (c) $r = 0.897$ and (d) $r = 0.915$. Here T_t and T_b stand for Turing bifurcation associated with the top and bottom states, respectively.

legend refers to these folds as bounding the region of so-called localised peak solutions, because the u-component of these localised structures have positive maxima that are above the value of the background HSS.

Figure 4.2b for $r = 0.86$, which is marginly less than $\frac{8}{9}$, shows that the bifurcation diagram remains topologically the same, but the codimension-two Turing bifurcation and consequent localised-pattern region now extend to higher d-values. The Turing region in which there are periodic patterns becomes somewhat narrower in the process.

Figure 4.2c for $r = 0.91$, which is marginly greater than $\frac{8}{9}$ shows a rather different bifurcation diagram. Now there is a region, bounded by the two green curves in which there is bistability between two HSSs, we shall refer to these with the subscripts t for top and b for bottom, corresponding to their u-values. We also find a second codimension-two point Turing bifurcation, for d-values above which we find a region of localised hole solutions. For yet larger d, we also find that the region of existence of both peak and hole solutions is very thin and occurs in the neighbourhood of a certain curve on which there exists a heteroclinic cycle, a stationary pair of front and back solutions connecting the stable HSSs.

Figure 4.2d, for $r = 0.97$ shows yet more topological differences. Now there is only one codimension-two Turing bifurcation, which leads to hole solutions, and the peak solutions are now being born close to the fold of the lower HSS rather than at a Turing bifurcation. This diagram is qualitatively the same as for the Gray-Scott case, $r = 1$, as described in [66].

4.2.3 (b,r)-bifurcation diagrams

Clearly there are a complex sequence of transitions that occur between $r \approx 0.86$ and 0.97. The particular projection into the (b,d)-plane though does not ease the understanding of the particular bifurcations and solution structures involved. Hence we shall now look at some bifurcation diagrams as b-varies for fixed d. We choose to illustrate the case $d = 5.8$.

A key distinction between Figures 4.2c and 4.2d is what has happened to the BD line. For $r = 0.91$ this extends almost to the origin in the (b,d)-plane, whereas for $r = 0.97$ it appears to end along the right-most fold of HSSs, which is f_b. To illustrate what is happening to bifurcations of HSSs, Figure 4.3 presents one-parameter bifurcation diagrams with for four different values of $r \in (0.88, 0.92)$. Also shown in each panel are the spatial eigenvalues; that is eigenvalues $\sigma = ik$ obtained by substitution of the form (2.7) with $\lambda = 0$. Note that a Turing bifurcation corresponds to double imaginary eigenvalues $\sigma = \pm i\omega$, and a BD transition to a double real pair $\pm\sigma$. Temporal stability is implied by all four eigenvalues being pure imaginary.

Panel 4.3a shows the monostable regime of HSSs. Here, the spatial eigenvalues are initially complex conjugate before hitting the first Turing bifurcation T_b where they become pure imaginary. There is a second Turing at T_t when they become complex conjugate again. Panel 4.3b, shows the familiar S-shaped curve that occurs after transition through the cusp, where the three steady states – which we refer to as (u_b, v_b), (u_m, v_m) and (u_t, y_t) for bottom, middle and top – are connected through a pair of folds. One Turing bifurcation is associated with both the bottom branch and one with the top. Panel 4.3c shows how the bottom Turing bifurcation collides with the lower fold. This is form of Takens-Bogdanov bifurcation for reversible systems, which we refer to as a quadruple zero point (labelled QZ). For slightly higher r-values (panel 4.3d) the lower Turing bifurcation has been destroyed and a BD transition emerges onto the lower branch. The upper Turing bifurcation is unaffected and we find that this persists at least up until $r = 1$.

It seems these changes to the local bifurcation structure of the HSSs as r increases have a

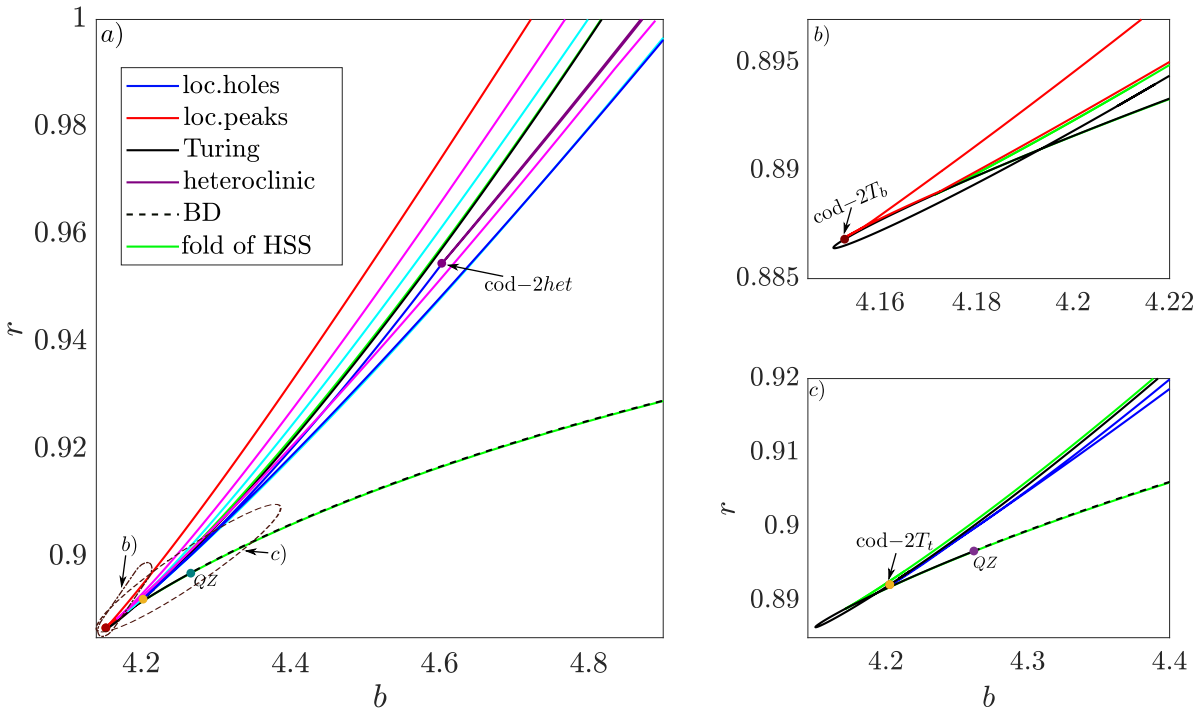

Figure 4.4: (a) Bifurcation diagram in the (b,r)-plane for (4.2) showing numerically determined regions of pattern solutions for $d = 5.8$ and $\delta = 0.225$. The red and blue lines represent the outer folds of the snaking curves of localised structures of peak and hole type respectively. Cyan and magenta lines are additional folds in the snaking region; the significance of these and all other curves are described in the text. (b,c) Zooms in the vicinity of the cusp point showing (b) only bifurcations involving peak solutions and (c) only those involving hole solutions. See text for further details.

profound effect on various global bifurcations of the spatial dynamical system. We have illustrated some of these effects in Figure 4.4, which gives an overview of various codimension-one and -two bifurcations in the (b,r)-plane for $r > 0.88$. Even with the two zooms near the cusp point, it is not clear how to understand the bifurcation diagrams. So, in the next two subsections we discuss in detail various one-parameter slices for fixed r.

4.2.4 Snaking structures of localised peak solutions

In the main panel of Figure 4.4 there are some additional curves, coloured magenta and and cyan that are not labelled in the legend. These are additional fold curves of peak-like localised patterns. To understand the genesis and significance of these additional folds, we present a further zoom in Figure 4.5, which indicates three separate values of r for which one-parameter bifurcation diagrams are presented in Figures 4.6–4.8.

Figure 4.6 shows the situation for peak-like solutions that pertains for all $r < 0.8885$. From the Turing bifurcation T_b there emerges two curves of localised patterns which snake in a sequence of folds to form the usual homoclinic snaking structure. Each successive pair of folds on each

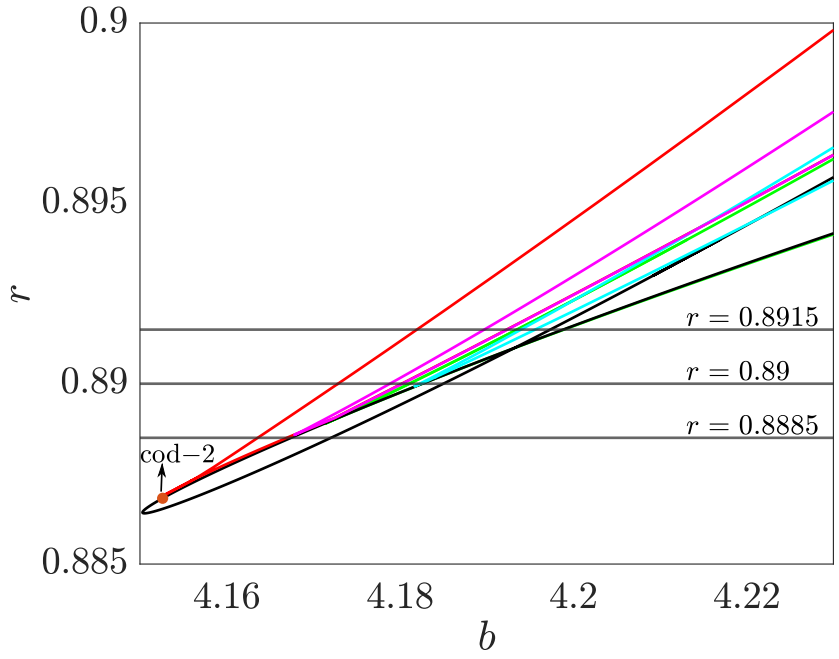

Figure 4.5: Zoom of the localised peak solution bifurcation diagram in the (b,r)-plane for the model (4.2) displaying numerically determined regions of pattern solutions for $d = 5.8$ and $\delta = 0.225$ of the peak solution. See Figure 4.4 for definition of each curve type.

branch creates a stable multi-humped pattern with one additional hump. Eventually the localised structures fill the whole domain. This homoclinic snaking bifurcation structure is similar to that seen in many other pattern-formation systems such as the Swift-Hohenberg equation [33, 89].

Figures 4.7 and 4.8 give more detail on the genesis of the magenta lines in Fig. 4.4, these are an additional pair of folds within the homoclinic snaking region which occur for higher r-values.

First, Figure 4.7, which is for an r-value 0.03 higher than in Figure 4.6, indicates increased complexity in the branch of simplest periodic orbits arising from the Turing bifurcation T_b. As indicated, there is a more complex bifurcation sequence including a pair of folds and a reverse period-doubling bifurcation. We have indicated regions of stable periodic orbits by thick red lines. Note the different spatial wavelengths of the periodic structures indicated in panels (b) and (e). It seems that the central core of the localised patterns within the homoclinic snake are the double-wavelength period orbits (b), which originate from T_b rather than the shorter wavelength orbits (e) that originate from T_t.

We also note that for the r-value depicted in Figure 4.7, that the lowest branches of the homoclinic snake have developed an extra kink, consisting of a pair of folds. These folds are represented by the magenta lines in Figure 4.4. The higher meanders of the snake also display kinks, which appear closer to cusp points. Each is on the verge of creating an additionl pair of folds for a marginally higher r-value. The localised states beyond each kink (such as in panels (g) and (i)) are all found to be unstable. It is interesting to note also that the cusp point of HSSs

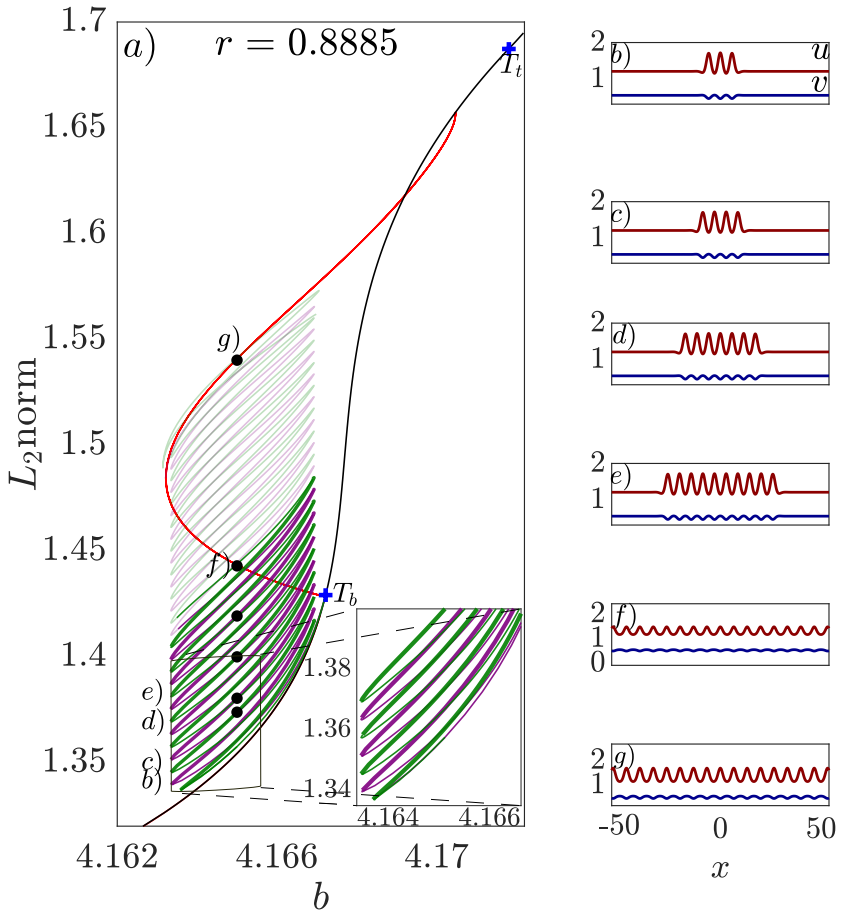

Figure 4.6: (a) One-parameter bifurcation diagram showing peak-like localised patterns and the simplest periodic pattern born at the subcritical Turing bifurcation for $r = 0.8885$, $d = 5.8$ and $\delta = 0.225$. In this and subsequent figures stability of localised structures is indicated by a thick line (and instability by a thin line), with a purple line colour used to indicate states with an even number of large maxima, and green used to indicate those with an odd number. Some lines are depicted with increased opacity for ease of illustration. Panels (b)-(g) show solution profiles at the labelled points.

happens between the two r-values in Figures 4.6 and 4.7, but it is not clear if the additional complexity of localised structures in Figure 4.7 is associated with the bistability of HSSs or not.

Figure 4.8 is for an r-value that is 0.015 higher than that in Figure 4.7. It shows the genesis of the additional pair of folds in the localised structures represented by the cyan lines in Figure 4.5. First, note that the previously observed kink in the snaking bifurcation diagram is now clear in each meander of the folds. For higher b-values though, there is more complex structure, whose outer folds are represented by the cyan lines in Figure 4.5. Instead of reaching a simple right-hand fold, each meander of the snake now collides with another snaking structure, which represents localised patterns whose core is the shorter-wavelength periodic pattern in panel (e). Note though that these more complex mixed-mode localised patterns (as in panels (g) and (k))

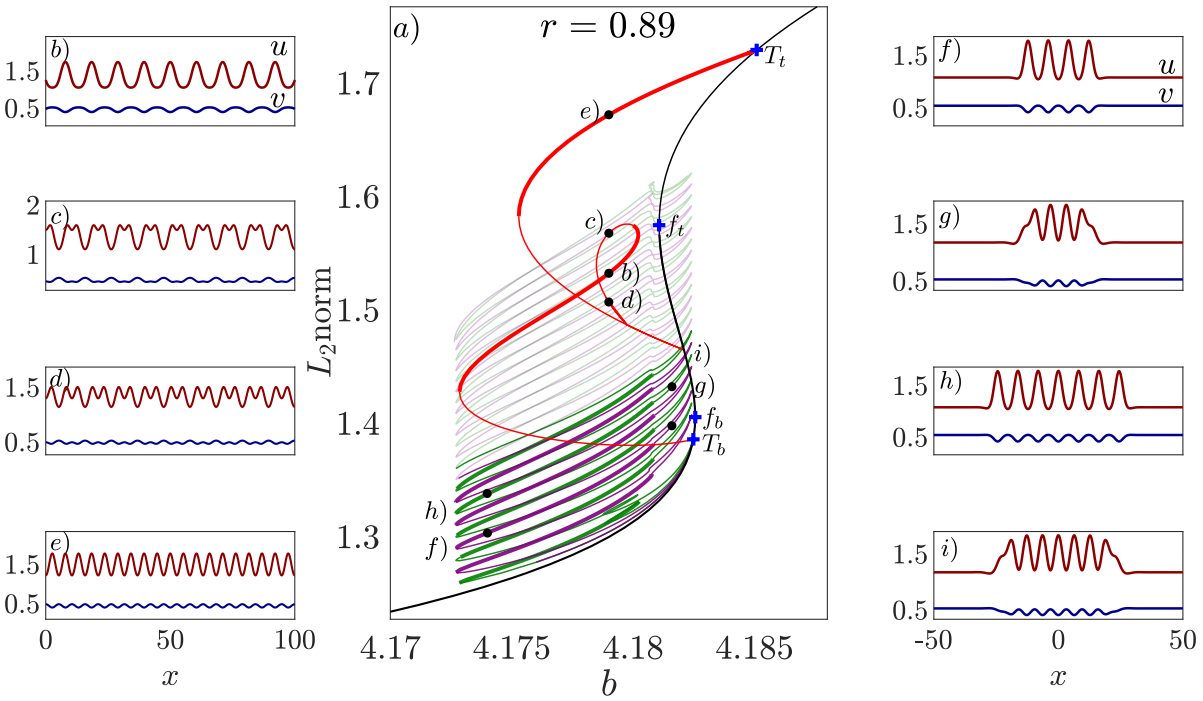

Figure 4.7: Similar to Fig. 4.6 but for $r = 0.89$.

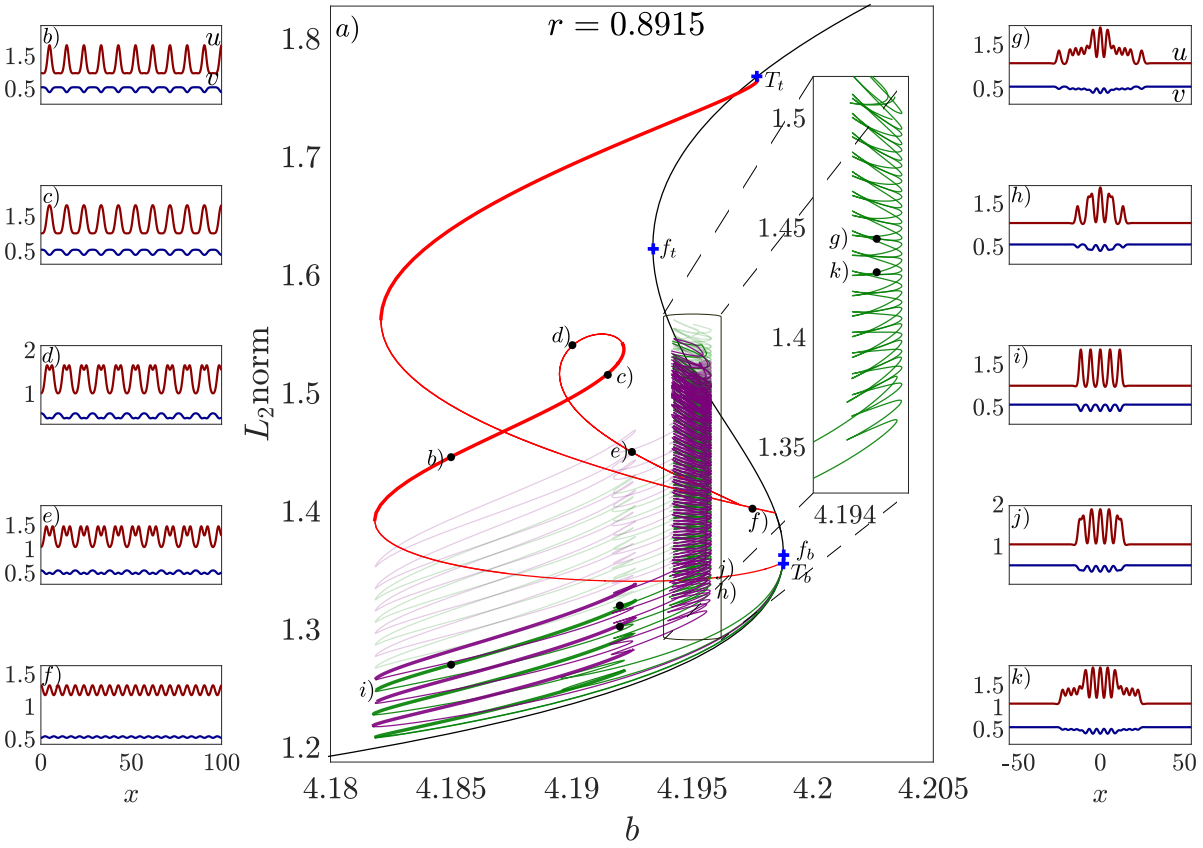

Figure 4.8: Similar to Fig. 4.6 but for $r = 0.8915$.

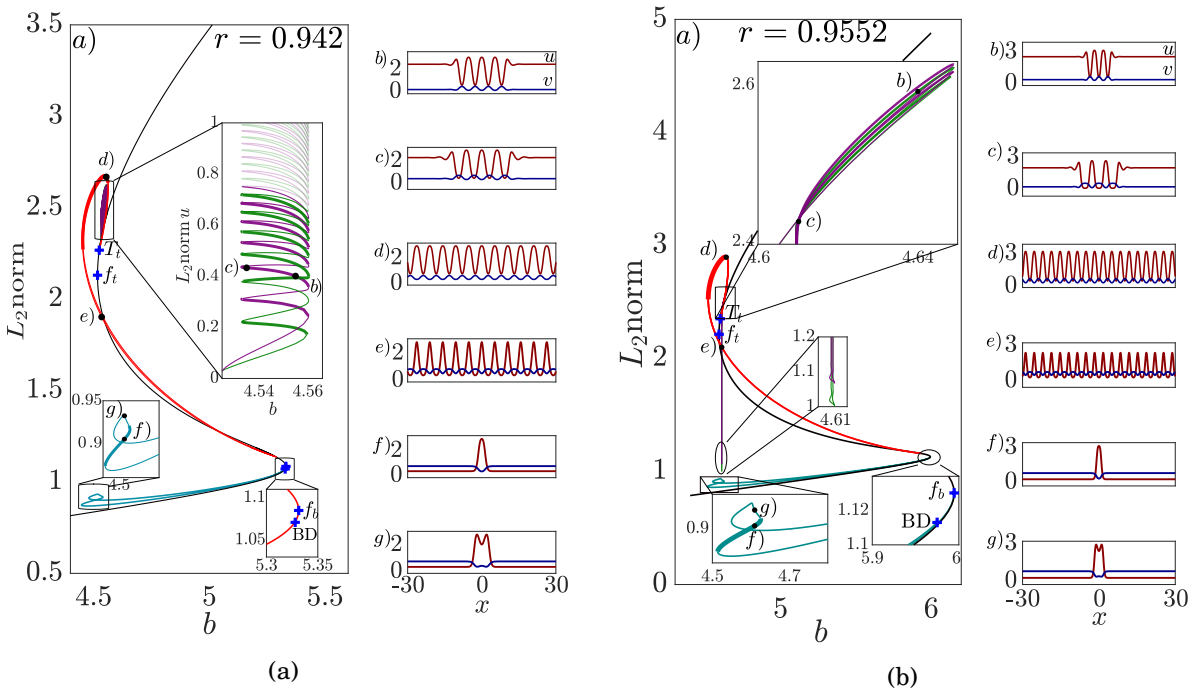

Figure 4.9: Two one-parameter bifurcation diagrams of localised structures for $d = 5.8$ and $\delta = 0.225$ and (a) $r = 0.942$ and (b) $r = 0.9552$.

are all unstable.

4.2.5 Localised holes and a heteroclinic connection

Figures 4.9 and 4.10 show slices for higher r-values. These r-values are all beyond the value of the QZ point at f_b, and the peak solutions no longer have oscillatory tails. Instead of snaking, these localised structures lie on S-shaped isolas whose right-hand folds are very close to the BD point. A similar process of transition of localised structures near a QZ point was described for the Lugiato-Lefever equation in [127, 128].

Figure 4.9a shows what happens to the hole solutions that are born at T_t which is typical for all r-values beyond which the Turing bifurcation becomes subcritical (at $r = 0.8922$ as depicted in Figure 4.4(c)). The localised patterns lie on a snaking structure, albeit one that occupies a narrow window of b-values. For the slightly larger r, as in Figure 4.9b, close to the left-hand fold on each meander of the snake, the periodic pattern in the core of the snake gets much wider, as it appears to be approaching the value of the lower HSS. This can be seen by a dramatic drop in the L_2-norm close to these folds. In terms of its norm-value the hole-solution branch almost seems to be reaching out to almost touch the peak solution.

Figure 4.10 shows what has happened. Specifically, it is found that for $r > 0.9552$ there is a heteroclinic connection between the top and bottom HSSs. Regions of both peak and hole solutions are bounded by this heteroclinic connection. Thus, following the hole solution branch that is born

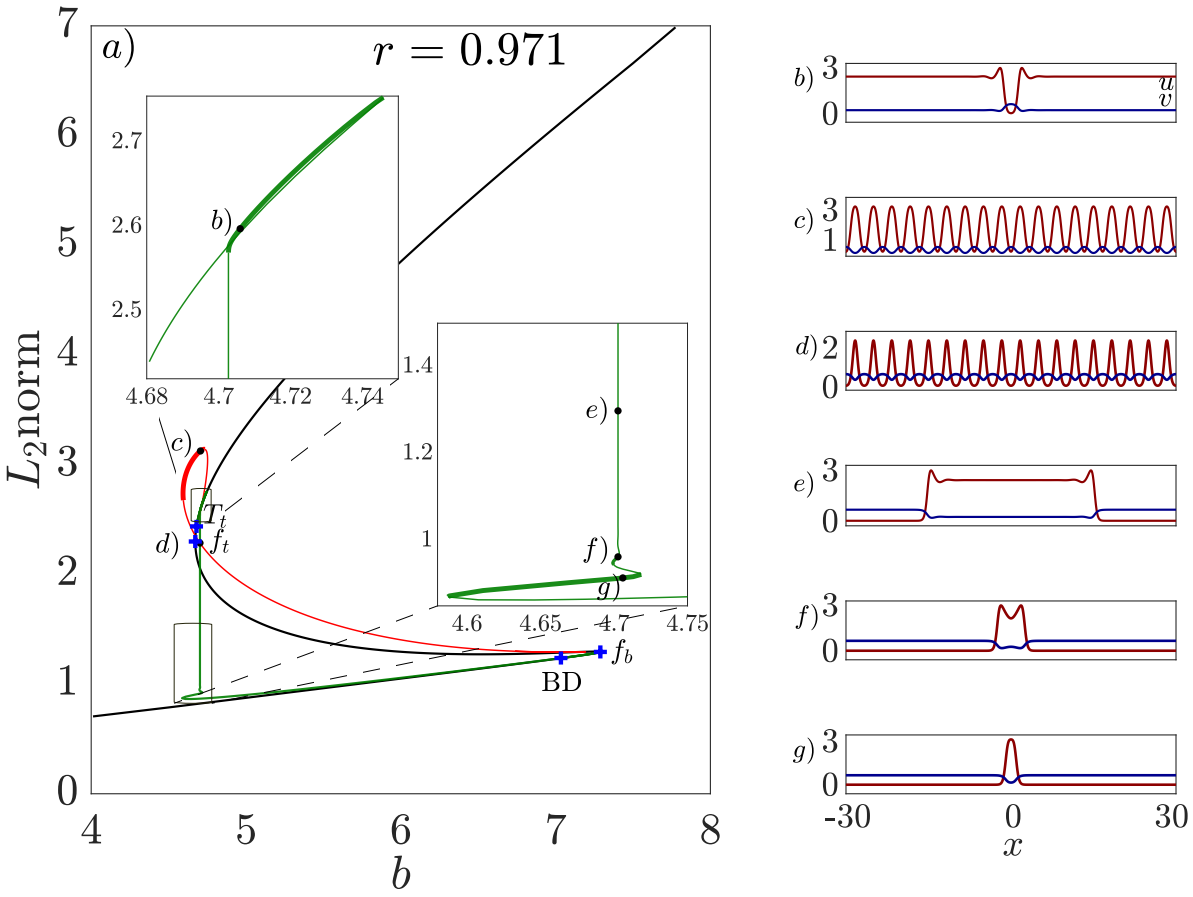

Figure 4.10: Similar to Fig. 4.9 but for $r = 0.971$.

at T_t, we find only a single humped solution, whose stable existence region is bounded by a fold for large b and the heteroclinic connection for small b. In contrast, the zoom in Figure 4.10 shows that the stable single-hump is actually bounded by a fold for both left and right b-values. This kind of structure has been referred to as collapsed snaking (see e.g. [128]).

The bifurcation diagram in Figure 4.10 is now qualitatively unchanged as we increase r up to the Gray-Scott case $r = 1$. It is clear that the final transition on increasing r then is the one that occurs at $r \approx 0.9552$. This appears to be where a heteroclinic loop is created. We conjecture that this codimension-two heteroclinic bifurcation can be explained using spatial dynamics, as being caused by a tangency between the two-dimensional stable manifold of the top HSS and the two-dimensional unstable manifold of the bottom HSS (and vice versa, due to spatial reversibility).

4.3 Gierer-Meinhardt model

We shall now study another well-studied activator-inhibitor model due to Gierer and Meinhardt [69]. This model has a rather different functional form than the Schnakenberg-like models we

have studied so far. The inhibition in the model comes not from depletion of an autocatalytic field u, but from the production of v which acts as an inhibitor of a quadratic activation process.

Nevertheless, it has been shown in previous works, e.g. [83, 169, 178], that the Gierer-Meinhardt model has localised patterns. Here we shall show that the Gierer-Meinhardt model contains bifurcation structures for localised patterns that qualitatively like either the case $r = 0$ or $r = 1$ in (4.2), depending on whether the constant feed term is in the activator or the inhibitor. Indeed, interpolating between these two cases we will find leads to a similar set of transitions.

The one-dimensional Gierer-Meinhardt model can be written in the form

$$\frac{\partial u}{\partial t} = a + \frac{u^2}{v} - u + \delta^2 \frac{\partial^2 u}{\partial x^2} \tag{4.6a}$$

$$\frac{\partial v}{\partial t} = b + u^2 - dv + \frac{\partial^2 v}{\partial x^2}, \tag{4.6b}$$

where $a, b \geq 0$ and $d, \delta > 0$ are free parameters. In what follows we shall ignore the singular case $a = b = 0$ and consider separately in the following two subsections, the cases $b = 0$ and $b > 0$. The results are intended to be illustrative rather than comprehensive. We shall assume the same spatial boundary conditions and use the same methodology to study it as we did for the generalised Gray-Scott model in Sec. 4.2.

4.3.1 The case $b = 0$

Under the restriction $b = 0$ with $d > 0$, so that there is a constant production term only in the inhibitor field, then there is a unique HSS of (4.6) (u_s, v_s) given by

$$u_s = a + d, \qquad v_s = \frac{(a+d)^2}{d}.$$

Performing the usual linear stability analysis around this equilibrium we find that the Turing instability and the critical wavenumber are given by

$$b\delta^2(a+d) + a - d = -2\sqrt{d}\,(a+d)\delta, \quad k_c = -\frac{d\delta^2(a+d) + a - d}{2(a+d)\delta^2}. \tag{4.7}$$

Additionally, the Belyakov-Devaney line occurs for

$$d\delta^2(a+d) + a - d = 2\sqrt{d}\,(a+d)\delta. \tag{4.8}$$

The curves (4.7) and (4.8) are depicted in Figure 4.11a along with curves of folds of localised structures. We find a curve in the (a, d) upon which a Turing bifurcation occurs (blue line). This undergoes a codimension-two super-to-subcritical transition (at the blue spot). From this point emerges a region (shaded green) of localised structures that is bounded by two fold bifurcation curves of localised states (black lines). This green region is divided in two by the BD line. The upper part of this region features homoclinic snaking, that is two intertwined branch of localised structures with an increasing number of spikes (see Figure 4.11b) Below the BD line there is

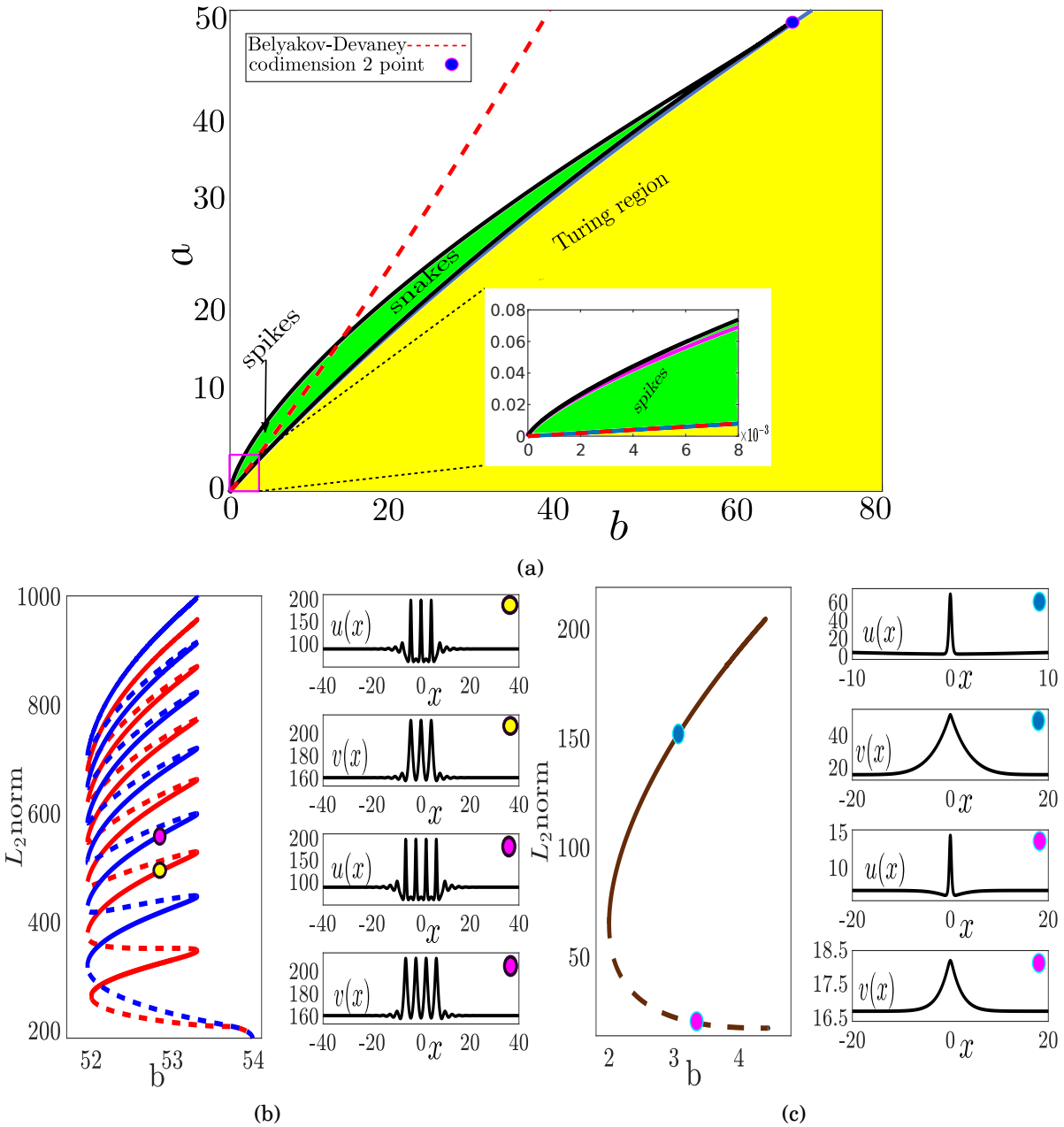

Figure 4.11: (a) The (b,a) plane for (4.6) with fixed $\delta = 0.01$ and $b = 0$. The yellow region presents the Turing instability and the green region expresses the localised structure that is obtained by AUTO. The circle marks the codimension two point and the red dashed line present the Belyakov-Devaney transition. (b) Bifurcation digram shows the the snaking ladder structure and samples of localized solution that are marks in the snaking with fixing $a = 39.7170$ as b varies. The continuous (dashed) line indicates stable (unstable) solutions where the blue (red) line is the odd (even) solution branch. (c) The one parameter continuation a long b in the spike region with fixing $a = 4.08804$. The panel to the right show example from the upper and lower branch indicated by light blue and magenta respectively

a single isolated stable spike (see Figure 4.11c). The spike regime is bounded on the left by a fold and on the right by where the background state undergoes the BD transition and the spike becomes delocalised. (Note that the seemingly large amplitudes of the u and v fields in the inset solution profiles in Figure 4.11b and 4.11c can be rescaled to be $\mathcal{O}(1)$ by other choices of dimensionless parameters).

Note that the bifurcation in Figure 4.11a is qualitatively the same as the universal one found in chapter 3 for Schnakenberg-like systems (3.1) subject to (3.6) so that they have a unique HSS. In chapter 3 we showed that the outer fold of the single spike on an infinite domain can be captured using the semi-strong asymptotic method due to Ward and collaborators (see e.g. [83, 168]). We shall now show that this analysis also extends to the Gierer-Meinhardt model, specifically in the limit that δ, a and d are small.

Following the method in Chapter 3, we start with the assumption that the parameters a and d are small and scaled according to

$$a = \delta\alpha, \quad d = \delta^2\beta.$$

Upon substituting the above rescaled parameters into (4.6) and considering only steady solutions, we have

$$\delta\alpha + \frac{u^2}{v} - u + \delta^2\frac{\partial^2 u}{\partial x^2} = 0, \quad x \in \mathbb{R}, \tag{4.9a}$$

$$u^2 - \delta^2\beta v + \frac{\partial^2 v}{\partial x^2} = 0, \quad x \in \mathbb{R}. \tag{4.9b}$$

We next introduce an inner scaling for (4.9) via setting

$$u = \overline{u}, \quad v = \overline{v}, \quad x = \delta y$$

and considering only leading-order terms in δ. The inner solution so-obtained is

$$\bar{v}(y) = \bar{v}(0) = \text{constant} := \kappa, \tag{4.10a}$$

$$\bar{u}(y) = \frac{3\kappa}{2}\operatorname{sech}^2\left(\frac{y}{2}\right), \tag{4.10b}$$

where κ remains to be determined.

An outer solution is defined by introducing new variables given by

$$u = \delta\hat{u}, \quad v = \hat{v}, \quad x = \frac{z}{\delta}$$

and again keeping only leading order terms in δ. The outer solution is then given by

$$\hat{u} = \alpha + \delta\beta, \tag{4.11a}$$

$$\hat{v} = (\kappa - \frac{(\alpha+\delta\beta)^2}{\beta})e^{-\sqrt{\beta}\,|\,z\,|} + \frac{(\alpha+\delta\beta)^2}{\beta}. \tag{4.11b}$$

The value of κ is obtained by matching the inner and outer solutions. To do this, we consider the v equation in the inner region

$$u^2 - \delta^2 \beta v + v_{xx} = 0, \tag{4.12}$$

and integrate over a domain that contains the entire inner region. We find

$$u^2 = \frac{9\kappa^2}{4} \int_{-\infty}^{\infty} \operatorname{sech}^4\left(\frac{x}{2}\right) dy = 6\delta\kappa^2, \tag{4.13a}$$

and

$$v_{xx} = \int_{0^-}^{0^+} \hat{v}_{zz} dz = -2\sqrt{d}\left(\kappa - \frac{(a+d)^2}{d}\right). \tag{4.13b}$$

Substituting (4.13) into (4.12), we obtain a quadratic equation for κ given by

$$6\delta\kappa^2 - 2\sqrt{d}\kappa + \frac{2(a+d)^2}{\sqrt{d}} = 0. \tag{4.14}$$

The roots of (4.14) are

$$\kappa_1 \approx \frac{\sqrt{d}}{3\delta} - \frac{(a+d)^2}{d} - \frac{3(a+d)^4\delta}{d^{5/2}}, \tag{4.15a}$$

$$\kappa_2 \approx \frac{(a+d)^2}{d} + \frac{3(a+d)^4\delta}{d^{5/2}}. \tag{4.15b}$$

Taking these values of $\kappa_{1,2}$ and substituting them back into (4.10) and (4.11), we obtain asymptotic approximations to the large and small-amplitude spike solutions for small δ, a and d. The results are found to match closely the numerical solutions obtained using AUTO.

Moreover, a double root of (4.14) with respect to κ as parameter a or d varies would represent a fold that connects the upper and lower single-spike solutions. Setting the discriminant to zero gives

$$\delta d^{3/2}\left(-12d^{4/2} - 24ad - 12a^2\right) + d^3 = 0. \tag{4.16}$$

This analytic approximation is depicted as a magenta line in the inset to Figure 4.11a and is shown to match well to the AUTO-computed fold in the limit that a and d are small.

In Figure 4.12 we validate our asymptotic solution with the numerical solution that obtain from AUTO. The comparison is done for $a = 0.06$, $b = 0.005$ and $\delta = 0.01$. It is obvious from the plots that there is a good agreement between the two solutions.

Numerically we find that the large-amplitude spike emanating from the fold is stable and the small-amplitude one is unstable. It should be possible to extend this analysis further, for a finite domain, to show existence of a Hopf bifurcation on the upper branch for sufficiently small δ as was done in [4] for the Schnakenberg model on an infinite domain. We leave such analysis

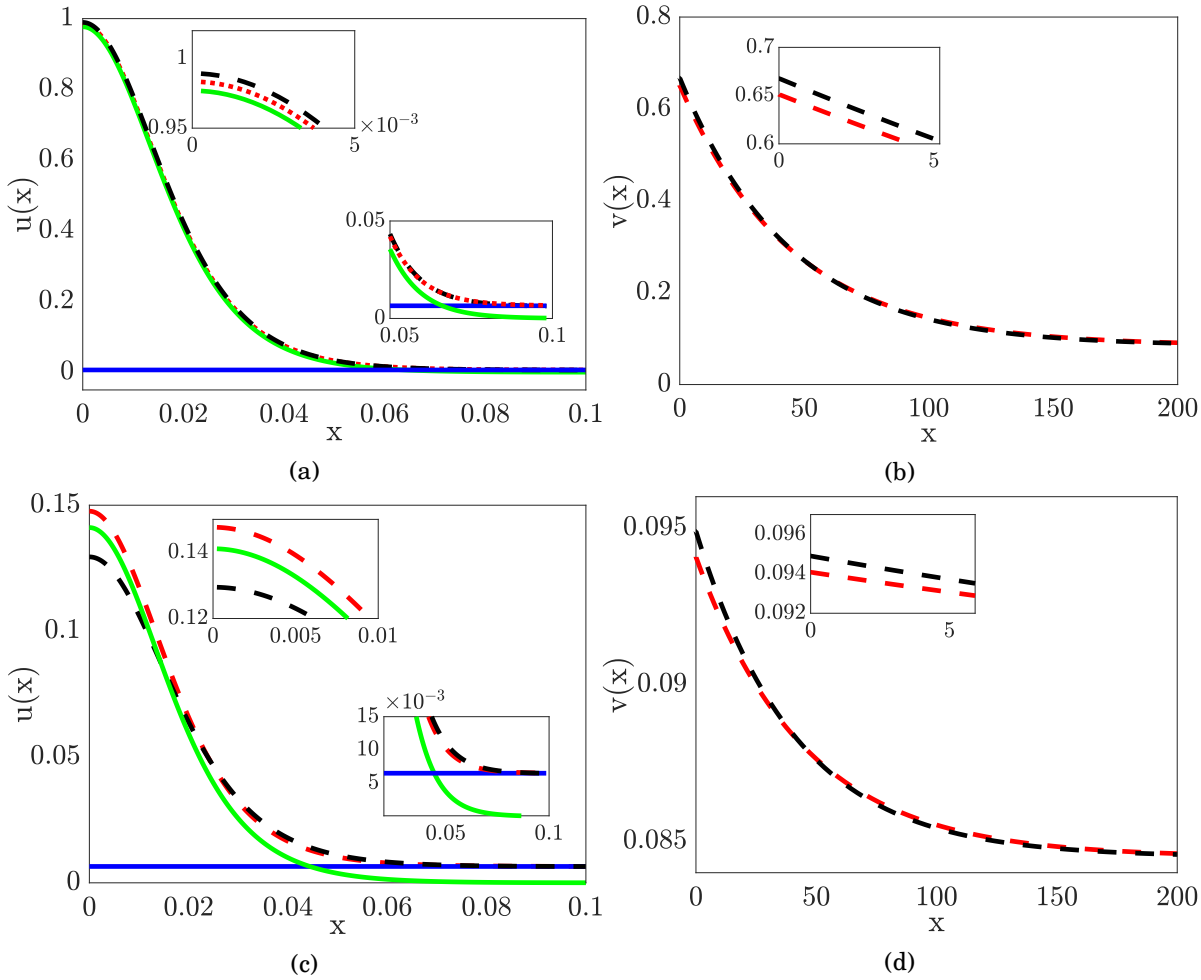

Figure 4.12: Plots compare between the approximate solution and the numerical solution for $a = 0.006$, $b = 0.0005$, $\delta = 0.01$ and $L = 1000$. (a)-(b) The plots of $u(x)$ and $v(x)$ solution versus x respectively for the upper branch with $\kappa = 0.09407965063$. The green and blue continuous line present the inner and outer where the red and black dashed line indicate the full asymptotic solution and the numerical respectively. (c)-(d) Plots show the $u(x)$ and $v(x)$ solutions for the lower branch respectively with $\kappa = 0.6512763417$. The colours code are similar to the upper branch solution.

to future work. Instead we rely exclusively in this chapter on numerical methods to evaluate stability of localised structures.

As with the Schnakenberg-like models, all the patterns featured in this universal bifurcation diagram are liable to a Hopf instability upon increasing δ. Figure 4.13 shows the location of two different kinds of Hopf bifurcation for the slightly larger value $\delta = 0.05$. The solid orange line shows the location of a global Hopf bifurcation of the HSS, that is a Hopf bifurcation with spatial wavenumber 0. This instability is found to be supercritical and to be inhereted by the periodic states in the Turing region. For yet larger δ, this solid line encroaches into the localised pattern region, whereupon the localised patterns become unstable to this global Hopf bifurcation.

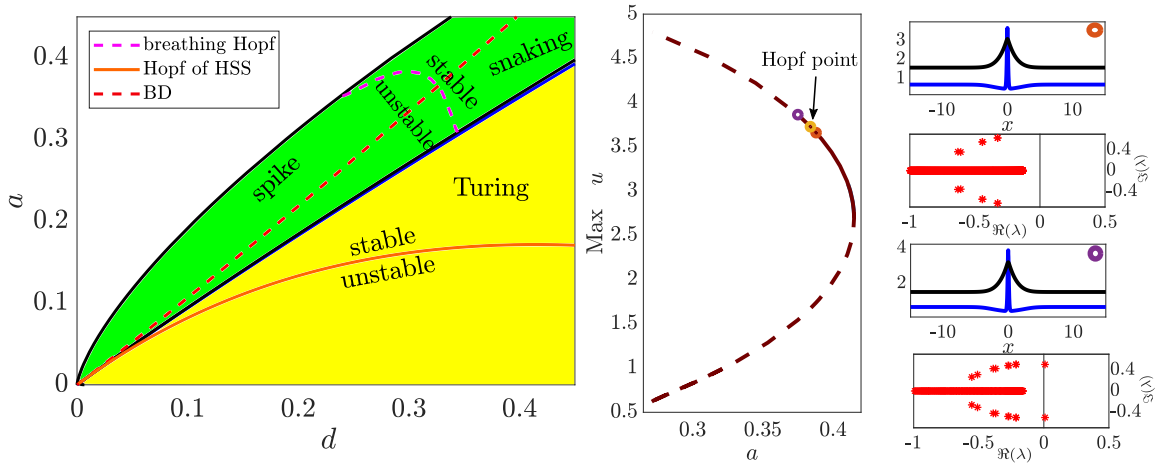

(a) (b)

Figure 4.13: A zoom of the spike region with $\delta = 0.05$ in the limit $l \to \infty$. (a) The blue curve indicates the Hopf. (b) Bifurcation diagram of vector max u versus a for fixed $b = 0.3$, showing the stable, unstable branches and the Hopf point at $a_h = 0.384$. The insert plots represent solutions and the corresponding linear spectrum stability.

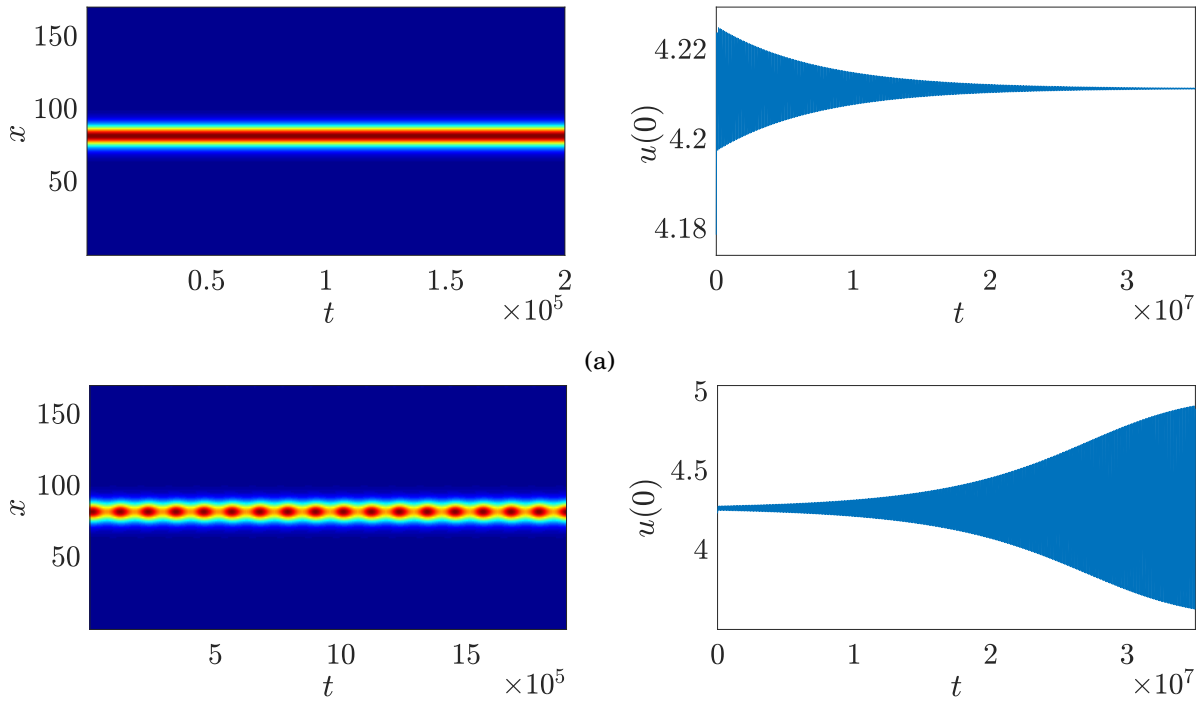

(a)

(b)

Figure 4.14: The direct simulation results of the full system (4.6) express by the plot of u component of the spike at $x = 0$ as function of time for fixed $b = 0.32$, $\delta = 0.05$ and two different values of a (a) $a = 0.3775$ after the Hopf point and (b) $a = 0.372$ before the Hopf point.

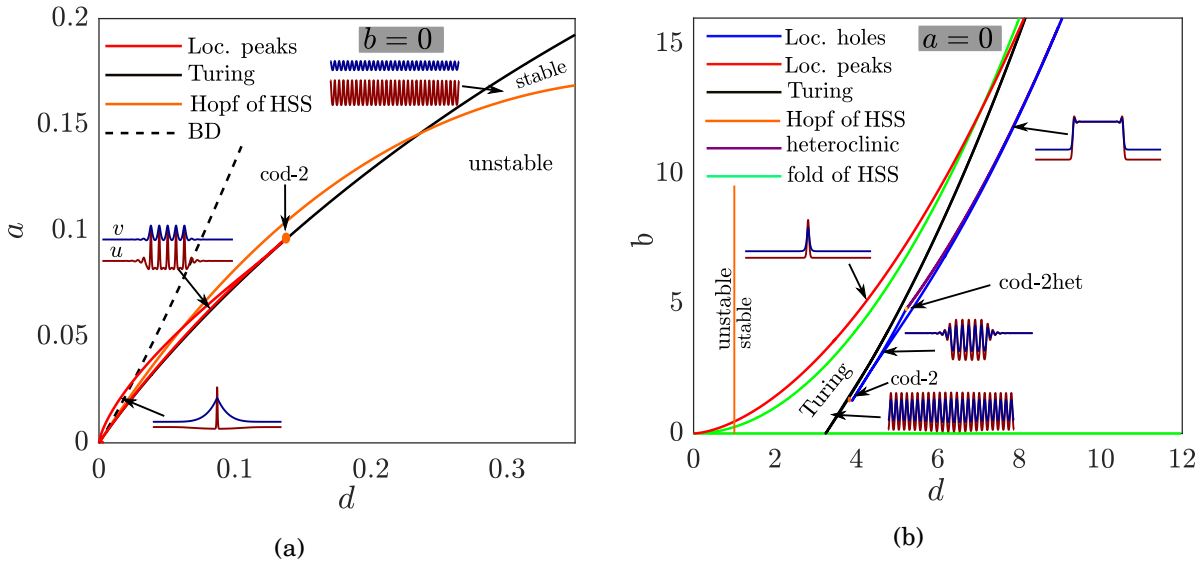

Figure 4.15: Two-parameter bifurcation diagrams for the Gierer-Meinhardt system (4.6) for $\delta = 0.23$. (a) Bifurcation diagram in the (d,a)-plane for $b = 0$. (b) Bifurcation diagram in the (d,b)-plane for $a = 0$. See text for further details.

4.3.2 The case $b > 0$.

Figure 4.15 shows two contrasting two-parameter bifurcation diagrams for larger δ still (chosen for ease of illustration). Figure 4.15a is for the case of $b = 0$ we have just considered, (albeit with the global Hopf bifurcation playing a more prominent role owing to the larger δ-value). Figure 4.15b shows the other extreme, which is for $a = 0$ and b now being the second bifurcation parameter (which was the case studied for a slightly modified version of the Gierer-Meinhardt model in [178]). Note how this second case is qualitatively similar to that of the Gray-Scott model, that is (4.2) for $r = 1$.

We have carried out further numerical bifurcation studies when both a and b are positive. We have found that for fixed $b > 0$ the parameter a plays a similar role as the parameter $1-r$ did for the model in the previous section. Specifically, for a large enough, we find there is a unique homogeneous equilibrium and the bifurcation diagram is like the case $b = 0$. As a is decreased towards zero, then a similar sequence of bifurcations occurs as was found as r is increased towards 1 in the model (4.2).

The results of a such a two-parameter continuation for fixed $b = 6.8$ is shown in Figure 4.16. In particular note the many similarities between Figure 4.16a and Figure 4.4 including the pivotal role played by the cusp of HSSs, two codimension-two Turing points giving birth to localised structures, a QZ point and a codimension-two heteroclinic connection. If anything though the present case is somewhat simpler. In particular we do not find the extra complexity that was associated with the additional magenta and cyan folds in Figure 4.4.

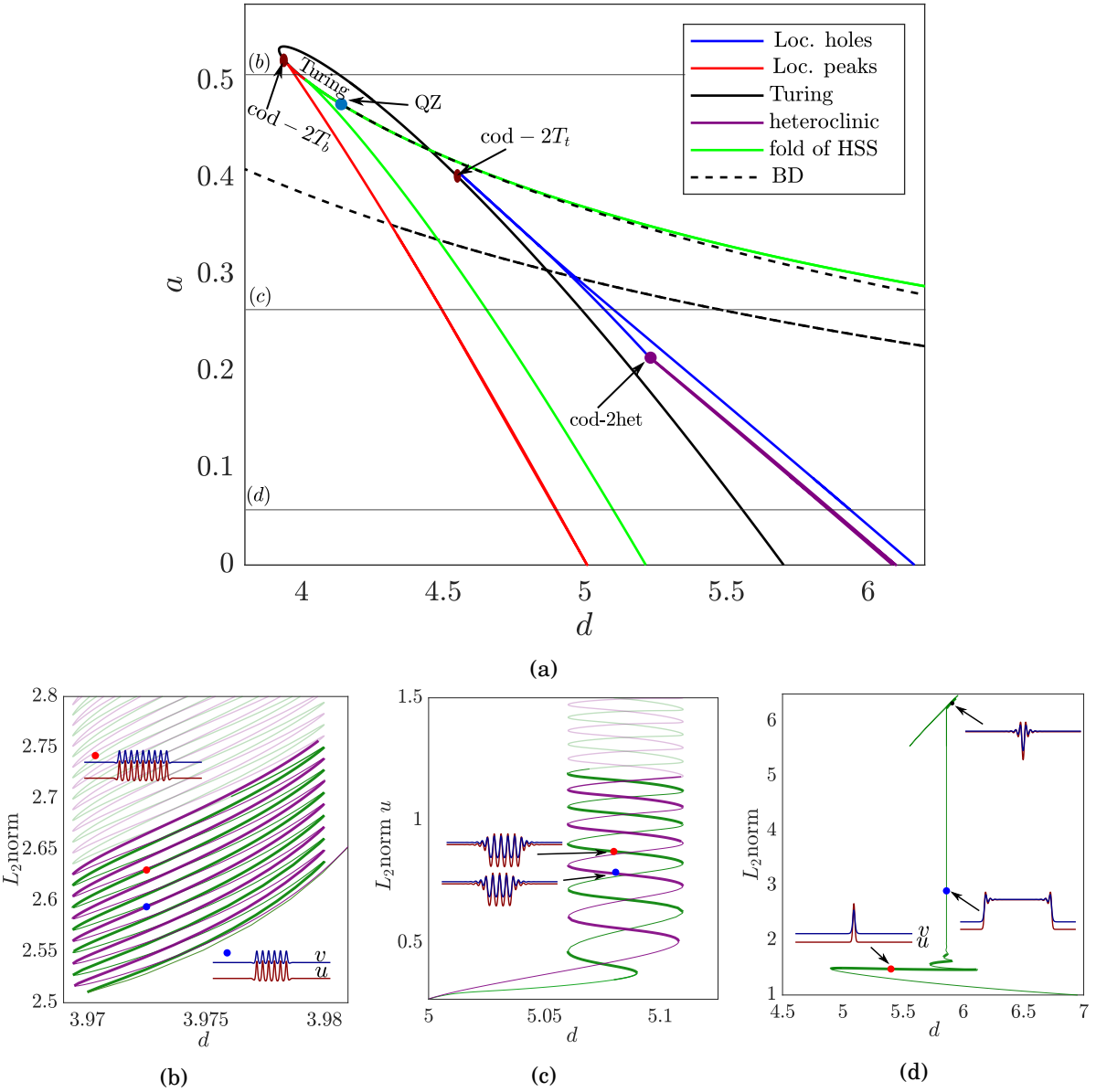

Figure 4.16: The bifurcation diagram in (d,a)-plane for the model (4.6) displaying numerically determined regions of pattern solutions for $\delta = 0.23$ and $b = 6.8$.(b) The peak homoclinic snaking , (c) the hole homoclinic snaking (d) the hertroclinic connection.

4.4 Discussion

A central theme of this chapter and its predecessor chapter 3 has been that of universality of bifurcation structures in a class of reaction-diffusion models in one spatial dimension. Starting from the assumption of simple cubic autocatalytic nonlinearity, we seem to have found there are two broad cases: Schnakenberg-like, where there is a unique homogeneous equilibrium; and Gray-Scott-like, where there is bistability between competing high- and low- intensity states. However, it seems that any universality is not just due to the particularly simple functional form. In fact, the Schnakenberg-like universality was first identified in [166] for a generalisation of a wave-pinning model of cell polarity [117, 165] and a model for crime-wave hotspots [103]. We have also found similar structures in models of similar bifurcations of predatory-prey systems [7]. Similar structures have also been observed in models of destertification [180, 181].

This chapter has attempted to illustrate one of the simplest extensions to the kind of models studied in chapter 3, namely the inclusion of a cusp bifurcation leading to regions of bistability between branches of homogeneous steady states. At least for the Gray-Scott and Gierer-Meinhardt models, we found significant additional complexity, involving various codimension-two bifurcations of peak-like and hole-like localised states. Given this complexity, it would seem at best premature to argue for any kind of universality. A more thorough multi-parameter investigation of other simple multi-parameter models, such as the modified Gierer-Meinhardt model studied in [178] might prove fruitful. See also the recent paper [128] for a review of similar bifurcation structures in the Lugiato-Lefevre equation. It would also be interesting to investigate how much of these stuctures can be predicted through an appropriate unfolding of a codimension-three singularity where a quadruple zero and cusp point of homogeneous steady states coincide.

The temporal stability of localised patterns has not been a major focus of the current chapter. In chapter 3 we highlighted how different kinds of Hopf bifurcation, both sub- and super-critical can be found in Schnakenberg-like models. There is also a rigorous literature on existence of Hopf bifurcations in Gierer-Meinhardt-like models, which uses geometric singular perturbation theory. See for example [57] and references therein for the general theory of Hopf destabilisation of periodic pattern branches in the long domain limit, albeit in a different singular limit than that studied here. See also [164] for explicit results for the Gierer-Meinhardt model for the case $a = b = 0$. There precise conditions are derived for the existence of breathing Hopf bifurcations of localised patterns, as in Figure 4.14. It would be interesting in future work to seek to understand the connection between the results presented here and the rigorous theory of so-called Busse balloons on long finite domains.

CHAPTER 5

STATIONARY AND OSCILLATORY LOCALISED PATTERNS IN RATIO-DEPENDENT PREDATOR-PREY SYSTEMS

This chapter is based on publication [6]

5.1 Introduction

The purpose of this chapter is to show the kinds of localised patterns observed in chapter 3 are not unique to a particular form of nonlinearity. Also, in this chapter we show more detail of the spatio-temporal behaviour beyond the Hopf bifurcation of the localised patterns. Finally, we present some evidence that similar behaviour occurs in two spatial dimensions.

The rest of this chapter is organised as follows. After a general introduction to predator-prey modelling in section 5.2, section 5.3 presents a particular system of reaction diffusion equations that represent a predator-prey model with a modified Holling type-II nonlinearity. That section also contains linear and weakly-nonlinear analysis in the spirit of sections 2.2 and 2.3. Section 5.4 then contains numerical bifurcation analysis for the system posed on a long 1D domain in the spirit of chapter 3. Furthermore, section 5.5 studies the same model numerically in two spatial dimensions, and evidence is found of 2D localised patterns and spatio-temporal chaos for similar parameter values. Section 5.6 shows that qualitatively similar results can be found in a generalised Holling type-III ratio-dependent model. Finally, section 5.7 contains concluding remarks.

5.2 Predator-prey dynamics

Spatial ecology is a relatively recently introduced term for the study of spatial effects in ecology, see [64] for an overview. As originally introduced by Tilman and Karieva [153] the term mostly refers to statistical methodologies for studying the autocorrelation of ecosystems in different spatial locations, as well as the effect of landscape change and animal movement. However, the study of spatial effects in ecological models actually goes back much further than that, see for example the groundbreaking work of Skellam [149] and the independent work by Fisher and by Kolmogorov, Pitrovski & Piskunov in 1937 that led to the famous Fischer-KPP reaction-diffusion model that is known to support travelling wave fronts, see e.g. [74] and references therein. There is now a rich literature within theoretical ecology of models that can give rise to complex spatio-temporal patterns.

The particular question of interest in this chapter is whether predator-prey interaction can give rise to stable spatial hotspots. That is, temporally stable localised patterns of high or low population density within a homogeneous environment. There are comparatively fewer studies that consider theories for such patterns in ecological systems. Notable exceptions are early works by Okubu and Leven, see [124]; see also [112] and references therein. There is also recent theoretical work seeking to explain vegetation patterns in semi-arid zones (e.g. [19, 65, 113] or rainforest-savanna systems [173]).

The context in which we choose to address this question is that of classical predator-prey systems, where typically the interaction times are faster than many of the vegetation-pattern models. In the late 1950s and early 1960s Holling [77, 78] postulated three different types of functional relationships between predator and prey, from a simple multilinear interaction (type I), to rational rational Hill-type nonlinearities of power 1 (type II) or higher (type III). See [45] for a modern rigorous definition of these kinds of nonlinear terms as the limits of random processes. Actually, type II functional responses were first considered by Rosenzweig and MacArthur [140]. The existence of Hopf bifurcations in this model is ecologically significant, especially because the bifurcation occurs as the prey carrying capacity is increased. This is known as the paradox of enrichment [139, 141] for which spatial dispersal has been argued as one solution, at least on some timescales [73]. In fact, it has been known for almost 30 years that this model, when spatially extended by diffusion, can exhibit spatio-temporal chaos [130].

We also restrict attention to models that use simple second-order diffusion to model random dispersal of spatially structured populations, which is at best only an approximation to how real populations move. See for the example the review by Potts and Lewis [135] for models that incorporate territoriality, home-range analysis, and other kinds of taxis in pattern-forming behaviours where demographics (birth and death) can be ignored. Others have considered slightly longer timescales, and thus included demography alongside more complicated models of movement than random dispersal, see e.g. [152] and references therein.

Our study was originally inspired by the works [26, 27, 41], which study predator-prey-like

models that might underlie the onset of spatio-temporal patchiness. Our analysis is also in the same spirit as recent relevant bifurcation analyses such as in the work of [15, 102, 110, 118, 174]. In particular, in the context of Holling type-II and III predator-prey models we mention the work of [22, 81]. Also the existence of Turing patterns and the chaos considered in [16, 110] and the existence of stable limit cycle was shown in [175].

5.3 A ratio-dependent predator-prey model

Consider the ratio-dependent predator-prey reaction-diffusion system of non-linear partial differential equations (PDEs) studied in [95]:

$$u_t = f(u,v) + \delta\nabla^2 u = u(1-u) - \frac{\beta uv}{u+v} + \delta\nabla^2 u, \tag{5.1a}$$

$$v_t = g(u,v) + \nabla^2 v = \frac{\alpha uv}{u+v} - \gamma v + \nabla^2 v. \tag{5.1b}$$

Here $u(z,t)$ and $v(z,t)$ represent, respectively, dimensionless prey and predator population densities at position z. In what follows we shall consider the problem in one spatial dimension, in which case $z = x$, or in 2D, in which case (x,y). We assume that the domain is large and there are homogeneous Neumann boundary conditions at $x = \pm l$ and, if appropriate, $y = \pm l$ for some $l \gg 1$.

The parameters in (5.1) can be interpreted as follows: α is a conversion coefficient that measures the positive effect of the predator's interaction with the prey; and β is the corresponding negative effect on the prey; γ is ratio of net death rate of the predator to the birth rate of the prey in the absence of interaction; and $\delta \ll 1$ is the ratio of diffusion of the relatively static prey to the much more mobile predators.

In the absence of the diffusion terms in (5.1), a straightforward calculation shows that the solution (u,v) admits three homogeneous steady state points. These being:

(i) The extinct steady state $S_1 = (0,0)$.

(ii) The predator-free steady state $S_2 = (1,0)$.

(iii) The coexistence steady state $S_3 = (u^*, v^*)$ with

$$u^* = \frac{\beta(\gamma-\alpha)+\alpha}{\alpha}, \quad v^* = \frac{u^*(\gamma-\alpha)}{\gamma} \tag{5.2}$$

exists under the following conditions $\alpha > \beta(\alpha-\gamma)$ and $\gamma > \alpha$.

Several authors, e.g. [17, 175], have considered how ratio-dependent predator-prey systems require some additional rule in order to be well-defined at the origin. In our case, the trivial steady state S_1 is at the edge of the allowed domain for (u,v) and is unstable in all parameter regions we investigate. Also, from a biological perspective, we are interested in localised patterns that have as background the nonzero steady state S_3.

To develop a basic analytical understanding, we first consider (5.1) in one spatial dimension only. Hence, for the remainder of this section, we will shall assume $\nabla^2 = \dfrac{\partial^2}{\partial x^2}$.

5.3.1 Linear stability analysis

Following the linear stability analysis developed in section 2.2, we find the Jacobian matrix of the system linearized about the equilibrium S_3 to de

$$J = \begin{pmatrix} \frac{(\beta-1)\alpha^2-\beta\gamma^2}{\alpha^2} & -\frac{\beta\gamma^2}{\alpha^2} \\ \frac{(\alpha-\gamma)^2}{\alpha} & -\frac{(\alpha-\gamma)\gamma}{\alpha} \end{pmatrix}. \tag{5.3}$$

A straightforward analysis from the condition (2.10), we obtain a Hopf bifurcation occurs at the critical value of $\alpha = \alpha_H$ given by

$$\left(\beta-\gamma-1\right)\alpha_H{}^2+\gamma^2\left(\alpha_H-\beta\right)=0. \tag{5.4}$$

Next, to look for a pattern-formation, or Turing, instability of S_3, we follow the standard approach in section 2.2 by considering the ansatz (2.7). The corresponding dispersion relation is

$$\lambda(k)^2 - T_k\lambda(k) + D_k = 0 \tag{5.5}$$

where

$$T_k = \frac{\left(\beta-(\gamma+1)-(\delta+1)k^2\right)\alpha^2+\left(\alpha-\beta\right)\gamma^2}{\alpha^2}$$

and

$$D_k = \frac{\left(k^2+\gamma\right)\left(\delta k^2-\beta+1\right)\alpha^2-\gamma^2\left(\delta k^2-2\beta+1\right)\alpha+\beta\gamma^2\left(k^2-\gamma\right)}{\alpha^2}.$$

From (5.5), we have $\lambda(k) = \frac{T_k \pm \sqrt{T_k^2-4D_k}}{2}$. The solution is stable whenever $\Re(\lambda) < 0$ for all k and the conditions for a Turing instability with critical wave number k_c is (2.11). Note that S_3 is stable for the spatially homogeneous mode $k = 0$.

Applying (2.11) to (5.5), we find:

$$\left(-\delta\gamma+\beta-1\right)\alpha^2+\gamma^2\left(\alpha\,\delta-\beta\right)=2\,\alpha\sqrt{\delta\gamma\left(\alpha-\gamma\right)\left(\beta\left(\gamma-\alpha\right)+\alpha\right)}, \tag{5.7a}$$

$$k_c^2 = \frac{\left(-\delta\gamma+\beta-1\right)\alpha^2+\gamma^2\left(\alpha\,\delta-\beta\right)}{2\alpha^2\delta}. \tag{5.7b}$$

Thus (5.7) gives the value $k = k_c$ and the parameter condition for Turing instability. Figure 5.1 displays various dispersion curves for $\Re(\lambda)$ in (5.5) versus k for specific values of the parameters β, δ and δ while varying the bifurcation parameter α. The figure shows different scenarios of solution stability for (5.1). Specifically: $\alpha > \alpha_c$ (solid red curve) represents instability where there

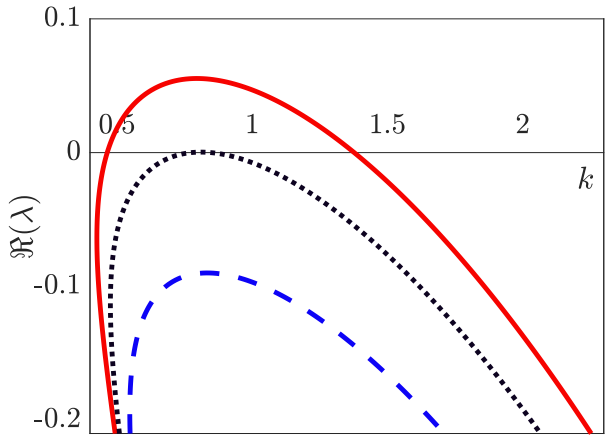

Figure 5.1: Dispersion curves $\Re(\lambda)$ in (5.5) versus k for $\beta = 2.3$, $\gamma = 0.3$, $\delta = 0.1$ and three different bifurcation values of α: $\alpha = 0.4$ (solid red line), $\alpha = 0.39188$ (dotted black line) and $\alpha = 0.390$ (dashed blue line.

are positive eigenvalues λ for a range of k-values; $\alpha = \alpha_c$ (dotted black curve) represents the critical case of a Turing bifurcation where for $k = k_c$ $\lambda = 0$ and $\frac{d\lambda}{dk} = 0$; and $\alpha < \alpha_c$ (blue dashed curve) which corresponds to instability as $\lambda < 0$ for all k.

Moreover, we obtain the following condition for the existence of double real spatial eigenvalue (sometimes referred to as a Belyakov-Devaney (BD) transition,

$$\left(-\delta^2\gamma+\beta-1\right)\alpha^2+\gamma^2\left(\alpha\delta^2-\beta\right)=-2\,\alpha\,\delta\sqrt{\gamma\left(\alpha-\gamma\right)\left(\beta\left(\gamma-\alpha\right)+\alpha\right)} \tag{5.8}$$

the significance of which is explained in the next section.

5.3.2 Weakly nonlinear analysis

We now seek an analytical expression for the codimension-two point for (5.1) where the Turing bifurcation changes from a super to sub-critical bifurcation. This is achieved by using normal form analysis developed in section 2.3. We omit the detail here for brevity. We do this using code developed in Maple. Figure 5.2a plots the value of L_3 as a function of the single variable α with $\delta = \delta(\alpha)$. The point $L_3 = 0$ is indicated by a yellow circle. This represents a codimension-two point where the Turing bifurcation changes from being subcritical (red) to a supercritical (blue). Figure 5.2b presents the location of the codimension-two point in the (δ, α)-plane. As explained in chapter 2, the existence of a subcritical region leads to a bi-stability region between the homogeneous state and the bifurcating periodic patterned state in which we might expect to find localized structures.

5.4 Bifurcation analysis and numerical simulation

We now use the local bifurcations in the previous section as the starting point of an investigation into localised pattern solutions to (5.1). These are solutions that asymptote to the coexistence

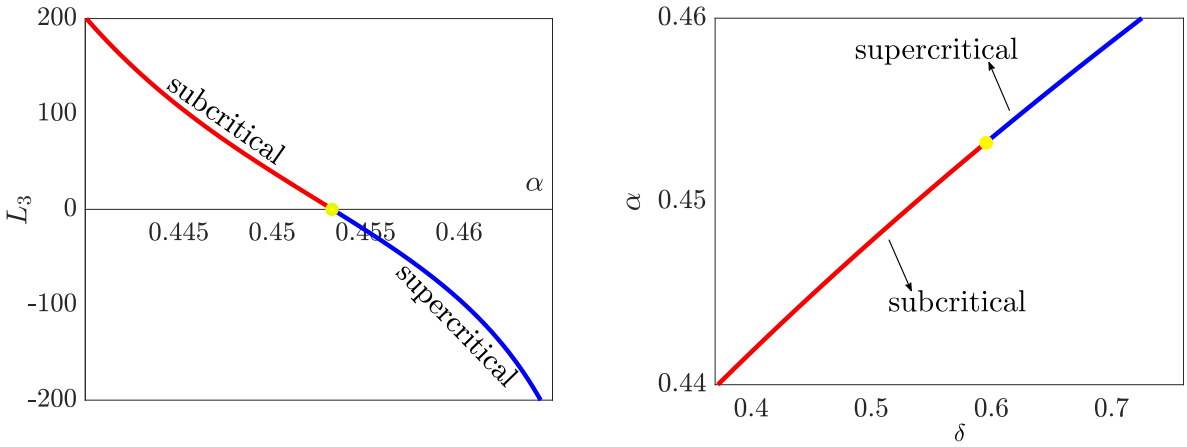

(a) (b)

Figure 5.2: The fixed parameters values of $\beta = 2.3$ and $\gamma = 0.3$ are used. (a) A plot of $L_3 = L_3(\alpha)$ where the yellow coloured circle indicates the zero of L_3. (b) A plot of δ vs α along the critical curve in (5.7) where the co-dimensional two point $(\delta_c, \alpha_c) = (0.6044768459, 0.4537)$ is indicated by the yellow coloured circle. In both figures, the coloured yellow circle indicates that there is a change in Turing bifurcation from being subcritical (red curve) to supercritical (blue curve).

homogeneous state. In what follows, unless otherwise stated, we fix

$$\beta = 2.3, \qquad \gamma = 0.3 \tag{5.9}$$

and treat α and δ as bifurcation parameters.

5.4.1 Parameter space investigation in 1D

Figure 5.3 depicts an overall summary of the two-parameter bifurcation diagram. Note that the qualitative features of the two-parameter bifurcation diagram are just like the Schnakenberg-like models in chapter 3. The figure indicates the linear stability boundaries and parameter regions where different kinds of solutions are observed. The particular curves plot consists of several boundaries: the Hopf bifurcation of S_3 (red line) given by (5.4); the Turing bifurcation (blue) (5.7); the BD transition curve (dashed green) (5.8) and, the boundary of the parameter regime in which we numerical find localised structures (black lines). It is clear that, the Hopf line divides the bifurcation diagram into two parts; $\alpha > \alpha_H$ where solutions are unstable to a global (spatially uniform) oscillatory mode, and $\alpha < \alpha_H$ where solutions are stable to such perturbations.

Also in the figure are three coloured regions that identify various types of steady-state solution for (5.1). These regions are classified as: stable homogeneous solution region (white); periodic spatial pattern region (green); and the 'pinning region' (yellow) in which localised structures occur. Note that the localised structure region is separated into three pieces by the BD transition curve and the Hopf bifurcation line, whereas the periodic-pattern region is divided into two parts by the Hopf line. Note the yellow circle which represents the codimension-two point (δ_c, α_c) found

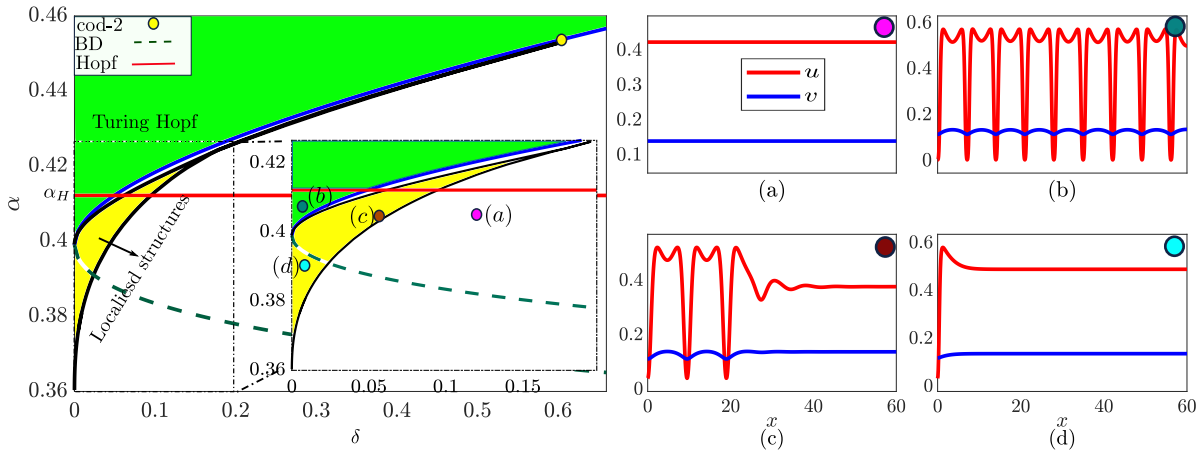

Figure 5.3: (Left): Bifurcation diagram of (δ,α) with white, green, yellow coloured regions to identify the different types of solution $(u(x),v(x))$ for (5.1). All solution curves are obtained analytically except thin black lines which are a numerically contained curve of folds of the single-patch localised structure shown in panel (d). In addition above the Hopf bifurcation line (red curve) steady state solutions are unstable to an oscillatory instability. (Right):Solution profiles of typical steady-state at the points labelled (a)-(d) in the left-hand plot.

in Sec. 5.3.2 where the Turing bifurcation changes critically. We see that this is the origin of the (yellow) localised structure region, which becomes exponentially thin as it approaches this point, just as predicted by the theory [94].

The right-hand plots in Figure 5.3 illustrates four different types of steady-state solution at parameter values represented in the left-hand diagram. All points are taken for $\alpha < \alpha_H$ where the solutions are stable to the global Hopf mode.

Point (a), $(\delta,\alpha) = (0.11, 0.413)$ represents the unique attracting homogeneous solution S_3 in the white parameter region.

Point (b) which has $(\delta,\alpha) = (0.01, 0.409)$, represents a typical solution from the green parameter region of large-amplitude spatially (quasi-) periodic patterns. The nature of the pattern here is that of a multi-scale pattern in which there are repeated patches in which the population $u(x)$ of prey is significantly reduced. Note that the precise pattern observed on a long domain is a delicate function of parameters and domain size, as is well known in the theory of Turing patterns (see e.g. [106, 119]). A difference here from the usual case, owing to the sub-critical Turing bifurcation, is that there is no stable small-amplitude pattern close to the Turing bifurcation. Instead, fully-formed large-amplitude patterns emerge from a fold bifurcation (close to the outer black line delineating the yellow pinning region).

Point (c), for $(\delta,\alpha) = (0.05, 0.408)$, is an example of a localised structure from within the yellow parameter region above the BD line. Such solutions, with an arbitrary finite number of large-amplitude u-oscillations within a background of the homogeneous state S_3 coexist with fully periodic solutions. Note that above the BD curve corresponds to where localised solutions have oscillatory tails. Typically, such solutions lie on snaking bifurcation diagrams. We also found

for Schnakenberg-like models in chapter 3.

Finally, point (d), for $(\delta, \alpha) = (0.013, 0.39)$ shows an example of a single isolated peak solution within the yellow region beneath the BD curve. Here there is a single isolated patch of prey degradation which has monotonic decay to the homogeneous steady state S_3. The mechanism of transition between such localised structures and single-peak states across the BD curve seems to occur via exactly the same process that was explained in [166].

5.4.2 Homoclinic snaking and instability of localised patterns

Figure 5.4 shows a one-parameter bifurcation diagram with α of localised structures from the yellow parameter region of Figure 5.3 above the BD curve. The norm used is vector L_2 – norm of u, v and their first spatial derivatives. Representative solution profiles and their spectra are depicted in Figure 5.5. Several features can be observed from these two figures, which we now explain.

The first feature to note is the usual snaking structure that is typically observed within a Pomeau pinning region that emerges from a sub-critical Turing bifurcation [20, 89, 94, 171]. The inner and outer extent of the pinning region is delineated by the accumulation of the fold curves on the left and right-hand sides of the snaking diagram. Following one of these folds in two parameters results in the black lines that delineate the yellow region in Fig. 5.3. At every successive fold bifurcation each of the branches loses stability, or regains it in a fold bifurcation.

A feature of this snaking bifurcation diagram, is the presence of the Hopf bifurcation of the background state that cuts the bifurcation diagram in two. A natural question would be to seek to understand the relation between the Hopf bifurcation of the background state and a corresponding instability of the localised states. From the figures it is clear that the instability is indeed inherited by the localised states, but not at the same parameter values (cf. the location of the green dots in Figure 5.4 and the vertical line $\alpha = \alpha_H$). At each of the green circles we have found that the complex eigenvector that corresponds to the complex conjugate pair of eigenvalues that cross the imaginary axis is indeed a global, approximately spatially homogeneous, mode corresponding to the associated eigenvector of the Hopf bifurcation of the homogeneous state (result not shown).

Interestingly, the lowest part of the red curve in Figure 5.4, which corresponds to the primary, single pulsed solution has its Hopf bifurcation at α_H. Where all other multi-patch solutions on the snaking curve have their Hopf instability at α-values that are less than α_H, which means that they destabilise while the background state is still stable. What happens beyond the Hopf instability forms the subject of the next subsection.

Before investigating more complex spatio-temporal behaviour, Figure 5.6 completes the bifurcation picture for localised solutions, by showing the one-parameter diagram with α of a single-patch solution, below the BD curve. The depicted curve of solutions lies exclusively below the Hopf bifurcation line for the parameter values chosen. Here, there is a single fold that

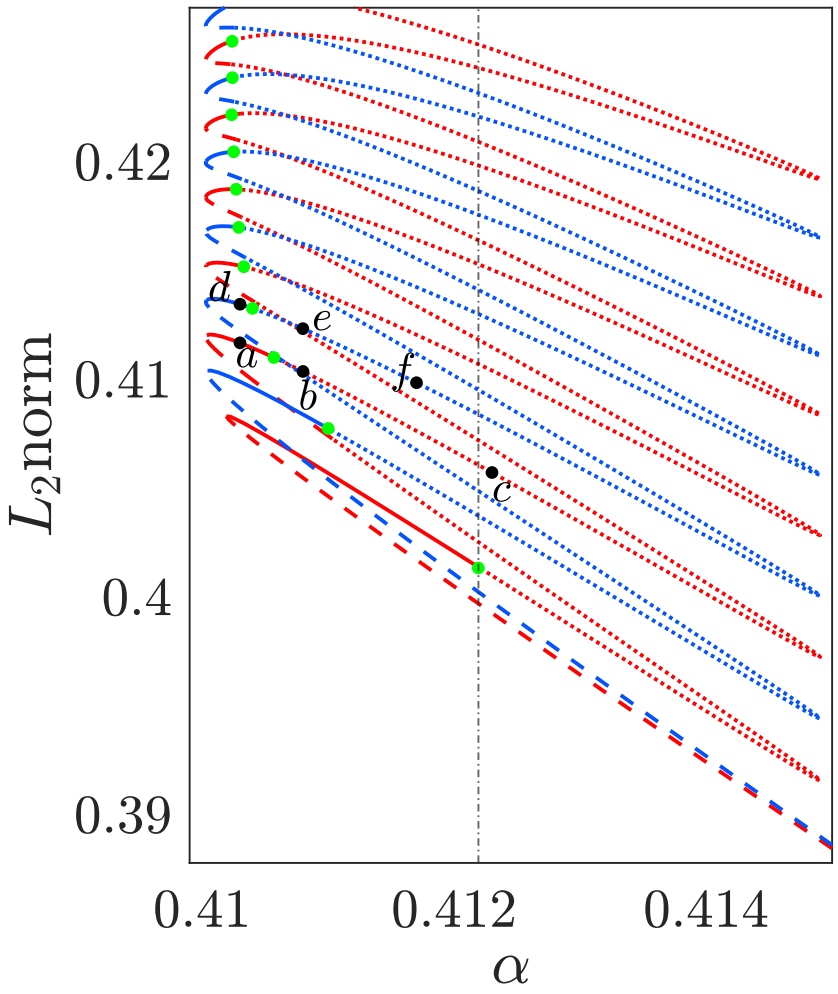

Figure 5.4: Numerical bifurcation diagram showing paths of localised structures for $\delta = 0.085$ as α varies. Red/blue lines indicate solutions with an odd/even number of localised patches. Profiles and spectra of solutions at the points labelled a to f are depicted in Figure 5.5. The vertical dashed line $\alpha = \alpha_H$ indicates the Hopf bifurcation of the homogeneous solution S_3. Green dots indicate Hopf bifurcation points causing loss of stability of localised structures. More generally, stability information is encoded in the line type: continuous lines represent stable branches, whereas the dashed lines represent branches that are unstable to a real-eigenvalue instability (through a fold in the homoclinic snake) and dotted lines indicate branches that are unstable to an oscillatory instability.

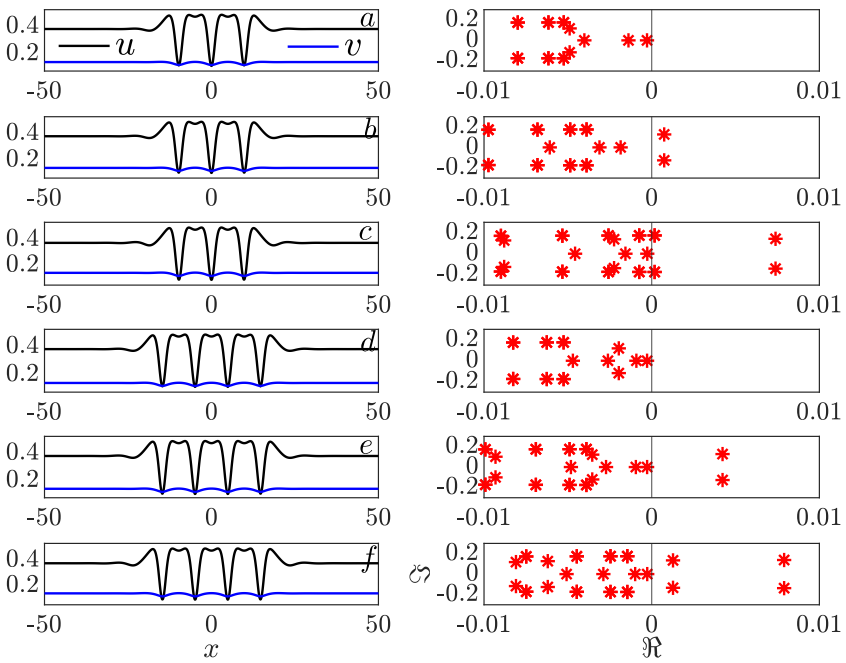

Figure 5.5: Numerical spectral analysis of the localised patterns at the points labeled (a) to (f) in Fig. 5.4 (Left): solution profiles. (Right): the largest few temporal eigenvalues of the problem linearised about these profiles; all other eigenvalues have real parts that are more negative.

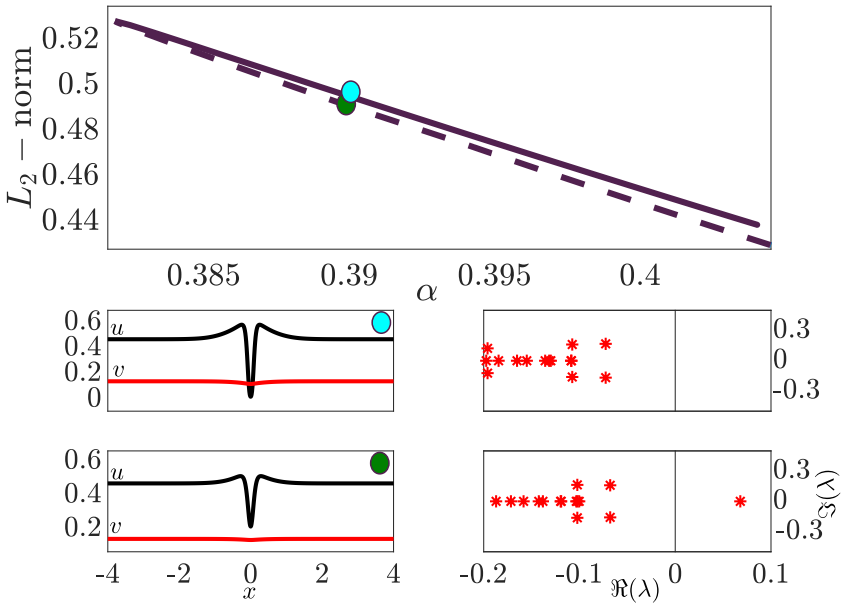

Figure 5.6: (Top:) Numerical bifurcation diagram with α of the single-patch state for $\delta = 0.01$. The continuous/dashed line indicates stable/unstable solutions. (Lower plots): Solution profiles at the colored points with their corresponding eigenvalues with largest real parts.

connects a larger-amplitude (stable) solution to a smaller amplitude (unstable) one. Note that the only instability detected here is the fold, but the analysis of chapter 3 suggests that for very small values of δ there may be a breathing-mode Hopf bifurcation, which corresponds to a localised eigenvector. We shall not explore that singular limit further here.

5.4.3 Onset of spatiotemporal chaos

Using the snaking diagram in Figure 5.4 we choose six values of α from the odd/even (red/blue) curve in the vicinity of the Hopf bifurcation to numerically generate Figure 5.7. Here we carefully choose the parameter values and initial conditions so that α is: on the stable side of the corresponding Hopf bifurcation which are shown in plots (a) and (d); just beyond the Hopf bifurcation which are displayed in plots (b) and (e), and, a little further beyond the bifurcation point that are depicted in plots (c) and (f). It should be noted that the α values used in (a)-(c) are from the odd curve while (d)-(f) are values taken from the even curve. In each case, we plot the results of the simulation as a heat map (upper part) and as the time series of the u-value at a single point in the domain.

From these simulations, we notice that the Hopf bifurcation for both kinds of solution is supercritical. That is, just beyond the bifurcation point there is a stable limit cycle. Moreover, as can be seen from the close inspection of the heat map plot, this limit cycle is a kind of "breather" solution where all points in the domain are subject to amplitude modulation. We find that this limit cycle only exists for a narrow parameter window and the amplitude of the oscillation changes rapidly with $\alpha - \alpha_H$. In each of the branches, we find that a secondary instability occurs in which outer patches collapse. This leads to what appears to be spatio-temporal chaos that is somehow reminiscent of weak turbulence. Here the trajectory intermittently visits neighbourhoods of states with different even numbers of localised patches. For much higher values of α the solution is observed to become more irregular.

5.5 2D Simulation results

A natural question arises whether analogues of the kind of structures we have observed in one spatial dimension exists in 2D. To seek a preliminary answer, we have performed numerical simulations using 2nd-order finite differences on a square domain $(x, y) \in [0, l] \times [0, l]$, using Neumann boundary conditions. As with the 1D simulations, we solve the resulting large system of ODEs in time using Matlab's `ode15s` again taking care to choose stepsizes that avoid numerical instability. The domain size L is chosen to be sufficiently large such that obvious boundary effects do not apply. Moreover, we retain the parameter values (5.9) from the 1D case while varying α and δ. Nevertheless the computational results are intended to be illustrative rather than exhaustive.

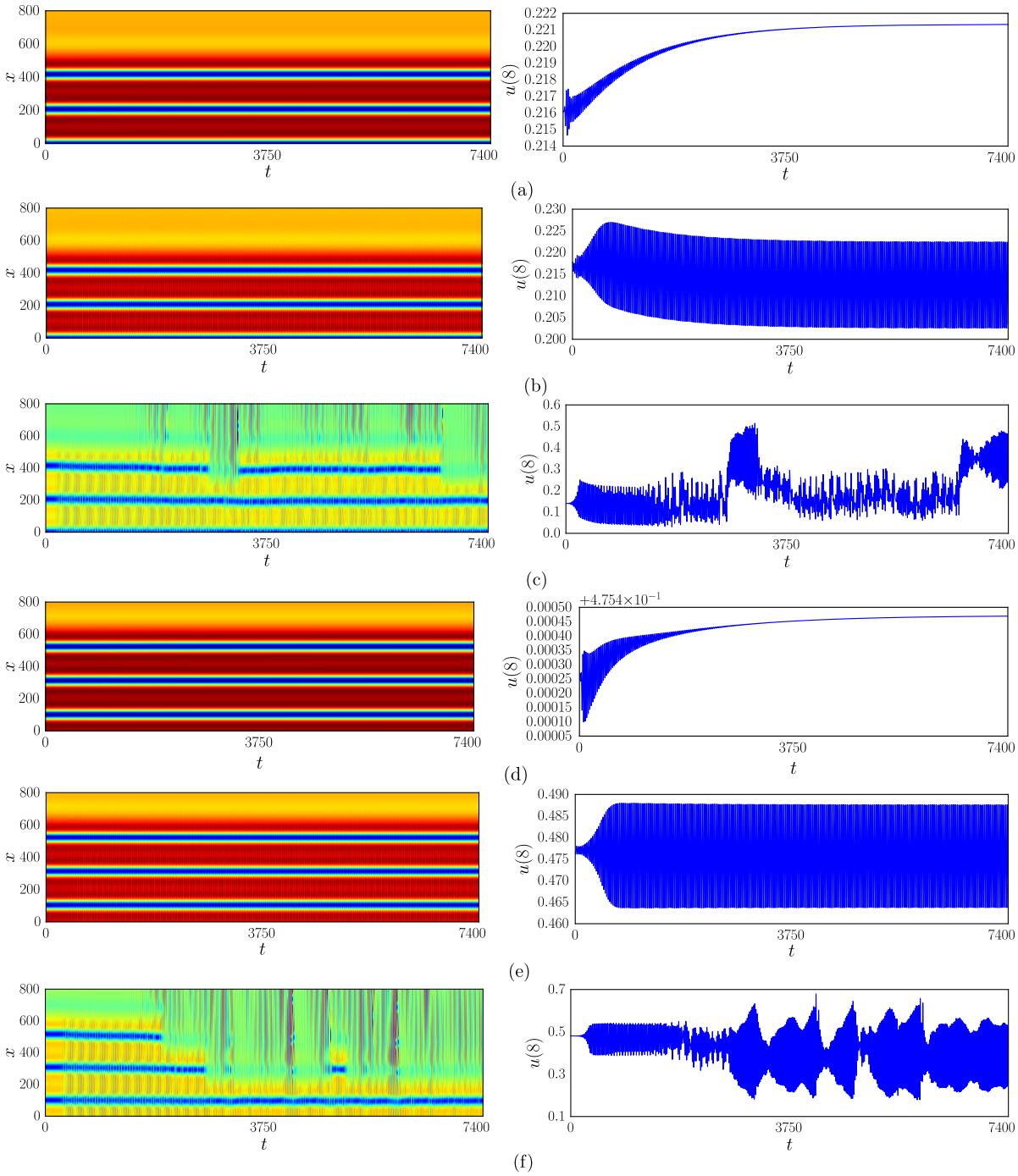

Figure 5.7: Numerical simulation of (5.1) depicted as a heat map of the u component (red/blue are higher/lower amplitude values) on left and time series of the point $u(8)$ on right for six different values of α from branches from Figure 5.4 with odd and even numbers of patches, by fixing $\delta = 0.085$ using: (a) $\alpha = 0.41025$; (b) $\alpha = 0.4105$; (c) $\alpha = 0.4135$; (d) $\alpha = 0.4103$; (e) $\alpha = 0.41055$, and, (f) $\alpha = 0.4135$.

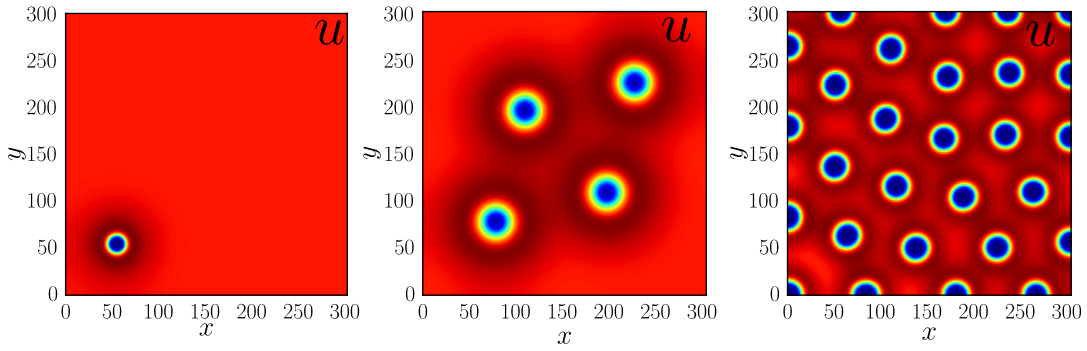

(a) (b) (c)

Figure 5.8: 2D solution patterns obtained by numerical simulation of (5.1). Figures represent typical pattern solutions at the following parameter values (a) a single spike for $(\delta, \alpha) = (0.01, 0.39)$, (b) a localised pattern at $(\delta, \alpha) = (0.05, 0.4)$ and (c) a periodic-Turing pattern with $(\delta, \alpha) = (0.02, 0.41)$.

First, we choose values of δ and α from below the Hopf bifurcation curve in Figure 5.3, where the 1D model has attractors that are steady pattern states. Figure 5.8a shows corresponding 2D solutions from the isolated patch region; Figure 5.8b shows a solution corresponding to a localised patterned state; and Figure 5.8c shows a spatially periodic solution from inside the Turing region. In these plots we show the concentration of prey as a coloured map. It can be seen that as we move from the isolated patch region through to the snake region and then to the Turing region, there is an increase in the density of depleted-prey patches.

Figure 5.9 in contrast shows the results of similar simulations for parameter values which correspond in the 1D case to being above the Hopf-bifurcation line but in the localised pattern region. The upper plots, Figures 5.9a–5.9c show three different time-slices of the prey field plot as a colour map from a particular initial condition which has a single depleted prey patch within a background close to S_3. We have used other initial conditions in this parameter region and have found no evidence that the simulation reaches any steady state, other than the trivial one S_3 for small enough perturbations from it. For sufficiently large perturbations we find that these non-repeating dynamics appear to be spatio-temporally chaotic. This chaotic dynamics is further indicated by the time series of Figure 5.9d, which shows the u-field at a single point in space.

5.6 Related results for Holling type-III model

To reinforce that what we have observed is in some way generic to a class of predator-prey models, we shall briefly indicate results for a further model with a different nonlinearity, namely a Holling type-III predator-prey model. This model was studied in [167] who found evidence for Turing instability, traveling waves and stationary patches. Our aim is to show that a similar bifurcation diagram applies here too.

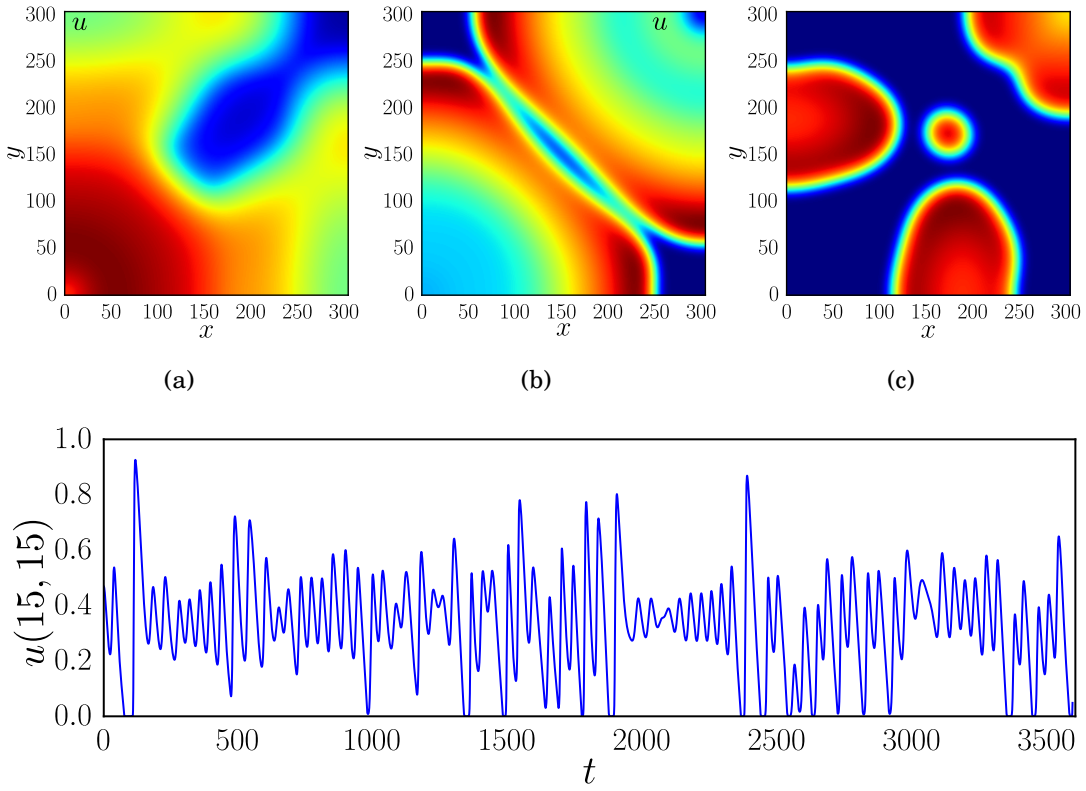

Figure 5.9: 2D solution patterns by numerically solving (5.1). Figures represent typical pattern solutions in the snaking region with parameter values $(\delta,\alpha)=(0.125,0.416)$ at three different time steps: (a) t=200; (b) t=1700; (c) t=3500, and, (d) Time evolution of the u-field at a single point in the domain $(x,y)=(15,15)$.

The model in question is represented by the following system of nonlinear PDEs:

$$u_t = u(1-u) - \frac{\alpha u^2 v}{v^2+u^2} + \delta\nabla^2 u, \quad t>0, \tag{5.10a}$$

$$v_t = \frac{\beta u^2 v}{v^2+u^2} - \gamma v + \nabla^2 v, \quad t>0, \tag{5.10b}$$

subject to Neumann boundary conditions. For simplicity, we shall present results only in 1D, for $x\in(-l,l)$, with $l\gg 1$. The positive parameters have similar meaning as they did in 5.1; α denotes the consumption rate of the prey by the predators, β is the half-saturation constant, γ is the death rate of the predator and $\delta\ll 1$ is the prey to predator diffusion ratio.

The model has many similar properties to 5.1 and can be analysed similarly. We omit most of the details. There are again three spatially homogeneous equilibria: $S_1(0,0)$, $S_2(1,0)$ and $S_3(u^*,v^*)$ where

$$u^* = \frac{\beta-\xi}{\beta}, \quad v^* = \frac{u^*\xi}{\alpha\gamma}, \quad \xi = \sqrt{\alpha^2\gamma(\beta-\gamma)}.$$

Note that both components are positive if $\beta > \gamma$ and $\beta > \xi$, which is a constraint on the parameters in order for the coexistence state to exist.

Figure 5.10a presents the linear and weakly nonlinear analysis, which is presented in exactly the same ways as Figure 5.3. We note that the results are qualitatively highly similar to those of the previous model and the method introduce in chapter 3. Numerical simulation has also indicated presence of the oscillatory behaviour above the Hopf bifurcation line.

Interestingly, even though the qualitative results are similar, the models cannot be mapped onto one another by any simple transformation, owing to the different powers in the interaction terms. Also, note the differences in the values of the parameters in Figures 5.3 and 5.10a. Thus, the similarity between results points to a certain generality of the bifurcation structures beyond pure cubic form studied in chapter 3.

5.7 Discussion

The purpose of this chapter has been to systematically investigate the propensity of predator-prey systems to develop spatially localised dynamics, without the need for any spatial heterogeneity. Although, previous studies have explored spatio-temporal dynamics of predator-prey models within the Turing-Hopf region (as outlined in the Introduction) we believe this is the first attempt at a systematic study showing how spatially localised structures can occur on large domains.

Remarkably, the global bifurcation structure of stationary patterns in two parameters is found to follow a similar pattern to that observed in Schnakenberg-type reaction diffusion equations, which do not have a predator-prey structure.

We have deliberately chosen parameter values in which the Hopf bifurcation of the background state interacts with the region in which the sub-critical Turing bifurcation and localised structures exist. This led to interesting novel observations on the nature of the Hopf bifurcations occurring on branches of localised steady states. These were found to all be supercritical, yet to occur for parameter values that are different from that of the homogeneous Hopf bifurcation. We also found that the Hopf bifurcation gives a route to localised spatio-temporal chaos within this parameter region. It would be interesting in future work to consider an unfolding of the codimension-three point where the super- to sub-critical Turing bifurcation transition occurs simultaneously with the Hopf bifurcation.

Most of our results were presented in one spatial dimension. Although much remains to be done to explore these mechanisms in 2D, we nevertheless provided evidence of two-dimensional analogues of these 1D structures occurring at similar parameter values.

This chapter is not primarily designed to contribute to practical understanding of spatial ecology. Nevertheless, there is one broad conclusion, namely that the observation of spatially localised patterns of high or low species concentrations (whether spatial or spatio-temporal) do not necessarily imply the existence of spatial heterogeneous causes. Specifically, within the

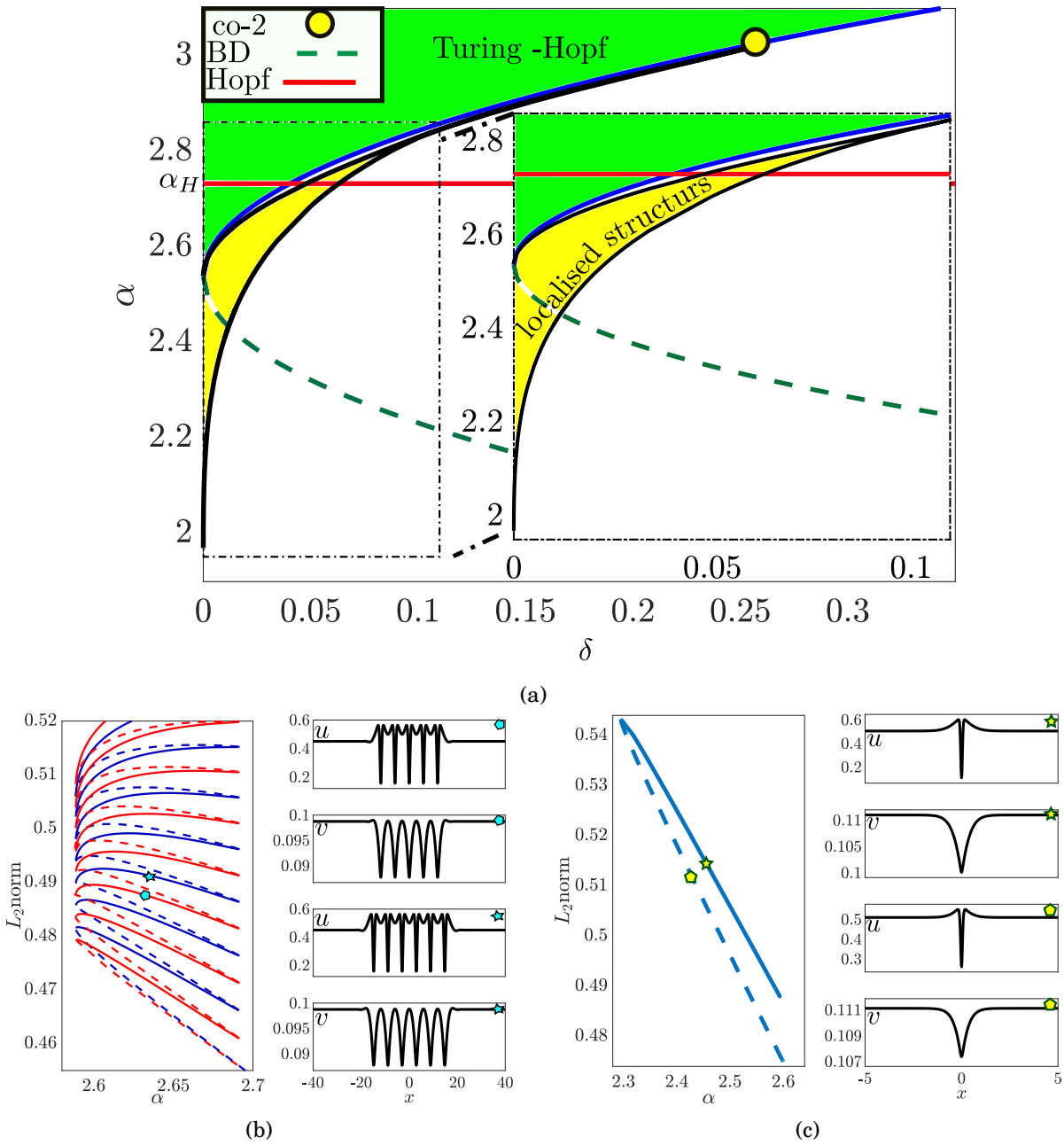

Figure 5.10: (a) Two-parameter bifurcation diagram of steady solutions to (5.10) in the (δ, α)-plane for fixed $\gamma = 0.86$ and $\beta = 0.9$. The meaning of colours and symbols is as in Figure 5.3, as is the method of computation. (b) Homoclinic snaking for $\delta = 0.03$ as α varies. The continuous (dashed) line indicates stable (unstable) solution, whereas red (blue) indicates that the number of peaks in the solution is odd (even). Two stable solutions with different number of peaks marked by the hexagon and star in the snaking diagram are shown alongside. (c) One-parameter continuation of the single patch solution for $\delta = 0.004$, showing a stable large-amplitude state being connected to an unstable lower-amplitude one via a fold.

simplest generic predator-prey models there are parameter regimes where the Turing bifurcation is sub-critical and localised patterns are to be expected. In the models we have studied, the parameter limit in question requires that the prey is relatively static while the predator diffuses more rapidly. One particular application of this limit could be the existence of localised vegetation patches in an arid environment where the prey is associated with the vegetation ecosystem which the predator is associated with the wider environment of the region; see e.g. [26, 27, 41].

CHAPTER 6

INTRACELLULAR PARTITIONING MODELS FOR CELL POLARITY

6.1 Introduction

This chapter provides a detailed study of the cell polarity models including the effect of the source and loss terms. The motivation for including the extra source and loses terms comes from the works of Payne and Grierson [131] and Verschueren and Champneys [165] in order to consider sligtly longer time scales in which inactive species are created by cell nucleons and active species are used in the promotion of microtubule controlled growth processes . In particular, the related works proposed by [32, 165] in studying the formation of localised patterns with plants cells has been a prime motivation for this work. The fundamental difference between those models and the models for cell polarity reviewed in section 1.3.2 is the number of state variables. Here, we consider a more realistic model with four components which can represent two different ROPs (A and B) which can occur in active and inactive forms. In what follows, we shall consider (1.1) with the source and loss terms. Hence we have

$$\frac{\partial A^*}{\partial t} = D_{A^*}\frac{\partial^2 A^*}{\partial x^2} + F(A^*,A,B^*,B) - \epsilon\xi A^*, \tag{6.1a}$$

$$\frac{\partial A}{\partial t} = D_A\frac{\partial^2 A}{\partial x^2} - F(A^*,A,B^*,B) + \epsilon\theta, \tag{6.1b}$$

$$\frac{\partial B^*}{\partial t} = D_{B^*}\frac{\partial^2 B^*}{\partial x^2} + G(A^*,A,B^*,B) - \epsilon\xi B^*, \tag{6.1c}$$

$$\frac{\partial B}{\partial t} = D_B\frac{\partial^2 B}{\partial x^2} - G(A^*,A,B^*,B) + \epsilon\theta, \tag{6.1d}$$

where ξ represent the strength of a constant source of inactive form; θ is the linear loss of active form and ϵ expresses the importance of the source of inactive form and the loss in the active form. Different possible functional forms for F and G where are given in (1.3)-(1.6) in section 1.3.2.

Without loss of generality the calculations that follow shall use the modified Abley et al model (1.4) by default. Recall that for this model we have

$$F = \left(\eta A^{*2} + \rho\right) A - \left(\alpha B^{*} + \mu\right) A^{*} \tag{6.2a}$$

$$G = \left(\eta B^{*2} + \rho\right) B - \left(\alpha A^{*} + \mu\right) B^{*}. \tag{6.2b}$$

We shall briefly consider the other three forms of F and G introduced in section 1.3.2 at the end of this chapter.

6.2 Linear stability analysis

In this section, we perform the linear stability analysis of full system (6.1) to be able to determine under which conditions spatial instability occurs for some values of the given parameters. We also seek to demonstrate important information on Turing type behaviour for the specific model being used. Hence, our initial point is to find the homogeneous equilibrium points of (6.1), given this is achieved by letting

$$\partial_t A^{*} = \partial_t A = \partial_t B^{*} = \partial_t B = \partial^2_{xx} A^{*} = \partial^2_{xx} A = \partial^2_{xx} B^{*} = \partial^2_{xx} B = 0,$$

in (6.1) and then solving a system of nonlinear algebraic equations. Consequently, the homogeneous steady state solution is found to be unique and given by

$$A^{*}_0 = B^{*}_0 = \frac{\theta}{\xi}, \quad A_0 = B_0 = \frac{\theta\left(\epsilon\xi^2 + \alpha\theta + \mu\xi\right)}{\eta\theta^2 + \xi^2\rho}. \tag{6.3}$$

To investigate the spatial instability of the full nonlinear system (6.1), we follow Section 2.2. Hence, we introduce the new variable (2.4) and we write (6.1) in the following form

$$(u_1, u_2, u_3, u_4)^T_t = (J + D\partial_{xx})(u_1, u_2, u_3, u_4)^T + NL. \tag{6.4}$$

Here J is given by

$$J = \begin{pmatrix} a & b & -c & 0 \\ d & -b & c & 0 \\ -c & 0 & a & b \\ c & 0 & d & -b \end{pmatrix}, \tag{6.5}$$

where

$$a = \frac{\left(\eta\theta^2 - \xi^2\rho\right)\left(\epsilon\xi^2 + \alpha\theta + \mu\xi\right)}{\left(\eta\theta^2 + \xi^2\rho\right)\xi},$$

$$b = \frac{\eta\theta^2 + \xi^2\rho}{\xi^2},$$

$$c = \frac{\alpha\theta}{\xi},$$

$$d = \frac{-\alpha\eta\theta^3 - \eta\xi\left(2\epsilon\xi + \mu\right)\theta^2 + \alpha\xi^2\rho\theta + \mu\xi^3\rho}{\left(\eta\theta^2 + \xi^2\rho\right)\xi},$$

D is the diffusion matrix which is given by

$$D = \begin{pmatrix} \delta & 0 & 0 & 0 \\ 0 & 1 & 0 & 0 \\ 0 & 0 & \delta & 0 \\ 0 & 0 & 0 & 1 \end{pmatrix}, \tag{6.6}$$

and NL contains the nonlinear terms. By substituting the ansatz (2.7) into the linear part of (6.4), we obtain the classical eigenvalue problem (2.8). Accordingly, spatial instability will appear when any modes of the dispersion relation (2.9) cross zero; that is when $\Re(\lambda(k)) = 0$ for one of the branches of the eigenvalues $\lambda(k)$. Taking the maximal $\Re(\lambda)$ and demanding that $\lambda(k)$ first touches zero, we gain the spatial instability curve given by the conditions (2.11). Using standard calculus techniques, we find the spatial instability curve and the critical value for the wave number k_c to be given by the solution to the pair of simultaneous equation

$$\delta^2 k_c^4 + S_1 k_c^3 + S_2 k_c^2 + S_3 k_c + S_4 = 0, \tag{6.7a}$$

$$4\delta^2 k_c^3 + 3S_1 k_c^2 + 2S_2 k_c + S_3 = 0, \tag{6.7b}$$

where

$$S_1 = 2\delta\left(\delta b - a\right),$$

$$S_2 = b^2\delta^2 - 4b\left(a + \frac{b}{2}d\right)\delta + a^2 - c^2,$$

$$S_3 = 2b(a+d)(-b\delta + a),$$

$$S_4 = b^2(a+d)^2.$$

The system (6.1) has six parameters and it is difficult to examine the effect of every possible combination. Hence, we investigate (6.1) by considering the auto-activation rate η and the membrane activator diffusion constants δ as a bifurcation parameters. We fix the other parameters as follows

$$\alpha = 0.005, \quad \epsilon = 0.01, \quad \mu = 0.05, \quad \rho = 0.06, \quad \xi = 2.7, \quad \rho = 0.06, \quad \theta = 0.5.$$

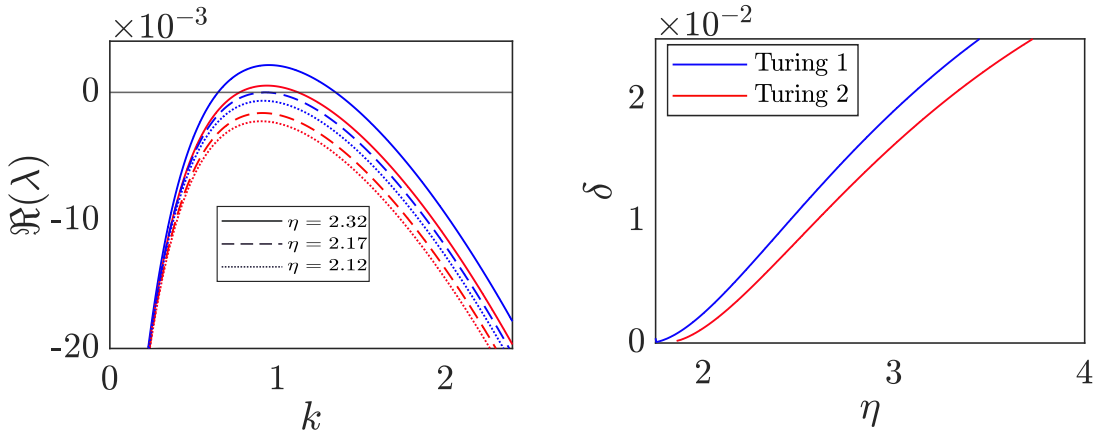

(a) (b)

Figure 6.1: (a) Dispersion relation of (6.1) for three parameters choices for η with fixed $\delta = 0.005$. (b) Turing instability curve as function of the parameters η and δ where the blue (red) curve present the first (second) mode of instability.

The values of parameters α, μ and ρ come from the experimental work in [1], and the parameters ϵ, θ and ψ were selected by us but are commensurate with the values used in [165]. Figure 6.1a shows the real part of the dispersion relation as a function of the wave number k for three different values of η. We detect that as η decreases, the largest $\Re(\lambda(k))$ instability mode decreases also. The instability disappears all together for η sufficiently small. It is worth noting that the dispersion relation in this case consists of two distinct curves, because of the 4th-order equation (6.7). Hence, we gain two distinct modes of spatial instability with different wave numbers. Because of this, in Figure 6.1b we obtain two critical curves for instability in the $(\eta - \delta)$-plane. These curves corresponds to different modes of instability. The blue curve represents the first mode of instability of the dispersion relation upon increasing η and the red curve gives the second mode. Note in the parameter region investigated we have not found any temporal Hopf bifurcation.

To differentiate between these two modes of instability, we plot the critical spatial eigenmodes for each mode. Figure 6.2a exhibits the spatial eigenmode from the first mode of instability, which shows that the spatial eigenvalues for A^* and B^* are perfectly out of phase (see Figure 6.2b). Hence, we will call the first mode of instability an *interleaved* pattern. In comparison, in the second mode of instability, the spatial eigenmodes are perfectly in phase. Hence, we call the second mode of instability an *overlaid* patten.

6.2.1 Weakly nonlinear analysis

After achieving the conditions for spatial instability, a weakly nonlinear analysis of the Turing bifurcation can be calculated using the normal form theory in Section 2.3. We now present the results at each order, omitting the detail which we carried out in Maple.

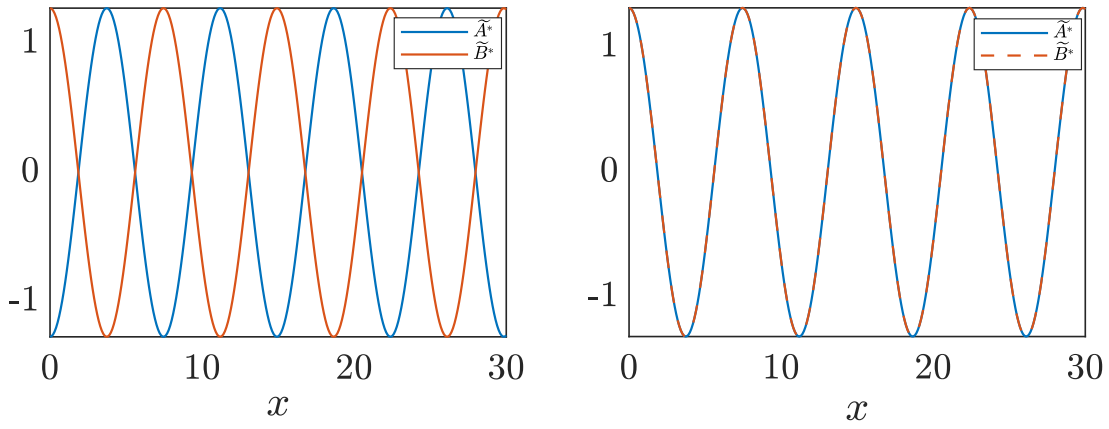

(a) (b)

Figure 6.2: The A^* and B^* components spatial eigenmodes for the instability for (a) interleaved case and (b) the overlaid case with $\delta = 0.015$ and $\eta = 2.8$.

Order 1

At this order, (6.4) is equivalent to the linear problem. Since the linear operator at this order is singular, the solution of $\boldsymbol{W}^{(1)}$ can be written as follows:

$$\boldsymbol{W}^{(1)} = \boldsymbol{\psi}(Ae^{ik_c x} + c.c), \tag{6.8}$$

where we choose to scale the eigenvector $\boldsymbol{\psi}$ so that

$$\begin{aligned}
\psi_1 &= -\frac{bck^2}{P}, \\
\psi_2 &= -\frac{bc\left(-\delta k^2 + a + d\right)}{P}, \\
\psi_3 &= -\frac{b\left(\left(-\delta k^2 + a + d\right)b + k^2\left(-\delta k^2 + a\right)\right)}{P}, \\
\psi_4 &= 1,
\end{aligned}$$

where

$$P(k) = \delta^2 k^6 + \left(b\delta^2 - 2a\delta\right)k^4 + \left(-(2a+d)\delta b + a^2 - c^2\right)k^2 + ab(a+d).$$

Order 2

At this order, (6.4) becomes

$$f^2 \partial_A \boldsymbol{W}^{(1)} + c.c = (J + D\partial_{xx})\boldsymbol{W}^{(2)} + \boldsymbol{m}_{20}|A|^2 + c.c) + \boldsymbol{m}_{22}(A^2 e^{2ik_c x} + c.c.), \tag{6.10}$$

where

$$
\begin{aligned}
m^1_{20} = m^1_{22} =& A_0\eta\psi_1^2 + 2\eta A_0^*\psi_1\psi_2 - \alpha\psi_1\psi_3,\\
m^2_{20} = m^2_{22} =& -m^1_{20},\\
m^3_{20} = m^3_{22} =& B_0\eta\psi_3^2 - \alpha\psi_1\psi_3 + 2\eta B_0^*\psi_3\psi_4,\\
m^4_{20} = m^4_{22} =& -m^3_{20}.
\end{aligned}
$$

Since no secular terms are observed, we can then assume that $f^{(2)} = 0$ and substitute the ansatz (2.21) into (6.10). Therefore, the uncoupled linear system is obtained which is given by (2.22). By solving (2.22), the solution for the first correction in the change of variable (6.4) is achieved.

Order 3

At this order, we have the following

$$
f^3\partial_A \boldsymbol{W}^{(1)} + c.c = (J + D\partial_{xx})\boldsymbol{W}^{(3)} + \boldsymbol{m}_{31}(|A^2|Ae^{ik_c x} + c.c.) + \boldsymbol{m}_{33}(A^3 e^{3ik_c x} + c.c.), \tag{6.12}
$$

where

$$
\begin{aligned}
m^1_{31} =& 2\psi_1 A_0(2Q^1_{20} + Q^1_{22}) + 2A_0^*\eta(2\psi_2 Q^1_{20} + \psi_2 Q^1_{22} + 2\psi_1 Q^2_{20} + \psi_1 Q^2_{22})\\
&+ \alpha(2\psi_3 Q^1_{20} + \psi_3 Q^1_{22} + 2\psi_1 Q^3_{20} + \psi_1 Q^3_{22}) + 3\eta\psi_1^2\psi_2,\\
m^2_{31} =& -m^1_{31},\\
m^3_{31} =& 2\psi_3 B_0(2Q^3_{20} + Q^3_{22}) + 2B_0^*\eta(2\psi_4 Q^3_{20} + \psi_4 Q^3_{22} + 2\psi_3 Q^4_{20} + \psi_3 Q^4_{22})\\
&+ \alpha(2\psi_3 Q^1_{20} + \psi_3 Q^1_{22} + 2\psi_1 Q^3_{20} + \psi_1 Q^3_{22}) + 3\eta\psi_3^2\psi_4,\\
m^4_{31} =& -m^3_{31},\\
m^1_{33} =& 2\eta A_0\psi_1 Q^1_{22} + 2A_0^*\eta(\psi_2 Q^1_{22} + \psi_1 Q^2_{22}) + \alpha(\psi_3 Q^1_{22} + \psi_1 Q^3_{22}) + \eta\psi_1^2\psi_2,\\
m^2_{33} =& -m^1_{33},\\
m^3_{33} =& B_0\psi_3 Q^3_{22} + \alpha(\psi_3 Q^1_{22} + \psi_1 Q^3_{22}) + 2B_0^*\eta(\psi_4 Q^3_{22} + \psi_3 Q^4_{22}) + \eta\psi_3^2\psi_4,\\
m^4_{33} =& -m^3_{33}.
\end{aligned}
$$

As a consequence of having a secular term at this order, we need to ensure the solvability of (6.12). To do so, the orthogonality between the right-hand side of (6.12) and the kernel of the adjoint needs to be met. Thus, we require the adjoint of the linear operator which is found to be

$$
(J + D\partial_{xx})^* = (J^T + D\partial_{xx}), \tag{6.14}
$$

and the kernel of the adjoint is

$$
W^* = \boldsymbol{\psi}^*(e^{ik_c x} + c.c.). \tag{6.15}
$$

Here

$$\psi_1^* = \frac{\left(k^2+b\right)\left(\left(-\delta k^2+a+d\right)b+k^2\left(-\delta k^2+a\right)\right)}{bck^2},$$
$$\psi_2^* = \frac{\left(-\delta k^2+a+d\right)b+k^2\left(-\delta k^2+a\right)}{ck^2},$$
$$\psi_3^* = \frac{k^2+b}{b},$$
$$\psi_4^* = 1.$$

After simple calculations, the expression for the solvability condition is obtained as follows

$$f^3\langle \boldsymbol{\psi}, \boldsymbol{\psi}^*\rangle + \langle -\boldsymbol{m}_{31}, \boldsymbol{\psi}^*\rangle |A|^2 A = 0. \tag{6.17}$$

Solving (6.17) for f^3, we have

$$f^3 = \frac{\langle \boldsymbol{m}_{31}, \boldsymbol{\psi}^*\rangle}{\langle \boldsymbol{\psi}, \boldsymbol{\psi}^*\rangle} |A|^2 A = L_3 |A|^2 A. \tag{6.18}$$

By applying the condition (6.18) and substituting the ansatz (2.34) into (6.12), we obtain the uncoupled solvable linear system given by (2.35) which provides the solution up to third order.

After achieving the analytic expression for L_3 we can now investigate where this might change sign. That would be a point at which the Turing instability changes from being subcritical to supercritical. As we present in Figure 6.1b, the system (6.1) has two spatial instability curves, which we shall call Turing 1 and Turing 2. Hence, we will examine the criticality for each curve. For the Turing 1 curve (the interleaved mode), we find the curve changes from subcritical to supercritical at $(\eta_c, \delta_c) = (3.302771, 0.020334)$. Similarly, we detect that the Turing 2 curve (the overlaid mode) changes criticality at $(\eta_c, \delta_c) = (3.072274, 0.020149)$. As we show in chapter 2 and 3, a subcritical bifurcation is a crucial element for the birth of localised structures in the reaction diffusion systems.

6.3 Homoclinic snaking and localised spikes

In this section, we provide detailed results on the creation of localised structures away from the vicinity of each codimension-two Turing bifurcation. As shown in chapter 2, spatial dynamics is an essential element for understanding the existence of different kinds of localised patterns. Hence, we rewrite the steady-state model of the full system (6.1) as an eight-dimensional dynamical system with the spatial coordinate playing the role of time. Linearising the spatial system about the homogenous steady state, we obtain nine possible eigenvalues configurations (see Figure 6.3). As explained in chapter 2, a temporal Turing instability corresponds to a Hamiltonian-Hopf bifurcation in which there are imaginary double pair of spatial eigenvalues. It can be noted from the spatial configuration in Figure 6.3 that there are two spatial instabilities that occur in (6.1). The first instability appears on the blue curve (Turing 1 for interleaved pattern) and the second

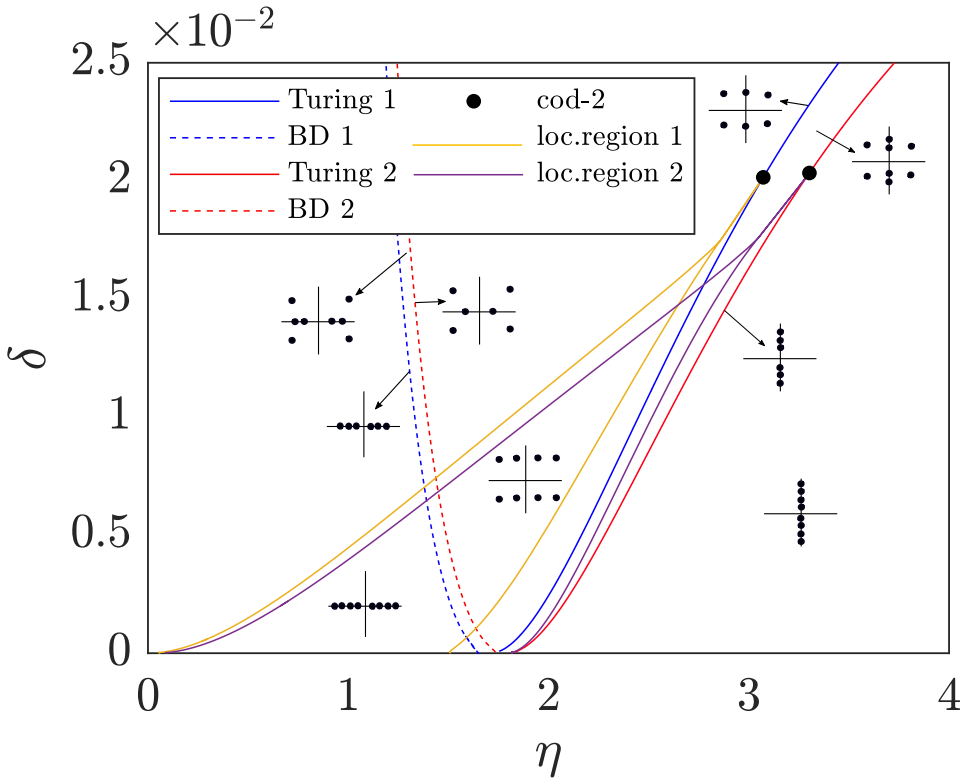

Figure 6.3: The bifurcation digram for (η, δ) fixing the other parameter values: $\alpha = 0.005$, $\epsilon = 0.01$, $\mu = 0.05$, $\rho = 0.06$, $\xi = 2.7$, $\rho = 0.06$, $\theta = 0.5$. The blue (red) curve represents the interleaved (overlaid) Turing instability curve. The yellow (magenta) curve shows the pinning region for the interleaved (overlaid) case. The blue and red dashed curves correspond to BD transition for the interleaved and overlaid cases, respectively. The sketches in the figure show the organization of the spatial eigenvalues.

instability is in the red curve (Turing 2 for overlaid pattern). Furthermore, we also know from chapter 2 that the BD transition gives the boundary between the homoclinic snaking and the isolated spikes. Specifically, this transition is where two double real spatial eigenvalues are found. Hence, we observe two BD transitions as depicted in Figure 6.3.

Figure 6.3 also displays the location of both codimension two points computed in the previous section. The figure also exhibits the extent of the two regions of the localised patterns obtained by following the outer fold of the localised patterns using AUTO in a similar manner to chapter 2. These regions give different kinds of localised patterns: interleaved (yellow curve) and overlaid (magenta curve). Let us now describe details on the types of patterns in each region, as well as, their stability.

6.3.1 Homoclinic snaking for the interleaved case

Figure 6.4a depicts the overall bifurcation diagram in (η, δ)-plane for the interleaved case. Interestingly, the bifurcation diagram is analogous to the Schnakenberg-like cases in chapter 2.

In particular, we encounter a curve for spatial instability, which undergoes a codimension-two sub-to -supercritical transition. From this point, the localised patterns region for interleaved type solution is born. This region is separated by the BD curve into two sub-regions: snaking and isolated spike. The snaking region produces the homoclinic snaking, which is two twisted branches of localised patterns with an increasing number of spikes (see Figure 6.4b). What is observed for these patterns is qualitatively just the same as we saw for the Schnakenberg-like models in chapter 3, but with no Hopf instability form in this parameter regimes. The snaking diagram is born from a Turing bifurcation at small amplitude, then gains stability after the first fold on the left-hand side of the snaking diagram. This then becomes unstable after the first fold on the right-hand side of the snake but gains a pair of peaks on either side of the central peak. Subsequently, as we move up the snaking diagram, each successive fold on the right-hand side leads to loos of stability and the addition of a pair of peaks to the central core. In contrast, the folds on the left-hand side of the snaking diagram lead to regaining stability.

The spike region is on the left-hand side of the BD curve in Figure 6.4a, where a single fold that connects two solutions: stable(unstable) with large (small) amplitude (see Figure 6.4c).

In the case of smaller δ-values, we compute the one-parameter bifurcation diagram with η and find that there are a lot of extra branches, causing the bifurcation to become complicated. Studying reasons for the appearance of these extra branches within the homoclinic snaking is beyond the scope of this thesis. Figure 6.5 represents the complex snaking bifurcation with examples of solution localised patterns that are associated with these extra branches. Note these solutions are generally unstable.

6.3.2 Homoclinic snaking for the overlaid case

Figure 6.6a displays the corresponding bifurcation diagram in the (η, δ)-plane for overlaid localised patterns. It is easy to note that both bifurcation diagrams for the interleaved and the overlaid are qualitatively equivalent. However, the spectrum computation for the snaking branches and the fold of the isolated spike reveals that all the solutions on the overlaid branches are unstable see Figure 6.6b and 6.6c for details.

In Figure 6.7, we illustrate examples of unstable solutions, the leading eigenvalues and the critical eigenfunctions. Here, parts of the branches that would otherwise have been stable in the previous case are found to have n additional unstable modes where n is the number of the large amplitude humps in the localised patterns. Thus, for the solution shown in 6.7a which is the 1-hump solution on the odd branch we see a single localised unstable eigenmode which corresponds to the A^* and B^* components separation. Whereas Figure 6.7b is for the 2-hump solution we see two such localised eigenmodes which correspond to the combination of A^*- B^* separation and humps moving apart.

Now, we explore the dynamics of model (6.1) through numerical integration of the complete PDE system using the explicit second-order finite difference method with zero flux boundary

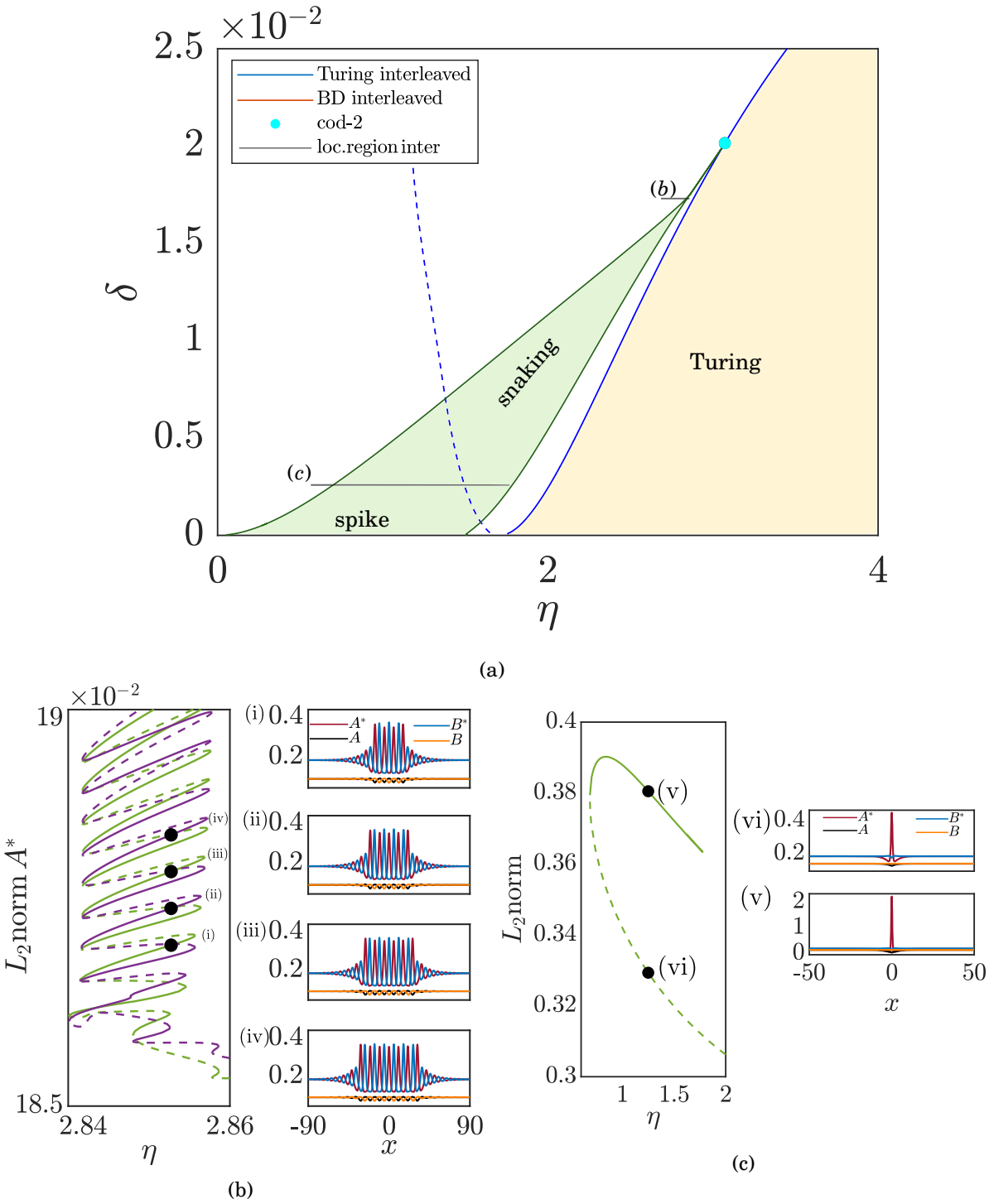

Figure 6.4: The (η, δ) bifurcation diagram for the interleaved case. Parameter values as in Figure 6.3. (b)-(c) Results of one parameter continuation from the snaking and the spike regions for $\delta = 0.01748$ and $\delta = 0.0025$ respectively. Note the solid lines represent stable branches and the dashed line unstable branches.

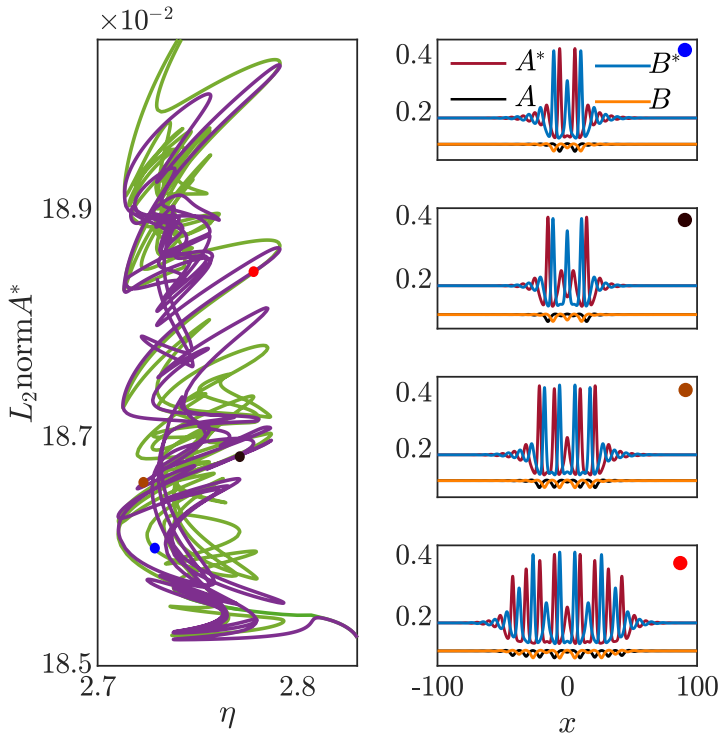

Figure 6.5: The homoclinic snaking bifurcation for $\delta = 0.0165$ which is less than δ in figure 6.4b. Note the solid lines do not necessary indicate stability which has not computed in this case.

conditions (see Section 2.6). We consider the even solution in Figure 6.7b as an initial condition with small spatial perturbation to the A^* and A components. Hence, the initial condition is $(A^*(x,0),A(x,0),B^*(x,0),B(x,0)) = \hat{A}^*(x)+\omega,\hat{A}(x)+\omega,\hat{B}^*(x),\hat{B}(x)$, where $(\hat{A}^*(x),\hat{A}(x),\hat{B}^*(x),\hat{B}(x)$ are the station localised solution with two overlaid peaks .

Figure 6.8 illustrates the result of the direct numerical integration. The result reveals that the overlaid solution quickly evolves into a bound state of two interleaved localised solutions which then appears to propagate stably.

6.4 Related results for another model

To confirm that what we have shown for the modified Abley model is in some sense universal to a four component wave pinning model, we shall briefly display the results of a further model with different nonlinearity, namely the juicy model (1.5). Models (1.5) and (1.4) have many analogous properties, therefore, one can analyse them in the same manner. Consequently, we omit most of the details. A straightforward calculation expose that system (1.5) has a single homogeneous steady state which is given by

$$A_0^* = B_0^* = \frac{\theta}{\xi}, \quad A_0 = B_0 = \frac{\theta\left(\left(\mu^2 c_a+\alpha\right)\xi^2+2\theta^2 c_a\right)\left(\epsilon\xi+\rho\right)}{\left(\beta\left(\mu^2 c_a+\alpha\right)\xi^2+c_a\theta^2\left(\eta\alpha\mu^2+2\beta\right)\right)\xi}. \tag{6.19}$$

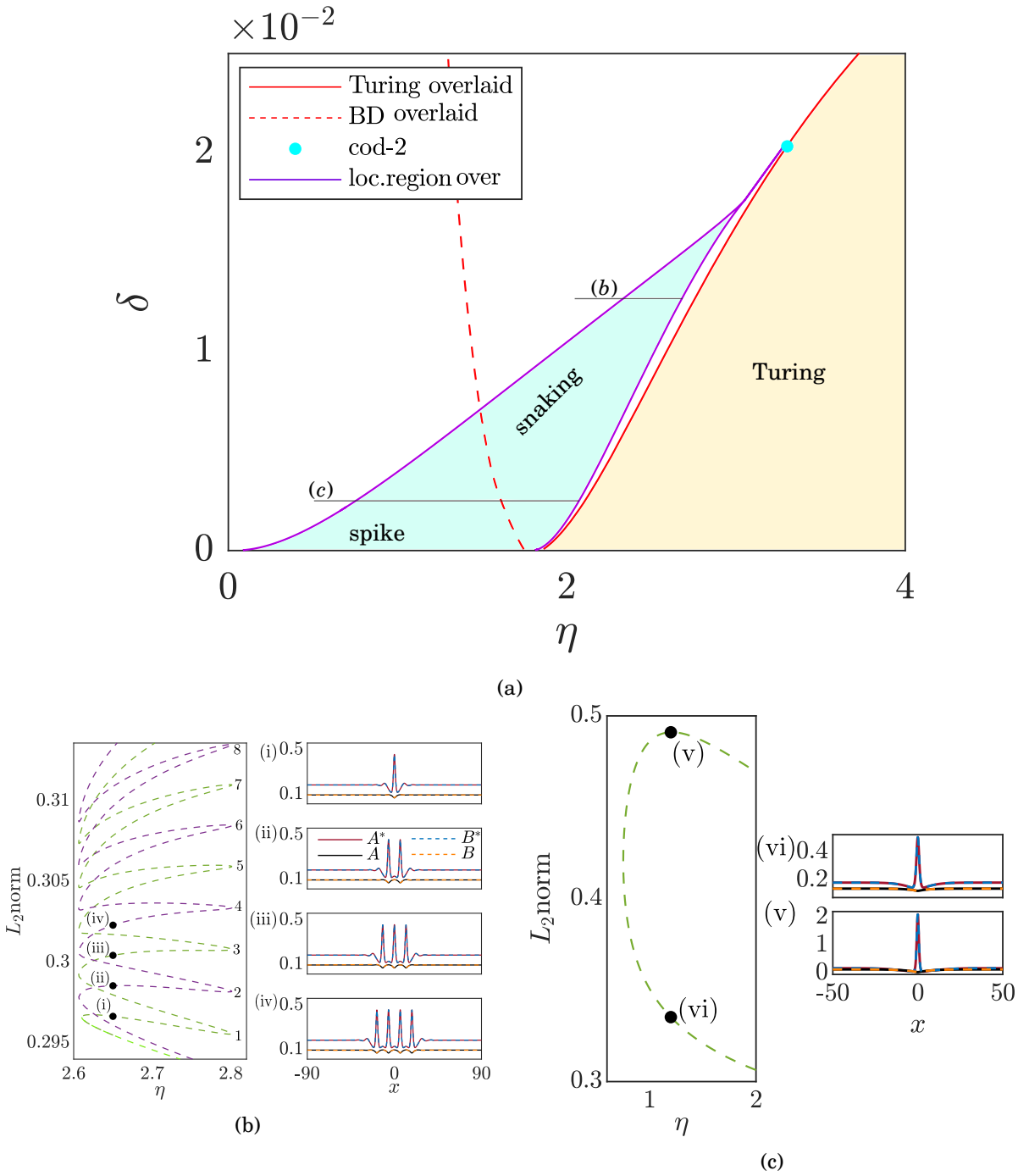

Figure 6.6: The (η, δ) bifurcation diagram for the overlaid case. Parameter values as in Figure 6.3. (b)-(c) Results of one parameter continuation from the snaking and the spike regions for $\delta = 0.0145$ and $\delta = 0.0025$ respectively.

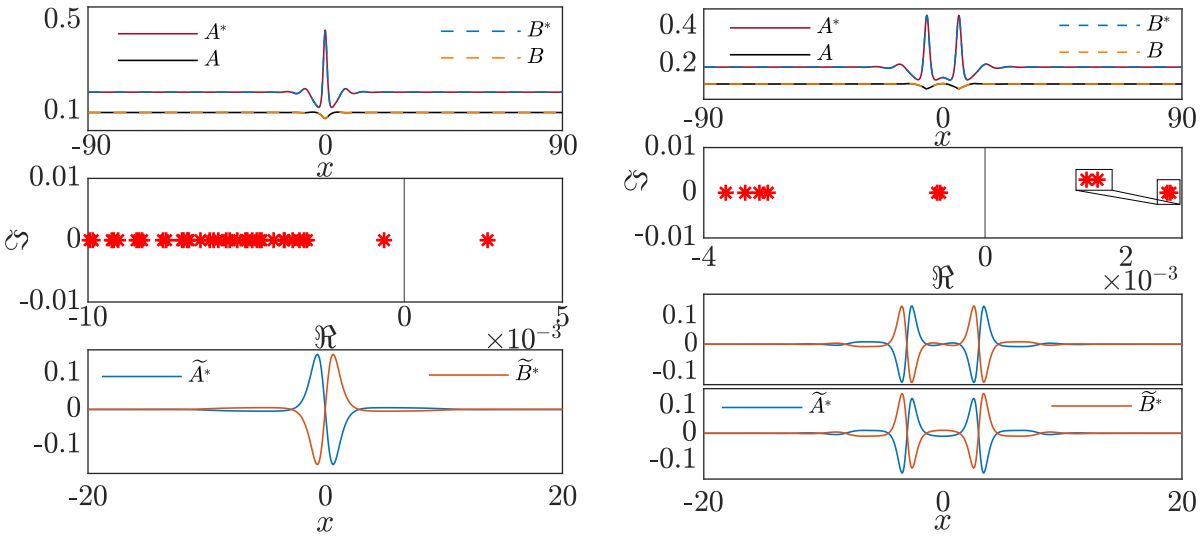

Figure 6.7: (a) Example solutions from the odd branch, the corresponding linear spectrum and the leading eigenmode. Panel (b): solution from the even branch, the corresponding linear spectrum and the leading eigenmode; note the zoom in the middle panel shows that extreme right eigenvalue is actually two nearby real eigenvalues.

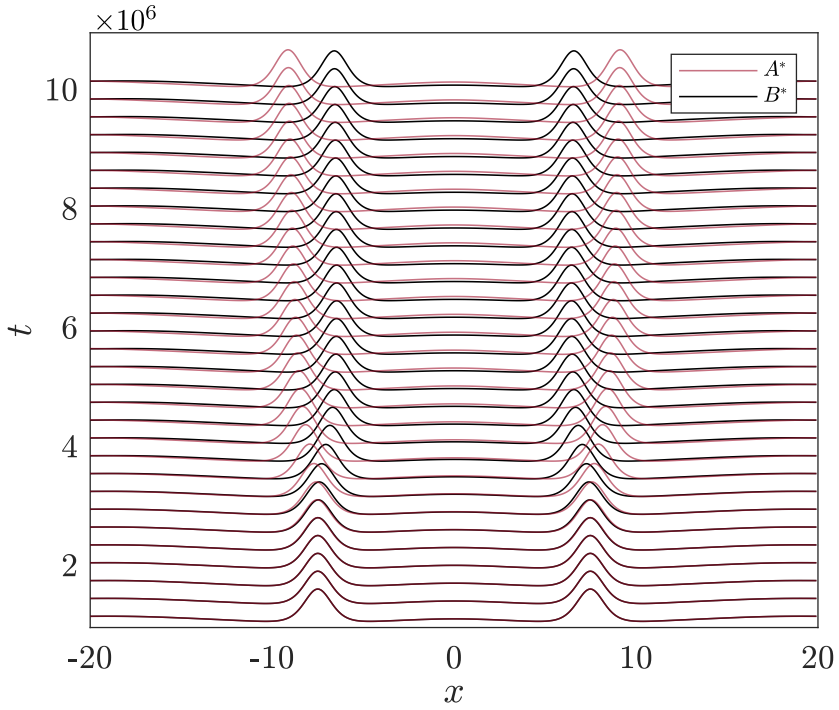

Figure 6.8: A direct numerical simulation of model (6.1) conducted using two spikes of the overlaid patterns as initial conditions with $\delta = 0.011$, $\eta = 2.24$. Other parameter values: as in Figure 6.3

Having determined the homogenous steady state, we implement the linear stability analysis followed by the weakly nonlinear analysis outlined in Sections 2.2 and 2.3, respectively. The bifurcation diagram in Figure 6.9 displays the fruit of the linear and weakly nonlinear analysis for fixed $\alpha = 80, \beta = 0.12, c_a = 20, \epsilon = 0.01, \mu = 0.5, \xi = 1, \rho = 0.2, \theta = 0.2$, shown precisely in the same form as Figure 6.3. We note that Figure 6.9 demonstrates qualitatively highly similar results to Figure 6.3. Fascinatingly, although the qualitative results are equivalent, any simple translation can not transform the models onto one another because of the difference in nonlinear terms. Therefore, the similarity between results suggests a particular generality of the bifurcation structures revealed.

6.5 The limit of conservation of mass

As the mass conservation limit approaches, the obvious question that arises is what is going to happen to the region of localised patterns as we approach the limit. As a response to this question, we will closely follow the work of Verschueren and Champneys [165]. Also, we will consider the choice of interleaved patterns since they provide a stable solution, and we are interested in stable solutions.

The first step one needs to do in order to understand the case when $\epsilon \to 0$ is to examine the bifurcation diagram 6.4 and understand the behaviour defined by both the Turing bifurcation and BD transition curves. Using an analytical expression for these curves (6.7), we can examine them to see how they change as ϵ approaches zero. In Figure 6.10a we can see how the bifurcation diagram 6.4 for different values of ϵ can appear. With $\epsilon \to 0$, we can easily deduce that both conditions for the Turing bifurcation and the BD curve become identical. Consequently, we will only have a pure real spatial eigenvalue. Thus in the limit of $\epsilon \to 0$, we will only be able to have localised spikes solutions and the snaking region will become vanishingly small.

The next step in the process is to compute the localised structure region for each ϵ value selected in Figure 6.10a. For finite ϵ this can be achieved by following folds in the branch of the localised patterns, just as it was in chapters 3 to 5 for the two-component model. Figure 6.10b illustrates a variety of localised patterns region for each ϵ value. According to the figure, the size of the localised patterns region increases substantially as the value of ϵ approaches zero. Since we now know that ϵ is closing in on zero, the only remaining solution would be to have localised spikes, as we discussed earlier. The consequent question that needs to be asked is, how do localised spikes broaden to become pair of two front as ϵ tends toward zero? This result was addressed asymptomatic in [165] using singular perturbation theory for the case of two component model. There it was found that the spike-like structures transform as $\epsilon \to 0$ into 'mesa state comprising two equal and opposite front (and back) solution. These fronts which are now described by the heterocinic rather then homoclinic solutions in the spatial dynamics, turn out precisely the steady states that are described by wave-pinning in the mass-conserved limit,

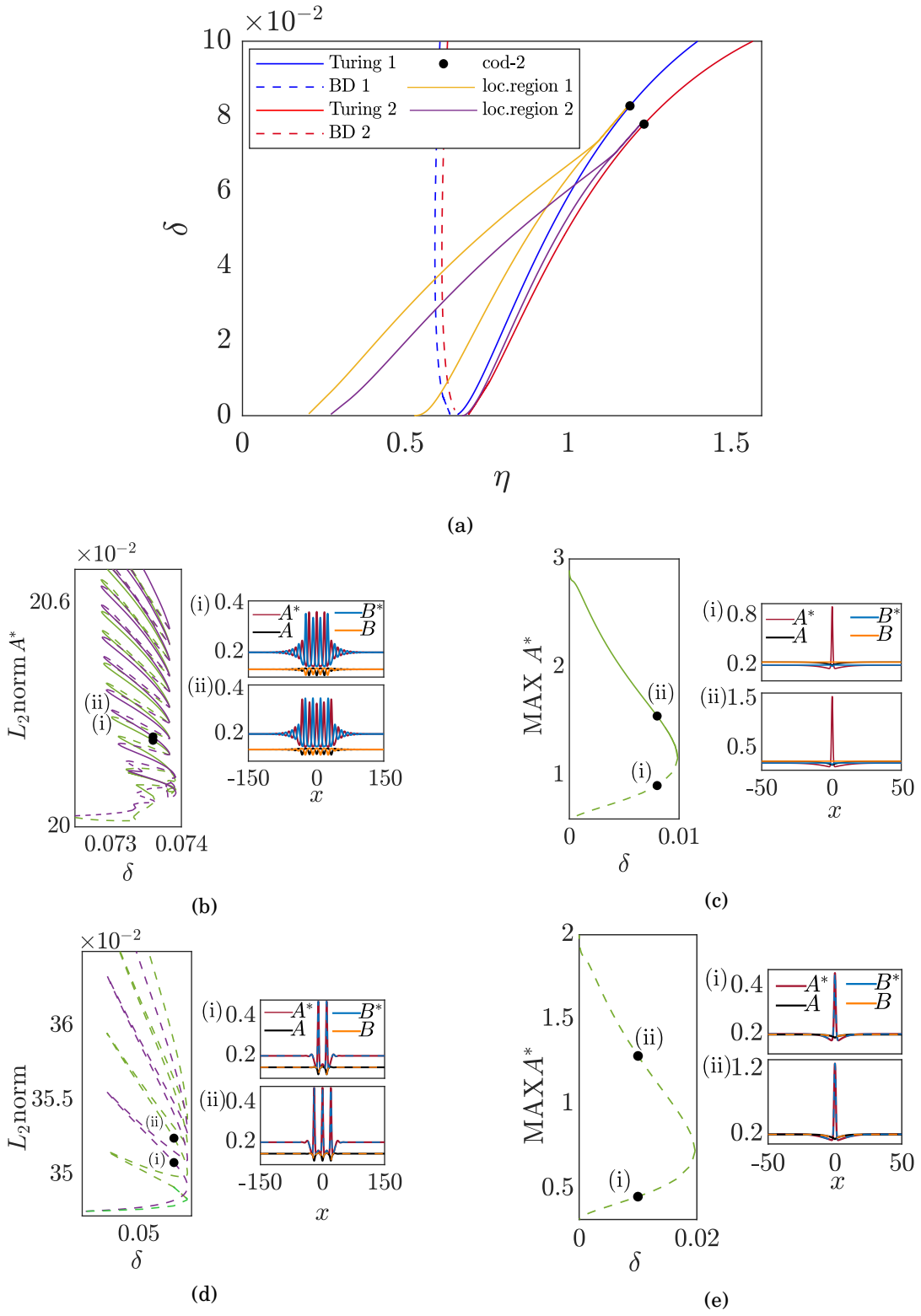

Figure 6.9: (a) Similar to Figure 6.3 for model (1.5). (b)-(c) Results of one parameter continuation in δ within the snaking and the spike regions for $\eta = 0.31$ and $\eta = 0.16$, respectively for the interleaved case. (d)-(e) Results of one parameter continuation in δ within the snaking and the spike regions for $\eta = 0.31$ and $\eta = 0.16$, respectively for the overlaid case. See Text for details.

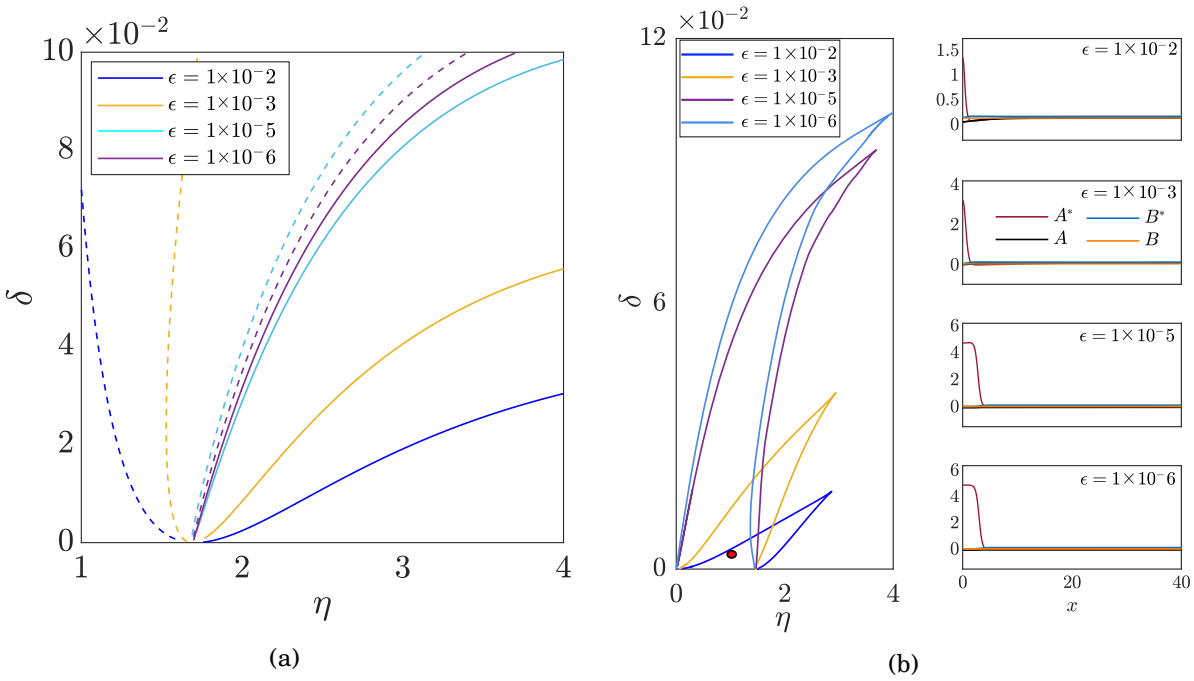

Figure 6.10: (a) A (η,δ)-plane bifurcation curve for different values of ϵ. Solid coloured curves indicate Turing bifurcation (spatial instability) and dashed coloured curves indicate BD transition.(b) Comparing the different localisation regions of various ϵ values. The red point is $(\eta,\delta) = (0,01,16,8)$, which lies within the region for all epsilon values displayed. [Right]: Spike solution over a half domain $[0,l]$ at this point, plotted for different ϵ values. Other parameter values: as in Figure 6.3 .

see [80, 86, 116]. An asymptotic analysis as in [165] is beyond the scope of this thesis. Note the mass-conserved model in this case leads to a fourth order spatial dynamics model which is not amenable to phase plane analysis like the mass-conserved model was in [165]. Instead here we merely illustrate what happens numerically. A complete story of the mass-conserved case ($\epsilon = 0$) will form the subject of the next chapter. The right-hand panels in Figure 6.10b illustrate how the spike solution is converted as the value of ϵ is decreased for fixed values of δ and η. Consequently, the δ and η values are chosen from the localized patterns of different ϵ-values in the vicinity of where they intersect. Also, the centre of the spike solution is taken to be the middle of the domain. Hence, we compute the numerical continuation on the half-domain. According to these profiled in the right hand-side of Figure 6.10b , as ϵ decreases, we can observe that the solutions for all components A, $A*$, B and $B*$ start to develop an elongated section which eventually will be front and back over the whole domain. Note we do not understand how the wedge shaped region does not appear to fill the whole of the section of the parameter space where the front solution exist; see Figure 6.11.

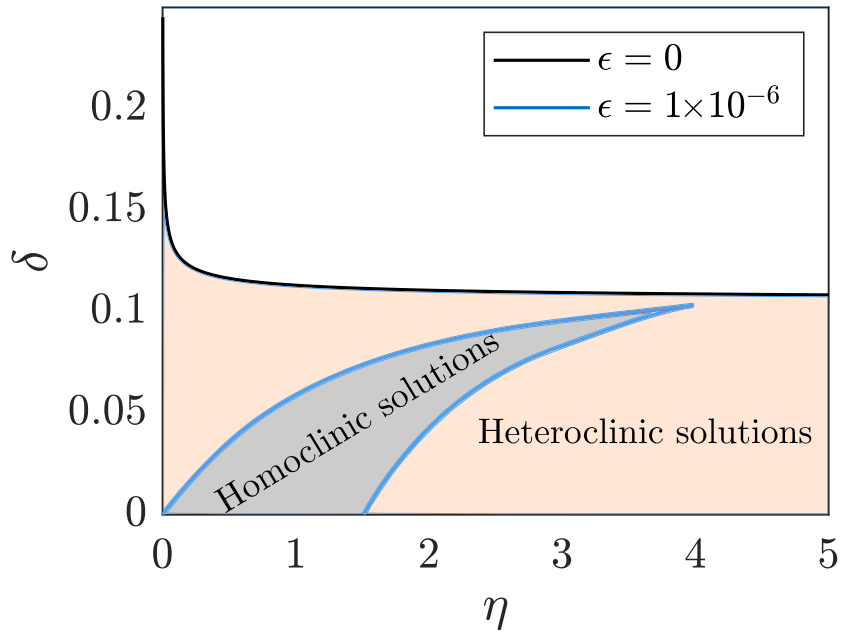

Figure 6.11: A (η, δ)-plane bifurcation curve for two different values of epsilon. The gray coloured region indicates the homoclinic solution for $\epsilon = 1 \times 10^{-6}$, while the peach coloured region indicates the heteroclinic solution for $\epsilon = 0$. Other parameter values: as in Figure 6.3.

6.6 Conclusion

In this chapter, we have investigated in detail the bifurcation diagrams and stability of localised patterns in cell polarity models of the form (6.1). The linear stability analysis for (6.1) demonstrates two possible modes of spatial (Turing) instability. These modes are called interleaved and overlaid because the two different ROP species are either interdigitated (out of phase) or are completely in phase.

The normal form analysis shows that each of these Turing instabilities undergo a sub-supercritical bifurcation transition at a codimension-two point. From this point, an envelope in the parameter space of each instabilty (i.e. the interleaved instabilty and the overlaid instabilty) is created inside which localised patterns occur. Each localised structures region, is just as shown in earlier chapters, and is separated by the BD transition curve into two subregions. These subregions are the snaking region and the single isolated spike region. Since there are two region of localised structures, we have investigated each region separately.

For the interleaved case, we obtain the usual homoclinic snaking bifurcation observed in Section 2.5.3 which contains two branches with odd and even number of peaks. Also, we have found a single fold that connects a stable and an unstable spike solution. Further, we have noticed that the homoclinic snaking structure breaks as we move down in the snaking region; including extra branches, which are unstable. The main reason for the appearance of these branches is unknown, which we leave as an open question for future research. Contrarily, for the overlaid

case, we show that localised pattern solutions from the snaking and the single spike regions are all unstable. The instability here is due to eigenmodes that cause a separation of the overlaid humps resulting in interleaved humps. Furthermore, to illustrate how our results are general for any models of the form (6.1), we present another example using different nonlinear terms. The findings reveal that the second example has qualitatively similar results to the first.

Finally, we also considered the limit as $\epsilon \to 0$. But in the next chapter we will investigate the actual case $\epsilon = 0$ in more detail where all spikes are replaced by fronts. Specifically, we would like to understand the structure of different front solutions at $\epsilon = 0$, because as in [165] for single ROP-species case, a detailed analysis of those fronts are first step to unfolding what happens as $\epsilon \to 0$. This will be the goal for the next chapter.

CHAPTER 7

CELL POLARITY MODELS IN THE MASS-CONSERVATION LIMIT

This chapter has been written up as a preprint with co-authors Alan Champneys and Mike Jeffrey

7.1 Introduction

Chapter 6 analysed the cell polarity system (1.1) when the total masses (integral over the whole domain) of $(A^* + A)$ and $(B + B^*)$ are not conserved. In this chapter, we are interested in understanding the scenario when the total masses are conserved, which was the setting for the original models analysed by [1, 72, 80] . Mathematically, it is fascinating to ask how the localised patterns observed in the previous chapter convert to the kind of front and back structures observed in the mass conservation case. Specifically, these structures represent heteroclinic solutions in one-dimensional domain and are the essential ingredients to cell polarisation. Therefore, we seek here to investigate the conserved mass system and its connection to the non-conserved system. Recall that the dynamics of this intracellular partitioning based on the auto-activation and cross-inhibition without sources and losses terms is mathematically expressed by the following system of reaction-diffusion equation the inactive forms (A,B) and the active forms (A^*,B^*)

$$\frac{\partial A^*}{\partial t} = D_{A^*}\frac{\partial^2 A^*}{\partial x^2} + F(A^*,A,B^*,B), \tag{7.1a}$$

$$\frac{\partial A}{\partial t} = D_A\frac{\partial^2 A}{\partial x^2} - F(A^*,A,B^*,B), \tag{7.1b}$$

$$\frac{\partial B^*}{\partial t} = D_{B^*}\frac{\partial^2 B^*}{\partial x^2} + G(A^*,A,B^*,B), \tag{7.1c}$$

$$\frac{\partial B}{\partial t} = D_B\frac{\partial^2 B}{\partial x^2} - G(A^*,A,B^*,B), \tag{7.1d}$$

where functions F and G describe the activation and inhabition dynamics of two ROP species A and B; see equations (1.3)-(1.6) in chapter 1 for different forms of F and G . In what follows we suppose $D_{A^*}, D_{B^*} \ll D_A, D_B$ specifically that $D_{A^*} = D_{B^*} = \delta$ and $D_A = D_B = 1$. Since the active and inactive components cannot leave or enter the cell, we enforce Neumann boundary conditions in one spatial dimension which we think as slice along the cell's diameter. Here it shall also be important that we pose the system (7.1) on a finite domain $x \in (-l, l)$.

We suppose for each ROP species there is the inter-conversion between active and inactive forms, yet each ROP is neither created nor destroyed. Therefore, the total ROP concentration within the cell must satisfy conservation laws. Adding (7.1a) and (7.1b) and then integrating whole domain we have

$$\int_{-l}^{l} \frac{\mathrm{d}}{\mathrm{d}t} \hat{A} dx = \int_{-l}^{l} \left[D_{A^*} A^*_{xx} + D_A A_{xx} \right] dx. \tag{7.2}$$

where $\hat{A} = A^* + A$. From the boundary condition, this leads to

$$\frac{\mathrm{d}}{\mathrm{d}t} \int \hat{A} = 0 \Rightarrow \int \hat{A} = constant := A_T, \tag{7.3}$$

and similarly for B. In [165], Verschueren et al. have applied the theory so-called Maxwell equal energy condition point on a system of a single ROP-species model to produce conditions for front solutions. Their results show that a system of two second-order differential equations can be reduced to a single second-order differential equation to predict when the system can present a heteroclinic solution in the parameter space. This can explain the so-called wave pinning phenomenon when the PDE steady state is such a front solution pinned to some portion of the domain. Here, we shall attempt to adopt the same theory but extend it to a two ROP species model. Consequently, we look for steady-state solutions by introducing new variables as follows

$$S(x) = \delta A^*(x) + A, \quad u(x) = \delta A^*(x) - A \tag{7.4a}$$

$$E(x) = \delta B^*(x) + B, \quad v(x) = \delta B^*(x) - B. \tag{7.4b}$$

Then substituting (7.4) into the time-independent version of (7.1), we obtain the following spatial system:

$$\frac{\partial^2 S}{\partial x^2} = 0, \tag{7.5a}$$

$$\frac{\partial^2 u}{\partial x^2} = -2F(u, S, v, E), \tag{7.5b}$$

$$\frac{\partial^2 E}{\partial x^2} = 0, \tag{7.5c}$$

$$\frac{\partial^2 v}{\partial x^2} = -2G(u, S, v, E). \tag{7.5d}$$

Due to the boundary conditions, the solutions of (7.5a) and (7.5c) are constant such that S and E become independent parameters. Therefore, the system (7.5) is reduced to two second-order

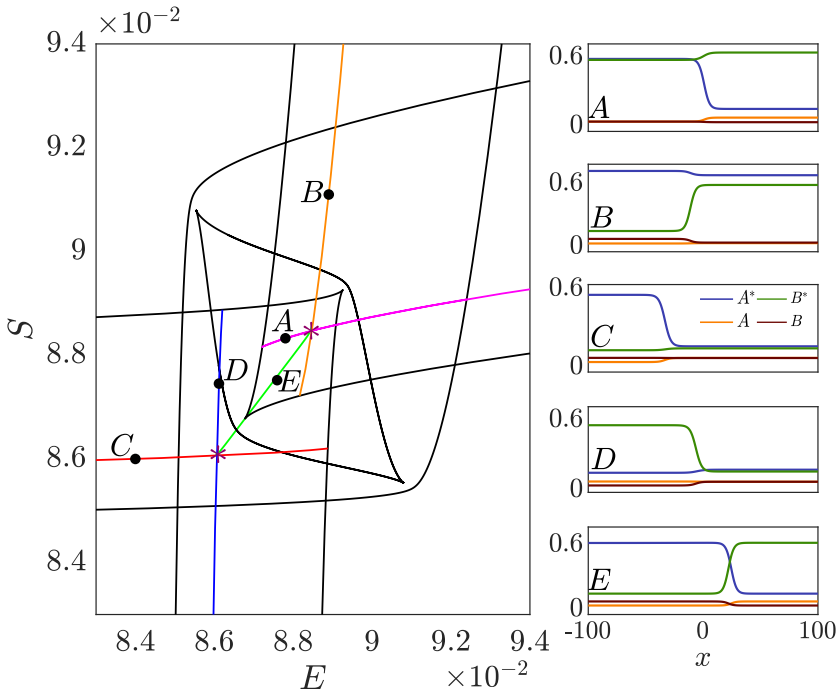

Figure 7.1: Bifurcation diagram of the reduce system of (7.6). Parameter values $\eta = 2$, $\mu = 0.05$, $\rho = 0.06$, $\alpha = 0.005$ and $\delta = 0.08$. For the detailed explanation see section 7.2 and section 7.3.

equations in variables u and v. This reduction allow a simpler explanation of the wave pinning phenomena as we will see later.

In general we will consider each of the specific forms of the function F and G listed in chapter 1; which are given by equations (1.4)-(1.6). However, for the development of the theory in this chapter we shell exclusively study the the modified Abley et al model as our worked example. Recall that for this model

$$F = \left(\eta A^{*2} + \rho\right) A - \left(\alpha B^* + \mu\right) A^* \tag{7.6a}$$

$$G = \left(\eta B^{*2} + \rho\right) B - \left(\alpha A^* + \mu\right) B^*, \tag{7.6b}$$

where the parameters α, η, μ and ρ have the same definition as in (1.3). Related results for other models are briefly mentioned in Section 7.5.

The rest of this chapter is outlined as follows. Section 7.2 will describe the set of homogeneous equilibria to (7.5) and how they change as either the parameters E and S or the system parameters vary. Then in section 7.3, we will consider possible heteroclinic connections between these steady states. Then section 7.4 will consider how the mass conservation properties of (7.2) affect the choice of polarised solution as a function of initial conditions. Section 7.5 will briefly summarise related overall results for other models, while section 7.6 will present brief conclusions.

7.2 Steady states and their heteroclinic connection

To characterise the heteroclinic solutions of (7.1) and (7.6), it is useful to look first at the steady states that they connect. Up to nine steady states can exist in the modified Ableу model. In this section we find their stability and the region of parameter space where they exist, to determine which are connected by the heterclinic orbits. Note this direct computation of conditions for equilibria can be formalised using catastrophe theory. See Appendix A for how to write generic conditions for bifurcations of different codimension between these equilibria.

The time independent system (7.5) can be written as

$$\begin{aligned} u'' &= -2F \\ &= 2\rho(u-S) + \left(\frac{2\mu}{\delta} + \frac{\eta}{2\delta^2}(u^2-S^2) + \frac{\alpha}{\delta^2}(v+E)\right)(u+S)\,, \\ v'' &= -2G \\ &= 2\rho(v-E) + \left(\frac{2\mu}{\delta} + \frac{\eta}{2\delta^2}(v^2-E^2) + \frac{\alpha}{\delta^2}(u+S)\right)(v+E)\,. \end{aligned} \tag{7.7}$$

Letting $u = x - \frac{1}{3}S$ and $v = y - \frac{1}{3}E$ eliminates the u^2 and v^2 terms to give the simpler expression

$$\begin{aligned} x'' &= \frac{\eta}{2\delta^2}\hat{f}\,, \qquad \hat{f} = x^3 + kxy + ax + ry + b\,, \\ y'' &= \frac{\eta}{2\delta^2}\hat{g}\,, \qquad \hat{g} = y^3 + kxy + cy + sx + d\,, \end{aligned} \tag{7.8}$$

where

$$\begin{aligned} k &= \frac{2\alpha}{\eta}\,, \qquad r = \frac{4\alpha S}{3\eta}\,, \qquad s = \frac{4\alpha E}{3\eta}\,, \\ a &= \frac{4}{\eta}\left\{\frac{\alpha E - \eta S^2}{3} + \delta(\mu + \delta\rho)\right\}\,, \\ c &= \frac{4}{\eta}\left\{\frac{\alpha S - \eta E^2}{3} + \delta(\mu + \delta\rho)\right\}\,, \\ b &= \frac{8S}{3\eta}\left\{\frac{1}{3}(\alpha E - \frac{2}{3}\eta S^2) + \delta(\mu - 2\rho\delta)\right\}\,, \\ d &= \frac{8E}{3\eta}\left\{\frac{1}{3}(\alpha S - \frac{2}{3}\eta E^2) + \delta(\mu - 2\rho\delta)\right\}\,. \end{aligned} \tag{7.9}$$

The x and y symmetry of the system (7.9) suggest changing to new set of variables. Let

$$X = x + y\,, \qquad Y = x - y\,, \tag{7.10}$$

then $(X'', Y'') = \frac{\eta}{2\delta^2}(\hat{F}, \hat{G})$, where

$$\begin{aligned} \hat{F} &= \frac{1}{4}X(X^2 + 3Y^2) + \frac{1}{2}k(X^2 - Y^2) + \frac{1}{2}(a + c + r + s)X \\ &\quad + \frac{1}{2}(a - c - r + s)Y + b + d\,, \\ \hat{G} &= \frac{1}{4}Y(3X^2 + Y^2) + \frac{1}{2}(a - c + r - s)X + \frac{1}{2}(a + c - r - s)Y \\ &\quad + b - d\,. \end{aligned} \tag{7.11}$$

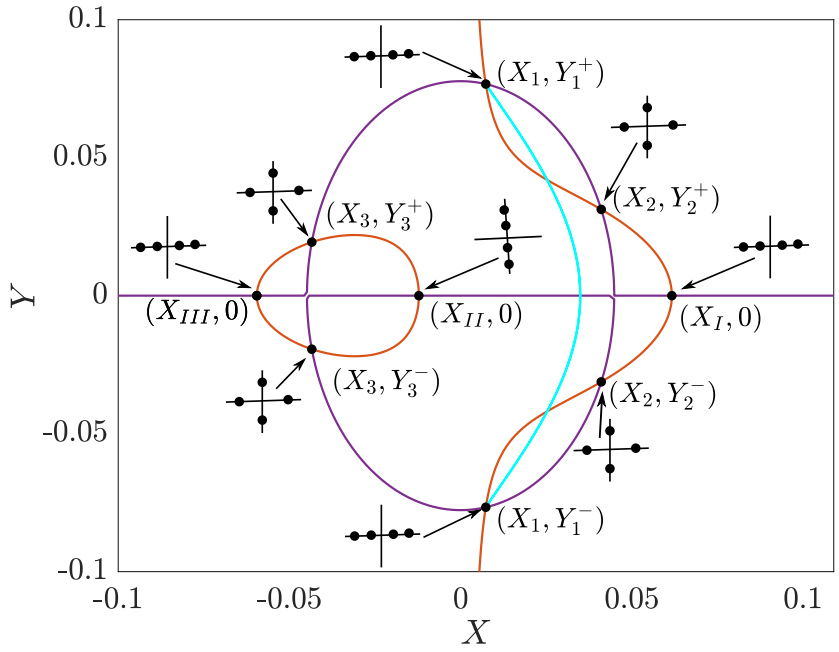

Figure 7.2: The nine equilibria lie at the intersections of the nullclines $\hat{F} = 0$ (purple) and $\hat{G} = 0$ (red). The heteroclinic solution (cyan) connects the '1+' and '1−' equilibria. The spatial eigenvalues of each equilibrium are shown (these will be derived in section 7.2.3. Shown for $\eta = 2$, $\mu = 0.05$, $\rho = 0.06$, $\alpha = 0.005$ and $\delta = 0.08$, and $S = E = 0.0878$.

To write this as a first order 4-dimensional system let $(X', Y') = \frac{\eta}{2\delta^2}(Z, W)$, giving

$$(X', Z', Y', W') = \left(\frac{\eta}{2\delta^2} Z,\, \hat{F},\, \frac{\eta}{2\delta^2} W,\, \hat{G}\right). \tag{7.12}$$

We will show in the following two subsections that this has up to nine equilibria, and we can label these as follows. There are three equilibria that we label

$$(X_I, Y_I), \quad (X_{II}, Y_{II}), \quad (X_{III}, Y_{III}), \tag{7.13}$$

and when $S = E$ these lie on an invariant subsystem of (7.12) where $Y = Y' = 0$. The remaining six equilibria lie on an invariant ellipse when $S = E$, and we label these as three pairs of points

$$(X_1^\pm, Y_1^\pm), \quad (X_2^\pm, Y_2^\pm), \quad (X_3^\pm, Y_3^\pm). \tag{7.14}$$

Examples of these are illustrated in Figure 7.2 for $E = S$, and in Figure 7.3 for $E \neq S$. The equilibria lie on the nullclines $X'' = 0$ (purple curves) and $Y'' = 0$ (red curves), and we find expressions for these in section 7.2.1. Also shown is the stability of the equilibria, which we will find in section 7.2.3. The system is symmetric about $Y = 0$ when $S = E$, and in Figure 7.2 a heteroclinic solution (cyan) is shown connected the '1+' and '1−' equilibria. This symmetry is broken when $S \neq E$, and in Figure 7.2 a heteroclinic solution (cyan) is shown connected the '1+' and 'I' equilibria.

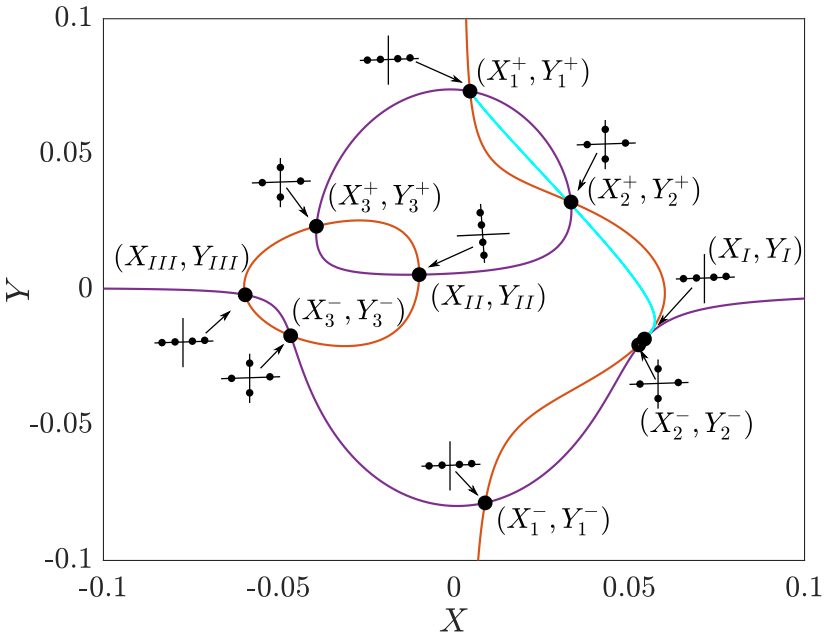

Figure 7.3: A perturbation of Figure 7.2 to $\eta = 2$, $\mu = 0.05$, $\rho = 0.06$, $\alpha = 0.005$ and $\delta = 0.08$, $E = 0.0881606$ and $S = 0.0872160$, showing the 9 equilibria slightly perturbed from the case in Figure 7.2. The heteroclinic solutions now connects the '1+' and 'I' equilibria. (Note the heteroclinic solution does not pass through the '2+' equilibrium in the full 4-dimensional space of (X, X', Y, Y'). Curve are as in Figure 7.2.

7.2.1 Locating the equilibria

To identify the equilibria of this system it is useful to begin with the simplification that occurs when $S = E$. From (7.9) this gives $a = c$, $r = s$, $b = d$, and substituting these into (7.11) gives

$$\begin{aligned} \hat{F} &= \frac{1}{4}X(X^2+3Y^2) + \frac{1}{2}k(X^2-Y^2) + (a+r)X + 2b\,, \\ \hat{G} &= Y\left\{\frac{1}{4}(3X^2+Y^2) + (a-r)\right\}. \end{aligned} \tag{7.15}$$

Like the general system this has up to nine equilibria, but here they decouple into two invariant subsystems with equilibria given by (7.13) and (7.14).

The system (7.15) has one invariant set on $Y' = Y = 0$ where

$$\begin{aligned} X' &= \frac{\eta}{2\delta^2}Z\,, \qquad Y'' = Y' = 0\,, \\ Z' &= \frac{1}{4}X^3 + \frac{1}{2}kX^2 + (a+r)X + 2b\,. \end{aligned} \tag{7.16}$$

This subsystem itself has three equilibria, which we denote by (7.13), so $Y_i = 0$ for $i = I, II, III$, and X_I, X_{II}, X_{III}, are the real roots of

$$\frac{1}{4}X_i^3 + \frac{1}{2}kX_i^2 + (a+r)X_i + 2b = 0\,, \qquad i = I, II, III\,. \tag{7.17}$$

For $S \neq E$ the surface $Y = 0$ ceases to be invariant, but we use this same labeling by continuation away from $S = E$.

On the elliptical surface $3X^2 + Y^2 = 4(r-a)$ we obtain another subsystem where, from (7.15),

$$X' = \frac{\eta}{2\delta^2} Z\,, \quad Z' = 0\,, \quad 3X^2 + Y^2 = 4(r-a)\,,$$
$$\frac{1}{2} Z' = -X^3 + k(X^2 + (a-r)) + (2r-a)X + b\,. \tag{7.18}$$

This has 6 equilibria, which we denote by (7.14). They satisfy $X_i^+ = X_i^- := X_i$, where X_i are the roots of

$$-X_i^3 + k(X_i^2 + (a-r)) + (2r-a)X_i + b = 0\,, \qquad i = 1,2,3\,. \tag{7.19}$$

and $Y_i^\pm = \pm\{4(r-a) - 3X_i^2\}$. When $S \neq E$ the ellipse also ceases to be invariant, but we use this same labeling for the equilibria by continuation away from $S = E$ (note $X_i^+ \neq X_i^-$ for $S \neq E$).

These equilibria are shown in Figure 7.2 for $S = E$. We see the three equilibria (X_1, Y_1), (X_2, Y_2), (X_2, Y_2), lying on the line $Y = 0$, while the six equilibria $(X_I^\pm, Y_I^\pm)$, $(X_{II}^\pm, Y_{II}^\pm)$, $(X_{III}^\pm, Y_{III}^\pm)$, lie on the ellipse $3X^2 + Y^2 = 4(r-a)$, as described by the subsystems in (7.16) and (7.18), respectively. In Figure 7.3 the system no longer decouple exactly into these subsystems, but we see the persistence of the equilibria.

Figure 7.4(b) shows the equilibria, for a range of different parameters as indicated in Figure 7.4(a). Panels A,B,C,D, are taken with parameters $S = E$, panels E,F, are taken with $S \neq E$.

7.2.2 Bifurcations

The bifurcation diagram in Figure 7.4(a) shows several black curves on which fold bifurcations occur, that is, pairwise annihilations among the equilibria. Looking at Figure 7.4(b) it is easy to see how these might occur, as the nullclines deform to bring together pairs of equilibrium points (where the nullclines intersect). Panels E and F show a heteroclinic solution that exists at parameters where one of the equilibria that the solution connects is being destroyed in a fold, and as such, as seen in Figure 7.4(a), the line of heteroclinic solutions terminates at E and F.

There are a number of mechanisms by which these bifurcations occur. In the symmetric system with $S = E$, we are able to derive these events explicitly.

The subsystem in (7.16) has 3 equilibria when

$$k^2 > 3(a+r) \quad \text{and} \quad (27b + 2k^3 - 9k(a+r))^2 < 4(k^2 - 3(a+r))^3\,, \tag{7.20}$$

and only one equilibrium otherwise, with folds occurring at $(27b+2k^3-9k(a+r))^2 = 4(k^2-3(a+r))^3$ and a cusp at $b = k^3/27$, $a + r = k^2/3$. At these parameters, with $S = E$, the system therefore undergoes fold and cusp bifurcations. For $S \neq E$ the folds continue outward into parameter space to form some of the fold curves as seen in Figure 7.4(a).

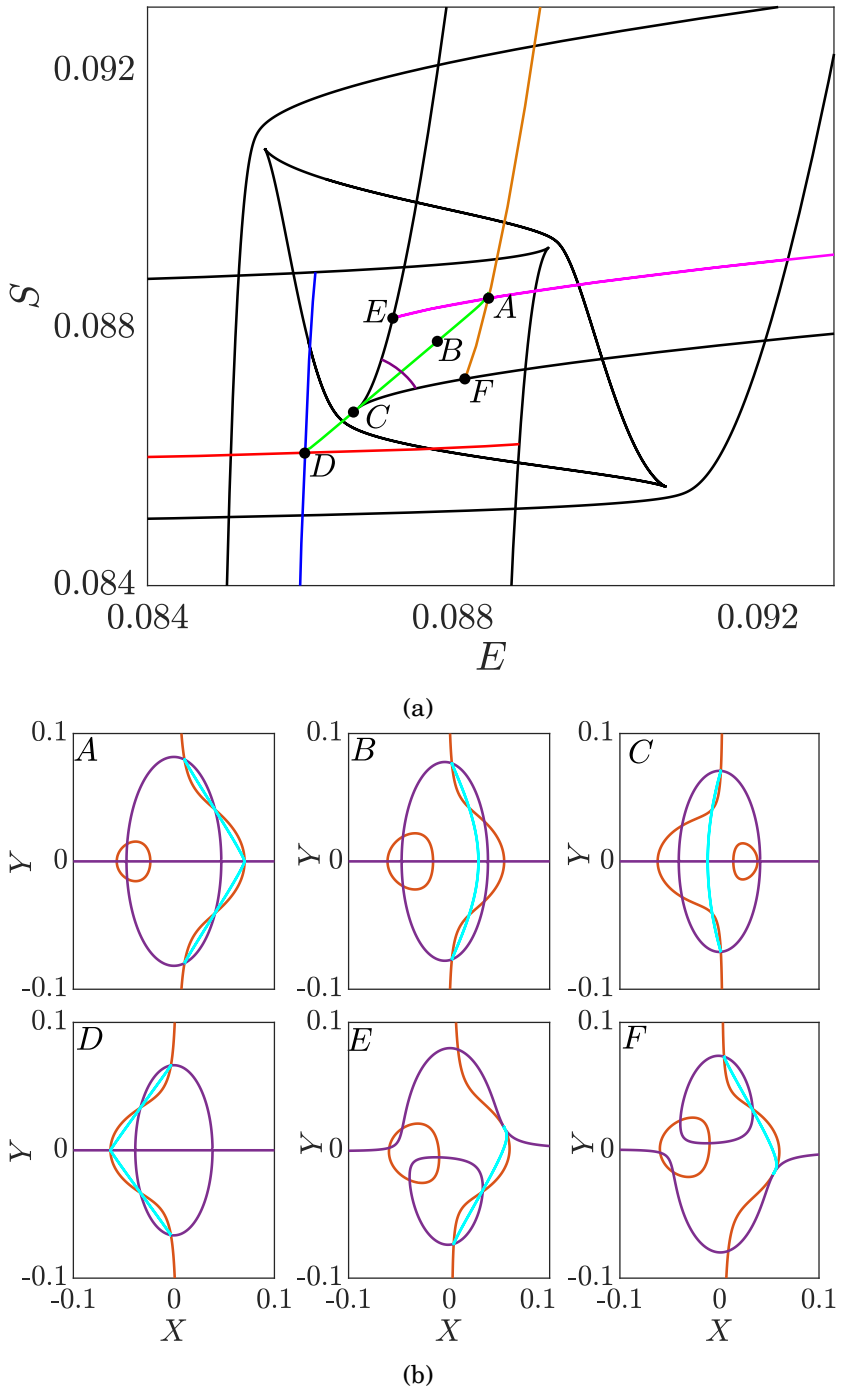

Figure 7.4: (a) Bifurcation diagram for (7.7). (b) The phase plane for (X,Y) in (7.11) with fixed $\eta = 2$, $\mu = 0.05$, $\rho = 0.06$, $\alpha = 0.005$ and $\delta = 0.08$, showing the nullclines $\hat{F} = 0$ (red) and $\hat{G} = 0$ (purple); the 9 equilibria lie at their intersections. The heteroclinic solution that exists in each case is shown.

The subsystem in (7.18) has 6 equilibria when

$$k^2 > 3a - 6r \quad \text{and} \quad 4(k^2+6r-3a)^3 > (54b+2k^3+18ak-9rk)^2\,, \tag{7.21}$$

and only two equilibria otherwise, with folds occurring at $4(k^2+6r-3a)^3 = (54b+2k^3+18ak-9rk)^2$ and a cusp at $108b = -27ak - 7k^3$, $3a-6r = k^2$. At these parameters, with $S = E$, the system therefore undergoes simultaneous fold and cusp bifurcations at symmetric values of Y. Again, for $S \neq E$ the folds continue outward into parameter space to form some of the fold curves as seen in Figure 7.4(a).

These two families of bifurcations occur where there are bifurcations in the roots $X_{I,II,III}$ of (7.17), and in the roots $X_{1,2,3}$ of (7.19). There is a further family of bifurcations where equilibria of the two subsystems annihilate with each other, and these turn out to be of most interest as they terminate the lines of heteroclinic solutions, as at the points E and F in Figure 7.4(a).

These addtinal bifurcations occur when a pair of equilibria on the ellipse $3X^2+Y^2 = 4(r-a)$ (belonging to the subsystem (7.18)) coalesce at $Y = 0$. When this occurs they also happen to coincide with an equilibrium from the $Y = 0$ invariant subsystem of (7.16). In this manner, 3 equilibria collide to create a cusp bifurcation at

$$\begin{aligned} b &= \frac{1}{3}\left(k(a-r) \mp \frac{2}{\sqrt{3}}(2r+a)\sqrt{r-a}\right)\,, \\ X^2 &= \frac{4}{3}(r-a)\,,\ Y = 0\,. \end{aligned} \tag{7.22}$$

One such cusp point lies at C in Figure 7.4(a). It can also happen that four equilibria from the ellipse subsystem collide with one from the $Y = 0$ subsystem, to create a butterfly bifurcation at

$$\begin{aligned} a &= \frac{2}{27}\left(9r - 4k^2 \pm 2k\sqrt{4k^2+9r}\right)\,, \\ b &= \frac{1}{27}\left(k(9r-18a-2k^2 \mp 2(k^2+6r-3a)^{3/2})\right)\,, \\ X &= \frac{k}{3} \pm \frac{1}{3}\sqrt{k^2+6r-3a}\,,\ Y = 0\,. \end{aligned} \tag{7.23}$$

Note these are each found only for the symmetric system with $S = E$, for which $a = c$ and $b = d$.

7.2.3 Local stability

Only some of the nine equilibria can be involved in generic heteroclinic orbits, namely those with at least a two-dimensional stable or unstable manifold. Let us determine which of the equilibria found in Section7.2.1 this applies to.

The Jacobian of the system (7.15) in (X, X', Y, Y') space is

$$J = \begin{pmatrix} 0 & 1 & 0 & 0 \\ \frac{3X^2}{4} + \frac{3Y^2}{4} + kX + a + r & 0 & \frac{3XY}{2} - kY & 0 \\ 0 & 0 & 0 & 1 \\ \frac{3XY}{2} & 0 & \frac{3X^2}{4} + \frac{3Y^2}{4} + a - r & 0 \end{pmatrix}. \tag{7.24}$$

For the invariant subsystem on $Y = 0$ given by (7.16) this simplifies to

$$J = \begin{pmatrix} 0 & 1 & 0 & 0 \\ \frac{3X^2}{4} + kX + a + r & 0 & 0 & 0 \\ 0 & 0 & 0 & 1 \\ 0 & 0 & \frac{3X^2}{4} + a - r & 0 \end{pmatrix}, \tag{7.25}$$

with eigenvalues

$$\lambda_1 = -\lambda_2 = \frac{1}{2}\sqrt{3X^2 + 4a - 4r}$$

and

$$\lambda_3 = -\lambda_4 = \frac{1}{2}\sqrt{3X^2 + 4kX + 4a + 4r}\,.$$

For the invariant subsystem on the ellipse given by (7.18) the Jacobian simplifies to

$$J = \begin{pmatrix} 0 & 1 & 0 & 0 \\ \frac{Y^2}{2} + kX + 2r & 0 & \frac{Y(3X-2k)}{2} & 0 \\ 0 & 0 & 0 & 1 \\ \frac{3XY}{2} & 0 & \frac{Y^2}{2} & 0 \end{pmatrix}, \tag{7.26}$$

with eigenvalues

$$\lambda_1 = -\lambda_2 = \frac{1}{2}\sqrt{M + 2\sqrt{\left(9Y^2 + k^2\right)X^2 - 6k\left(Y^2 - \frac{2}{3}r\right)X + 4r^2}}$$

and

$$\lambda_3 = -\lambda_4 = \frac{1}{2}\sqrt{M - 2\sqrt{\left(9Y^2 + k^2\right)X^2 - 6k\left(Y^2 - \frac{2}{3}r\right)X + 4r^2}}\,,$$

where $M = 3X^2 + 2kX + 3Y^2 + 4a$.

Each of these eigenvalue expressions must then be evaluated at the respective equilibria of the two subsystems. The resulting eigenvalues are shown as insets in Figure 7.2 and Figure 7.3 for each of the nine equilibria. These show that the 'II' equilibrium cannot from heteroclinics because it is a center, while '2' and '3' are saddle-centers with only 1-dimensional stable and unstable manifolds, so they do not generically form heteroclinic orbits.

So the equilibria 'I', 'III', and '1', as saddle-nodes, each having 2-dimensional stable and unstable manifolds, are the only possible source of the heteroclinics. In Figure 7.2 we see that the heteroclinic observed on the green curve in S, E, space connects the '1+' and '1−' equilibria.

7.2.4 Computation of heteroclinic orbits

Using the direct numerical method, we are able to solve (7.1) and obtain the heteroclinic solution. In the following step we will transfer the solution into the (u,E,v,S) coordinate by using formula (7.4). We then continue the heteroclinic solutions as parameters vary using AUTO. Specifically, we implement asymptotic boundary conditions based on the linearisation at each of the two distinct equilibria, as in the auto demo *she*.

Figure 7.5 shows in more detail how the heteroclinic solutions relate to these different equilibria and their bifurcations. On the symmetry line $S = E$, a heteroclinic solution connects the equilibria we labelled $(X_1^{\pm}, Y_1^{\pm})$, shown for a typical parameter value by A. At B a global bifurcation occurs in which this heteroclinic solution connects $(X_1^{\pm}, Y_1^{\pm})$ both to (X_I, Y_I). At this point this curve of heteroclinic solutions intersects two other curves, on which we take the points E and F as typical examples, on which lie heteroclinic solutions connecting (X_I, Y_I) to either (X_1^+, Y_1^+) (as at F) or (X_1^-, Y_1^-) (as at E). These curves of heteroclinic solutions terminate at folds curves at C and D, at which the heteroclinic orbit connects (X_1^+, Y_1^+) to (X_I, Y_I) as it undergoes a fold with (X_2^-, Y_2^-) (at C), or the heteroclinic orbit connects (X_1^-, Y_1^-) to (X_I, Y_I) as it undergoes a fold with (X_2^+, Y_2^+) (at D).

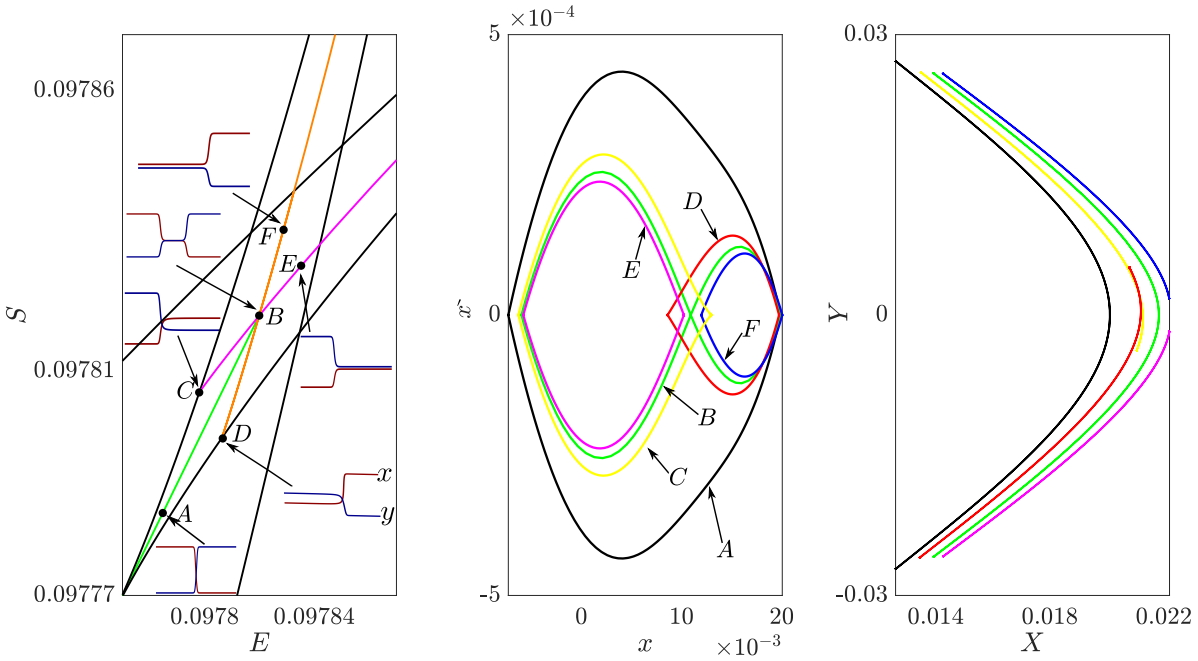

Figure 7.5: Bifurcation diagram for (7.8) with $\eta = 2$, $\mu = 0.05$, $\rho = 0.06$, $\alpha = 0.005$ and $\delta = 0.10995$. The heteroclinic orbits are plotted as graphs inset, and in the right two figures these are plotted in the original state space of (x,x'), and the transformed state space (X,Y).

A so-called butterfly singularity can be shown to be the codimension three singularity (i.e. on a curve in the four-dimension E, S, η and δ space) that destroys pairs of symmetric cusps in this system. Note that this bifurcation that would ordinarily be of codimension four is actually of

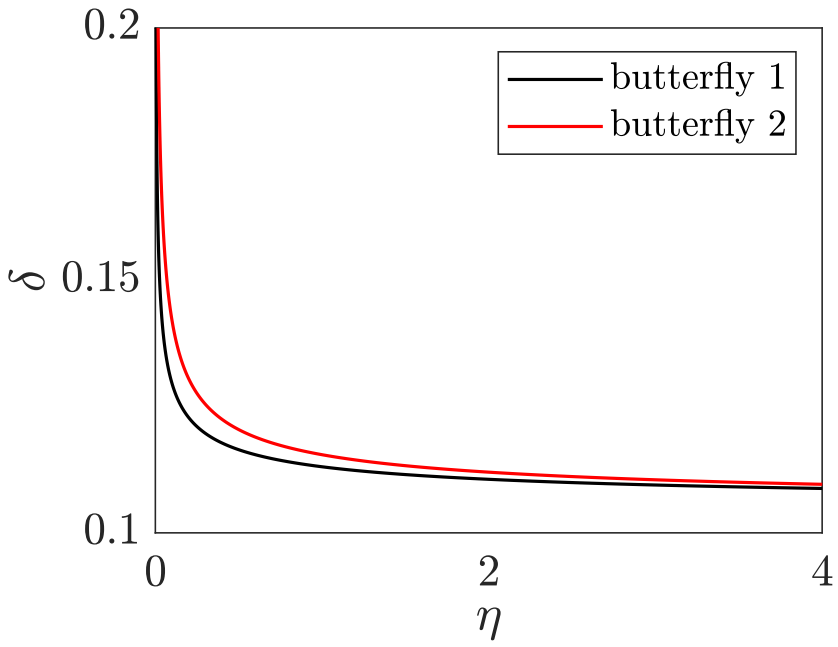

Figure 7.6: The bifurcation diagram for both butterflies in (η,δ)-plane. The remaining parameter values are as in Figure 7.7.

codimension three if the cusps occur along the line $E = S$. There are thus two butterfly singularies, destroying each of the two pairs of cusps (see Figure 7.7 below). The values of δ against η for which butterfly singularity occur is plotted in Figure 7.6.

7.3 Transition of the heteroclinic solutions and the steady state solutions

In this section, let us discuss the transition of the number of the steady-state solutions from the diagram in Figure 7.1 to the situation that occurs as δ-increases (as in Figure 7.5) to the upper portion of the Figure 7.6 in which there is a single steady state and no longer any heteroclinic connections. Figure 7.7 shows a series of snapshots of the steady-state and the heteroclinic bifurcation diagram in (E,S)-plane, for increasing set values of δ, for fixed η. We find that a similar sequence of transition can be found to occur for any value of $\eta \to 0$ as we increase δ towards and beyond the the red curve on which the butterfly singularity occurs in (η,δ)-plane in Figure 7.6.

We shall start from Figure 7.7(a), which is identical to Figure 7.1. For these parameter values in Figure 7.7(a), we can have nine separate steady-state solutions. Also, we can obtain five different kinds of heteroclinic solutions, which lie on the different colour lines in the diagram. Profiles of each kind of heteroclinic solution was given in Figure 7.1. Also notice the two special points that are labelled with an asterisk. Here is where the codimension heteroclinic orbit exist

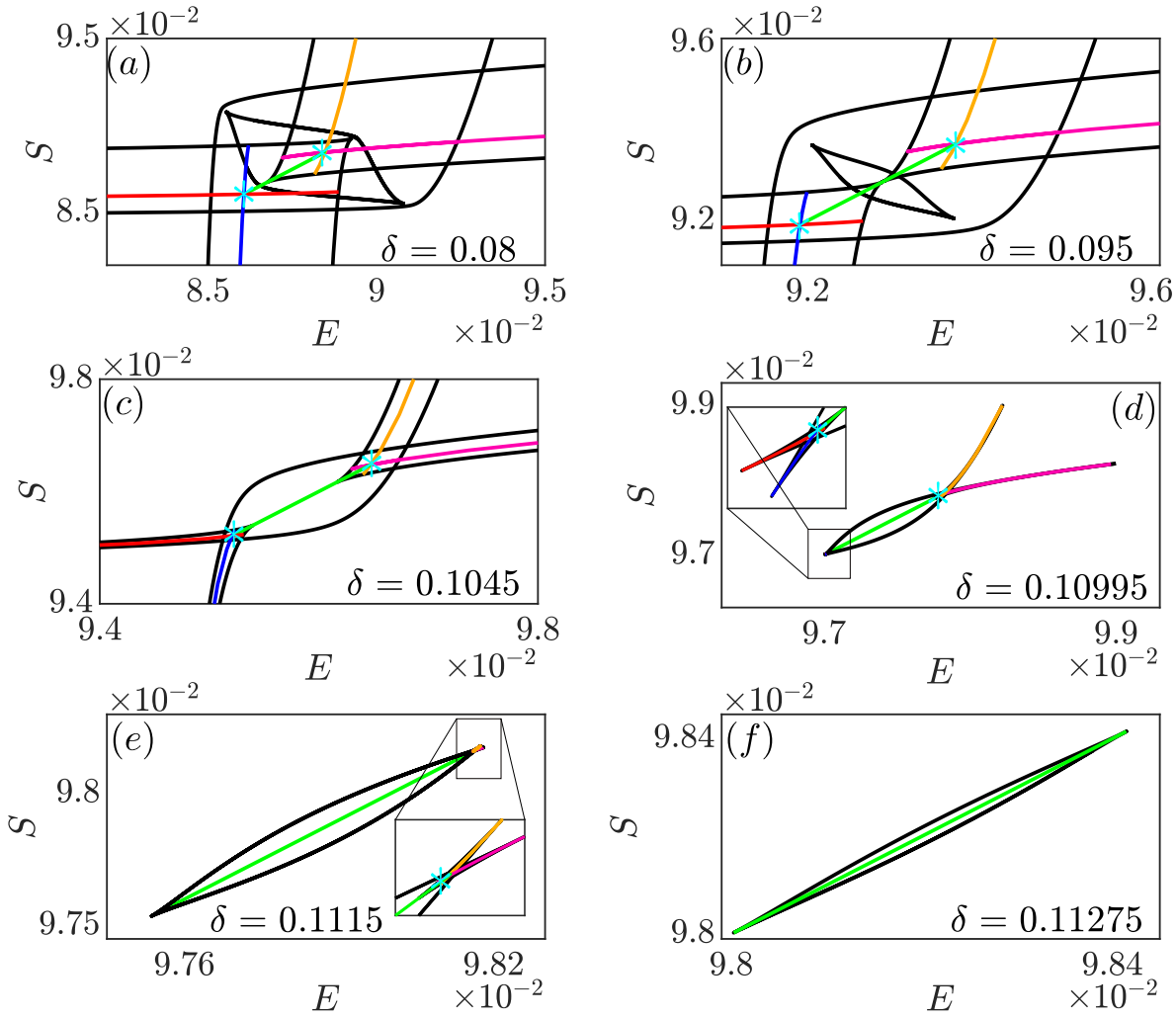

Figure 7.7: Bifurcation diagram of (7.7) showing the transition of homogeneous steady states as we vary the three parameter E, S and δ, with fixed $\eta = 2$, $\mu = 0.05$, $\rho = 0.06$, $\alpha = 0.005$.

between a pair of steady states, resulting in 'front and back' type cycles. Increasing δ from 0.08 beyond 0.1 results on change of topology of the fold and cusp curves, leading to there being a maximum of five steady states (see Figure 7.7 (b)-(d)). Through these changes though, the number of heteroclinic solutions that occur does not change. Further increasing the δ value destroys two heteroclinic solution branches through the first butterfly catastrophe (see Figure 7.7 (d) and (e)), as explained in section 7.2.4. Figure 7.7(f) shows the situation after the second butterfly catastrophe takes place; it is clear that two further heteroclinic branches have been destroyed. Finally we are left with a thin region bonded by pair of fold curves that meet at cusps and contain a single heteroclinic connection Figure 7.7(f). We find that for $\delta \approx 0.1122$ these two cusps annihilate each-other and there are no heteroclinic solutions at all for higher δ-values.

7.4 Polarity formation: solution to the initial-value problem

Note that E and S are not invariant of the PDE system, instead they can be consider as constant that parametrise different families of the steady-state and the heteroclinic solutions. However, for a given domain size l, each different value of E and S along a family of solutions will typically have different value of A_T and B_T, which are invariants of the full time-dependent PDEs. However, on a finite domain, translation of the heteroclinic in space will typically leads to different values of A_T and B_T. Thus we can ask the question for a given value of A_T and B_T, is there a unique steady state that the solution evolves to, or is the final obtained state sensitive function of the initial data. Remarkably, we have found no evidence for multistability. That is for each choice of values of A_T and B_T, for given set of the system parameters then there appears to be unique final steady state that is reached by the initial-value problem, irrespective of what initial data we take. We shall now describe the result of our numerical finding for the parameter values used in Figure 7.1.

Accordingly, we simulate the full PDE system (7.1) at these parameter values. For all parameter values in the system, we find the dynamics always settles to steady state. Note that the S and E values of the final steady state are emergent properties that are found to be always a unique function of the values of A_T and B_T, for every initial run tried. Figure 7.8 summarises the results for the same parameter values in Figure 7.1. In each coloured region we run multiple simulation from pseudo random initial conditions containing Heaviside-style jumps. In each case the simulations revealed qualitatively the same behaviour in each coloured region. We obtain the boundaries between the coloured regions by choosing the values of E and S to lie on the appropriate coloured curves in Figure 7.1 to represent the particular heteroclinic connection in equation(7.6). Then we shift the solution phase, that is the location in x of the heteroclinic jump, from the rightmost ($x = l$) to the leftmost ($x = -l$) point in the domain. Here we consider $l = 100$.

The simulation results for the parameter set in Figure 7.1 reveal eight distinct regions, see Figure 7.8a. The white regions represent the unpolarised area in which homogenous steady states are obtained (see the solution profiles H). The yellow and cyan regions are associated with the heteroclinic connection that with large differences between the polarised and depolarised A^* and more negligible differences between the polarised and depolarised B^*. The two regions differ in their overall concentration of B^*. In the yellow region, B^* is always in large excess of inactive B and close to the polarised amount of A^*. Whereas in the cyan region, the overall concentration of B^* is much lower and commensurate with the depolarised amount of A^* (see the solution profiles A and C in Figure 7.8b). In contrast, the green and the orange regions show heteroclinic orbit that with larger difference between the polarised and depolarised B^* and smaller different between the polarised and depolarised A^*. In the green region, the values of A^* is nearby the polarised amount of the B^* and far from the inactive A. Contrastingly, in the orange region A^* is closer to the depolarised amount of B^* (see the solution profiles B and D in Figure 7.8b). The pink region corresponds to an intermediate polarity solution where A^* and B^* have the same

height but different directions (see the solution profile E in Figure 7.8b). Finally, the brown and the grey regions are related to a particular polarity state that joins the dominant polarity state to the intermediate state. The difference between the two regions is that for the solution in the brown region the intermediate state has high concentration, whereas in the grey region the intermediate state has low concentration (see the solution profiles B and D in Figure 7.8b).

In Figure 7.9, we zoom in on the cyan region in Figure 7.8a to show that there is a distinct polarised solution with different phase shifts representing different values of E and S along the red curve labelled C in Figure 7.1. Specifically, the profiles solution W_1, W_2 and W_3 shown in Figure 7.9 represent solutions for varying values of E and S along the red curve in Figure 7.1, while the profile of the solution W_2, W_4, and W_5 exhibit solutions for the similar values of E and S but with various phase shifts. In Figure 7.10, we zoom in on the brown region of Figure 7.8a to demonstrate that the behaviours we obtain in Figure 7.9 are representative of all the regions presented in Figure 7.8a. The solutions in the brown region have the same value of E and S represented by an asterisk in Figure 7.1. Now to shift to a different solution within this region, we can vary two distinct phase shifts representing the two heteroclinic connections making up the profile at this special point in the (E,S)-plane.

7.5 Other Models

So far we have only consider the modified Abley et at. model (7.6). Let us now briefly consider the overall bifurcation diagram for each of the other forms of F and G that have been proposed in triturates. Let us now recall these other function forms, which were given in chapter 1

- Model I: a modification of the model in [1]:

$$F = \left(\eta A^{*2} + \rho\right) A - \left(\alpha B^* + \mu\right) A^* \tag{7.27a}$$

$$G = \left(\eta B^{*2} + \rho\right) B - \left(\alpha A^* + \mu\right) B^*, \tag{7.27b}$$

- Model II: intracellular partitioning model for juicy fruit by Grieneisen et al [72]:

$$F = \left(\beta + \eta\,\alpha\,\mu^2 A \left(\mu^2 + A^{*2} + B^{*2} + \frac{\alpha}{c_a}\right)^{-1}\right) A - \rho A^*, \tag{7.28a}$$

$$G = \left(\beta + \eta\,\alpha\,\mu^2 B \left(\mu^2 + A^{*2} + B^{*2} + \frac{\alpha}{c_a}\right)^{-1}\right) B - \rho B^*. \tag{7.28b}$$

- Model III: mutual inhibition introduced by Holmes et al [80]

$$F = \left(b + \frac{\alpha}{1 + B^{*n}}\right) A - d A^*, \tag{7.29a}$$

$$G = \left(b + \frac{\alpha}{1 + A^{*n}}\right) B - d B^*. \tag{7.29b}$$

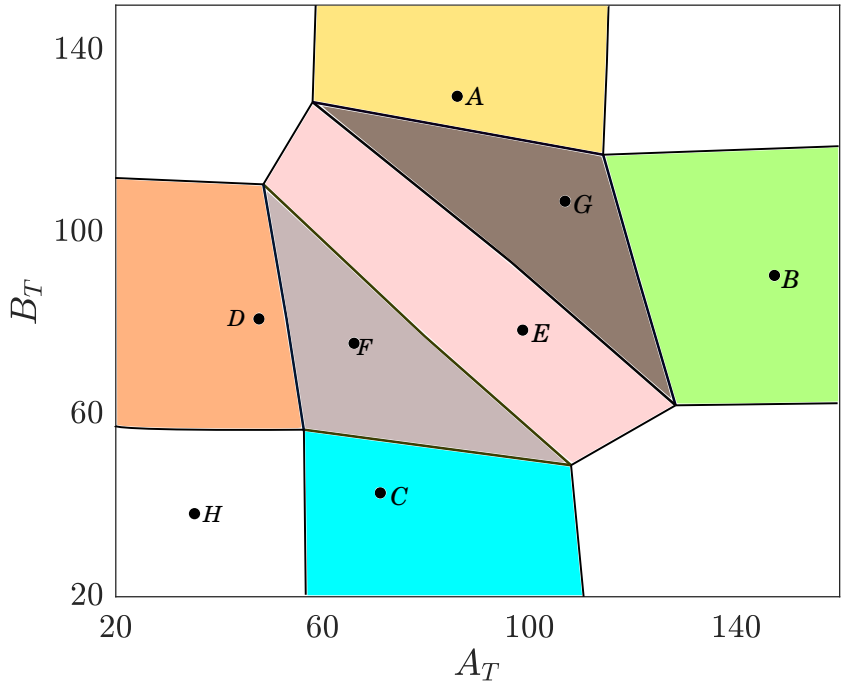

(a)

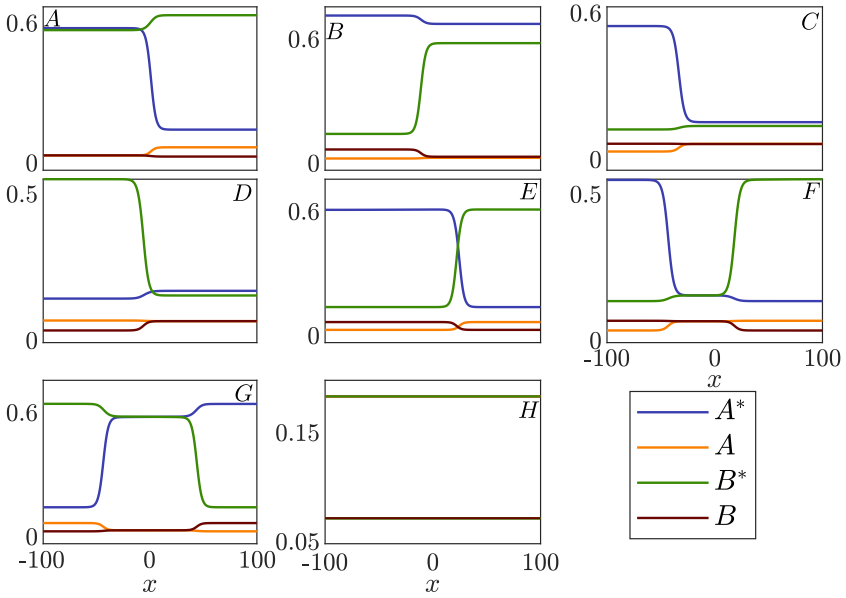

(b)

Figure 7.8: (a) (A_T, B_T) parameter space where the shaded region represent a map of different polarity behaviour can be obtain by solving the initial-value problem for in (1.4) at the parameter values as in Figure 7.1. (b) Example of the stable polarized steady state from each different region as a function of the initial value of A_T and B_T.

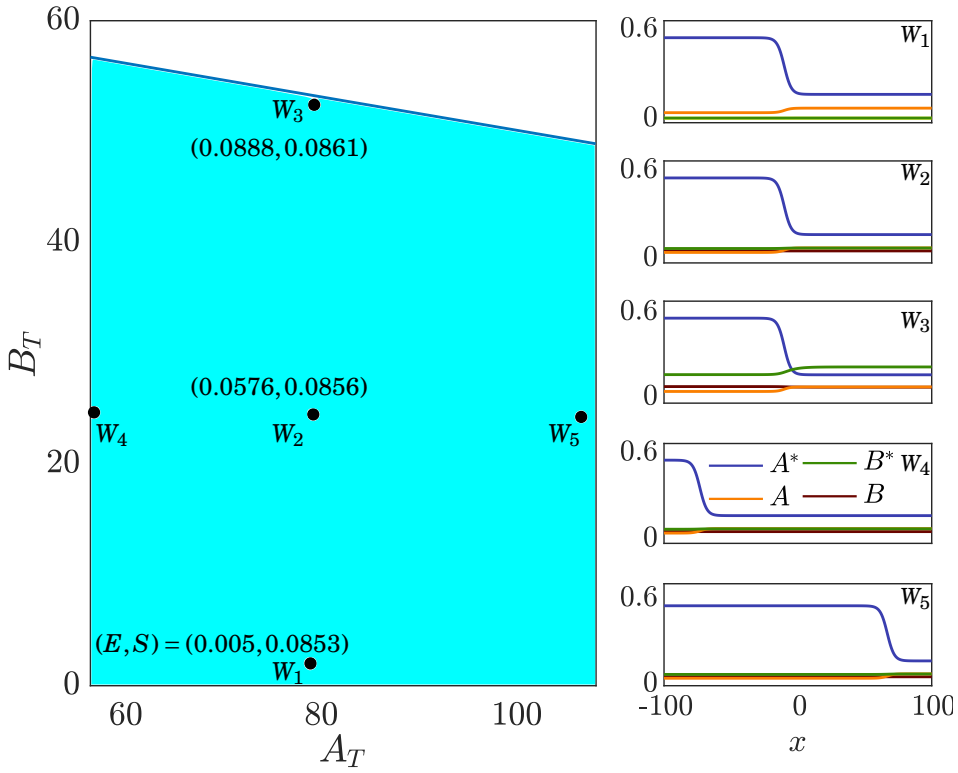

Figure 7.9: Zoom in the cyan region in Figure 7.8b.

Figure 7.11a exhibits the bifurcation diagram for the Abely model (7.27). The black curve shows the pairwise annihilation among the steady states, and the green curve denotes the symmetric line of the system with $E = S$. This system has only one type of heteroclinic solution which is on the symmetry line where $E = S$. This is the intermediate polarised state as in Figure 7.8 E. Furthermore, these heteroclinic solution is destroyed at a single cusp bifurcation.

Figure 7.11b displays the bifurcation diagram for mutual inhibition model (1.6). In general, the bifurcation diagram is similar to the Abely model Figure 7.11a, accept that here the heteroclinic solution is terminated at two cusp bifurcation.

Figure 7.11c expresses the bifurcation diagram for a Juicy model (1.5). The bifurcation diagrams is qualitatively analogous to Figure 7.1.

To conclude this section, we provide another numerical example to support the observations that for each value of E and S in Figure 7.11, there is a distinct polarised solution with different phase shifts. We consider the mutual inhibition model (1.6) as a second example. Figure 7.12 displays the polarity region for all values of E and S in Figure 7.11b. Also, the figure shows examples of polarised solutions which are selected from different parts of the polarity region. It is worth noting that these results agree with those presented by Holmes el. al [80].

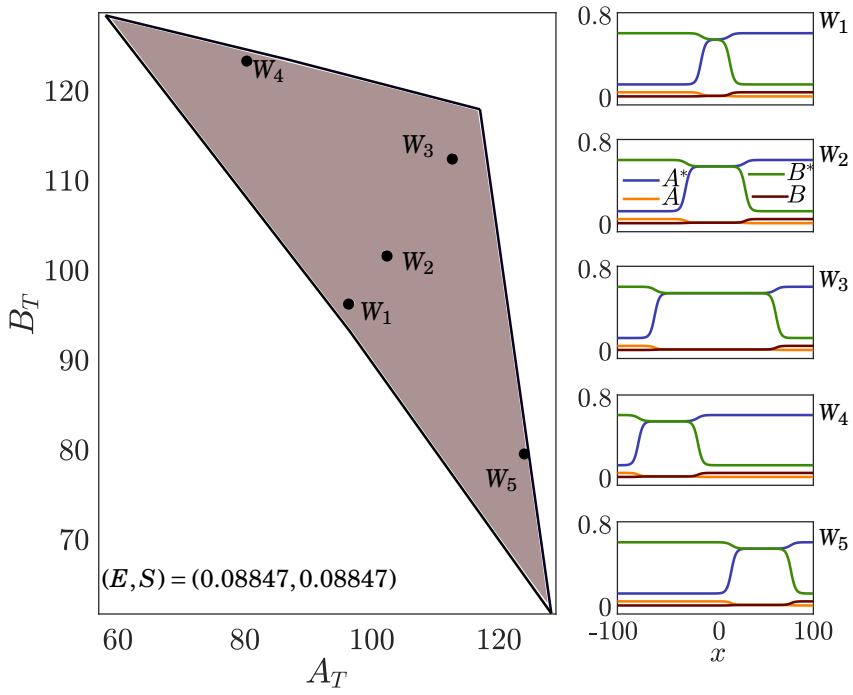

Figure 7.10: Zoom in the brown region in Figure 7.8b

.

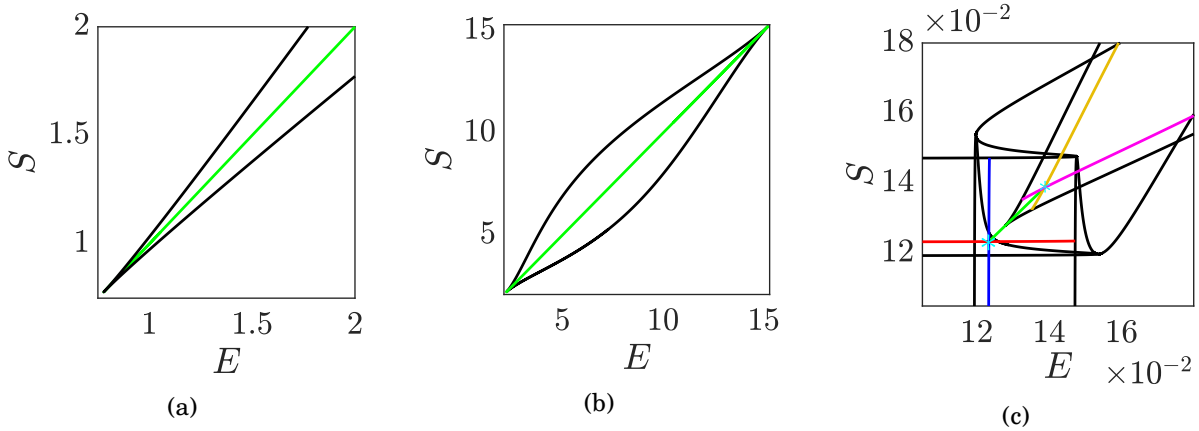

(a) (b) (c)

Figure 7.11: The bifurcation diagram in (E,S)-plane of the models (1.3) , (1.6) and (1.5), respectively. (a) Parameter values: $\alpha = 0.005$, $\delta = 0.03$, $\eta = 0.119$, $\mu = 0.05$ and $\rho = 0.06$. (b) Parameter values: $\alpha = 0.66$, $b = 0.1$, $d = 1$ and $\delta = 0.5$. (c) Parameter values: $\alpha = 80$, $\beta = 0.12$, $c_a = 20$, $\delta = 0.08$, $\eta = 1$, $\mu = 0.5$ and $\rho = 0.2$

.

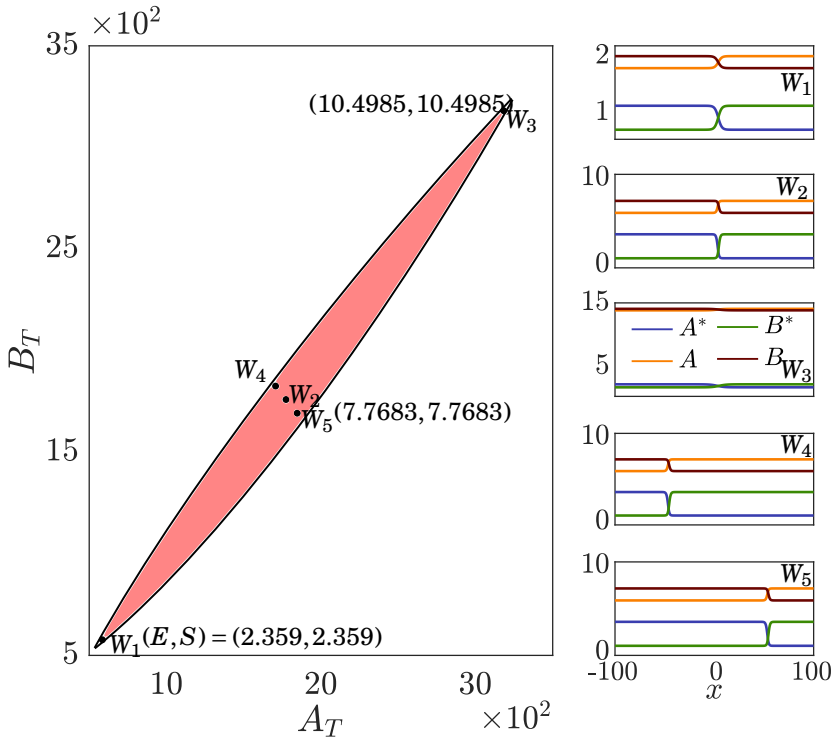

Figure 7.12: (A_T, B_T) parameter space where the shaded region represent a map of polarity behaviour can be obtain in (1.6) throughout the parameter space.The parameter values $\alpha = 0.66$, $b = 0.1$, $d = 1$ and $\delta = 0.5$

.

7.6 Conclusion

There are three essential observations that have been reported on cell shape diversity [183]. The first observation is that the cells show a limited and separate set of morphologies. The second observation is that the different types of cells can produce identical morphologies. Finally, the same kind of cells can also exhibit various cell shapes. This chapter provides a framework for how the cell morphologies may arise from different sets of GTPase proteins in a very simple two-species activator-inhibitor model. Consequently, the chapter gives some answers to the physical processes underlying these observations. We use the singularity theory to characterise the collection of the homogenous steady states in (7.1). Then we show the heteroclinic connections between these steady states. To help investigate the dynamics of (7.1), we numerically explore the parameter space to identify the regions of different polarities. The results we have obtained confirm the experimental results in [1, 72] and some of the numerical results in [80, 183].

There is much more to be explored for these models. For example, we have only here focused on one-dimensional space where the distribution of the GTPase on two and three dimensional space may give a better explanation of the morphologies of the cells. Therefore, extending the work to a more dimensional space is worthwhile to consider. Also, the connection between the non-conserved case ($\epsilon > 0$) considered in the previous chapter and conserved cases ($\epsilon = 0$) is worth

investigating. A key open equation is to understand why only one of the large families of the heteroclinic solutions seem to be selected to form a stable homoclinic for $\epsilon > 0$.

To wrap up, we have set the foundation to explore and understand the dynamics of the cell morphologies through the singularity theory reaction-diffusion systems and the organisation of the heteroclinic structures. Our observations suggest that the results of these studies will contribute a great deal to explaining the numerical results found in previous works [1, 72, 79, 80, 116].

CHAPTER 8

CONCLUSION

While this thesis has not been focused on a particular biological application, we claim that understanding the generic morphology of bistability and localised structures can be of considerable use to modellers in future when deriving, analysing and stress-testing models that can aid biological understanding. Perhaps, rather than worrying about specific parameter values and forms of the reaction nonlinearity, it is more helpful when working in real biological problems to ask more generic questions. For example, is there a difference in inherent diffusion rates of activator and inhibitor? Is there bistability of homogeneous steady states? Is there a natural small parameter limit that would lead to semi-strong interaction regime? Are there underlying features that would suggest localised patterns (with multi-humps) or single isolated patches, or stationary fronts? Is there a distinguished spatial co-ordinate leading to a (quasi-1D) long domain? These questions have been addressed in this thesis following a generic way of thinking.

A particular case study for application of this method of enquiry can be found in the series of papers by Breña *et al* who studied the processes of formation of hairs in the cells on the surface of *arabidopsis* roots [13, 30, 31]. Here the plant hormone auxin provides spatial inhomogeneity that causes a single isolated patch of active G-protein to form at the hair-initiation site at a certain distance (observed in wild type) from the apical end of the long, thin cell. The model, which in its simplest form is the root hair model analysed in chapter 3 relies on realistic assumptions rather than detailed measurements of biological processes for which measurement is not currently possible. The model was previously shown by Payne and Grierson [131] to be able to capture the multi-patches observed in mutants, and also the slow-fast dynamics of rapid patch formation and gradual drift.

Another motivation is the dynamical jigsaw instability of the plant leaf cells. These the kinds of models studied in chapter 6 and 7 have been used to describe the formation of lobes and indents

single cells [1, 72]. Moreover, the generic behaviour of small GTPases in controlling cell polarity has been the strong motivation for much of this work.

8.1 Summary of the key results

A key contribution has been to document, in chapter 2 a suite of tools that combines linear and nonlinear analysis with numerical continuation and simulation. We are not aware of all these method being collected in one place before. These tools are then applied in the rest of this thesis to obtain qualitative bifurcation structures for different reaction-diffusion models.

The purpose of chapter 3 was to show a certain generality of bifurcation structures for a range of activator-inhibitor models that have been widely studied in the literatures. We show a connection between the semi-stronge asymptotic analysis and the theory of homoclinic snaking in systems of reaction-diffusion equations (see also [137, 148] for earlier results in this direction). The former can be used to find analytic expressions for the structure and stability of spike solutions in a rather specific asymptotic limit. The latter, applies in the large but, apart from in a neighbourhood of a degenerate Turing bifurcation, cannot provide asymptotic estimates. The nature of the localised structures found by the two different theories are radically different too. The former finds isolated spike solutions where one field is much more localised. The latter finds solutions a plethora of localised solutions that many peaks. The results in this chapter go some way to demonstrating how the very different structures captured by the different theories can be connected in an appropriate multi-parameter bifurcation diagram.

The key to the results presented there, compared with other works to use the semi-strong asymptotic theory, has been to pose the problem on the infinite domain. Then we can find a fold as an appropriate parameter is varied. We find numerically that this fold forms the outer extent of the localised pattern region, which extends far away from the asymptotic limit and into the snaking region. Moreover, we have shown how the exponentially localised solutions found by taking an infinite domain, naturally transition to the solutions that are delocalised in the v-field via a quadratic tail, which is the solution type found on the standard finite-domain analysis.

An additional feature we found is the presence of a breathing Hopf bifurcation in the limit that parameters (including δ) are sufficiently small. We have also shown the existence of a global Hopf bifurcation and interactions between these two instabilities within the localised pattern regime for intermediate values of δ. Further, through numerical investigation, we show that the breathing Hopf bifurcation changes from sub- to super-critical as δ increases in each model. Finally, we illustrate that under an appropriate scaling, neither the existence of the Turing bifurcation nor its transition to sub-criticality and the onset of homoclinic snaking requires the diffusion ratio δ^2 to be small. However, when analysing these patterns' temporal stability, everything is unstable to a global Hopf bifurcation unless δ is sufficiently small.

Chapter 4 aims to study the morphing of one bifurcation diagram into the other for a different

class of system that has bistability between steady states, by studying a sequence of codimension-two bifurcation under a homotopy. We present in detail the transformation of the glycolysis model into the Gray-Scott. Using the methods from chapter 2, we produce a comprehensive set of two-parameter bifurcation diagrams for the homogenous steady-state and the localised patterns to trace how the universal diagram, displayed in chapter 3, morphs into a more complex one for Gray-Scott. we also have demonstrated that the classical Gierer-Meinhardt model, which has a vary different nonlinearity than the Schnakenberg-like models, can have a similar transformation. It should be noted that Schnakenberg-like models exhibit universal behaviour, such as Turing instability with a BD transition. There is also a codimension-two bifurcation point giving rise to a homoclinic snaking bifurcation of localised patterns. Additionally, these models exhibit a breathing Hopf bifurcation in the left corner of the two parameter space when the diffusion coefficient is small, which moves to the right when the diffusion coefficient increases and intersects a global Hopf bifurcation curve.

The aim of chapter 5 is to uncover the specific behaviour of models of ecological systems, particularly the wide class of predator-prey models which again have different types of nonlinearity to Schnakenberg-like models. Also, rather than exhaustive numerical studies, we have sought to explain a general morphology of the bifurcation diagram of such systems. In particular, we have shown that as we approach the singular limit where the ratio of diffusion constants between prey and predator tends to zero, the fundamental Turing bifurcation of the coexistence equilibrium again becomes subcritical just as it did for the models in chapter 3. Broadly speaking, we find exactly the same global bifurcation pattern of localised patterns in these models as we did in chapter 3. Also, we demonstrated through spectral computations and numerical simulations some complex dynamics of the localised patterns beyond their Hopf bifurcation leading to temporally periodic and chaotic localised patterns. Simulation results in 2D support the onset of complex spatio-temporal patterns within the corresponding parameter regions.

In chapters 6 and 7, we consider models for cell polarities that show the interaction between two generic ROPs within the cell these share some features of the models in chapter 3-5 but have four components rather then two. Chapter 6 analyses these models by breaking the conservation of the total masses by adding generic source and loss terms inspired by the work of [165] for a single species ROP model. Like the two component models, we have a single steady-state solution that loses stability. But now we have two distinct branches of Turing instability. It has been shown that both branches undergo a subcritical Turing bifurcation which gives two regions of localised patterns an interleaved pattern region and an overlaid patten region (c.f Figure 6.3). We show through spectral analysis that the localised patterns within the overlaid region are unstable, whereas the localised patterns within the interleaved region are stable. Numerical simulations suggest that overlaid patterns evolve into interleaved ones as result of their instability. We also carefully consider the limit that of the strength source and loss terms tend to zero.

Chapter 7 focuses on the mass-conserved case of the models studied in chapter 6. We start

the study by introducing new coordinates (S,E). Consequently, the spatial dynamics is reduced to a pair of second-order differential equations in space. Then we show that up to nine equilibria can occur and how these are destroyed. We present the conditions under which the steady states can have a heteroclinic connection, using the singularity theory. A key extra result is to show how different heteroclinic connections lead to different forms of polarity-formation as solutions to initial-value problem. These different forms can nicely be represented in two-parameter diagram. Here the two parameters represent the total concentration of each of the ROP species.

8.2 Future Research

Clearly, there is much left to be done to extend the work in this thesis. Our results are either purely numerical or are based on asymptotic expansions. Rigorous justification of some of our conjectures, perhaps using generic spatial dynamics argument, as in [20], or geometric singular perturbation theory, as in [56, 59, 148] is pressing.

We still have unresolved questions regarding how the breathing Hopf bifurcation appears to become supercritical with an increasing δ in each of the models described in chapter 3. As well, there remains a need to further explain the global dynamics of patterns beyond the fold and the Hopf instability of the different types of localised patterns. As an example, there is evidence in [4] that spike replication and in [56] that spike insertion may occur on finite domain beyond instability of the Schnakenberg model investigated there.

Then there is the restriction to one spatial dimension. There is much evidence in the literature to suggest that the models we have studied also give rise to complex spatio-temporal dynamics in two or more spatial dimensions, see e.g. [39, 123]. The analysis of localised patterns in multiple spatial dimensions is not only a challenging proposition, but also only a little is rigorously known about it (see e.g. [28, 104]). Also it seems the array of possible patterns and behaviours is so wide, that rather than taking a canonical approach as we have done here, it might be more fruitful to look at specific models that attempt to provide insight to particular biological systems.

In chapters 6 and 7 of this thesis, we have discussed polarity models. Chapter 6 discussed the transition between the spike and the front solutions and explained how it works. Although this is an initial step in understanding this transition, we have not entirely resolved this problem yet. As shown in chapter 7, there are seven different heteroclinic solutions when $\epsilon = 0$, and there is one homoclinic solution when ϵ does not equal zero. Therefore, one of the seven becomes a homoclinic solution whenever ϵ is not equal to zero. The future work should include a detailed explanation of why a specific solution has been chosen from the seven possible ones. There also remain a lot more to be done from the bioecological standpoint. It would be interesting to apply these insights to models containing cell growth or cell shape morphology as in [133] which presumably happen downstream of the ROP-patterning. Here, it would be useful to pose the phenomena in realistic geometries such as for the root hair [131] or parament cell [1, 72].

APPENDIX A

CONDITIONS FOR BUTTERFLY CATASTROPHE

This Appendix contains some preliminary results due to Mike Jeffrey [85] that propose generic conditions for the existence of different generic singularities in systems of the form (7.1). In section 7.2 we see that the existence of heteroclinic connections is bounded by the existence of the equilibria they connect, and this is determined by certain bifurcations that destroy those equilibria.

Unfortunately, there do not appear to be general criteria for $n > 1$ dimensional systems, to locate such bifurcations in general, beyond the fold or cusp. In particular there do not appear to be explicit criteria that can be evaluated by continuation software. Theoretical treatments appear to require performing a centre manifold reduction to reduce the system to $n = 1$. In [10] the bifurcations of interest are classified as "one zero eigenvalue and a μ-fold degeneracy in the nonlinear terms", class $A_{\mu+1}$, with principal families of the form $\dot{x} = \pm x^{\mu+2} + P_{\mu+1}(x,\epsilon)$ where $P_{\mu+1}$ is an order μ polynomial in x with coefficients ϵ_i.

We there need a set of conditions to locate such bifurcations in a system $\dot{\mathbf{x}} = \mathbf{F}(\mathbf{x};\boldsymbol{\mu})$, where $\mathbf{x} \in \mathbb{R}^n$, $\boldsymbol{\mu} \in \mathbb{R}^m$, and in our particular systems of interest $n = 4$ with $\boldsymbol{x} = (X,Z,Y,W)$ and $\boldsymbol{F}$ is the right hand-side of (7.12) and $(\mu_1,\mu_2) = (a,b)$.

We propose the following (the motivation behind these conditions can be found in [85]). Let $\boldsymbol{x} = (X,Z,Y,W)$ and $\boldsymbol{F} = (F_1,F_2,F_3,F_4)$, and define functions

$$Q_1 = \det\left|\frac{\partial(F_1,F_2,F_3,F_4)}{\partial(X,Z,Y,W)}\right|, \qquad O_1 = \det\left|\frac{\partial(F_1,F_2,F_3,F_4,Q_1)}{\partial(X,Z,Y,W,\mu_1)}\right|,$$
$$Q_2 = \det\left|\frac{\partial(F_1,F_2,F_3,Q_1)}{\partial(X,Z,Y,W)}\right|, \qquad O_2 = \det\left|\frac{\partial(F_1,F_2,F_3,Q_1,Q_2)}{\partial(X,Z,Y,W,\mu_1,\mu_2)}\right|,$$

and so on, expressible more generally for $r = 1, 2, ...$ as

$$Q_r = \det \left| \frac{\partial(F_1, ..., F_{n-r+1}, Q_1, ..., Q_{r-1})}{\partial(x_1, ..., x_n)} \right| ,$$
$$O_r = \det \left| \frac{\partial(F_1, ..., F_n, Q_1, ..., Q_r)}{\partial(x_1, ..., x_n, \mu_1, ..., \mu_r)} \right| . \tag{A.1}$$

In these expressions, the strings $F_1, ..., F_{n-r+1}$ can actually consist of any $n-r+1$ components of the vector $\boldsymbol{F} = (F_1, ..., F_n)$. We then propose that the follow conditions define the stated catastrophes:

$$\begin{aligned}
0 &= \boldsymbol{F} && \text{[equilibrium]} \\
0 &= \boldsymbol{F} = Q_1 \neq O_1 && \text{[fold]} \\
0 &= \boldsymbol{F} = Q_1 = Q_2 \neq O_2 && \text{[cusp]} \\
0 &= \boldsymbol{F} = Q_1 = Q_2 = Q_3 \neq O_3 && \text{[swallowtail]} \\
0 &= \boldsymbol{F} = Q_1 = Q_2 = Q_3 = Q_4 \neq O_4 && \text{[butterfly]}
\end{aligned} \tag{A.2a}$$

and so on for higher codimension bifurcations. To our knowledge these conditions have not been given previously.

Take the modified Abley example. As we saw in section 7.2 the bifurcation of of interest occur on the set $E = S$ where by (7.9) we have

$$x = y\,, \qquad r = s\,, \qquad a = c\,, \qquad b = d\,, \qquad S = E\,. \tag{A.3}$$

With these we can solve the butterfly conditions

$$0 = x' = y' = \hat{f} = \hat{g} = Q_1 = Q_2 = Q_3 = Q_4 \neq O_4, \tag{A.4}$$

and we find

$$\begin{aligned}
x = y &= \frac{1}{9}(2k - \sqrt{4k^2 + 9r}) \\
a = c &= \frac{2}{27}(9r - 4k^2 + 2k\sqrt{4k^2 + 9r}) \\
b = d &= \frac{1}{729}(-8k^3 - 297rk + 4(k^2 + 36r)\sqrt{4k^2 + 9r})
\end{aligned} \tag{A.5}$$

Combining (7.9) with (A.5) we have solutions for S, E, δ, in terms of the other parameters. E.g. if we take $\eta = 2$, $\mu = 0.05$, $\rho = 0.06$, $\alpha = 0.005$, we find numerically

$$\begin{aligned}
& S = E = 0.0972536... \qquad \delta = 0.110666... \\
\& \qquad & S = E = 0.0983051... \qquad \delta = 0.112176...
\end{aligned}$$

BIBLIOGRAPHY

[1] K. ABLEY, P. B. D. REUILLE, D. STRUTT, A. BANGHAM, P. PRUSINKIEWICZ, A. F. M. MARÉE, V. A. GRIENEISEN, AND E. COEN, *An intracellular partitioning-based framework for tissue cell polarity in plants and animals*, Development, 140 (2013), pp. 2061–2074.

[2] A. AHARONI, *Introduction to the Theory of Ferromagnetism*, International Series of Monogr, Clarendon Press, 2000.

[3] F. AL SAADI AND A. CHAMPNEYS, *Unified framework for localized patterns in reaction diffusion systems; the Gray-Scott and Gierer-Meinhardt cases*, Philosophical Transactions of the Royal Society A: Mathematical, Physical and Engineering Sciences, 379 (2021), p. 20200277.

[4] F. AL SAADI, A. CHAMPNEYS, C. GAI, AND T. KOLOKOLNIKOV, *Spikes and localized patterns for a novel Schnakenberg model in the semi-strong interaction regime*, European Journal of Applied Mathematics, 33 (2022), p. 133–152.

[5] F. AL SAADI, A. CHAMPNEYS, AND N. VERSCHUEREN, *Localized patterns and semi-strong interaction, a unifying framework for reaction–diffusion systems*, IMA Journal of Applied Mathematics, 86 (2021), pp. 1031–1065.

[6] F. AL SAADI, A. CHAMPNEYS, A. WORTHY, AND A. MSMALI, *Stationary and oscillatory localized patterns in ratio-dependent predator–prey systems*, IMA Journal of Applied Mathematics, 86 (2021), pp. 808–827.

[7] F. AL SAADI, A. WORTHY, J. R. PILLAI, AND A. MSMALI, *Localised structures in a virus-host model*, Journal of Mathematical Analysis and Applications, 499 (2021), p. 125014.

[8] H. ALRIHIELI, A. M. RUCKLIDGE, AND P. SUBRAMANIAN, *Spatial localization beyond steady states in the neighbourhood of the Takens–Bogdanov bifurcation*, IMA Journal of Applied Mathematics, 86 (2021), pp. 984–1009.

[9] A. J. ALVAREZ-SOCORRO, M. G. CLERC, AND M. TLIDI, *Spontaneous motion of localized structures induced by parity symmetry breaking transition*, Chaos: An Interdisciplinary Journal of Nonlinear Science, 28 (2018), p. 053119.

[10] V. I. ARNOLD, V. AFRAJMOVICH, Y. S. IL'YASHENKO, AND L. SHIL'NIKOV, *Dynamical systems: bifurcation theory and catastrophe theory*, vol. 5, Springer Science & Business Media, 2013.

[11] J. C. ARTÉS, J. LLIBRE, AND C. VALLS, *Dynamics of the Higgins–Selkov and Selkov systems*, Chaos, Solitons and Fractals, 114 (2018), pp. 145 – 150.

[12] Y. A. ASTROV, E. AMMELT, AND H. G. PURWINS, *Experimental evidence for zigzag instability of solitary stripes in a gas discharge system*, Phys. Rev. Lett., 78 (1997), pp. 3129–3132.

[13] D. AVITABILE, V. BRENA-MEDINA, AND M. WARD, *Spot dynamics in a reaction-diffusion model of plant root hair initiation*, SIAM Journal on Applied Mathematics, 78 (2018), pp. 291–319.

[14] R. BAKER, E. GAFFNEY, AND P. MAINI, *Partial differential equations for self-organization in cellular and developmental biology*, Nonlinearity, 21 (2008), p. R251.

[15] M. BANDYOPADHYAY AND J. CHATTOPADHYAY, *Ratio-dependent predator–prey model: effect of environmental fluctuation and stability*, Nonlinearity, 18 (2005), pp. 913–936.

[16] M. BANERJEE AND S. PETROVSKII, *Self-organised spatial patterns and chaos in a ratio-dependent predator–prey system*, Theoretical Ecology, 4 (2011), pp. 37–53.

[17] M. BANERJEE AND V. VOLPERT, *Spatio-temporal pattern formation in Rosenzweig–MacArthur model: Effect of nonlocal interactions*, Ecological Complexity, 30 (2017), pp. 2 – 10.

[18] S. BARLAND, S. COEN, M. ERKINTALO, M. GIUDICI, J. JAVALOYES, AND S. MURDOCH, *Temporal localized structures in optical resonators*, Advances in Physics: X, 2 (2017), pp. 496–517.

[19] R. BASTIAANSEN, O. JAIBI, M. DEBLAUWE, V. EPPINGA, K. SITEUR, E. SIERO, P. MERMOZ, A. BOUVET, A. DOELMAN, AND M. RIETKERK, *Multistability of model and real dryland ecosystems through spatial self-organization*, Proceedings of the National Academy of Sciences of the United States of America, 115 (2018), pp. 11256–11261.

[20] M. BECK, J. KNOBLOCH, D. LLOYD, B. SANDSTEDE, AND T. WAGENKNECHT, *Snakes, ladders, and isolas of localized patterns*, SIAM Journal on Mathematical Analysis, 41 (2009), pp. 936–972.

[21] D. L. BENSON, J. A. SHERRATT, AND P. K. MAINI, *Diffusion driven instability in inhomogeneous domain*, Bulletin of Mathematics Biology, 55 (1993), pp. 365–384.

[22] F. BEREZOVSKAYA, G. KAREV, AND R. ARDITI, *Parametric analysis of the ratio-dependent predator-prey model*, Journal of Mathematical Biology, 43 (2001), pp. 221–246.

[23] A. BERKEN, C. THOMAS, AND A. WITTINGHOFER, *A new family of RhoGEFs activates the Rop molecular switch in plants*, Nature, 436 (2005), p. 1176—1180.

[24] J. J. BLAKESLEE, A. BANDYOPADHYAY, O. R. LEE, J. MRAVEC, B. TITAPIWATANAKUN, M. SAUER, S. N. MAKAM, Y. CHENG, R. BOUCHARD, J. ADAMEC, M. GEISLER, A. NAGASHIMA, T. SAKAI, E. MARTINOIA, J. FRIML, W. A. PEER, AND A. S. MURPHY, *Interactions among pin-formed and p-glycoprotein auxin transporters in arabidopsis*, The Plant Cell, 19 (2007), pp. 131–147.

[25] J. BLAZEK, *Chapter 3 - principles of solution of the governing equations*, in Computational Fluid Dynamics: Principles and Applications (Second Edition), J. Blazek, ed., Elsevier Science, Oxford, 2005, pp. 29 – 75.

[26] I. BORDEU, M. CLERC, P. COUTERON, R. LEFEVER, AND M. TLIDI, *Self-replication of localized vegetation patches in scarce environments*, Scientific Reports, 6 (2016).

[27] F. BORGOGNO, P. D'ODORICO, F. LAIO, AND L. RIDOLFI, *Mathematical models of vegetation pattern formation in ecohydrology*, Reviews of Geophysics, 47 (2009).

[28] J. BRAMBURGER, D. ALTSCHULER, T. AVERY, C. SANGSAWANG, M. BECK, P. CARTER, AND B. SANDSTEDE, *Localized radial roll patterns in higher space dimensions*, SIAM Journal on Applied Dynamical Systems, 18 (2019).

[29] J. J. BRAMBURGER AND B. SANDSTEDE, *Spatially localized structures in lattice dynamical systems*, Journal of Nonlinear Science, 30 (2020), pp. 603–644.

[30] V. BREÑA–MEDINA, D. AVITABILE, A. CHAMPNEYS, AND M. WARD, *Stripe to spot transition in a plant root hair initiation model*, SIAM Journal on Applied Mathematics, 75 (2015), pp. 1090–1119.

[31] V. BREÑA–MEDINA, A. CHAMPNEYS, C. GRIERSON, AND M. WARD, *Mathematical modeling of plant root hair initiation: Dynamics of localized patches*, SIAM Journal on Applied Dynamical Systems, 13 (2014), pp. 210–248.

[32] V. BRENA–MEDINA AND A. R. CHAMPNEYS, *Subcritical Turing bifurcation and the morphogenesis of localized patterns*, Physical Review E, 90 (2014), p. 032923.

[33] J. BURKE AND E. KNOBLOCH, *Snakes and ladders: Localized states in the Swift–Hohenberg equation*, Physics Letters A, 360 (2006), pp. 681–688.

[34] J. CARBALLIDO-LANDEIRA, V. K. VANAG, AND I. R. EPSTEIN, *Patterns in the Belousov–Zhabotinsky reaction in water-in-oil microemulsion induced by a temperature gradient*, Physical Chemistry Chemical Physics, 12 (2010), pp. 3656–3665.

[35] A. CHAMPNEYS, *Homoclinic orbits in reversible systems and their applications in mechanics, fluids and optics*, Physica D: Nonlinear Phenomena, 112 (1998), pp. 158–186.
Proceedings of the Workshop on Time-Reversal Symmetry in Dynamical Systems.

[36] A. CHAMPNEYS, *Editorial to Homoclinic snaking at 21: in memory of Patrick Woods*, IMA Journal of Applied Mathematics, 86 (2021), pp. 845–855.

[37] A. CHAMPNEYS, F. AL SAADI, V. BREÑA–MEDINA, V. GRIENEISEN, A. MARÉE, N. VERSCHUEREN, AND B. WUYTS, *Bistability, wave pinning and localisation in natural reaction-diffusion systems*, Physica D, 416 (2021), p. 132735.

[38] S. CHAPMAN AND G. KOZYREFF, *Exponential asymptotics of localised patterns and snaking bifurcation diagrams*, Physica D, 238 (2009), pp. 319–354.

[39] M. CHEN, R. WU, AND L. CHEN, *Pattern dynamics in a diffusive Gierer-Meinhardt model*, Int. J. Bifurcation Chaos, 30 (2020), p. Art. No. 2030035.

[40] S. K. CHRISTENSEN, N. DAGENAIS, J. CHORY, AND D. WEIGEL, *Regulation of auxin response by the protein kinase pinoid*, Cell, 100 (2000), pp. 469 – 478.

[41] C. A. COBBOLD, F. LUTSCHER, AND J. A. SHERRATT, *Diffusion-driven instabilities and emerging spatial patterns in patchy landscapes*, Ecological Complexity, 24 (2015), pp. 69 – 81.

[42] R. COURANT, K. FRIEDRICHS, AND H. LEWY, *On the partial difference equations of mathematical physics*, IBM Journal of Research and Development, 11 (1967), pp. 215–234.

[43] D. J. COVE, *The generation and modification of cell polarity*, Journal of Experimental Botany, 51 (2000), pp. 831–838.

[44] M. C. CROSS AND P. C. HOHENBERG, *Pattern formation outside of equilibrium*, Rev. Mod. Phys., 65 (1993), pp. 851–1112.

[45] J. DAWES AND M. SOUZA, *A derivation of Holling's type I, II and III functional responses in predator-prey systems*, Journal of Theoretical Biology, 327 (2013), pp. 11–22.

[46] J. H. DAWES, *The emergence of a coherent structure for coherent structure: localized state in nonlinear system*, Phil. Trans. R. Soc, 368 (2010), pp. 3519–3534.

[47] J. H. DAWES, *After 1952: The later development of Alan Turing's ideas on the mathematics of pattern formation*, Historia Mathematica, 43 (2016), pp. 49–64.

[48] A. DE WIT, D. LIMA, G. DEWEL, AND P. BORCKMANS, *Spatiotemporal dynamics near a codimension-two point*, Physical Review E, 54 (1996), pp. 261–271.

[49] A. DEAN, P. MATTHEWS, S. COX, AND J. KING, *Exponential asymptotics of homoclinic snaking*, Nonlinearity, 24 (2011), pp. 3323–3351.

[50] B. DECONINCK AND J. N. KUTZ, *Computing spectra of linear operators using the floquet–fourier–hill method*, Journal of Computational Physics, 219 (2006), pp. 296 – 321.

[51] L. DESHU, R. HUIBO, AND F. YING, *Rop GTPase-mediated auxin signaling regulates pavement cell interdigitation in arabidopsis thaliana*, Journal of Integrative Plant Biology, 57, pp. 31–39.

[52] J. DETTMER AND J. FRIML, *Cell polarity in plants: When two do the same, it is not the same....*, Current Opinion in Cell Biology., 23 (2011), pp. 686–696.

[53] R. L. DEVANEY, *Reversible diffeomorphisms and flows*, Trans. Amer. Math. Soc., 218 (1976), pp. 89–113.

[54] E. DOEDEL AND B. OLDEMAN *et al.*, *Auto-07p: Continuation and bifurcation software for ordinary differential equations*, (2020).
Latest version at `https://github.com/auto-07p`.

[55] A. DOELMAN AND T. KAPER, *Semistrong pulse interactions in a class of coupled reaction-diffusion equations*, SIAM Journal on Applied Dynamical Systems, 2 (2003), pp. 53–96.

[56] A. DOELMAN, T. J. KAPER, AND P. A. ZEGELING, *Pattern formation in the one-dimensional Gray - Scott model*, Nonlinearity, 10 (1997), p. 523.

[57] A. DOELMAN, J. RADEMACHER, B. DE RIJK, AND F. VEERMAN, *Destabilization mechanisms of periodic pulse patterns near a homoclinic limit*, SIAM J. Appl. Dyn. Syst., 17 (2018), p. 1833–1890.

[58] A. DOELMAN AND F. VEERMAN, *An explicit theory for pulses in two component, singularly perturbed, reaction–diffusion equations*, Journal of Dynamics and Differential Equations, 27 (2015), pp. 555–595.

[59] ——, *An explicit theory for pulses in two component, singularly perturbed, reaction–diffusion equations*, Journal of Dynamics and Differential Equations, 27 (2015), pp. 555–595.

[60] M. H. DULAC, *Solutions d'un systém d'équations différétilles dans le voisinage de valeure singuliéres bull*, Soc. Math. France, 40 (1912), p. 324–83.

[61] C. ELPHICK, E. TIRAPEGUI, M. BRACHET, C. P., AND G. IOOSS, *A simple global characterization for normal forms of singular vector fields*, Physica D: Nonlinear Phenomena, 29 (1987), pp. 95 – 127.

[62] R. J. FIELD AND M. BURGER, *Oscillations and traveling waves in chemical systems*, JohnWiley and Sons, (1985).

[63] W. J. FIRTH AND A. J. SCROGGIE, *Optical bullet holes: Robust controllable localized states of a nonlinear cavity*, Phys. Rev. Lett., 76 (1996), pp. 1623–1626.

[64] R. FLETCHER AND M. FORTIN, *Spatial ecology and conservation modelling. Applications with R*, Springer, Berlin, 2018.

[65] P. GANDHI, L. WERNER, S. IAMS, K. GOWDA, AND M. SILBER, *A topographic mechanism for arcing of dryland vegetation bands*, Journal of the Royal Society Interface, 15 (2018), p. 20180508.

[66] P. GANDHI, Y. ZELNIK, AND E. KNOBLOCH, *Spatially localized structures in the Gray–Scott model*, Philosophical Transactions of The Royal Society A Mathematical Physical and Engineering Sciences, 376 (2018), p. 20170375.

[67] J. F. L. GARREC, P. LOPEZ, AND M. KERSZBERG, *Establishment and maintenance of planar epithelial cell polarity by asymmetric cadherin bridges: A computer model*, Developmental Dynamics, 235 (2006), pp. 235–246.

[68] J. F. GIBSON AND T. M. SCHNEIDER, *Homoclinic snaking in plane Couette flow: bending, skewing and finite-size effects*, Journal of Fluid Mechanics, 749 (2016), pp. 530–551.

[69] A. GIERER AND H. MEINHARDT, *A theory of biological pattern formation*, Kybernetik, 12 (1972), pp. 30–39.

[70] A. GOLDBETTER AND G. NICOLIS, *Allosteric enzyme model with positive feedback applied to the glycolytic oscillations*, Progress in Theoretical Biology, (1976), p. 65=160.

[71] P. GRAY AND S. K. SCOTT, *Autocatalytic reactions in the isothermal, continuous stirred tank reactor*, Chem. Eng. Sci, 39 (1984), p. 1087–1097.

[72] V. A. GRIENEISEN, A. F.M.MARÉE, AND L. ØSTERGAARD, *Juicy stories on female reproductive tissue development: Coordinating the hormone flows*, Journal of Integrative Plant Biology, 55, pp. 847–863.

[73] P. GRINDROD, *Models of individual aggregation or clustering in single and multi-species communities*, Journal of Mathematical Biology, 26 (1988), pp. 651–660.

[74] ——, *The theory and applications of reaction-diffusion equations: Patterns and waves*, Clarendon Press, Oxford, second ed., 1996.

[75] S. GUREVICH, S. AMIRANASHVILI, AND H.-G. PURWINS, *Breathing dissipative solitons in three-component reaction-diffusion system*, Physical Review E, 74 (2006), p. 066201.

[76] M. HARAGUS AND G. IOOSS, *Local Bifurcations, Center Manifolds and Normal Forms in Infinite Dimensional Dynamical Systems*, Springer, New York, 2007.

[77] C. HOLLING, *Some characteristics of simple types of predation and parasitism*, Canadian Entomologist, 91 (1959b), pp. 385–398.

[78] C. S. HOLLING, *The functional response of predators to prey density and its role in mimicry and population regulation*, Memoirs of the Entomological Society of Canada, 97 (1965), p. 5–60.

[79] W. R. HOLMES, *An efficient, nonlinear stability analysis for detecting pattern formation in reaction diffusion systems*, Bulletin of Mathematical Biology, 76 (2014), pp. 157–183.

[80] W. R. HOLMES AND L. EDELSTEIN-KESHET, *Analysis of a minimal Rho-GTPase circuit regulating cell shape*, Physical Biology, 13 (2016), p. 046001.

[81] S.-B. HSU, T.-W. HWANG, AND Y. KUANG, *Global analysis of the Michaelis–Menten-type ratio-dependent predator-prey system*, Journal of Mathematical Biology, 42 (2001), pp. 489–506.

[82] G. HUNT, M. PELETIER, A. CHAMPNEYS, P. WOODS, A. WADEE, C. BUDD, AND G. LORD, *Cellular buckling in long structures*, Nonlinear dynamics, 21 (2000), pp. 3–29.

[83] D. IRON, J. WEI, AND M. WINTER, *Stability analysis of Turing patterns generated by the Schnakenberg model*, Journal of Mathematical Biology, 49 (2004), pp. 358–390.

[84] H. JAMGOTCHIAN, N. BERGEON, D. BENIELLI, P. VOGE, B. BILLIA, AND R. GUÉRIN, *Localized microstructures induced by fluid flow in directional solidification*, Phys. Rev. Lett., 87 (2001), p. 166105.

[85] M. R. JEFFREY, *Catastrophe conditions for vector fields and varieties in Rn*, 2022. draft.

[86] A. JILKINE AND L. EDELSTEIN-KESHET, *A comparison of mathematical models for polarization of single eukaryotic cells in response to guided cues*, PLoS computational biology, 7 (2011), p. e1001121.

[87] H. JÖNSSON, M. G. HEISLER, B. E. SHAPIRO, E. M. MEYEROWITZ, AND E. MJOLSNESS, *An auxin-driven polarized transport model for phyllotaxis*, Proceedings of the National Academy of Sciences, 103 (2006), pp. 1633–1638.

[88] J. KLEINE-VEHN AND J. FRIML, *Polar targeting and endocytic recycling in auxin-dependent plant development*, Annual Review of Cell and Developmental Biology, 24 (2008), pp. 447–473.

[89] E. KNOBLOCH, *Spatial localization in dissipative systems*, Annual Review of Condensed Matter Physics, 6 (2015), pp. 325–359.

[90] J. KNOBLOCH, M. VIELITZ, AND T. WAGENKNECHT, *Non-reversible perturbations of homoclinic snaking scenarios*, Nonlinearity, 25 (2012), p. 3469.

[91] T. KOLOKOLNIKOV, W. SUN, AND M. WARD, *The stability of a stripe for the Gierer-Meinhardt model and the effect of saturation*, SIAM J App Dynamical Sys., 5 (2006), pp. 313–363.

[92] S. KONDO AND T. MIURA, *Reaction-diffusion model as a framework for understanding biological pattern formation*, science, 329 (2010), pp. 1616–1620.

[93] B. KOSTET, M. TLIDI, F. TABBERT, T. FROHOFF-HÜLSMANN, S. V. GUREVICH, E. AVERLANT, R. ROJAS, G. SONNINO, AND K. PANAJOTOV, *Stationary localized structures and the effect of the delayed feedback in the Brusselator model*, Philosophical Transactions of the Royal Society A: Mathematical, Physical and Engineering Sciences, 376 (2018), p. 20170385.

[94] G. KOZYREFF AND S. J. CHAPMAN, *Asymptotics of large bound states of localized structures*, Physical Review Letters, 97 (2006), p. 044502.

[95] Y. KUANG AND E. BERETTA, *Global qualitative analysis of a ratio-dependent predator-prey system*, Journal of Mathematical Biology, 36 (1998), pp. 389–406.

[96] R. KUSDIANTARA AND H. SUSANTO, *Homoclinic snaking in the discrete swift-hohenberg equation*, Physical Review E, 96 (2017), p. 062214.

[97] S. P. KUZNETSOV, E. MOSEKILDE, G. DEWEL, AND P. BORCKMANS, *Absolute and convective instabilities in a one-dimensional Brusselator flow model*, The Journal of Chemical Physics, 106 (1997), pp. 7609–7616.

[98] D. LACITIGNOLA, B. BOZZINI, M. FRITTELLI, AND I. SGURA, *Turing pattern formation on the sphere for a morphochemical reaction-diffusion model for electrodeposition*, Communications in Nonlinear Science and Numerical Simulation., 48 (2017), pp. 484–508.

[99] L. LAPIDUS AND G. F. PINDER, *Numerical solution of partial differential equations in science and engineering*, J. Wiley & Sons, 2011.

[100] O. LEYSER, *Auxin, self-organisation, and the colonial nature of plants*, Current Biology, 21 (2011), pp. R331 – R337.

[101] B. LI, F. WANG, AND X. ZHANG, *Analysis on a generalized Sel'kov–Schnakenberg reaction–diffusion system*, Nonlinear Analysis: Real World Applications, 44 (2018), pp. 537 – 558.

[102] Y. LI AND J. JIANG, *Pattern formation of a Schnakenberg-type plant root hair initiation model*, Electronic Journal of Qualitative Theory of Differential Equations, 88 (2018), pp. 1–19.

[103] D. LLOYD AND H. O'FARRELL, *On localised hotspots of an urban crime model*, Physica D: Nonlinear Phenomena, 253 (2013), pp. 23 – 39.

[104] D. LLOYD, B. SANDSTEDE, D. AVITABILE, AND A. CHAMPNEYS, *Localized hexagon patterns of the planar swift-hohenberg equation*, SIAM J. Appl. Dyn. Syst., 7 (2008), pp. 1049–1100.

[105] P. K. MAINI, K. J. PAINTER, AND H. N. P. CHAU, *Spatial pattern formation in chemical and biological systems*, J. Chem. Soc. Faraday Trans., 93 (1997), pp. 3601–3610.

[106] P. K. MAINI, K. J. PAINTER, AND H. N. P. CHAU, *Spatial pattern formation in chemical and biological systems*, J. Chem. Soc. Faraday Trans., 93 (1997), pp. 3601–3610.

[107] P. K. MAINI AND T. E. WOOLLEY, *The Turing model for biological pattern formation*, The dynamics of biological systems, (2019), pp. 189–204.

[108] A. F. M. MARÉE, A. JILKINE, A. DAWES, V. A. GRIENEISEN, AND L. EDELSTEIN-KESHET, *Polarization and movement of keratocytes: A multiscale modelling approach*, Bulletin of Mathematical Biology, 68 (2006), pp. 1169–1211.

[109] N. MCCULLEN AND T. WAGENKNECHT, *Pattern formation on networks: from localised activity to Turing patterns*, Scientific Reports, 6 (2016), pp. 1–8.

[110] A. B. MEDVINSKY, S. V. PETROVSKII, I. A. TIKHONOVA, H. MALCHOW, AND B.-L. LI, *Spatiotemporal complexity of plankton and fish dynamics*, SIAM Review, 44 (2002), pp. 311–370.

[111] M. MEIXNER, A. DE WIT, S. BOSE, AND E. SCHÖLL, *Generic spatiotemporal dynamics near codimension-two turing-hopf bifurcations*, Physical Review E, 55 (1997), pp. 6690–6697.

[112] E. MERON, *Nonlinear Physics of Ecosystems*, CRC Press, 3rd ed., 2015.

[113] ——, *Vegetation pattern formation: The mechanisms behind the forms*, Physics Today, 72 (2019).

[114] D. MIHALACHE, *Localized optical structures: An overview of recent theoretical and experimental developments*, Proceedings of the Romanian Academy Series A - Mathematics Physics Technical Sciences Information Science, 16 (2015), pp. 62–69.

[115] J. MOON, H. CANDELA, AND S. HAKE, *The liguleless narrow mutation affects proximal-distal signaling and leaf growth*, Development, 140 (2013), pp. 405–412.

[116] Y. MORI, A. JILKINE, AND L. EDELSTEIN-KESHET, *Wave-pinning and cell polarity from a bistable reaction-diffusion system*, Biophysical Journal, 94 (2008), pp. 3684–3697.

[117] Y. MORI, A. JILKINE, AND L. EDELSTEIN-KESHET, *Asymptotic and bifurcation analysis of wave-pinning in a reaction-diffusion model for cell polarization*, SIAM Journal on Applied Mathematics, 71 (2011), pp. 1401–1427.

[118] N. MUKHERJEE, S. GHORAI, AND M. BANERJEE, *Effects of density dependent cross-diffusion on the chaotic patterns in a ratio-dependent prey-predator model*, Ecological Complexity, 36 (2018), pp. 276 – 289.

[119] J. MURRAY, *Mathematical Biology II: Spatial Models and Biomedical Applications*, Springer-Verlag, New York, 3rd ed., 2002.

[120] W. NAGATA, H. R. ZANGENEH, AND D. M. HOLLOWAY, *Reaction-diffusion patterns in plant tip morphogenesis: bifurcations on spherical caps*, Bulletin of Mathematical Biology, 75 (2013), pp. 2346–2371.

[121] S. NAGAWA, T. XU, AND Z. YANG, *RHO GTPase in plants*, Small GTPases, 1 (2010), pp. 78–88.

[122] J. J. NIEMELA, G. AHLERS, AND D. S. CANNELL, *Localized traveling-wave states in binary-fluid convection*, Phys. Rev. Lett., 64 (1990), pp. 1365–1368.

[123] Y. NISHURA, *Spatio-temporal chaos for the Gray–Scott model*, Physica D: Nonlinear Phenomena, 150 (2001), pp. 137–162.

[124] A. OKUBU AND S. LEVIN, *Diffusion and ecological problems: modern perspectives*, Springer, New York, 2001.

[125] L. G. P. COLET, M. A. MATÍAS AND D. GOMILA, *Formation of localized structures in bistable systems through nonlocal spatial coupling.*, Physical Review E, 89 (2014), p. 012914.

[126] X. PAN, J. CHEN, AND Z. YANG, *Auxin regulation of cell polarity in plants*, Current Opinion in Plant Biology, 28 (2015), pp. 144 – 153.

[127] P. PARRA-RIVAS, D. GOMILA, L. GELENS, AND E. KNOBLOCH, *Bifurcation structure of localized states in the Lugiato-Lefever equation with anomalous dispersion*, Physical Review E, 97 (2018), p. 042204.

[128] P. PARRA-RIVAS, E. KNOBLOCH, L. GELENS, AND D. GOMILA, *Origin, bifurcation structure and stability of localized states in kerr dispersive optical cavities*, IMA Journal of Applied Mathematics, 86 (2021), pp. 856–895.

[129] P. PARRA-RIVAS, C. MAS-ARABÍ, AND F. LEO, *Parametric localized patterns and breathers in dispersive quadratic cavities*, Physical Review A, 101 (2020), p. 063817.

[130] M. PASCUAL, *Diffusion-induced chaos in a spatial predator-prey system*, Proceedings of the Royal Society of London. Series B: Biological Sciences, 251 (1993), pp. 1–7.

[131] R. PAYNE AND C. GRIERSON, *A theoretical model for rop localisation by auxin in arabidopsis root hair cells*, PLoS ONE, 4 (2009).

[132] B. PEÑA AND C. PÉREZ-GARCÍA, *Stability of turing patterns in the Brusselator model*, Physical Review E, 64 (2001), p. 056213.

[133] S. M. PLOURDE, P. AMOM, M. TAN, A. T. DAWES, AND A. A. DOBRITSA, *Changes in morphogen kinetics and pollen grain size are potential mechanisms of aberrant pollen aperture patterning in previously observed and novel mutants of arabidopsis thaliana*, PLoS Computational Biology, 15 (2019), p. e1006800.

[134] Y. POMEAU, *Front motion, metastability and subcritical bifurcations in hydrodynamics*, Physica D: Nonlinear Phenomena, 23 (1986), pp. 3 – 11.

[135] J. POTTS AND M. LEWIS, *Spatial memory and taxis-driven pattern formation in model ecosystems*, Bulletin of Mathematical Biology, 81 (2019), pp. 1–23.

[136] I. PRIGOGINE AND R. LEFEVER, *Symmetry breaking instabilities in dissipative systems. ii*, Chemical Physics, 48 (1968), pp. 1695–1700.

[137] J. RADEMACHER, *First and second order semistrong interaction in reaction-diffusion systems*, SIAM J. Appl. Dyn. Sys., 12 (2013), pp. 175–203.

[138] D. REINHARDT, T. MANDEL, AND C. KUHLEMEIER, *Auxin regulates the initiation and radial position of plant lateral organs*, The Plant Cell, 12 (2000), pp. 507–518.

[139] M. ROSENZWEIG, *Paradox of enrichment: destabilization of exploitation ecosystems in ecological time*, Science, 171 (1971), pp. 385–387.

[140] M. ROSENZWEIG AND R. MACARTHUR, *Graphical representation and stability conditions of predator-prey interactions*, The American Naturalist, 97 (1963), pp. 209–223.

[141] S. ROY AND J. CHATTOPADHYAY, *The stability of ecosystems: A brief overview of the paradox of enrichment*, Journal of Biosciences, 32 (2007), pp. 421–8.

[142] T. SACHS, *Cell polarity and tissue patterning in plants*, Development, 112 (1991), pp. 83–93.

[143] J. SCHNAKENBERG, *Simple chemical reaction system with limit cycle behavior*, theoretical Biology, 81 (1979), pp. 389–400.

[144] G. SCHNEIDER, *The validity of generalized Ginzburg-Landau equations.*, Mathematical Methods in the Applied Sciences, 19 (1996), p. 717–736.

[145] E. SEL'KOV, *Self-oscillations in glycolysis. 1. a simple kinetic model*, European Journal of Biochemistry, 4 (1968), p. 79—86.

[146] L. J. SHAW AND J. D. MURRY, *Analysis of a model for complex skin pattern*, SIAM Journal on Applied Math, 50 (1990), pp. 628–648.

[147] M. A. SIMON, *Planar cell polarity in the drosophila eye is directed by graded Four-jointed and Dachsous expression*, Development, 131 (2004), pp. 6175–6184.

[148] K. SITEUR, E. SIERO, M. EPPINGA, J. RADEMACHER, A. DOELMAN, AND M. RIETKERK, *Beyond Turing: The response of patterned ecosystems to environmental change*, Ecological Complexity, 20 (2014), pp. 81–96.

[149] J. G. SKELLAM, *Random dispersal in theoretical populations*, Biometrika, 38 (1951), pp. 196–218.

[150] S. SOH, M. BYRSKA, K. KANDERE-GRZYBOWSKA, AND B. A. GRZYBOWSKI, *Reaction -diffusion systems in intracellular molecular transport and control*, Angewandte Chemie, 49 (2017), pp. 4170–4198.

[151] J. C. STRIKWERDA, *Finite Difference Schemes and Partial Differential Equations, Second Edition*, Society for Industrial and Applied Mathematics, 2004.

[152] N. TAYLOR, H. KIM, A. KRAUSE, AND R. VAN GORDER, *A non-local cross-diffusion model of population dynamics I: Emergent spatial and spatiotemporal patterns*, Bulletin of Mathematical Biology, 82 (2020).

[153] D. TILMAN AND P. KAREIVA, *Spatial ecology: the role of space in population dynamics and interspecific interactions*, Princeton University Press, Princeton, NJ, 1997.

[154] J. TYSON AND S. KAUFFMAN, *Control of mitosis by a continuous biochemical oscillation: Synchronization; spatially inhomogeneous oscillations*, Journal of Mathematical Biology, 1 (1975), pp. 289–310.

[155] J. TZOU, Y.-P. MA, A. BAYLISS, B. J. MATKOWSKY, AND V. A. VOLPERT, *Homoclinic snaking near a codimension-two Turing-hopf bifurcation point in the Brusselator model*, Physical Review E, 87 (2013), p. 022908.

[156] J. C. TZOU, Y. NEC, AND M. J. WARD, *The stability of localized spikes for the 1-d Brusselator reaction–diffusion model*, European Journal of Applied Mathematics, 24 (2013), p. 515–564.

[157] H. UECKER AND D. WETZEL, *Numerical results for snaking of patterns over patterns in some 2d Selkov–Schnakenberg reaction-diffusion systems*, SIAM Journal on Applied Dynamical Systems, 13 (2014), pp. 94–128.

[158] K. URSZULA, M. FENDRYCH, AND J. FRIML, *Polar delivery in plants; commonalities and differences to animal epithelial cells.*, Open Biology, 4 (2014), p. 140017.

[159] K. VAN BERKEL, R. J. DE BOER, B. SCHERES, AND K. TEN TUSSCHER, *Polar auxin transport: models and mechanisms*, Development, 140 (2013), pp. 2253–2268.

[160] V. K. VANAG AND I. R. EPSTEIN, *Pattern formation in a tunable medium: The Belousov-Zhabotinsky reaction in an aerosol ot microemulsion*, Phys. Rev. Lett., 87 (2001), p. 228301.

[161] ——, *Segmented spiral waves in a reaction-diffusion system*, Proceedings of the National Academy of Sciences, 100 (2003), pp. 14635–14638.

[162] ——, *Stationary and oscillatory localized patterns, and subcritical bifurcations*, Phys. Rev. Lett., 92 (2004), p. 128301.

[163] V. K. VANAG AND I. R. EPSTEIN, *Pattern formation mechanisms in reaction-diffusion systems*, International Journal of Developmental Biology, 53 (2009), pp. 673–681.

[164] F. VEERMAN, *Breathing pulses in singularly perturbed reaction-diffusion systems*, Nonlinearity, 28 (2015), pp. 2211–2246.

[165] N. VERSCHUEREN AND A. CHAMPNEYS, *A model for cell polarization without mass conservation*, SIAM Journal on Applied Dynamical Systems, 16:4 (2017), pp. 1797–1830.

[166] N. VERSCHUEREN AND A. CHAMPNEYS, *Dissecting the snake: transition from localized patterns to spike solutions*, Physica D, 419 (2021), p. 132858.

[167] L. WANG, *Spatial pattern formation of a ratio-dependent predator prey model*, Chinese Physics B, 19 (2010), p. 090206.

[168] M. J. WARD AND J. WEI, *The existence and stability of asymmetric spike patterns for the Schnakenberg model*, Studies in Applied Mathematics, 109 (2002), pp. 229–264.

[169] J. WEI AND M. WINTER, *Stationary multiple spots for reaction–diffusion systems*, Journal of Mathematical Biology, 57 (2008), pp. 53–89.

[170] M. WEI, J. WU, AND G. GUO, *Steady state bifurcations for a glycolysis model in biochemical reaction*, Nonlinear Analysis: Real World Applications, 22 (2015), pp. 155 – 175.

[171] P. D. WOODS AND A. R. CHAMPNEYS, *Heteroclinic tangles and homoclinic snaking in the unfolding of a degenerate reversible hamiltonian-hopf bifurcation*, Journal of Physics D, 129 (1999), pp. 170–174.

[172] T. WOOLLEY, A. KRAUSE, AND E. GAFFNEY, *Bespoke turing systems*, Bulletin of Mathematical Biology, 83 (2021).

[173] B. WUYTS, A. CHAMPNEYS, AND J. HOUSE, *Amazonian forest-savanna bistability and human impact*, Nature Communications, 8 (2017), p. 15519.

[174] D. XIAO AND L. S. JENNINGS, *Bifurcations of a ratio-dependent predator-prey system with constant rate harvesting*, SIAM Journal on Applied Mathematics, 65 (2005), pp. 737–753.

[175] D. XIAO AND S. RUAN, *Global dynamics of a ratio-dependent predator-prey system*, Journal of Mathematical Biology, 43 (2001), pp. 268–290.

[176] T. XU, M. WEN, S. NAGAWA, Y. FU, J.-G. CHEN, M.-J. WU, C. PERROT-RECHENMANN, J. FRIML, A. M. JONES, AND Z. YANG, *Cell surface- and Rho GTPase-based auxin signaling controls cellular interdigitation in arabidopsis*, Cell, 143 (2010), pp. 99 – 110.

[177] L. YANG, M. DOLNIK, A. M. ZHABOTINSKY, AND I. R. EPSTEIN, *Pattern formation arising from interactions between turing and wave instabilities*, The Journal of Chemical Physics, 117 (2002), pp. 7259–7265.

[178] A. YOCHELIS AND A. GARFINKEL, *Front motion and localized states in an asymmetric bistable activator-inhibitor system with saturation*, Physical Review E, 77 (2008), p. 035204.

[179] Y. ZELNIK, P. GANDHI, E. KNOBLOCH, AND E. MERON, *Implications of tristability in pattern-forming ecosystems*, Chaos, 28 (2018), p. 033609.

[180] Y. ZELNIK, H. UECKER, U. FEUDEL, AND E. MERON, *Desertification by front propagation?*, Journal of Theoretical Biology, 418 (2017), pp. 27 – 35.

[181] Y. R. ZELNIK, E. MERON, AND G. BEL, *Localized states qualitatively change the response of ecosystems to varying conditions and local disturbances*, Ecological Complexity, 25 (2016), pp. 26 – 34.

[182] J. ZHOU AND J. SHI, *Pattern formation in a general glycolysis reaction–diffusion system*, IMA Journal of Applied Mathematics, 80 (2015), pp. 1703–1738.

[183] C. ZMURCHOK AND W. R. HOLMES, *Simple Rho GTPase dynamics generate a complex regulatory landscape associated with cell shape*, Biophysical Journal, 118 (2020), pp. 1438–1454.